On flexible Green function methods for atomistic/continuum coupling

THÈSE N^{O} 8829 (2018)

PRÉSENTÉE LE 7 SEPTEMBRE 2018
À LA FACULTÉ DES SCIENCES ET TECHNIQUES DE L'INGÉNIEUR
LABORATOIRE DE MODÉLISATION MÉCANIQUE MULTI-ÉCHELLE
PROGRAMME DOCTORAL EN MÉCANIQUE

ÉCOLE POLYTECHNIQUE FÉDÉRALE DE LAUSANNE

POUR L'OBTENTION DU GRADE DE DOCTEUR ÈS SCIENCES

PAR

Max Ludwig HODAPP

acceptée sur proposition du jury:

Prof. J.-F. Molinari, président du jury
Prof. W. Curtin, directeur de thèse
Prof. D. Kochmann, rapporteur
Prof. L. Pastewka, rapporteur
Dr G. Anciaux, rapporteur

ÉCOLE POLYTECHNIQUE
FÉDÉRALE DE LAUSANNE

Suisse
2018

It was supposed to take two days.
— Ben S.

To my parents…

Acknowledgements

First, I would like to thank Prof. William Curtin for introducing me to the field of atomistic/continuum coupling and, more broadly, to nanoscale plasticity. The trust in my work and the provided academic freedom gave me the opportunity to explore this fascinating area of research based on personal interest and style which I highly appreciate. Furthermore, his advice and exceptional physical intuition was an indispensable help for me to keep focused and not to delve into gratuitous details. Additionally, I am greatly indebted for his understanding and support during my longterm injury in 2016.

I wish to express my gratitude to Guillaume Anciaux who accompanied my entire journey as a sort of second advisor. His guidance, especially on many aspects in computer science, tremendously helped me to improve my programming skills and scientific writing. I highly enjoyed our endless stimulating and detailed discussions which hopefully continue in the future. Moreover, I would like to thank the other members of the jury, namely Prof. Jean-François Molinari, Prof. Dennis Kochmann and Prof. Lars Pastewka, for revising the thesis and the fruitful discussions during several meetings and conferences.

Further, I would like to express my thanks to the "LAMMM family" for the friendly and relaxing atmosphere during the many scientific discussions and other social activities that we shared. Specifically, I would like to thank all members who were involved in the CADD-3d project, and, therefore, contributed to this thesis in one way or the other, including Fabio Pavia, Ben Szajewski, Phil Moseley, Till Junge and Jaehyun Cho. In addition, I thank Markus Stricker for proofreading parts of the present manuscript.

Last, I would like to thank all my friends and my family. Their help and understanding was crucial to me, especially in phases when I was stuck. In particular, I thank my parents for their unconditionally strong support.

Lausanne, July 2018 Max Hodapp

Abstract

Atomistic/continuum (A/C) coupling schemes have been developed during the past twenty years to overcome the vast computational cost of fully atomistic models, but have not yet reached full maturity to address many problems of practical interest. This work is therefore devoted to the development and analysis of flexible Green function methods for A/C coupling. Thereby, the Green function of the harmonic crystal is computed a priori and subsequently employed during the simulation of a fully nonlinear atomistic problem to update its boundary conditions on-the-fly, based on the motion of the atoms and without the need of an explicit numerical discretization of the bulk material.

The first part is devoted to the construction of a discrete boundary element method (DBEM) which bears several advantages over its continuous analog, i.a. nonsingular Green kernels and direct application to nonlocal elasticity. As is well-known from integral problems, the DBEM leads to dense system matrices which become quickly unfeasible due to their quadratic complexity. To overcome this computational burden, an implicit approximate representation using hierarchical matrices is proposed which have proven their efficiency in the context of boundary integral equations while preserving overall accuracy. In order to solve the coupled atomistic/DBEM problem, several staggered and monolithic solution procedures are assessed. An improvement of the overall accuracy by several orders of magnitude is found in comparison with naive clamped boundary conditions.

To further account for plasticity in the continuum domain the coupled atomistic/discrete dislocations (CADD) method is examined, including the treatment of hybrid dislocation lines that span between the two domains. In particular, a detailed derivation of a quasi-static problem formulation is covered and a general algorithm to simulate the motion of the hybrid dislocations along A/C interfaces is presented. In addition, to avoid solving the complementary elasticity problem, a simplified solution procedure, which updates the boundary conditions based on the Green function of the entire dislocation network for obtaining accurate stress and displacement fields, is introduced and validated. The test problem consists of the bowout of a single dislocation in a semi-periodic box under an applied shear stress, and excellent results are obtained in comparison to fully-atomistic solutions of the same problem.

Keywords: Multiscale modeling; Model reduction; Atomistic/continuum coupling; Flexible boundary conditions; Lattice Green function; Discrete boundary element method; Hierarchical matrices; Plasticity; Dislocations

Résumé

Plusieurs méthodes de couplage atomique/continu (A/C) ont été développées au cours des vingt dernières années afin de surmonter l'énorme coût de calcul des modèles entièrement atomiques, mais elles sont toujours trop limitées pour permettre de résoudre de nombreux problèmes d'intérêt pratique. Cette thèse se concentre donc sur le développement et l'analyse de méthodes flexibles de couplage A/C, basées sur des fonctions de Green. Ce faisant, la fonction de Green d'un cristal harmonique est calculée et utilisée pour la mise à jour des conditions aux limites d'un problème atomique non linéaire. Ce couplage ne discrétise donc pas le continuum qui entoure le domaine atomique et s'appuie uniquement sur le déplacement des atomes.

La première partie est consacrée à la construction d'une méthode d'éléments de frontière discrète (DBEM) qui présente plusieurs avantages par rapport à son analogue continu: les noyaux de Green discrets sont non singuliers et ils peuvent prendre en compte les problèmes d'élasticité non-locale. Comme cela est bien connu des équation intégrales, la DBEM contient des matrices denses qui deviennent rapidement trop grandes pour pouvoir être manipulées (complexités quadratiques de leurs tailles). Pour surmonter ce coût de calcul, une représentation approximative basée sur des matrices hiérarchiques est proposée, car, pour des équations intégrales, l'efficacité de ces dernières à été démontrée tout en préservant la précision globale. Afin de résoudre un problème couplé atomistique/DBEM, plusieurs procédures de résolutions alternées et monolithiques sont proposées et évaluées. Une amélioration de la précision globale (de plusieurs ordres de grandeurs) est obtenue par rapport aux résolutions qui utilisent des conditions aux limites naïves.

Pour tenir compte de la plasticité dans un milieu continu, la méthode de couplage entre dislocations discrètes et atomiques (CADD) est examinée, y compris concernant le traitement des lignes de dislocations hybrides qui s'étendent entre les deux milieux. En particulier, la dérivation détaillée d'une formulation du problème quasi-statique est présentée ainsi qu'un algorithme général simulant le mouvement des dislocations hybrides le long des interfaces A/C. De plus, pour éviter de résoudre le problème d'élasticité complémentaire, une procédure simplifiée est introduite et validée. Cette dernière met à jour les conditions aux limites du réseau de dislocations complets grâce à une fonction Green, permettant d'obtenir des champs de contrainte et de déplacement précis. Le problème consistant en une unique boucle de dislocation dans un milieu semi-périodique évoluant du fait de l'application d'une contrainte de cisaillement est considéré. D'excellents résultats sont mis en évidence par comparaison à des solutions entièrement atomiques du même problème.

Mots clés: Modélisation multi-échelle; Réduction de modèle; Couplage atomique/continu; Conditions aux limites flexibles; Fonction de Green d'un réseau; Méthode d'éléments de frontière discrète; Matrices hiérarchiques; Plasticité; Dislocations

Contents

Acknowledgements **v**

Abstract (English/Français) **vii**

List of figures **xv**

List of tables **xix**

Introduction **1**

Notation **7**

1 Modeling plasticity across different length scales **11**

- 1.1 Overview . . . 11
- 1.2 Dislocations as the main carrier of plasticity . . . 13
- 1.3 Classical continuum mechanics . . . 14
  - 1.3.1 Kinematics and balance equations . . . 15
  - 1.3.2 Constitutive modeling . . . 18
  - 1.3.3 Phenomenological plasticity models . . . 20
- 1.4 Discrete dislocations dynamics . . . 21
  - 1.4.1 Configurational material forces . . . 21
  - 1.4.2 Dislocations as eigenstrains in elastic continua . . . 24
  - 1.4.3 Dislocation core energy — how to deal with the singularity . . . 29
  - 1.4.4 Informing classical plasticity models from discrete dislocations dynamics simulations . . . 34
- 1.5 Atomistic modeling . . . 35
  - 1.5.1 Molecular statics . . . 35
  - 1.5.2 Interatomic potentials . . . 37
  - 1.5.3 Boundary conditions on atomistic problems . . . 38
  - 1.5.4 Calibration of the dislocation core energy to atomistic results . . . 40

2 Flexible boundary conditions for atomistic problems **43**

- 2.1 Introduction . . . 43
- 2.2 Problem statement . . . 44

2.3 Force-based atomistic/continuum coupling . . . 45
  2.3.1 Linearization of the atomistic model . . . 45
  2.3.2 Lattice Green function . . . 47
  2.3.3 Domain decomposition . . . 48
2.4 Revisiting Sinclair's method . . . 49
2.5 Discrete boundary element method for atomistic/continuum coupling . 53
  2.5.1 Rigorous derivation of a boundary summation equation for the application to monolithic solvers . . . 53
  2.5.2 Symmetric discrete boundary element method . . . 57
  2.5.3 Computation of stresses inside the body . . . 60
  2.5.4 Bounded problems . . . 61
2.6 Implementation of the discrete boundary element method . . . 63
  2.6.1 Algebraic discrete boundary element method . . . 63
  2.6.2 Approximation of the lattice Green functions . . . 64
  2.6.3 Data sparse approximation of the boundary matrices . . . 65
2.7 Iterative solution procedures for the coupled problem . . . 69
  2.7.1 Staggered schemes . . . 69
  2.7.2 Monolithic stabilized Newton-GMRes solver . . . 70
  2.7.3 Computer implementation . . . 75
  2.7.4 Algorithmic comparison . . . 76

3 Coupled atomistic and discrete dislocations in three dimensions 79
3.1 Motivation . . . 79
3.2 Coupled atomistic and discrete dislocations in two dimensions . . . 80
3.3 Challenges . . . 83
  3.3.1 Concept of hybrid dislocations . . . 83
  3.3.2 Dislocation motion . . . 86
3.4 Dislocation detection in atomistic systems . . . 87
  3.4.1 Detection based on continuum kinematics . . . 87
  3.4.2 Detection based on discrete Burgers circuits . . . 88
  3.4.3 Examples . . . 90
3.5 Dislocation core templates . . . 93
3.6 Problem formulation . . . 97
  3.6.1 Assumptions . . . 97
  3.6.2 Governing equations . . . 100
3.7 Semi-monolithic solution procedure . . . 102
3.8 Simplified solution procedure . . . 107
  3.8.1 Approximation of the coupled problem . . . 107
  3.8.2 Updated Green function method . . . 109
3.9 Computational complexity compared to related methods . . . 112
3.10 Computer implementation . . . 115

4 Computational results 117
4.1 Validation of the discrete boundary element method 117
4.1.1 Two-dimensional test cases for hexagonal lattices 117
4.1.1.1 Vacancy relaxation 118
4.1.1.2 Dislocation core relaxation 120
4.1.1.3 Spurious stresses on dislocations near interfaces 122
4.1.2 Three-dimensional test cases for face-centered cubic lattices . . . 125
4.1.2.1 Void relaxation 125
4.1.2.2 Void growth under uniaxial tension 127
4.2 Validation of the updated Green function method 128
4.2.1 Reference problem 128
4.2.2 Comparison with a fully coupled scheme 131
4.3 Validation of CADD-3d for hybrid dislocations 132
4.3.1 Reference problem 132
4.3.2 Line tension model 133
4.3.3 Atomistic and discrete dislocation dynamics reference solutions . 134
4.3.4 CADD-3d problem 137
4.3.5 Assessment of CADD-3d 139

5 Conclusions 145

A Appendix 151
A.1 Green functions in anisotropic media 151
A.1.1 General solution 152
A.1.2 Isotropic solution 152
A.1.3 Principle of superposition 153
A.2 Green functions for straight dislocations 153
A.2.1 Isotropic solution for screw dislocations 154
A.2.2 Isotropic solution for edge dislocations 154
A.2.3 Isotropic solution for mixed dislocations 155
A.2.4 General solution 155
A.2.5 Periodic arrays of straight dislocations 156
A.3 Green functions for curved dislocations 159
A.3.1 Triangular dislocation loops 159
A.3.2 Periodic arrays of bowing dislocations 162
A.4 Lattice Green functions 163
A.4.1 Construction of $\boldsymbol{G}^{\mathrm{lgf}}$ 163
A.4.2 Lattice Green function for linear elasticity 164
A.4.3 Error estimates 165

Bibliography 181

Glossary 183

List of Figures

1 Schematic illustration of the hierarchical multiscale approach to plasticity; the second image from left is reprinted by courtesy of Dr. Stefan Sandfeld; the rightmost two images are reprinted from (Fritzen and Hodapp, 2016) by courtesy of John Wiley and Sons 2

1.1 Computational methods for modeling plasticity on various length scales 12
1.2 (a) Screw and edge dislocations in a simple cubic lattice. (b) Formation of a dislocation network in a nanobeam (by courtesy of Dr. Wolfram Nöhring) 14
1.3 Schematic illustration of the deformation of a continuous material body 15
1.4 Schematic illustrations of typical stress strain curves for (a) cyclic loading and an isotropic hardening model, (b) cyclic loading and kinematic hardening and (c) for uniaxial tension and different specimen sizes . . . 21
1.5 Schematic illustration of the motion of a material body for the small strain DDD problem. The dislocation line γ is depicted as an infinite straight line 25
1.6 (a) Unit cells for an fcc and a bcc lattice. (b) Schematic illustration of the interaction range $\mathcal{R}_\xi$ of interatomic potentials 36
1.7 (a) Schematic illustration of the nonconvex energy landscape of atomistic models. (b) Morse potential from Example 1.6 as a function of the (here: scalar) differential displacement 38
1.8 (a) E^{core} as a function of the outer radius R. (b) Total atomistic, elastic and continuum (:= elastic + core contribution) energies vs. $\ln\left(R/r_{\mathrm{cut}}^{\mathrm{core}}\right)$. 41

2.1 Partition of an atomistic domain in parts which contain material defects and parts which undergo small deformations 44
2.2 Schematic illustration of the problem decomposition (2.21) into a finite nonlocal/nonlinear atomistic region (here: third nearest neighbor interactions) and an infinite but local/linear continuum bulk region (the domain $\mathit{\Lambda}^{\mathrm{i\text{-}}}$ will be defined in Section 2.5.2) 49
2.3 Abstract formulation of Sinclair's algorithm 51
2.4 (a) Bounded domain with interface $\mathit{\Lambda}^{\mathrm{I}}$. (b) Atomistic/continuum domain decomposition for bounded problems 61
2.5 (a) Interface and pad region $\mathit{\Lambda}^{\mathrm{i}}$ and $\mathit{\Lambda}^{\mathrm{p}}$ of a spherical computational domain ($\mathit{\Lambda}^{\mathrm{a}} \setminus \mathit{\Lambda}^{\mathrm{i}}$ not shown). (b) A realistic hierarchical partitioning for the matrix corresponding to the last value in Figure 2.6, where $3N^{\mathrm{i}} = 263718$ 67

2.6 Memory consumption for the matrix $\hat{G}^{\mathrm{i/i}}$ when using the hierarchical approximation, opposed to the dense version 68

2.7 Data processing steps of the A/DBEM coupling. **Offline phase**: computation of the system matrices. **Online phase**: solution of the coupled problem (Algorithm 3) 75

2.8 (a) Relative error (2.120) inside the atomistic domain for the force quadrupole problem defined in Section 2.7.4. (b) Residual vs. global iteration for the Schwarz and Sinclair's method for the particular case of $r_{\mathrm{cut}} = 7$ 77

3.1 (a) Domain decomposition of a material body into an atomic lattice Λ^{a} and a continuum domain Ω^{c} at time $t = t_0$. (b) Domain decomposition after the dislocation has evolved into the (former) continuum region at $t_1 > t_0$ 79

3.2 a) Schematic illustration of the evolution of one-dimensional chain of atoms. b) The equivalent CADD problem 81

3.3 Schematic illustration of the characteristic feature of CADD: a) Detection of a dislocation in the atomistic domain. b) Passing of the detected dislocation to the continuum region as a discrete entity. The left figure is reprinted from Warner et al. (2007) with permission from Springer Nature 83

3.4 Schematic illustration of the boundary value problem for CADD-3d . . . 84

3.5 Spurious forces on boundary atoms in the vicinity of a hybrid dislocation due to a continuum solution with compact core structure; the atoms are colored according to their centrosymmetry parameter (CSP, Kelchner et al., 1998) 85

3.6 (a) Evolution of a hybrid dislocation along Γ_{i}. (b) Dislocation moving beyond Γ_{i}, thus eventually becoming a hybrid dislocation 86

3.7 Schematic illustration of the identification of the reference lattice vectors corresponding to the lattice vectors in the current configuration 89

3.8 (a) DXA dislocation detection. (b) Perfect lattice. (c) CADD dislocation detection 92

3.9 Detection of full and partial dislocations in FCC lattices 92

3.10 (a) Projection of the lattice sites according to (3.11) for an fcc lattice. (b) Application range of the core template 94

3.11 Schematic illustration of the boundary value problem for CADD-3d . . . 100

3.12 Schematic illustration of the problem decomposition of $\mathcal{P}^{\mathrm{cadd}}$ (3.38) corresponding to the semi-monolithic solution procedure from Section 3.7 104

3.13 Artificial boundary conditions on the physical subproblem $\mathcal{P}^{\mathrm{p}}$ from Algorithm 5, line 4, at any iteration j of the numerical solver 106

3.14 Schematic illustration of the semi-monolithic algorithm for CADD-3d . . 107

3.15 Schematic illustration of the problem decomposition of the *approximate* problem $\tilde{\mathcal{P}}^{\mathrm{cadd}}$ (3.38) corresponding to the solution procedure from Section 3.8.1 . . . 109
3.16 Schematic illustration of the updated Green function algorithm for CADD-3d . . . 110
3.17 DDD simulation of a Frank-Read source which is subjected to an applied shear stress τ; the figure is used by courtesy of Dr. Markus Stricker . . . 114

4.1 Schematic illustration of the domain decomposition for (a) the vacancy problem, (b) the dislocation problem . . . 118
4.2 (a) Energy error vs. number of real atoms N^{a} for the vacancy problem for clamped and flexible boundary conditions. (b) Number of force evaluations corresponding to each data point in (a) . . . 119
4.3 (a) Energy error vs. number of real atoms N^{a} for the dislocation problem for clamped and flexible boundary conditions. (b) Number of force evaluations corresponding to each data point in (a) . . . 121
4.4 (a) Schematic view of the dislocation halting at a distance d from the artificial interface. (b) Spurious stress $\sigma_{12}^{\mathrm{sp}}(d) = \sigma_{12}^{\mathrm{app}}(d) - \sigma_{12}^{\mathrm{peierls}}$ as a function of d . . . 123
4.5 Illustration of an fcc lattice containing a void subject to a uniaxial remote tensile stress . . . 126
4.6 (a) Energy error vs. number of real atoms N^{a} for the void problem for clamped and flexible boundary conditions. (b) Number of force evaluations corresponding to each data point in (a) . . . 127
4.7 (a) Converged microstructure of a nanovoid under uniaxial tension when using flexible and clamped boundary conditions; the coloring of the real atoms is according to the centro-symmetry parameter CSP (Kelchner et al., 1998) (only atoms with $CSP > 5$ are shown in the fully atomistic domain). (b) Corresponding dislocation network as predicted by the DXA within Ovito (Stukowski, 2010, `www.ovito.org`) . . . 128
4.8 Schematic illustration of the numerical test to determine the spurious stress exerted on an edge dislocation near artificial interfaces. The reference configuration is given in (a). Subsequently a predictor for an edge dislocation is applied to the reference configuration in (b). An applied shear stress τ^{app} will eventually move the dislocation to the stable position in (c) . . . 129
4.9 Spurious stress τ_{SP} on a stable edge dislocation as a function of its distance to the artificial interface d . . . 131
4.10 Schematic illustration of the bow-out of a nominal straight dislocation for (a) the coupled CADD-3d problem, (b) the fully atomistic model (only the atoms in the core region are visualized), and (c) the continuum DDD model 133

4.11 Comparison between fully atomistic calculations and the continuum model (solid line) for different applied shear stresses 137
4.12 Schematic top view of the domain decomposition for the PAD geometry (a). A side view along the dislocation line direction is shown in (b) to illustrate where the detection algorithm generates nodal positions of γ^{a} (the interface node is located in region 1, its neighboring node in region 2 etc.) 138
4.13 Solution of the coupled problem for $w_{\mathrm{a}} = l_1/4$ for different choices of the transmission node $\boldsymbol{s}^{\mathrm{trans}}$ (a)-(c). Real and pad atoms are highlighted with respect to the centrosymmetry parameter (CSP Kelchner et al., 1998) according to (d) 141
4.14 Solution of the coupled problem for $w_{\mathrm{a}} = l_1/2$. Real and pad atoms are highlighted with respect to the centrosymmetry parameter (CSP Kelchner et al., 1998) according to Figure 4.13 (d) 142
4.15 Solution of the coupled problem for $w_{\mathrm{a}} = l_1/4$ using the classical Volterra solution in the core region. Real and pad atoms are highlighted with respect to the centrosymmetry parameter (CSP Kelchner et al., 1998) according to Figure 4.13 (d) 142

A.1 Example for a triangular dislocation loop 160
A.2 Schematic illustration of the summation scheme for the computation of the elastic displacement field of periodic arrays of curved dislocations . 163
A.3 Simplicial partitioning of various Bravais lattice types 164
A.4 Absolute and relative errors of the CGF when compared to the LGF . . . 165

List of Tables

1.1 Three modeling approaches for the dislocation core energy corresponding to Example 1.3, 1.4 and 1.5 . . . 30

3.1 Complexity estimates for the QC method and CADD-3d (with FEM or DBEM); it is assumed that CADD-3d uses fast summation methods . . . 113

4.1 Number of force evaluations corresponding to the Newton-GMRes and Sinclair's method for the moving dislocation problem from Figure 4.4 . . 124
4.2 Error in the bow-out between the hybrid dislocation and the detected atomistic dislocation from the reference calculation. The third column specifies the width w of the domain over which the error is measured . . 143

Introduction

Motivation

The mechanical behavior of metals underpins the structural performance of components and systems across the entire spectrum of modern technologies. With new demands on material performance per unit cost or weight increase, there is a decisive need to understand the origins of mechanical behavior as well as a need to design new materials with improved properties (e.g. yield strength, ductility, fatigue or corrosion resistance). This in turn requires a thorough understanding of the crystalline picture of the metal which is usually perturbed by "defects", i.e. vacancies, solutes, dislocations or grain boundaries, which break the symmetry of the lattice structure. Although the word defect suggests some negative influence, their presence is highly useful for enabling plastic flow in manufacturing which can prevent failure of the material due to brittle fracture. Understanding their fundamental mechanisms is thus inevitable to tune the material properties, i.e. by controlling the behavior of the defects through solid solution strengthening or precipitation hardening.

"Crystals are like people, it is the defects in them which tend to make them interesting!"
— Sir Frederick Charles Frank (1911-1998)

Predictive mathematical tools for modeling plasticity at different length scales began to develop in the beginning of the last century. The current theoretical frameworks can be hierarchically grouped into nano-, meso-, micro- and macroscale models, describing phenomena across scales from individual dislocation motion in nanometer specimens to accumulated plastic flow in large structures (c.f. Figure 1). It is now widely recognized that "plasticity" depends on the size of the region being deformed, generally obeying the adage "smaller is stronger". Such size effects are due to the fundamental structuring of the dislocation defects over mesoscopic scales on the order of microns.

Classical atomistic modeling has become a highly valuable tool for studying material properties on the nanoscale (Frenkel and Smit, 1996). With the development of modern high-performance computer architectures, these methods have seen great attention over the past 20 twenty years in computational physics and related fields. The fundamental

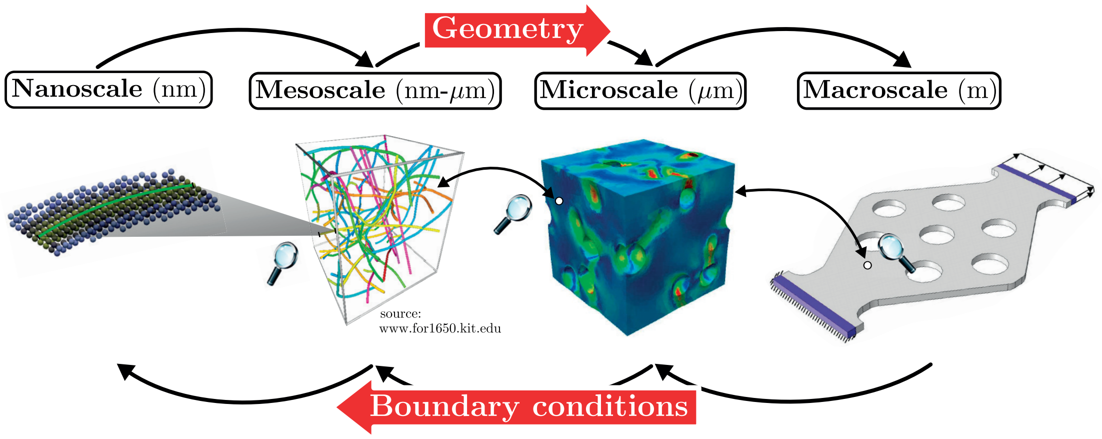

Figure 1: Schematic illustration of the hierarchical multiscale approach to plasticity; the second image from left is reprinted by courtesy of Dr. Stefan Sandfeld; the rightmost two images are reprinted from (Fritzen and Hodapp, 2016) by courtesy of John Wiley and Sons

mechanisms for the formation, evolution and annihilation of dislocations are intrinsically atomistic phenomena which can therefore be considered as an "ab initio" method for plasticity. However, treating atoms individually comes along with high computational cost with increasing simulation sizes (which are needed to describe the bulk behavior), especially in three dimensions, that are beyond the scope of state-of-the-art supercomputers. Capturing plasticity at several scales therefore requires the development and use of multiscale models.

The discrete dislocation dynamics (DDD) method has been developed to study metal plasticity at the mesoscale by following the collective motion of complex dislocation arrays. The DDD method must be informed by rules/laws regarding dislocation mobility, dislocation reactions, and interactions of dislocations with metallurgical defects. Atomistic simulations can be used to provide the necessary input in many simple cases. This so-called "hierarchical method" relies, however, on the strong assumption that there exists a clear separation of scales of phenomena. However, dislocation nucleation and interactions with defects (crack tips, voids, solutes, grain boundaries) involves an inherently atomistic response that can be difficult to characterize at the level of discrete dislocation line defects. The issue of scale separation requires the development of so-called "concurrent" methods that seamlessly integrate material descriptions at several scales within a single computational framework. This can be accomplished by a systematic coarse-graining of the fully atomistic description to reduce the order of the problem while retaining fully atomistic refinement only where necessary, e.g. near a crack tip or an indenter.

Existing approaches

In order to reduce the prohibitive computational cost of atomistic models order reduction methods have been developed over the past decades. The two most common approaches are:

- Reducing the solution space by choosing a subset of representative atoms. Atoms not considered in this subset are only *implicitly* defined via interpolation between neighboring representative atoms.
- Reducing the complexity of the fully nonlinear/nonlocal atomistic model by a linearization of the atomic interactions.

Both approaches are usually combined in regions where the deformation is homogeneous such that the atomistic model behaves like a smooth continuum. The idea of an atomistic/continuum (A/C) coupling of mechanical fields wherein all inelastic phenomena are contained only in a region with full atomistic resolution goes back to the work of Sinclair (1971, 1975) who studied the behavior of isolated crystalline defects. In order to take complex boundary conditions into account Kohlhoff and Schmauder (1989) and Kohlhoff et al. (1991) coupled a fully atomistic region to a discretized continuum problem which was solved via the finite element method (FEM). The first fully variational A/C coupling scheme was introduced by Tadmor et al. (1996) who coined the prominent term *quasicontinuum* (QC) method. The original QC method was succeeded by a plethora of approaches, i.a. by Knap and Ortiz (2001); Xiao and Belytschko (2004); Shimokawa et al. (2004); Kochmann and Venturini (2014) and Amelang et al. (2015), and continue to evolve today. These methods mainly differ in their coarse-graining techniques and numerical treatment.

For isolated defects embedded in an effectively infinite domain the method by Sinclair and co-workers remains to be among the most popular approaches. Therein, the continuum domain is evolved by means of predefined Green functions akin to the exterior boundary element method (BEM, Brebbia, 1978) which was developed around the same period of time. Contrary to the above-named QC methods it does not require an explicit discretization of the continuum domain and does therefore not introduce any error due to mesh coarsening. To date, the method has been successfully applied to dislocation (Sinclair et al., 1978; Rao et al., 1998) or crack problems (Sinclair, 1975).

Extending the methods to handle dislocation plasticity in the continuum domain, and with nearly seamless passing of dislocations back and forth between atomistic and continuum domains, was achieved in the two-dimensional plane strain limit by the *coupled atomistic and discrete dislocations* (CADD) method (Shilkrot et al., 2002a, 2004; Miller et al., 2004). In two dimensions, where the dislocation line direction is perpendicular to the plane of analysis, the individual dislocations are wholly contained within the atomistic domain or the DDD domain. While three dimensional methods can also handle dislocations solely in both domains, there has been no practical method for dealing with the full problem wherein individual dislocation lines exist in *both* domains simultaneously, so-called **hybrid dislocations**. Since many dislocation phenomena occur in three dimensions, the development of a full three dimensional CADD method provides powerful new capability for realistic multiscale simulation of dislocation plasticity.

Syllabus

In this work, the development of a CADD method in three dimensions (henceforth CADD-3d) is addressed. This method was first mentioned by Junge (2014) and later conceptually defined in a series of papers by Anciaux et al. (2018); Hodapp et al. (2018a); Cho et al. (2018). The transition region of a hybrid dislocation between atomistic and continuum-line representations is accomplished through a **template** imposed at the A/C interface that enriches the continuum-line description with an atomistic description of the dislocation core structure. This template thus approximates the atomistic environment that the atomistic system would have if embedded in a fully atomistic domain, and thus minimizes coupling errors at the crucial core region of the dislocation as the line passes from one description to the other. This enables the atomic region to experience accurate forces from the dislocation(s) spanning both domains. This key feature of CADD-3d is discussed within the quasi-static formulation of Hodapp et al. (2018a) which is rigorously derived and critically assessed. To solve the coupled problem numerically, a novel *semi-monolithic scheme* is introduced which iterates between the physical subproblem (i.e. with respect to the atomistic *and* continuum displacements) and the DDD problem. Furthermore, an approximate solution procedure is proposed which is simple to implement and valid in infinite domains, and when the atomistic domain only contains dislocations (no other defects).

The *semi-monolithic scheme* requires a numerical solver for the standard A/C problem. Since CADD does not require re-meshing, Green function techniques are eminently suitable, given that one is usually *only* interested in resolving *atomic* degrees of freedom during post-processing. Several Green function methods have been proposed in (Hodapp et al., 2018c) including a variant of Sinclair's method and an atomistic problem coupled with a **discrete boundary element method** (atomistic/DBEM). These methods will be analyzed in detail on an abstract and algebraic level. To overcome the problem of memory consumption due to the dense boundary matrices, hierarchical matrices ($\mathscr{H}$-matrices Hackbusch, 1999, 2015) are exploited which provide an efficient means for approximating the system matrices, emerging from the Green function methods, and the corresponding linear algebraic operations for *general* interfaces with almost linear complexity. Their implementation into existing MD codes will be shown.

The work is organized as follows:

Chapter 1 serves as an introduction to the relevant models which are used throughout this work. The basic equations for classical continuum mechanics, DDD and atomistics are presented in detail in Section 1.3-1.5. Their individual role in computational plasticity is outlined. Weaknesses and strengths of each model are highlighted and a connectivity between the length scales is established by providing details about individual constitutive calibration from lower-scale models.

In Chapter 2 several Green function methods for A/C coupling are developed. Attention is drawn to problems containing a finite atomistic region, surrounded by an infinite continuum domain. First, a new representation of Sinclair's method is derived in Section 2.4 by an operator splitting technique which separates the *infinite* harmonic and the *finite* anharmonic subproblem. Starting from Sinclair's iteration equation for the displacements, the DBEM is rigorously derived and analyzed in Section 2.5. Subsequently, the algebraic problem is investigated in Section 2.6 and practical guidance regarding its implementation will be given. Various solution procedures for the coupled problem are presented in Section 2.7 including a memory efficient version of Sinclair's method and a monolithic Newton-Krylov solver. An extension of the methodology to bounded continuum domains is given in Section 2.5.4.

Chapter 3 covers the implementation of CADD-3d. The notation is self-contained such that experienced readers who are already familiar with the underlying fundamentals from Chapter 1 may directly jump here. The necessary ingredients of the method, namely the dislocation detection algorithm and the construction of the core templates, are discussed in Section 3.4 and Section 3.5, respectively. The quasi-static boundary value problem for CADD-3d is derived in Section 3.6 and the corresponding numerical solution algorithms are presented in Section 3.7 and Section 3.8. Computer implementation aspects will be discussed in Section 3.10.

In Chapter 4 the methods proposed in Chapter 2 and Chapter 3 are validated with numerical experiments. The accuracy and efficiency of the general atomistic/DBEM coupling is examined in Section 4.1 by studying various practical test cases for (quasi-)static equilibration of isolated and moving defects in two and three dimensions. Subsequently, the simplified solution procedure proposed in Section 3.8 is assessed in Section 4.2 by quantifying spurious effects on dislocations in the atomistic domain depending on the complexity of the linear elastic solution used to compute the dislocation fields of the atomic dislocation. In Section 4.3, the CADD-3d method is applied to a periodic bow-out problem of a single dislocation, for which reference solutions in essentially infinite domains can be obtained for both fully atomistic and fully DDD problems. This test problem allows to isolate the modeling of the evolution of a hybrid dislocation along the artificial interface and demonstrate minimal errors relative to the reference fully atomistic solution.

Notation

Normal letters denote scalars (and zeroth-order tensors), e.g. b, $\mathit{\Pi}$. Vectors (first-order tensors) are defined via lowercase bold letters, e.g. $\boldsymbol{\xi}$, $\boldsymbol{x}$, $\boldsymbol{u}$. Second-order tensors are defined via uppercase bold letters, e.g. $\boldsymbol{G}$, $\boldsymbol{K}$. Fourth-order tensors use the typesetting $\mathbb{C}$ if not stated otherwise. Non-tensorial vectors and matrices are denoted by $\hat{u}$, $\hat{L}$. A direct notation is preferred throughout this work.

Tensor algebra

Attention is drawn to problems in the d-dimensional Euclidean space $\mathbb{R}^d$ ($d = 1, ..., 3$). All tensorial quantities will be defined with respect to the orthonormal basis system $\{\boldsymbol{e}_i\}$. Using Einstein's summation convention a vector $\boldsymbol{a}$ and a second-order tensor $\boldsymbol{A}$ are then defined as

$$\boldsymbol{a} = a_i \boldsymbol{e}_i, \qquad \boldsymbol{A} = A_{ij} \boldsymbol{e}_i \otimes \boldsymbol{e}_j. \tag{1}$$

The Euclidean inner product for vectors and the inner product between second- and higher order tensors are defined

$$\boldsymbol{a}^{\mathsf{T}} \cdot \boldsymbol{b} = a_i b_i, \qquad \boldsymbol{A} \cdot \boldsymbol{B} = A_{ij} B_{ij}. \tag{2}$$

The inner products induce the norms

$$\|\boldsymbol{a}\| = \sqrt{\boldsymbol{a}^{\mathsf{T}} \cdot \boldsymbol{a}}, \qquad \|\boldsymbol{A}\|_{\mathrm{fro}} = \sqrt{\boldsymbol{A} \cdot \boldsymbol{A}}. \tag{3}$$

The same notation will be used for non-tensorial vectors and matrices $\hat{a}$, $\hat{A}$, ie. $\hat{a}^{\mathsf{T}} \cdot \hat{a}$, $\hat{A} \cdot \hat{A}$ etc.

The space of Lebesgue-integrable functions f, g with domain $\mathit{\Omega} \subseteq \mathbb{R}^d$ is denoted $L^p(\mathit{\Omega})$ for $1 \leq p \leq \infty$. For $p = 2$ it is a Hilbert space with inner product and associated norm

$$\langle f, g \rangle_{L^2(\mathit{\Omega})} = \int_{\mathit{\Omega}} f(\boldsymbol{x}) g(\boldsymbol{x}) \, \mathrm{d}V, \qquad \|f\|_{L^2(\mathit{\Omega})} = \sqrt{\langle f, f \rangle_{L^2(\mathit{\Omega})}}. \tag{4}$$

Further, the Hilbert space $H^k(\Omega)$, $k \geq 1$, is the space of functions $f \in L^2(\Omega)$ with weak derivatives $\nabla f \in L^2(\Omega), ..., \nabla^k f \in L^2(\Omega)$.

For discrete domains Λ the corresponding sequence space is $l^p(\Lambda)$. The space of square-summable sequences f, g is a Hilbert space with inner product and associated norm

$$\langle f, g\rangle_{l^2(\Lambda)} = \sum_{\boldsymbol{\xi}\in\Lambda} f(\boldsymbol{\xi})g(\boldsymbol{\xi}), \qquad \|f\|_{l^2(\Lambda)} = \sqrt{\langle f, f\rangle_{l^2(\Lambda)}}. \tag{5}$$

Tensor analysis

Gradient. Let $A(\boldsymbol{x})$ be an N-th order tensor. The M-th gradient of A at $\boldsymbol{x} \in \mathbb{R}^d$ is defined as

$$\nabla_x^M A(\boldsymbol{x}) = \frac{\partial^M A_{i_1\cdots i_N}}{\partial x_{j_1}\cdots\partial x_{j_M}} \boldsymbol{e}_{i_1} \otimes \cdots \otimes \boldsymbol{e}_{i_N} \otimes \boldsymbol{e}_{j_1} \otimes \cdots \otimes \boldsymbol{e}_{j_M} = A_{i_1\cdots i_N, j_1\cdots j_M}. \tag{6}$$

Generally, the gradient operator increases the order of a tensor by one.

Divergence. Let $A(\boldsymbol{x})$ be an N-th order tensor. The divergence of A at $\boldsymbol{x} \in \mathbb{R}^d$ is defined as

$$\nabla_x \cdot A(\boldsymbol{x}) = \frac{\partial A_{i_1\cdots i_N}}{\partial x_{j_N}} \boldsymbol{e}_{i_1} \otimes \cdots \otimes \boldsymbol{e}_{i_{N-1}} = A_{i_1\cdots i_N, i_N}. \tag{7}$$

Generally, the divergence operator decreases the order of a tensor by one.

Curl. The curl of first and second order tensors $\boldsymbol{a}$, $\boldsymbol{A}$ is given by

$$\nabla_x \times \boldsymbol{a}(\boldsymbol{x}) = \epsilon_{ijk} a_{j,i}, \qquad \nabla_x \times \boldsymbol{A}(\boldsymbol{x}) = \epsilon_{ijk} A_{lj,i}, \tag{8}$$

with the third-order Levi-Civita permutation tensor $\boldsymbol{\epsilon}$ defined as

$$\epsilon_{ijk} = \begin{cases} +1 & \text{if } ijk = 123,\ 312 \text{ or } 231, \\ -1 & \text{if } ijk = 321,\ 213 \text{ or } 132, \\ 0 & \text{if } i = j,\ i = k \text{ or } j = k. \end{cases} \tag{9}$$

Variational derivative. Let $\mathcal{X}$ be a continuous vector space. The first variation of a functional $F \in C^2(\mathcal{X})$, given by $F(u) = \int f(u(x))\,\mathrm{d}V$, $u \in \mathcal{X}$, is then defined as

$$\forall\, u, v \in \mathcal{X} \qquad \delta F \equiv \langle \delta F(u), v\rangle_{L^2} = \int \delta_u F v\,\mathrm{d}V, \tag{10}$$

with the variational derivative

$$\delta_u F = \lim_{\varepsilon\to 0} \frac{f(u(x) + \varepsilon v(x)) - f(u(x))}{\varepsilon}. \tag{11}$$

The second variation of F is

$$\forall\, u, v, w \in \mathcal{X} \qquad \delta^2 F \equiv \langle \delta^2 F(u)v, w \rangle_{L^2}. \tag{12}$$

The definition for discrete vector spaces is analog.

Domain indicators

A superscripted domain indicator is attached to a physical quantity $\bullet$ which belongs to a certain region, e.g. $\bullet^{\mathrm{a}}$. Following the domain decomposition from Section 2.3.3, the corresponding domain indicators are listed below:

Index	Description
a	atomistic domain
c	continuum domain
p	pad domain
i	interface between the atomistic and the continuum domain
i+	pad atoms which are coupled to interface atoms according to a local continuum (only Chapter 2)
i-	elements in the atomistic domain which interact with the interface atoms according a local continuum (only Chapter 2)
i′	elements in the atomistic domain which interact with the interface atoms according the (nonlocal) atomistic interaction law (only Chapter 2; not highlighted in Figure 2.2)

A quantity may refer to the actual domain, e.g. the atomic lattice $\Lambda^{\mathrm{a}} \subset \Lambda$. In addition, $\bullet$ can refer to a vectorized quantity defined on Λ, e.g. the displacement $\boldsymbol{u}^{\mathrm{a}} : \Lambda^{\mathrm{a}} \to \mathbb{R}^d$.

On the other hand, domain indicators can be attached to operators acting on elements which belong to one domain and produce elements in another. For example, the continuum operator $\mathcal{L}_{\mathrm{h}}^{\mathrm{c}}$ (see Section 2.3.3) acts on the entire displacement field $\boldsymbol{u} : \Lambda \to \mathbb{R}^d$ and produces the force vector $\boldsymbol{f}^{\mathrm{c}}$, defined on Λ^{c}, i.e. $\mathcal{L}_{\mathrm{h}}^{\mathrm{c}}[\boldsymbol{u}] = \boldsymbol{f}^{\mathrm{c}}$. Since $\boldsymbol{f}^{\mathrm{c}}$ is only impacted by the displacements $\boldsymbol{u}^{\mathrm{i}}$ and $\boldsymbol{u}^{\mathrm{c}}$ and alternative expression is $\mathcal{L}_{\mathrm{h}}^{\mathrm{c/i\cup c}}[\boldsymbol{u}^{\mathrm{c/i\cup c}}]$. Thereby, the indicators before and after the forward slash indicate the domain and the co-domain, respectively.

1 Modeling plasticity across different length scales

1.1 Overview

The theoretical framework of today's engineering sciences can be broadly grouped into nano-, meso-, micro- and macroscale models, describing phenomena across scales from the motion of individual dislocations on the nanoscale to accumulated plastic flow on the scale of meters (see Figure 1.1). Experiments and design of new high-performance materials show that size plays an important role, e.g. when studying strength or ductility of materials, and neglecting the mechanical behavior on one length scale can lead to an incomplete understanding of the overall macroscopic behavior. A key challenge in modern computational physics is thus the development of accurate multiscale methods, which exploit the strengths of different models to create a single coherent framework. This section therefore serves as a basic introduction to computational plasticity at different scales, subsequently motivating the coupling of length scales by means of hybrid multiscale methods.

Macro- and microscale models. Classical continuum models, e.g. phenomenological models, crystal plasticity etc. (Roters et al., 2011), which represent plastic flow in a homogenized fashion can not account for size effects in the stress-strain response observed in real experiments. It has long been recognized that incorporating strain gradients into the constitutive assumptions gives rise to size effects (e.g. Fleck and Hutchinson, 2001). This idea was extended only recently via the so-called "micromorphic" approach by Forest (2009) which allows for additional state or internal variables (e.g. gradients of the plastic strain) which describe the underlying material behavior. After the discovery of dislocations occurring on the atomic scale (e.g. Taylor, 1934) as the elementary carriers of plastic flow in crystalline solids, much effort was also devoted to the development of a continuum theory of dislocations. The foundation of this theory is largely accredited to Nye (1953) and Kröner (1958) who postulated the dislocation density tensor as a continuum measure for the motion of dislocations. The corresponding models require kinematic and/or kinetic equations to describe the evolution of the dislocation density.

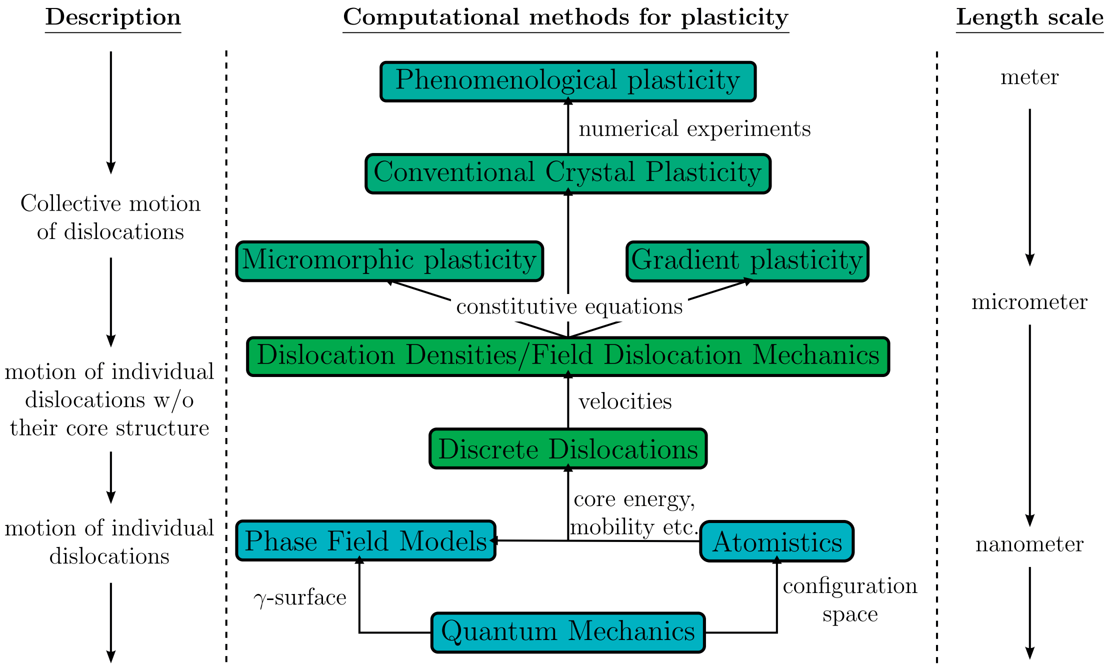
Description
Computational methods for plasticity
Length scale
Phenomenological plasticity
numerical experiments
Conventional Crystal Plasticity
Collective motion of dislocations
Micromorphic plasticity
Gradient plasticity
constitutive equations
Dislocation Densities/Field Dislocation Mechanics
velocities
motion of individual dislocations w/o their core structure
Discrete Dislocations
core energy, mobility etc.
motion of individual dislocations
Phase Field Models
Atomistics
γ-surface
configuration space
Quantum Mechanics
meter
micrometer
nanometer

Figure 1.1: Computational methods for modeling plasticity on various length scales

Notable contributions in this direction are due to Steinmann (1996); Acharya and Bassani (2000); Gurtin (2002); Regueiro et al. (2002); Hochrainer et al. (2007); Forest and Guéoninchault (2013); Hochrainer et al. (2014).

Mesoscale models. All methods described above share one major drawback in the sense that they only account for *collective* dislocation motion. Although the gradient and micromorphic approaches were introduced in order to model phenomena on different length scales, the classical continuum theory is inherently *scale independent*. Hence, artificial length scales parameters have to be incorporated in the corresponding constitutive equations to describe the size effects. Calibrating these parameters requires a thorough understanding of the motion of *individual* dislocations. Considering single dislocations as eigenstrains in elastic continua was pioneered during the first half of the twentieth century by, e.g. Volterra (1907), Leibfried and Lücke (1949) or Eshelby (1949), to just name a few. Later, this idea was extended by various authors to model large arrangements of dislocations (e.g. Amodeo and Ghoniem, 1990; Lubarda et al., 1993; Van Der Giessen and Needleman, 1995) which coined the term *Discrete Dislocation Dynamics* (DDD).[1] Newer approaches consider three-dimensional problems, e.g. Weygand et al. (2002) and Arsenlis et al. (2007) study complex dislocation networks including topological changes by taking into account dislocation climb, cross slip etc.

Atomic scale models. Similar to classical continuum mechanics DDD requires "constitutive models" which relate the force exerted on a dislocation to their velocity. This relation can be established by means of educated calibration to finer-scale models, i.e. atomistics. Although atomistic models were studied as early as the late 1950s (see, e.g. Alder and Wainwright, 1959), it did not become popular until the 1990s, largely due to the development of modern supercomputers. Atomistic models rely on the Born-Oppenheimer approximation (Born and Oppenheimer, 1927) which states that electrons react instantaneously to the motion of the nuclei. As a consequence, they can be treated separately. In addition, the nuclei are assumed to be much heavier than the electrons and may be treated as point particles carrying potential energy. Atoms may therefore be described in the framework of classical mechanics in terms of their position and momentum. A great challenge in atomistic modeling is the construction of the interatomic potentials. These potentials are usually calibrated with respect to a well-defined set of energetic configurations coming from ab initio calculations, e.g. using the density functional theory (DFT, Hohenberg and Kohn, 1964).

---

[1] Here, the term "discrete dislocation" refers to an explicit description of the dislocation line which shall not be confused with numerical discretization

1.2 Dislocations as the main carrier of plasticity

The origins of the theory of dislocations go back to the ongoing efforts in the beginning of the 20th century to theoretically predict the strength of materials, i.e. the regime where the material does not undergo fracture or plastic deformation. One of the first models was developed by Frenkel (1926) in order to predict the theoretical shear strength of crystalline materials. However, this early model was based on the assumption of a perfect crystal without defects — such that plasticity develops by *fully* shifting neighboring crystallographic planes with respect to each other — and the theoretical predictions were several orders of magnitude higher than the material strength observed in real experiments. In the 1930s Taylor (1934) discovered that plastic slip occurs *incrementally*, guided by the motion of dislocation lines which separate slipped an unslipped portions of the material.

The relative slip between two parts of the crystal is given through the Burgers vector $\boldsymbol{b}$. The Burgers vector of a dislocation can be identified as the difference between a circuit around the center of the dislocation core, shown in Figure 1.2 (a), and its replica in the undeformed crystal (Frank, 1951; Bilby et al., 1955). If the Burgers vector is parallel to the line direction the dislocation is referred to as a screw dislocation. On the other hand, an edge dislocation has a Burgers vector perpendicular to the line direction. A dislocation with inclined Burgers vector is a mixed dislocation, i.e. a linear combination of a screw and an edge dislocation. Dislocation motion occurs within preferred slip systems which depend on the lattice structure. A slip system is defined as

$$\text{slip system} \quad = \quad \text{glide plane} \quad + \quad \text{glide direction.}$$

In general, the glide planes on which dislocations move are the energetically-favorable closed-packed planes of the crystal lattice. The glide direction, i.e the direction in which the dislocation moves, is usually confined to the given glide plane for edge dislocations but screw dislocations may also cross-slip between different glide planes.

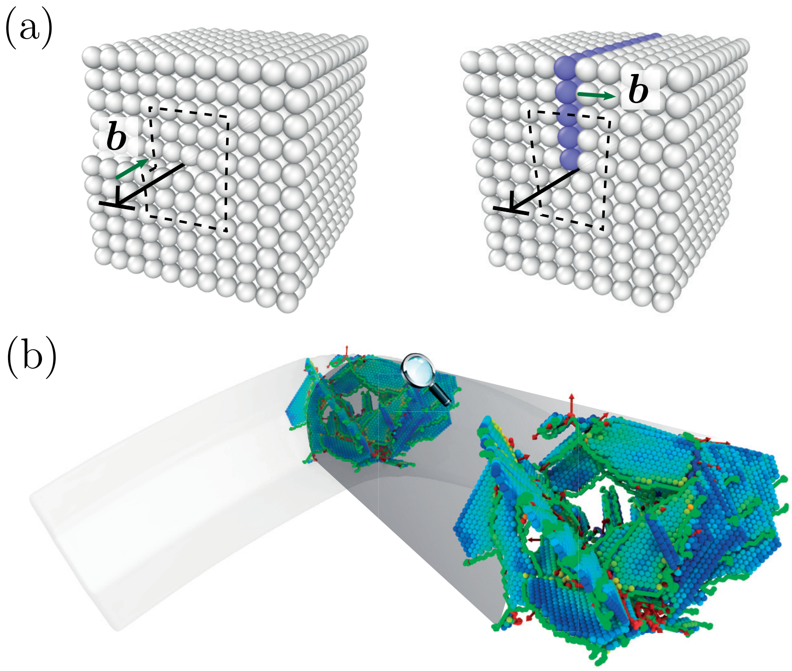

Figure 1.2: (a) Screw and edge dislocations in a simple cubic lattice. (b) Formation of a dislocation network in a nanobeam (by courtesy of Dr. Wolfram Nöhring)

Plastic deformation in real materials occurs due to the motion, multiplication and annihilation of thousands of dislocations which can form complex networks as shown in Figure 1.2 (b). Several theoretical models in dislocation-based plasticity will be discussed in the following sections, ranging from the collective motion of dislocations on the continuum scale to the motion of individual, atomistically resolved, dislocations.

1.3 Classical continuum mechanics

In this section, the basics of classical continuum mechanics will be reviewed with focus on the essential kinematics, balance laws and constitutive models for dislocation-based plasticity. Continuum mechanics is governed by field equations, i.e. partial differential equations (PDEs) — contrary to atomistic models which are discussed in Section 1.5. This section shall serve as a concise introduction to the important continuum physics used throughout this work and to familiarize the reader with the notation. For further details the reader is referred to the seminal work of Truesdell and Noll (1965) or to one of the numerous introductory books on the topic (e.g. Jirasek and Bazant, 2002; Bertram, 2012).

1.3.1 Kinematics and balance equations

In the following the motion of an initially stress-free material body $\Omega_0 \subseteq \mathbb{R}^d$ of dimension $d = 1, ..., 3$ with boundary $\partial\Omega_0$ is considered. Attention is drawn to quasi-static problems, i.e. only the initial configuration Ω_0 and its final placement Ω will be defined. The elements of Ω_0 are denoted as the material points $\boldsymbol{X}$.

The deformation of $\boldsymbol{X}$ is the motion $\chi(\boldsymbol{X})$ which is assumed to be invertible, that is interpenetration of matter and fracture are not considered. The motion is identified via displacements $\boldsymbol{u} : \Omega_0 \to \mathbb{R}^d$ such that $\chi(\boldsymbol{X}) = \boldsymbol{X} + \boldsymbol{u}(\boldsymbol{X})$ as shown in Figure 1.3. Then, the elements $\boldsymbol{x} \in \Omega$ are uniquely defined via $\boldsymbol{x} = \chi(\boldsymbol{X})$.

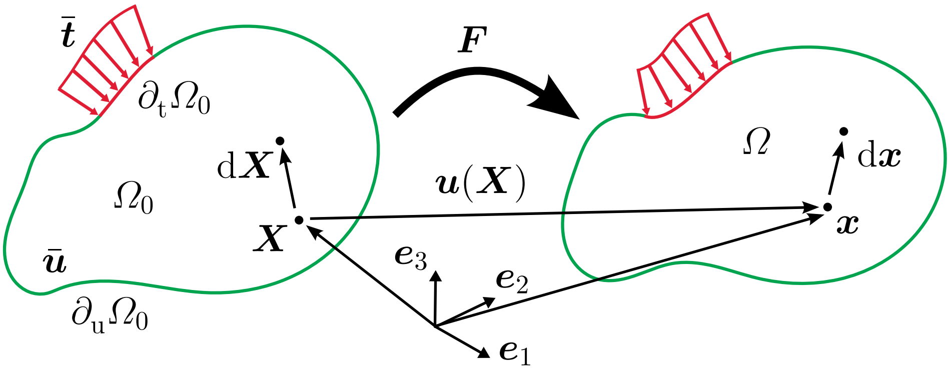
$\bar{\boldsymbol{t}}$
$\boldsymbol{F}$
$\partial_t\Omega_0$
Ω
$\mathrm{d}\boldsymbol{x}$
$\mathrm{d}\boldsymbol{X}$
$\boldsymbol{u}(\boldsymbol{X})$
Ω_0
$\boldsymbol{x}$
$\boldsymbol{X}$
$\bar{\boldsymbol{u}}$
$\boldsymbol{e}_3$
$\boldsymbol{e}_2$
$\partial_u\Omega_0$
$\boldsymbol{e}_1$

Figure 1.3: Schematic illustration of the deformation of a continuous material body

Let $\boldsymbol{Y} \in \Omega_0$. The motion of $\boldsymbol{Y}$ can be expanded by a Taylor series as

$$\chi(\boldsymbol{Y}) = \chi(\boldsymbol{X}) + \nabla_X \chi(\boldsymbol{X})\mathrm{d}\boldsymbol{X} + \mathcal{O}(\|\mathrm{d}\boldsymbol{X}\|^2). \tag{1.1}$$

For infinitesimal line elements $\mathrm{d}\boldsymbol{X}$, i.e. for $\|\mathrm{d}\boldsymbol{X}\| \to 0$, the higher order terms can be neglected which yields

$$\chi(\boldsymbol{Y}) - \chi(\boldsymbol{X}) = \boldsymbol{y} - \boldsymbol{x} = \mathrm{d}\boldsymbol{x} = \boldsymbol{F}(\boldsymbol{X})\mathrm{d}\boldsymbol{X}, \tag{1.2}$$

with the *deformation gradient*

$$\boldsymbol{F}(\boldsymbol{X}) = \nabla_X \chi(\boldsymbol{X}) = \frac{\partial \boldsymbol{x}(\boldsymbol{X})}{\partial \boldsymbol{X}}. \tag{1.3}$$

The displacement gradient is defined accordingly as

$$\nabla_X \boldsymbol{u}(\boldsymbol{X}) = \boldsymbol{F}(\boldsymbol{X}) - \boldsymbol{I}. \tag{1.4}$$

Strain energy density. Potential-based models assign energetic quantities to material points which measure the usable and dissipated work of the material body. For non-dissipative solids, the Helmholtz free energy density fully describes the essential thermodynamics of the material. The free energy is then defined in terms of the deformation gradient $\boldsymbol{F}$ as

$$\psi(\boldsymbol{X}) = \psi\big(\boldsymbol{F}(\boldsymbol{X})\big). \tag{1.5}$$

In the following it is assumed that ψ is a convex function of $\boldsymbol{F}$.

Remark 1.3.1. *Equation* (1.5) *is valid for local continua, that is if the macroscopic length scale L (e.g. the size of the material body from Figure 1.3) and the microscopic length scale l (the grain size or lattice spacing) are well separated, i.e. $L \gg l$. However, if $L \approx l$, nonlocal effects become important (c.f. Eringen, 2002). The total energy then depends on an energy density W which itself depends on the differential displacements $\boldsymbol{u}(\boldsymbol{X}) - \boldsymbol{u}(\boldsymbol{X}')$ within a finite interaction range $\mathcal{R} \subset \mathbb{R}^d$ whose size is associated with the internal length in the sense that $\mathcal{R} \in \mathcal{O}(l)$. The total energy of the system can then be written as*

$$\varPi = \int_{\varOmega} \left(\int_{\mathcal{R}} W\big(\boldsymbol{u}(\boldsymbol{X}) - \boldsymbol{u}(\boldsymbol{X}')\big) \,\mathrm{d}V' \right) \mathrm{d}V. \tag{1.6}$$

A direct relation to gradient continua can be established under the assumption of a sufficiently smooth displacement field $\boldsymbol{u}$. A Taylor expansion of $\boldsymbol{u}$ around $\boldsymbol{X}$ then yields

$$\boldsymbol{u}(\boldsymbol{X}') - \boldsymbol{u}(\boldsymbol{X}) = \nabla_X \boldsymbol{u}(\boldsymbol{X})(\boldsymbol{X} - \boldsymbol{X}') + \frac{1}{2} \nabla^2_X \boldsymbol{u}(\boldsymbol{X}) \big((\boldsymbol{X} - \boldsymbol{X}') \otimes (\boldsymbol{X} - \boldsymbol{X}')\big) + \ldots \tag{1.7}$$

After plugging (1.7) *back into* (1.6)*, it can be seen that W now depends on $\boldsymbol{X} - \boldsymbol{X}'$ and the gradients of $\boldsymbol{u}$ at $\boldsymbol{X}$. Roughly speaking, the total energy can be brought into the form*

$$\varPi = \int_{\varOmega} \bar{\psi}(\nabla_X \boldsymbol{u}(\boldsymbol{X}), l \nabla^2_X \boldsymbol{u}(\boldsymbol{X}), \ldots) \,\mathrm{d}V, \tag{1.8}$$

where $\bar{\psi}$ is an effective strain energy density energy which is be obtained after integrating W over $\mathcal{R}$. In the limit of local action, i.e. when $|\mathcal{R}| \to 0$, the local strain energy density (1.5) *is recovered.*

In the following a local continuum (also: Cauchy continuum) is considered. In this case the total energy of the mechanical system is defined as

$$\varPi(\boldsymbol{u}, \boldsymbol{F}) = \varPi^{\mathrm{int}}(\boldsymbol{F}) + \varPi^{\mathrm{ext}}(\boldsymbol{u}). \tag{1.9}$$

The internal and external contributions are given by

$$\varPi^{\mathrm{int}}(\boldsymbol{F}) = \int_{\varOmega_0} \psi\big(\boldsymbol{F}(\boldsymbol{X})\big) \,\mathrm{d}V, \tag{1.10}$$

$$\varPi^{\mathrm{ext}}(\boldsymbol{u}) = -\int_{\varOmega_0} (\boldsymbol{f}^{\mathrm{body}})^{\mathsf{T}}(\boldsymbol{X}) \cdot \boldsymbol{u}(\boldsymbol{X}) \,\mathrm{d}V - \int_{\partial_{\mathrm{t}} \varOmega_0} \bar{\boldsymbol{t}}^{\mathsf{T}}(\boldsymbol{X}) \cdot \boldsymbol{u}(\boldsymbol{X}) \,\mathrm{d}A, \tag{1.11}$$

where $\boldsymbol{f}^{\text{body}} \in [L^2(\mathit{\Omega}_0)]^d$ is an additional body force and $\bar{\boldsymbol{t}}$ is a predefined traction on the boundary $\partial_{\text{t}}\mathit{\Omega}_0 \subset \partial\mathit{\Omega}_0$.

For quasi-static problems, an admissible final configuration $\mathit{\Omega}$ is the one which minimizes the total energy $\mathit{\Pi}$. That is, for a given set of boundary conditions, e.g.

- prescribed *displacements* $\bar{\boldsymbol{u}}$ on $\partial_{\text{u}}\mathit{\Omega}_0 \subseteq \partial\mathit{\Omega}_0$,
- prescribed *tractions* $\bar{\boldsymbol{t}}$ on $\partial_{\text{t}}\mathit{\Omega}_0 = \partial\mathit{\Omega}_0 \setminus \partial_{\text{u}}\mathit{\Omega}_0$, (1.12)
- or *Robin-type* (mixed) conditions ($\bar{\boldsymbol{u}}$ and $\bar{\boldsymbol{t}}$ simultaneously defined),

admissible minimizers $\boldsymbol{u}$ of $\mathit{\Pi}$ from a suitably chosen function space

$$\mathcal{V} := \{\, \delta\boldsymbol{u} \in [H^1(\mathit{\Omega}_0)]^d \,|\, \delta\boldsymbol{u} \text{ satisfies (1.12)} \,\} \tag{1.13}$$

are sought-after. The optimization problem is then defined as

$$\boldsymbol{u} := \operatorname{Arg}\left\{ \min_{\delta\boldsymbol{u}\in\mathcal{V}} \mathit{\Pi}(\delta\boldsymbol{u}, \delta\boldsymbol{F}) \right\}, \tag{1.14}$$

where $\delta\boldsymbol{F} = \delta(\boldsymbol{I} + \nabla_X\boldsymbol{u}) = \nabla_X\delta\boldsymbol{u}$.

To solve problem (1.14) the variational method is used. The first variation of $\mathit{\Pi}$ reads

$$\delta\mathit{\Pi} = \int_{\mathit{\Omega}_0} \delta_F\mathit{\Pi}^{\text{int}} \cdot \delta\boldsymbol{F}\,\mathrm{d}V - \int_{\mathit{\Omega}_0} (\boldsymbol{f}^{\text{body}})^{\mathsf{T}} \cdot \delta\boldsymbol{u}\,\mathrm{d}V - \int_{\partial_{\text{t}}\mathit{\Omega}_0} \bar{\boldsymbol{t}}^{\mathsf{T}} \cdot \delta\boldsymbol{u}\,\mathrm{d}A, \tag{1.15}$$

where

$$\delta_F\mathit{\Pi}^{\text{int}} = \boldsymbol{P} = \frac{\partial\psi(\boldsymbol{F})}{\partial\boldsymbol{F}}. \tag{1.16}$$

Here, $\boldsymbol{P}$ is the first Piola-Kirchhoff stress tensor. In equilibrium the first variation of $\mathit{\Pi}$ is zero such that

$$\forall\,\delta\boldsymbol{u} \in \mathcal{V} \qquad \delta\mathit{\Pi} \overset{!}{=} 0 = \int_{\mathit{\Omega}_0} \boldsymbol{P}\cdot(\nabla_X\delta\boldsymbol{u})\,\mathrm{d}V - \int_{\mathit{\Omega}_0} (\boldsymbol{f}^{\text{body}})^{\mathsf{T}}\cdot\delta\boldsymbol{u}\,\mathrm{d}V - \int_{\partial_{\text{t}}\mathit{\Omega}_0} \bar{\boldsymbol{t}}^{\mathsf{T}}\cdot\delta\boldsymbol{u}\,\mathrm{d}A \tag{1.17}$$

which is nothing but the weak form of elastostatics. Applying the product rule and Gauss' theorem to the first term leads to

$$\begin{aligned} \forall\,\delta\boldsymbol{u} \in \mathcal{V} \qquad 0 = & \int_{\mathit{\Omega}_0} \nabla_X \cdot (\boldsymbol{P}\delta\boldsymbol{u})\,\mathrm{d}V - \int_{\mathit{\Omega}_0} (\nabla_X \cdot \boldsymbol{P}) \cdot \delta\boldsymbol{u}\,\mathrm{d}V \\ & - \int_{\mathit{\Omega}_0} (\boldsymbol{f}^{\text{body}})^{\mathsf{T}} \cdot \delta\boldsymbol{u}\,\mathrm{d}V - \int_{\partial_{\text{t}}\mathit{\Omega}_0} \bar{\boldsymbol{t}}^{\mathsf{T}} \cdot \delta\boldsymbol{u}\,\mathrm{d}A \\ = & \int_{\mathit{\Omega}_0} (\nabla_X \cdot \boldsymbol{P} + \boldsymbol{f}^{\text{body}}) \cdot \delta\boldsymbol{u}\,\mathrm{d}V. \end{aligned} \tag{1.18}$$

Due to the arbitrariness of the variation $\delta\boldsymbol{u}$ the local field problem is deduced: find $\boldsymbol{u} \in [H^2(\Omega_0)]^d$ such that

$$\boxed{\begin{cases} \nabla_X \cdot \boldsymbol{P} + \boldsymbol{f}^{\text{body}} = \boldsymbol{0} & \text{in } \Omega_0, \\ \quad + \text{boundary conditions (1.12).} \end{cases}} \tag{1.19}$$

Small strain limit

In the important limit of small deformations the displacement gradient is assumed to be sufficiently small, i.e.

$$\|\nabla_X \boldsymbol{u}\|_{\text{fro}} \ll 1. \tag{1.20}$$

If this condition is satisfied a *geometric linearization* is possible. Hence, the following limiting cases are obtained

$$\boxed{\boxed{\begin{array}{ccc} \Omega_0 & \longrightarrow & \Omega, \\ \psi(\boldsymbol{F}) & \longrightarrow & \psi(\boldsymbol{\varepsilon}), \\ \boldsymbol{P}(\boldsymbol{F}) & \longrightarrow & \boldsymbol{\sigma}(\boldsymbol{\varepsilon}), \end{array}}} \tag{1.21}$$

with the Cauchy stress $\boldsymbol{\sigma}(\boldsymbol{\varepsilon})$ and the *small strain tensor*

$$\boldsymbol{\varepsilon} = \text{sym}(\nabla_x \boldsymbol{u}). \tag{1.22}$$

Therefore the deformation of the body is solely described by $\boldsymbol{\varepsilon}$ and no distinction is made between reference and current configurations.

For small strains, the weak form (1.17) becomes

$$\forall\, \delta\boldsymbol{u} \in \mathcal{V} \qquad 0 = \int_\Omega \boldsymbol{\sigma} \cdot (\nabla_x \delta\boldsymbol{u})\, \mathrm{d}V - \int_\Omega (\boldsymbol{f}^{\text{body}})^\mathsf{T} \cdot \delta\boldsymbol{u}\, \mathrm{d}V - \int_{\partial_\mathrm{t}\Omega} \bar{\boldsymbol{t}}^\mathsf{T} \cdot \delta\boldsymbol{u}\, \mathrm{d}A. \tag{1.23}$$

Since the variations are arbitrary the balance equation for small strains reads: find $\boldsymbol{u} \in [H^2(\Omega)]^d$ such that

$$\boxed{\begin{cases} \nabla_x \cdot \boldsymbol{\sigma} + \boldsymbol{f}^{\text{body}} = \boldsymbol{0} & \text{in } \Omega, \\ \quad + \text{boundary conditions (1.12).} \end{cases}} \tag{1.24}$$

1.3.2 Constitutive modeling

Classical continuum theories require a governing relationship between stresses and strains in order to characterize the reaction of the material body in response to external forces. Constitutive models can be broadly grouped into reversible (elastic) and irreversible (dissipative) processes which will be discussed in the following for the particular case of small deformations.

Linear elasticity. If the deformation is purely elastic, i.e. $\boldsymbol{\varepsilon} = \boldsymbol{\varepsilon}^{\mathrm{e}}$, the Cauchy stress depends linearly on the strain according to Hooke's law

$$\boldsymbol{\sigma} = \mathbb{C}[\boldsymbol{\varepsilon}^{\mathrm{e}}], \tag{1.25}$$

where $\mathbb{C}$ is the fourth-order stiffness tensor which possesses the major and both minor symmetries. Consequently, the free energy density takes the form

$$\psi(\boldsymbol{\varepsilon}^{\mathrm{e}}) = \frac{1}{2}\boldsymbol{\varepsilon}^{\mathrm{e}} \cdot (\mathbb{C}[\boldsymbol{\varepsilon}^{\mathrm{e}}]) \tag{1.26}$$

such that $\boldsymbol{\sigma} = \partial\psi(\boldsymbol{\varepsilon}^{\mathrm{e}})/\partial\boldsymbol{\varepsilon}^{\mathrm{e}}$ is satisfied. For the special case of isotropic elasticity the stiffness tensor takes the form

$$\mathbb{C} = \lambda \boldsymbol{I} \otimes \boldsymbol{I} + 2\mu\mathbb{I}^{\mathrm{s}}, \tag{1.27}$$

where $\boldsymbol{I}$ is the identity tensor and $\mathbb{I}^{\mathrm{s}}$ is a fourth-order tensor which maps every second order tensor $\boldsymbol{A}$ onto its symmetric part, i.e. $\mathbb{I}^{\mathrm{s}}[\boldsymbol{A}] = \mathrm{sym}(\boldsymbol{A})$.

Dissipative processes. Accounting for dissipative processes in classical continuum models is possible by enriching the mechanical state with a set of internal variables $\hat{\alpha}$, e.g. the plastic strain $\boldsymbol{\varepsilon}^{\mathrm{p}}$, hardening variables etc. (Coleman and Gurtin, 1967). The free energy density is then assumed to be a function of the total strain $\boldsymbol{\varepsilon}$ and $\hat{\alpha}$, i.e. $\psi = \psi(\boldsymbol{\varepsilon}, \hat{\alpha})$. A non-negative dissipation rate can be ensured by incorporating the second law of thermodynamics via the Clausius-Duhem inequality (Truesdell and Toupin, 1960)

$$\left(\boldsymbol{\sigma} - \frac{\partial\psi(\boldsymbol{\varepsilon}, \hat{\alpha})}{\partial\boldsymbol{\varepsilon}}\right) \cdot \dot{\boldsymbol{\varepsilon}} - \frac{\partial\psi(\boldsymbol{\varepsilon}, \hat{\alpha})}{\partial\hat{\alpha}} \cdot \dot{\hat{\alpha}} \geq 0. \tag{1.28}$$

For reversible processes the entropy production is zero. Thus, it follows

$$\boldsymbol{\sigma} = \frac{\partial\psi(\boldsymbol{\varepsilon}, \hat{\alpha})}{\partial\boldsymbol{\varepsilon}}. \tag{1.29}$$

The stress field is assumed to satisfy mechanical equilibrium according to (1.24). In order to close the system of equations, an evolution law for the internal variables is needed. This is accomplished by introducing a dissipation potential which relates the rate of the internal variables $\dot{\hat{\alpha}}$ to their thermodynamic conjugate driving forces $\hat{r} = \partial\psi/\partial\hat{\alpha}$ (c.f. Jirasek and Bazant, 2002). In continuum plasticity the dissipation potential is the flow function $f = f(\hat{r})$ such that the plastic strain is given by

$$\dot{\boldsymbol{\varepsilon}}^{\mathrm{p}} = \frac{\partial f(\hat{r})}{\partial\hat{r}}. \tag{1.30}$$

If f is a convex function of $\hat{r}$, unconditional stability of (1.28) is guaranteed a priori.

1.3.3 Phenomenological plasticity models

From the previous discussion it follows that classical plasticity models require the definition of at least two potentials, namely the free energy density ψ and the flow function f. Two examples are discussed in the following.

Example 1.1 (Isotropic von Mises plasticity with kinematic hardening). This simple yet powerful model requires two internal variables, namely the plastic strain $\boldsymbol{\varepsilon}^{\mathrm{p}} = \boldsymbol{\varepsilon} - \boldsymbol{\varepsilon}^{\mathrm{e}}$ and a scalar hardening variable q which can be interpreted as an accumulated plastic strain. The free energy density is given by

$$\psi(\boldsymbol{\varepsilon}^{\mathrm{e}}, \boldsymbol{\varepsilon}^{\mathrm{p}}, q) = \frac{1}{2}\boldsymbol{\varepsilon}^{\mathrm{e}} \cdot \mathbb{C}[\boldsymbol{\varepsilon}^{\mathrm{e}}] + \sigma_{\mathrm{h}} q + \frac{1}{2}\boldsymbol{\varepsilon}^{\mathrm{p}} \cdot \mathbb{H}[\boldsymbol{\varepsilon}^{\mathrm{p}}], \tag{1.31}$$

where σ_{h} is the hardening modulus and $\mathbb{H}$ is a hardening metric. The forces conjugate to $\boldsymbol{\varepsilon}^{\mathrm{p}}$ and q are consequently defined as

$$-\frac{\partial \psi}{\partial \boldsymbol{\varepsilon}^{\mathrm{p}}} = \boldsymbol{\sigma} - \mathbb{H}[\boldsymbol{\varepsilon}^{\mathrm{p}}], \qquad -\frac{\partial \psi}{\partial q} = -\sigma_{\mathrm{h}}. \tag{1.32}$$

The flow function in terms of the conjugate forces reads

$$f(\boldsymbol{\sigma} - \mathbb{H}[\boldsymbol{\varepsilon}^{\mathrm{p}}], \sigma_{\mathrm{h}}) = \max\{\, 0,\ |\mathrm{dev}(\boldsymbol{\sigma} - \mathbb{H}[\boldsymbol{\varepsilon}^{\mathrm{p}}])| - \sqrt{2/3}\sigma_{\mathrm{h}}\,\}, \tag{1.33}$$

where $\mathrm{dev}(\bullet)$ denotes the deviatoric part of second order tensors. The rates for the internal variables follow by differentiating f with respect to the conjugate forces

$$\dot{\boldsymbol{\varepsilon}}^{\mathrm{p}} = \dot{\lambda}\frac{\mathrm{dev}(\boldsymbol{\sigma} - \mathbb{H}[\boldsymbol{\varepsilon}^{\mathrm{p}}])}{\|\mathrm{dev}(\boldsymbol{\sigma} - \mathbb{H}[\boldsymbol{\varepsilon}^{\mathrm{p}}])\|}, \qquad \dot{q} = \sqrt{\frac{2}{3}}\dot{\lambda}. \tag{1.34}$$

Here, the Lagrange multiplier $\dot{\lambda}$ ensures that $f < 0$ in the elastic regime and $f = 0$ if the body deforms plastically. If the parameter k is set to zero no kinematic hardening is considered. However, for many cases, e.g. cyclic loading ("Bauschinger effect"), it can be useful to consider kinematic hardening in order to allow the yield surface to translate in stress space without changing its shape (c.f. Figure 1.4 (a) and (b)). □

Example 1.2 (Crystal plasticity). Crystal plasticity models account for the underlying lattice structure of the material. In metals, plastic flow occurs primarily on slip systems. For a crystal with N slip systems with vectors normal to glide plane $\boldsymbol{n}^{\beta}$ and vectors parallel to the glide direction $\boldsymbol{m}^{\beta}$, the second order tensors

$$\boldsymbol{M}^{\beta} = \boldsymbol{n}^{\beta} \otimes \boldsymbol{m}^{\beta} \tag{1.35}$$

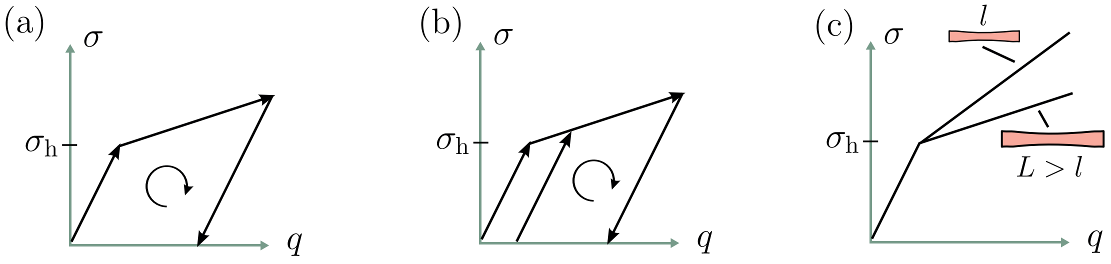

Figure 1.4: Schematic illustrations of typical stress strain curves for (a) cyclic loading and an isotropic hardening model, (b) cyclic loading and kinematic hardening and (c) for uniaxial tension and different specimen sizes

are defined for all $\beta = 1, ..., N$ to project the local stress state onto the slip system β. Plastic deformation occurs whenever the resolved shear stress on a slip system exceeds a threshold parameter τ_{crit}. The corresponding flow function reads

$$f(\boldsymbol{\sigma} - \mathbb{H}[\boldsymbol{\varepsilon}^{\mathrm{p}}], \sigma_{\mathrm{h}}) = \max \left\{ 0, \sum_{\beta=1}^{N} \gamma_0^{\beta} \left(|\operatorname{sym}(\boldsymbol{M}^{\beta}) \cdot (\boldsymbol{\sigma} - \mathbb{H}[\boldsymbol{\varepsilon}^{\mathrm{p}}])| - \sigma_{\mathrm{h}} - \tau_{\text{crit}} \right) \right\}, \quad (1.36)$$

where the quantity $\operatorname{sym}(\boldsymbol{M}^{\beta}) \cdot (\boldsymbol{\sigma} - \mathbb{H}[\boldsymbol{\varepsilon}^{\mathrm{p}}])$ is the resolved shear stress on the slip system and γ_0^{β} is a reference slip rate (c.f. Roters et al., 2011). Differentiating (1.36) with respect to the conjugate forces gives the evolution of the plastic strain and of the N hardening variables

$$\dot{\boldsymbol{\varepsilon}}^{\mathrm{p}} = \sum_{\beta=1}^{N} \dot{\lambda}^{\beta} \gamma_0^{\beta} \operatorname{sym}(\boldsymbol{M}^{\beta}), \qquad \dot{q}^{\beta} = \gamma_0^{\beta} \dot{\lambda}^{\beta}, \quad (1.37)$$

where the Lagrange multiplier is the accumulated plastic slip with respect to the slip system β. The reference slip rates γ_0^{β} have to be determined from material models on lower length scales, e.g. DDD simulations (c.f. Section 1.4.4). □

1.4 Discrete dislocations dynamics

1.4.1 Configurational material forces

Configurational mechanics has emerged during the second half of the 20th century as a side branch of classical mechanics. Since then it has seen great attention in analytical as well as computational mechanics and has manifested its right to exist in modeling complex behavior of materials endowed with a microstructure, accompanying other approaches within the framework of generalized continua (e.g. Cosserat, gradient models etc., see e.g. Maugin, 2016, for a recent review) which were developed around the same period of time. Originally the idea was introduced by Eshelby during the 1950s who was the first who defined a *material force* acting on imperfections in an otherwise defect-free material body. The concept of material forces as the *driving force* of the considered defect opened the possibility in studying interactions between defects and evolving microstructures in a continuum mechanical setting. Starting with Eshelby's seminal work on forces acting on singularities in a local linear elastic continuum (Eshelby, 1951) the method has been applied to wide range of crystalline defects such as dislocations, cracks or grain boundaries.

Later, this framework became widely used across materials physics in order to study different phenomena, for instance moving interfaces due to phase transitions (see e.g. Abeyaratne and Knowles, 1990). Only recently it was found that an evolving material frame (which can be considered as a generalization of moving defects) can be exploited for pure computational aspects, e.g. error estimators for numerical methods such as the finite element method (FEM). For example, Braun (1997) showed that the overall accuracy of the numerical solution can be improved by redistributing the nodal points of the mesh corresponding to a vanishing material force. An insightful path was taken by Epstein and Elzanowski (2007) who generalized the concept of material forces to an abstract mathematical framework which can be analyzed detached from the particular underlying physics by introducing "material implants" (i.e. inhomogeneities) attached to the body manifold. Comprehensive overviews on the topic can be found in the monographs of Maugin (1993, 2010), which contain a comprehensive physical classification with concise historical perspective, or the more mathematically motivated work of Gurtin (1999).

In the following the basic equations of configurational mechanics are briefly recalled. First, it is now assumed that the material body is possibly non-homogeneous due to the presence of impurities, defects etc. Changing the composition from $\Omega_0' \to \Omega_0$ consequently results in *material forces*, acting on the defects, which need to be balanced by *inhomogeneous forces* to keep the body in equilibrium. Therefore a material point $\boldsymbol{X}'$ is allowed to displace according to $\boldsymbol{u}^{\mathrm{m}} : \Omega_0' \to \Omega_0$ such that its motion can be written as

$$\kappa(\boldsymbol{X}') = \boldsymbol{X}' + \boldsymbol{u}^{\mathrm{m}}(\boldsymbol{X}'). \tag{1.38}$$

Assuming that the mapping $\kappa(\boldsymbol{X}')$ is bijective, a material point in Ω_0 can be uniquely identified via $\boldsymbol{X} = \kappa(\boldsymbol{X}')$. Accordingly, the *free energy* depends explicitly on the composition of Ω_0 which can be written as $\psi = \psi(\boldsymbol{F}, \boldsymbol{X})$. The total variation of Π is then carried out with respect to $\boldsymbol{F}$, $\boldsymbol{u}$ and $\boldsymbol{X}$ such that

$$\delta \Pi = \int_{\Omega_0} \delta_F \Pi \cdot \nabla_X \delta \boldsymbol{u} \,\mathrm{d}V + \int_{\Omega_0} \delta_u \Pi \cdot \delta \boldsymbol{u} \,\mathrm{d}V + \int_{\Omega_0} \delta_X \Pi^{\mathrm{int}} \cdot \delta \boldsymbol{X} \,\mathrm{d}V, \tag{1.39}$$

where $\delta_F \Pi = \boldsymbol{P}$ and $\delta_u \Pi = \boldsymbol{f}^{\mathrm{body}}$ (c.f. Section 1.3.1).

The goal is to find an expression for the functional derivative of Π^{int} with respect to $\boldsymbol{X}$, that is the local *material force*. To this end, note that the total differential of Π^{int} reads

$$d\Pi^{\mathrm{int}} = \boldsymbol{P} \cdot \nabla_X \delta \boldsymbol{u} + \delta_X \Pi^{\mathrm{int}} \cdot \delta \boldsymbol{X}. \tag{1.40}$$

Dividing both sides by the individual components of $\delta\boldsymbol{X}$ yields the total derivative with respect to $\boldsymbol{X}$ (:= *material derivative*)

$$d_X \mathit{\Pi}^{\text{int}} = \big(\nabla_X(\nabla_X^{\mathsf{T}}\boldsymbol{u})\big)\boldsymbol{P} + \delta_X \mathit{\Pi}^{\text{int}}. \tag{1.41}$$

Using the product rule the first term on the right hand side can be re-written as

$$\big(\nabla_X(\nabla_X^{\mathsf{T}}\boldsymbol{u})\big)\boldsymbol{P} = \nabla_X \cdot \big((\nabla_X^{\mathsf{T}}\boldsymbol{u})\boldsymbol{P}\big) - (\nabla_X^{\mathsf{T}}\boldsymbol{u})\underbrace{\nabla_X \cdot \boldsymbol{P}}_{=-\boldsymbol{f}^{\text{body}}}, \tag{1.42}$$

where the last term is due to the balance of linear momentum. Plugging the latter into (1.41) gives

$$d_X \mathit{\Pi}^{\text{int}} = \nabla_X \cdot \big((\nabla_X^{\mathsf{T}}\boldsymbol{u})\boldsymbol{P}\big) + (\nabla_X^{\mathsf{T}}\boldsymbol{u})\boldsymbol{f}^{\text{body}} + \delta_X \mathit{\Pi}^{\text{int}}. \tag{1.43}$$

With $d_X \mathit{\Pi}^{\text{int}} = \nabla_X \psi$, a rearrangement of the terms leads to

$$\delta_X \mathit{\Pi}^{\text{int}} = \nabla_X \cdot \big(\psi\boldsymbol{I} - (\nabla_X^{\mathsf{T}}\boldsymbol{u})\boldsymbol{P}\big) - (\nabla_X^{\mathsf{T}}\boldsymbol{u})\boldsymbol{f}^{\text{body}}, \tag{1.44}$$

where the first quantity in the parenthesis on the right hand side is commonly referred to as the Eshelby stress tensor (c.f. Maugin, 1993)

$$\boldsymbol{B} = \psi\boldsymbol{I} - (\nabla_X^{\mathsf{T}}\boldsymbol{u})\,\boldsymbol{P}. \tag{1.45}$$

In general, $\boldsymbol{B}$ does not possess any special symmetries. In addition, note that $\boldsymbol{B}$ is purely defined with respect to the reference configuration. As matter of fact, it could have been equivalently obtained by a pull-back of the balance equation (1.19) from the physical to the material frame.

The quantity $\delta_X \mathit{\Pi}^{\text{int}}$ is usually referred to as the local *material force*. The material force is a balanced quantity in the sense that

$$\nabla_X \cdot \boldsymbol{B} - (\nabla_X^{\mathsf{T}}\boldsymbol{u})\boldsymbol{f}^{\text{body}} + \boldsymbol{f}^{\text{inh}} = \boldsymbol{0} \qquad \text{in } \mathit{\Omega}_0, \tag{1.46}$$

where $\boldsymbol{f}^{\text{inh}}$ can be interpreted as the *inhomogeneous force* due to the presence of defects. If, further, the body is in mechanical equilibrium, it holds

$$\nabla_X^{\mathsf{T}}\boldsymbol{u}(\nabla_X \cdot \boldsymbol{P} + \boldsymbol{f}^{\text{body}}) + (\nabla_X \cdot \boldsymbol{B} - (\nabla_X^{\mathsf{T}}\boldsymbol{u})\boldsymbol{f}^{\text{body}} + \boldsymbol{f}^{\text{inh}}) = \boldsymbol{0} \qquad \text{in } \mathit{\Omega}_0, \tag{1.47}$$

which is commonly denoted as Ericksen's identity (Maugin, 2010).

In the small strain limit the Eshelby stress becomes

$$\boldsymbol{B} \sim \psi\boldsymbol{I} - (\nabla_x^{\mathsf{T}}\boldsymbol{u})\,\boldsymbol{\sigma} \qquad \text{as} \quad \|\nabla_X\boldsymbol{u}\|_{\text{fro}} \to 0. \tag{1.48}$$

Consequently, the material force balance reads

$$\nabla_x \cdot (\psi \boldsymbol{I} - (\nabla_x^{\mathsf{T}} \boldsymbol{u})\, \boldsymbol{\sigma}) - (\nabla_x^{\mathsf{T}} \boldsymbol{u}) \boldsymbol{f}^{\text{body}} + \boldsymbol{f}^{\text{inh}} = \boldsymbol{0} \qquad \text{in } \Omega, \tag{1.49}$$

with $\boldsymbol{f}^{\text{body}}$ being now defined with respect on Ω.

Remark 1.4.1. *Equation* (1.46) *and* (1.49) *are valid for static inhomogeneities. In the atomistic picture, atoms move in the vicinity of defects, such as cracks or dislocations, due to an external stress or the interactions with other defects, giving rise to a rearrangement of the inhomogeneity. Then, however,* $\delta_X \Pi^{\text{int}}$ *must be interpreted as the driving force of the material defects. The associated mechanical power due to* $\delta_X \Pi^{\text{int}}$ *is nothing but the rate of dissipation. Therefore the inhomogeneous forces must necessarily be used to formulate the corresponding evolution laws to be consistent with the second law of thermodynamics (see also Remark 1.4.3).*

1.4.2 Dislocations as eigenstrains in elastic continua

In the following the application of configurational mechanics to DDD is presented. Thereby, the driving force on the dislocation, the *Peach-Koehler force* (Peach and Koehler, 1950), is introduced as a special case of the divergence of the Eshelby stress tensor $\boldsymbol{B}$. Attention is drawn to the limiting case of small strains, that is $\|\nabla \boldsymbol{u}\|_{\text{fro}} \ll 1$ is assumed throughout the remainder of this section.

The evolution of an initially stress-free body $\Omega \subseteq \mathbb{R}^d$ is considered in the following. It is assumed that the body Ω contains an initial distribution of (discrete) dislocations. In order to simplify the notation only a single dislocation on a slip plane $\mathscr{S}$ with normal vector $\boldsymbol{n}$ and Burgers vector $\boldsymbol{b}$ is examined (Figure 1.5). The framework translates verbatim to arbitrarily many dislocations. By conceiving a continuum model which describes the evolution of a (discrete) atomistic problem, $\mathscr{S}$ can be understood as the plane centered between two layers of atoms associated with a glide plane corresponding to the underlying crystal structure (c.f. Figure 1.2 (a)). The motion of the dislocation, i.e. the motion of $\mathscr{S}$ is fully described by the motion of its boundary, namely the dislocation line $\gamma = \partial\mathscr{S}$. The dislocation line is defined via a sufficiently smooth parametric function $\boldsymbol{s}(u) : I \to \operatorname{span}(\boldsymbol{b}, \boldsymbol{b} \times \boldsymbol{n})$, where $I = [0, 1]$, such that $\gamma := \operatorname{Img}\{\, \boldsymbol{s}(u) \,|\, u \in I \,\}$. Moreover, the slipped parts of the body are implicitly defined by the line direction $\boldsymbol{t}(\boldsymbol{s})$. Further, the glide direction is denoted by $\boldsymbol{m}(\boldsymbol{s})$ (c.f. Figure 1.5). In the following, attention is drawn to dislocation glide, i.e. discrete events such as dislocation cross-slip or nucleation, which may occur in real (atomic) crystals, are not considered.

In order to give the dislocation line a “continuum” sense, an *eigenstrain* $\boldsymbol{\beta}^{\text{p}}$ (:= plastic distortion) is imposed on the slip plane. The decomposition of the displacement gradient into incompatible elastic and plastic parts is adopted here according to (c.f. Mura, 1982)

$$\nabla \boldsymbol{u} = \boldsymbol{\beta}^{\text{e}} + \boldsymbol{\beta}^{\text{p}}, \tag{1.50}$$

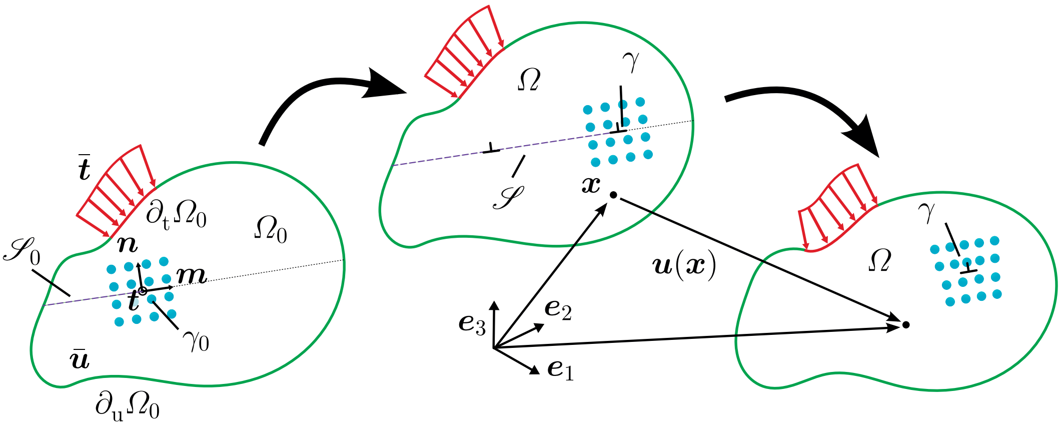
$\bar{\boldsymbol{t}}$
$\partial_{\mathrm{t}}\Omega_0$
Ω_0
$\mathscr{S}_0$
$\boldsymbol{n}$
$\boldsymbol{m}$
$\boldsymbol{t}$
γ_0
$\bar{\boldsymbol{u}}$
$\partial_{\mathrm{u}}\Omega_0$
Ω
γ
$\mathscr{S}$
$\boldsymbol{x}$
$\boldsymbol{u}(\boldsymbol{x})$
$\boldsymbol{e}_3$
$\boldsymbol{e}_2$
$\boldsymbol{e}_1$
γ
Ω

Figure 1.5: Schematic illustration of the motion of a material body for the small strain DDD problem. The dislocation line γ is depicted as an infinite straight line

where $\boldsymbol{\beta}^{\mathrm{e}}$ is the elastic strain (:= elastic distortion). Note that $\boldsymbol{\beta}^{\mathrm{e}}$ and $\boldsymbol{\beta}^{\mathrm{p}}$ are *not* gradients of a displacement field. The symmetric part of the displacement gradient is given by

$$\boldsymbol{\varepsilon} = \operatorname{sym}(\boldsymbol{\beta}) = \operatorname{sym}(\boldsymbol{\beta}^{\mathrm{e}}) + \operatorname{sym}(\boldsymbol{\beta}^{\mathrm{p}}) = \boldsymbol{\varepsilon}^{\mathrm{e}} + \boldsymbol{\varepsilon}^{\mathrm{p}}. \tag{1.51}$$

Within the DDD framework the plastic distortion is pre-defined as

$$\boldsymbol{\beta}^{\mathrm{p}}(\boldsymbol{x}) = \begin{cases} -\boldsymbol{b} \otimes \boldsymbol{n} & \text{on } \mathscr{S}, \\ \boldsymbol{0} & \text{else} \end{cases} \tag{1.52}$$

or alternatively

$$\boldsymbol{\beta}^{\mathrm{p}}(\boldsymbol{x}) = -\int_{\mathscr{S}} \delta(\boldsymbol{x} - \boldsymbol{x}')(\boldsymbol{b} \otimes \boldsymbol{n})\,\mathrm{d}A'. \tag{1.53}$$

Further, the dislocation density tensor is introduced as (Kröner, 1958)

$$\boldsymbol{\alpha} = -\nabla \times \boldsymbol{\beta}^{\mathrm{p}}. \tag{1.54}$$

Using the definition of the plastic distortion (1.53), the dislocation density can be rewritten as (c.f. Mura, 1982; Maugin, 2010)

$$\begin{aligned} -\nabla \times \boldsymbol{\beta}^{\mathrm{p}} &= -\int_{\mathscr{S}} \nabla \times \big(\delta(\boldsymbol{x} - \boldsymbol{x}')(\boldsymbol{b} \otimes \boldsymbol{n})\big)\,\mathrm{d}A' \\ &= -\int_{\mathscr{S}} \big(\nabla \times (\delta(\boldsymbol{x} - \boldsymbol{x}')\boldsymbol{b})\big) \otimes \mathrm{d}\boldsymbol{a}' \\ &= -\int_{\gamma} \delta(\boldsymbol{x} - \boldsymbol{x}')(\boldsymbol{b} \otimes \boldsymbol{t})\,\mathrm{d}C', \end{aligned} \tag{1.55}$$

where use was made of Stokes' theorem in order to transform the surface integral into a line integral.

The definition (1.52) imposes restrictions on the displacement field which is not continuous anymore over the *entire* space, more precisely, $\boldsymbol{u} \in [C^0(\mathit{\Omega} \setminus \mathscr{S})]^d$. Moreover, $\boldsymbol{u}$ is singular on γ which can directly be deduced from the definition of $\boldsymbol{\beta}^{\mathrm{p}}$ and so are the total strain and the Cauchy stress — although this can be remedied by smearing the Burgers vector over the slip plane as shown in the following section. Given the above-mentioned definitions the total energy is now defined as

$$\mathit{\Pi}(\boldsymbol{u}, \boldsymbol{\beta}^{\mathrm{e}}, \boldsymbol{s}) = \mathit{\Pi}^{\mathrm{e}}(\boldsymbol{u}, \boldsymbol{\beta}^{\mathrm{e}}, \boldsymbol{s}) + \mathit{\Pi}^{\mathrm{core}}(\boldsymbol{s}), \tag{1.56}$$

where $\mathit{\Pi}^{\mathrm{e}}(\boldsymbol{u}, \boldsymbol{\beta}^{\mathrm{e}}, \boldsymbol{s})$ is the elastic energy

$$\mathit{\Pi}^{\mathrm{e}}(\boldsymbol{u}, \boldsymbol{\beta}^{\mathrm{e}}, \boldsymbol{s}) = \int_{\mathit{\Omega}} \psi\big(\boldsymbol{\beta}^{\mathrm{e}}(\boldsymbol{x})\big)\,\mathrm{d}V - \int_{\mathit{\Omega}} (\boldsymbol{f}^{\mathrm{body}})^{\mathsf{T}}(\boldsymbol{x}) \cdot \boldsymbol{u}(\boldsymbol{x})\,\mathrm{d}V. \tag{1.57}$$

Note that $\psi\big(\boldsymbol{\beta}^{\mathrm{e}}(\boldsymbol{x})\big) = \psi\big(\boldsymbol{\varepsilon}^{\mathrm{e}}(\boldsymbol{x})\big)$ due to the symmetry properties of material stiffness tensor $\mathbb{C}$. The second contribution in (1.56) stems from an additional contribution which accounts for the mismatch between the elastic energy and the true energy which can be calculated from first principles, e.g. atomistics. The core energy can formally be defined as

$$\mathit{\Pi}^{\mathrm{core}}(\boldsymbol{s}) = \int_{\gamma} W^{\mathrm{core}}(\boldsymbol{s})\,\mathrm{d}C, \tag{1.58}$$

where $W^{\mathrm{core}}(\boldsymbol{s})$ is an energy density (per unit length) which depends on the local line orientation at $\boldsymbol{s}$. A precise definition of W^{core} will be given in the following section.

Having $\mathit{\Pi}^{\mathrm{e}}$ and $\mathit{\Pi}^{\mathrm{core}}$ well-defined, the first variation of $\mathit{\Pi}$ is then given by

$$\delta\mathit{\Pi} = \int_{\mathit{\Omega}} \delta_u \mathit{\Pi}^{\mathrm{e}} \cdot \delta\boldsymbol{u}\,\mathrm{d}V + \int_{\gamma} \delta_s \mathit{\Pi}^{\mathrm{int}} \cdot \delta\boldsymbol{s}\,\mathrm{d}C + \int_{\gamma} \delta_s \mathit{\Pi}^{\mathrm{core}} \cdot \delta\boldsymbol{s}\,\mathrm{d}C, \tag{1.59}$$

with $\delta_u \mathit{\Pi}^{\mathrm{e}} = \nabla \cdot \boldsymbol{\sigma} + \boldsymbol{f}^{\mathrm{body}}$ and

$$\delta_s \mathit{\Pi}^{\mathrm{int}} = -\boldsymbol{f}^{\mathrm{pk}}, \qquad \delta_s \mathit{\Pi}^{\mathrm{core}} = \frac{\partial W^{\mathrm{core}}(\boldsymbol{s})}{\partial \boldsymbol{s}} = -\boldsymbol{f}^{\mathrm{core}}. \tag{1.60}$$

Remark 1.4.2. *In DDD, a variation of the reference configuration is tantamount to a variation of the plastic distortion*

$$\delta_\varepsilon \boldsymbol{\beta}^{\mathrm{p}}(\boldsymbol{x}) = -\int_{\mathscr{S}} \delta(\delta_\varepsilon \boldsymbol{x} - \boldsymbol{x}')(\boldsymbol{b} \otimes \boldsymbol{n})\,\mathrm{d}A', \tag{1.61}$$

where $\delta_\varepsilon \boldsymbol{x} = \boldsymbol{x} + \varepsilon\delta\boldsymbol{u}^{\mathrm{m}}(\boldsymbol{x})$ *for some* $\varepsilon > 0$. *The first variation of* $\mathit{\Pi}$ *with respect to* $\boldsymbol{s}$ *is then loosely defined as*

$$\delta_s \mathit{\Pi}^{\mathrm{int}} \equiv \delta_{\boldsymbol{\beta}^{\mathrm{p}}} \mathit{\Pi}^{\mathrm{int}} = \lim_{\varepsilon \to 0} \frac{1}{2} \frac{(\boldsymbol{\beta} - \delta_\varepsilon \boldsymbol{\beta}^{\mathrm{p}}) \cdot \mathbb{C}\left[\boldsymbol{\beta} - \delta_\varepsilon \boldsymbol{\beta}^{\mathrm{p}}\right] - (\boldsymbol{\beta} - \boldsymbol{\beta}^{\mathrm{p}}) \cdot \mathbb{C}\left[\boldsymbol{\beta} - \boldsymbol{\beta}^{\mathrm{p}}\right]}{\varepsilon}. \tag{1.62}$$

In what follows an explicit expression of the Peach-Koehler force is sought-after. Therefore recall from the previous section that the second integral in (1.59) can be equivalently expressed as

$$\int_\gamma \delta_s \Pi^{\mathrm{int}} \cdot \delta \boldsymbol{s} \,\mathrm{d}C = \int_\Omega (\nabla \cdot \boldsymbol{B}) \cdot \delta \boldsymbol{x} \,\mathrm{d}V - \int_\Omega \left((\boldsymbol{\beta}^{\mathrm{e}})^\mathsf{T} \boldsymbol{f}^{\mathrm{body}} \right) \cdot \delta \boldsymbol{x} \,\mathrm{d}C. \tag{1.63}$$

However, this representation is not immediately useful since the term on the right hand side of (1.63) requires the integration over the entire volume. Hence, it must be converted into a line integral representation in order to reveal an explicit expression of $\boldsymbol{f}^{\mathrm{pk}}$ by taking into account that the variations $\delta \boldsymbol{x}$ are nonzero only on the glide plane. Using the definition of the strain energy density (1.26) it was shown by Mura (1982) that the divergence of the Eshelby stress can be written as (see also Maugin, 2010)

$$\nabla \cdot \boldsymbol{B} = \nabla \cdot (\psi \boldsymbol{I} - (\boldsymbol{\beta}^{\mathrm{e}})^\mathsf{T} \boldsymbol{\sigma}) = \boldsymbol{\epsilon}[\boldsymbol{\sigma}\boldsymbol{\alpha}] + (\boldsymbol{\beta}^{\mathrm{e}})^\mathsf{T} \boldsymbol{f}^{\mathrm{body}}. \tag{1.64}$$

Plugging the latter into (1.63) yields

$$\int_\gamma \delta_s \Pi^{\mathrm{int}} \cdot \delta \boldsymbol{s} \,\mathrm{d}C = - \int_\Omega \boldsymbol{\epsilon}[\boldsymbol{\sigma}(\nabla \times \boldsymbol{\beta}^{\mathrm{p}})] \cdot \delta \boldsymbol{x} \,\mathrm{d}V. \tag{1.65}$$

Using (1.55) and the properties of the delta function one obtains

$$\begin{aligned} - \int_\Omega \boldsymbol{\epsilon}[\boldsymbol{\sigma}(\nabla \times \boldsymbol{\beta}^{\mathrm{p}})] \,\mathrm{d}V &= - \int_\Omega \boldsymbol{\epsilon} \left[\boldsymbol{\sigma} \left(\int_\gamma \delta(\boldsymbol{s} - \boldsymbol{s}')(\boldsymbol{b} \otimes \boldsymbol{t}) \,\mathrm{d}C' \right) \right] \cdot \delta \boldsymbol{x} \,\mathrm{d}V \\ &= - \int_\Omega \left(\int_\gamma \delta(\boldsymbol{s} - \boldsymbol{s}') \, \boldsymbol{\epsilon}[\boldsymbol{\sigma}(\boldsymbol{b} \otimes \boldsymbol{t})] \,\mathrm{d}C' \right) \cdot \delta \boldsymbol{x} \,\mathrm{d}V \\ &= - \int_\gamma \boldsymbol{\epsilon}[\boldsymbol{\sigma}(\boldsymbol{b} \otimes \boldsymbol{t})] \cdot \delta \boldsymbol{s} \,\mathrm{d}C. \end{aligned} \tag{1.66}$$

Consequently, the Peach-Koehler force can be deduced as

$$\boldsymbol{f}^{\mathrm{pk}} = -\delta_s \Pi^{\mathrm{int}} = \boldsymbol{\epsilon}[\boldsymbol{\sigma}(\boldsymbol{b} \otimes \boldsymbol{t})] = (\boldsymbol{\sigma}\boldsymbol{b}) \times \boldsymbol{t}, \tag{1.67}$$

where the latter expression is the one first obtained by Peach and Koehler (1950) in the absence of body forces.

In what follows it is assumed that the system must be in equilibrium with respect to the displacement field $\boldsymbol{u}$ and the dislocation line γ. Therefore the following optimization problem is defined

$$\{\boldsymbol{u}, \boldsymbol{s}\} := \mathrm{Arg} \left\{ \min_{\delta \boldsymbol{u}} \min_{\delta \boldsymbol{s}} \Pi(\delta \boldsymbol{u}, \delta \boldsymbol{s}) \right\}. \tag{1.68}$$

Problem (1.68) is convex with respect to $\boldsymbol{u}$ but likely *nonconvex* with respect to $\boldsymbol{s}$, especially when multiple dislocations are present. Therefore the final solution is usually not unique and depends largely on the initial guess, that is the initial position of the dislocation line γ (see below).

The Euler-Lagrange equations corresponding to (1.68) are the momentum balance equations in the physical and the material space which are combined here as follows

$$\boxed{\mathcal{P}^{\mathrm{c}} \quad \begin{cases} \underline{\text{Physical problem } \mathcal{P}^{\mathrm{c/p}}\text{:}} \\ \nabla \cdot \boldsymbol{\sigma} + \boldsymbol{f}^{\mathrm{body}} = \boldsymbol{0} \qquad \text{in } \Omega, \\ \quad + \text{boundary conditions (1.12)}, \\ \underline{\text{DDD problem } \mathcal{P}^{\mathrm{c/dd}}\text{:}} \\ \quad \boldsymbol{f}^{\mathrm{pk}} + \boldsymbol{f}^{\mathrm{core}} = \boldsymbol{0} \qquad \text{on } \gamma, \\ \quad + \text{boundary conditions.} \end{cases}} \tag{1.69}$$

The coupled problem is consequently denoted as $\mathcal{P}^{\mathrm{c}} := \mathcal{P}^{\mathrm{c/p}} \wedge \mathcal{P}^{\mathrm{c/dd}}$. The physical problem $\mathcal{P}^{\mathrm{c/p}}$ is coupled to $\mathcal{P}^{\mathrm{c/dd}}$ via the position of γ which defines the plastic distortion $\boldsymbol{\beta}^{\mathrm{p}}$. Vice versa, the material sub-problem $\mathcal{P}^{\mathrm{c/dd}}$ is coupled to $\mathcal{P}^{\mathrm{c/p}}$ via the Cauchy stress $\boldsymbol{\sigma}$ which defines the driving force on the dislocation line. In the following it is tacitly assumed that a solution γ to (1.69) satisfies the stability requirement

$$\forall \text{ admissible } \delta \boldsymbol{s} \qquad \langle \delta_s^2 \Pi(\boldsymbol{s}) \delta \boldsymbol{s}, \delta \boldsymbol{s} \rangle_{L^2(\gamma)} > 0. \tag{1.70}$$

It is then guaranteed that solutions to $\mathcal{P}^{\mathrm{c}}$ are also minimizers of Π.

Remark 1.4.3. *Boundary conditions on the problem $\mathcal{P}^{\mathrm{c/dd}}$ usually imply pinning points of γ, i.e. Dirichlet-type boundary conditions, which mimic obstacles due to precipitation. Neumann-type boundary conditions could be incorporated via a body force $\boldsymbol{f}^{\mathrm{body}}$ in the physical balance equation (c.f. equation* (1.67)*).*

Dislocation line evolution

A delicate issue is the evolution of discrete dislocations. At first glance, problem (1.69), as stated, does not require any precise information about the motion of the dislocation γ — besides its kinematics which is assumed to be known — since only the final equilibrium state is sought-after. But, recall that the total energy Π is possibly nonconvex with respect to the positions of the dislocations. Applying a standard nonlinear solver to (1.69) can lead to unphysical results since the corresponding search directions may not be fundamentally energy-minimizing paths.[2] More precisely, DDD is inherently *event-driven*. Discrete events are based on the interaction with other dislocations when they come close together (junction formation, annihilation), on the local stress state (dislocation nucleation) or on stochastics (e.g. cross slip). Hence, a classical energy minimization may yield deceptive search directions.

---

[2] Here, "fundamentally energy-minimizing" refers to a comparable atomistic simulation

The inevitable requirement of a physical motion of the dislocation lines motivates the definition of an evolution law for γ. For quasi-static problems the evolution of the dislocation can be formulated as a gradient flow (Bulatov et al., 2006), that is the driving force on the dislocation and the dislocation velocity $\boldsymbol{v}$ are linearly related through the dislocation mobility tensor $\boldsymbol{M}$ such that

$$\boldsymbol{v} = \boldsymbol{M}(\boldsymbol{f}^{\text{pk}} + \boldsymbol{f}^{\text{core}}) \qquad \text{on } \gamma. \tag{1.71}$$

The dislocation mobility tensor $\boldsymbol{M}$ is defined similarly to (1.35) but is not merely a projection tensor and can also contain additional information, e.g. temperature dependence. The general form of the mobility tensor reads (e.g. Arsenlis et al., 2007)

$$\boldsymbol{M} = m^{\text{g}}\boldsymbol{P}^{\text{g}} + m^{\text{c}}\boldsymbol{P}^{\text{c}}, \tag{1.72}$$

with the projection tensors

$$\boldsymbol{P}^{\text{g}} = \boldsymbol{m} \otimes \boldsymbol{m}, \qquad \boldsymbol{P}^{\text{c}} = \boldsymbol{n} \otimes \boldsymbol{n}. \tag{1.73}$$

The superscripts $\bullet^{\text{g}}$ and $\bullet^{\text{c}}$ are related to dislocation glide (normal to the dislocation line) and climb (normal to the glide plane). Using the properties of projection tensors (i.e. $\boldsymbol{P}^{\text{g}}\boldsymbol{P}^{\text{g}} = \boldsymbol{P}^{\text{g}}$, $\boldsymbol{P}^{\text{g}}\boldsymbol{P}^{\text{c}} = \boldsymbol{0}$ etc.) one obtains the more common drag relation (Amodeo and Ghoniem, 1990)

$$\boldsymbol{D}\boldsymbol{v} = (\boldsymbol{P}^{\text{g}} + \boldsymbol{P}^{\text{c}})(\boldsymbol{f}^{\text{pk}} + \boldsymbol{f}^{\text{core}}) \qquad \text{with} \quad \boldsymbol{D} = d^{\text{g}}\boldsymbol{P}^{\text{g}} + d^{\text{c}}\boldsymbol{P}^{\text{c}}, \tag{1.74}$$

where the drag coefficients d^{g} and d^{c} are the inverted mobility coefficients.

Remark 1.4.4. *It can be checked that the evolution law* (1.71) *is thermodynamically consistent. Consider the second term in the dissipation inequality* (1.28)*. Since $\boldsymbol{s} \sim \boldsymbol{\varepsilon}^{\text{p}}$ one may write with $\hat{\alpha} = \boldsymbol{s}$*

$$\frac{\partial\psi(\boldsymbol{\varepsilon}, \boldsymbol{s})}{\partial \boldsymbol{s}} \cdot \dot{\boldsymbol{s}} = \frac{\partial\psi(\boldsymbol{\varepsilon}, \boldsymbol{s})}{\partial \boldsymbol{s}} \cdot \boldsymbol{v}. \tag{1.75}$$

With $\partial\psi/\partial\boldsymbol{s} = \boldsymbol{f}^{\text{pk}}$ it follows

$$(\boldsymbol{f}^{\text{pk}})^{\mathsf{T}} \cdot (\boldsymbol{M}\boldsymbol{f}^{\text{pk}}) \geq 0 \tag{1.76}$$

since the velocity always points in the direction of the force vector.

1.4.3 Dislocation core energy — how to deal with the singularity

An issue that has been left aside so far is a clear interpretation of the dislocation core structure. The particular choice of the plastic distortion $\boldsymbol{\beta}^{\text{p}}$ (1.53) effectively terminates the slip on the dislocation line and the strain energy density ψ therefore becomes singular. This is of no concern for two-dimensional problems where the dislocations are treated as infinite straight lines. In three dimensions, however, dislocation loops are allowed to expand or shrink, much like a flexible string. Hence, the driving force on a particular point on the dislocation line depends on the stress field of the loop itself. The computation of $\boldsymbol{f}^{\mathrm{pk}}$ is thus ill-defined since the Cauchy stress diverges as $r \to 0$, where r is the distance from any field point $\boldsymbol{x}$ to some point $\boldsymbol{s}$ on the dislocation line γ.

Two different approaches which circumvent the singularity problem are addressed in the following: (1) classical elasticity with core-cut off and (2) a nonsingular solution with spread Burgers vector. Further, another approach is discussed which assumes an, in principle arbitrary, regularization of the dislocation core (e.g. (1) or (2)) and introduces an additional core energy term. Every approach contains a single parameter which has to be calibrated to atomistics (c.f. Section 1.5.4). The parameters are listed in Table 1.1.

	Classical	Nonsingular	Extra core energy
Plastic distortion	$\boldsymbol{\beta}^{\mathrm{p}}$	$\boldsymbol{\beta}^{\mathrm{p}} * w$	any
Free parameter	$r_{\mathrm{cut}}^{\mathrm{core}}$	a	E^{core}

Table 1.1: Three modeling approaches for the dislocation core energy corresponding to Example 1.3, 1.4 and 1.5

Another interesting approach due to Lazar (2013); Po et al. (2014) is not considered in the following. Their approach uses a generalized continuum (c.f. Remark 1.3.1) which involves the first gradient of the small strain tensor in the free energy density. This construction naturally introduces an internal length scale parameter which is then calibrated to atomistics.

Example 1.3 (**Classical elasticity with core cut-off**). In the classical theory, the jump of the displacement field $[\![\boldsymbol{u}]\!]$ is constant over the entire glide plane. This renders all physical quantities singular on the dislocation line. In order to compute a finite energy, a standard approach is to exclude a tubular core region Ω^{core} with radius $r_{\mathrm{cut}}^{\mathrm{core}}$ from the whole body (c.f. Hirth and Lothe, 1982). The total energy then reads

$$\Pi = \int_{\Omega \setminus \Omega^{\mathrm{core}}} \psi(\boldsymbol{\beta}, \boldsymbol{\beta}^{\mathrm{p}}) \, \mathrm{d}V < \infty, \tag{1.77}$$

with $\boldsymbol{\beta}^{\mathrm{p}}$ given by (1.53). In practice, the total energy is usually cast into a line integral *before* introducing $r_{\mathrm{cut}}^{\mathrm{core}}$ which simplifies the computation of the stress fields (see, e.g. Indenbom and Lothe, 1992; Balluffi, 2012). The core cut-off is then interpreted as a truncation of this line integral. In order to calibrate the continuum energy to atomistic results, the core cut-off $r_{\mathrm{cut}}^{\mathrm{core}}$ is taken as a free parameter in order to match the energies for a specific configuration. Usually it is expected that $r_{\mathrm{cut}}^{\mathrm{core}} \in \mathcal{O}(b)$ (Hull and Bacon, 2001). ☐

Example 1.4 (Nonsingular elasticity). The classical regularization (1.77) suffers from several inconsistencies (c.f. Cai et al., 2006). For example, it was shown by LeSar (2004) that different line integral representations of (1.77) yield different energies, independent of $r_{\mathrm{cut}}^{\mathrm{core}}$. Another possibility to regularize the energy is to spread the Burgers vector around the dislocation line. Mathematically this is accomplished by convolving $\boldsymbol{\beta}^{\mathrm{p}}$ with a spreading function w. The nonsingular plastic distortion is then defined as

$$\boldsymbol{\beta}^{\mathrm{p,ns}} = \boldsymbol{\beta}^{\mathrm{p}} * w \qquad \Rightarrow \qquad \boldsymbol{\beta} = \boldsymbol{\beta}^{\mathrm{e}} + \boldsymbol{\beta}^{\mathrm{p,ns}}. \tag{1.78}$$

The elastic energy of a single dislocation in Ω is then given by

$$\begin{aligned} \Pi &= \frac{1}{2}\int_{\Omega} \boldsymbol{\sigma} \cdot \boldsymbol{\beta}^{\mathrm{e}} \, \mathrm{d}V = \frac{1}{2}\int_{\Omega} \boldsymbol{\sigma} \cdot \boldsymbol{\beta} \, \mathrm{d}V - \frac{1}{2}\int_{\Omega} \boldsymbol{\sigma} \cdot \boldsymbol{\beta}^{\mathrm{p,ns}} \, \mathrm{d}V \\ &= -\frac{1}{2}\int_{\Omega} \boldsymbol{\sigma} \cdot \boldsymbol{\beta}^{\mathrm{p,ns}} \, \mathrm{d}V = -\frac{1}{2}\int_{\Omega} \boldsymbol{\sigma} \cdot (\boldsymbol{\beta}^{\mathrm{p}} * w) \, \mathrm{d}V. \end{aligned} \tag{1.79}$$

In principle, there is great freedom in choosing an appropriate w, e.g. it may be calibrated to reproduce real atomistic cores structures. However, it is highly desirable from a practical point of view to obtain simple expressions for the stress fields since the interaction between dislocations is long-range. The only practical implementation that the author is aware of was suggested by Cai et al. (2006) for isotropic solids. Their ingenious idea is illustrated in the following. First, recall that the Cauchy stress can be expressed as convolution of a linear differential operator $\mathcal{L}$, acting on $r = \sqrt{x_1^2 + x_2^2 + x_3^2}$, with the dislocation density $\boldsymbol{\alpha}$ (e.g. Mura, 1982) such that

$$\begin{aligned} \boldsymbol{\sigma} &= \mathcal{L}(r) * \boldsymbol{\alpha} = -\mathcal{L}(r) * (\nabla \times \boldsymbol{\beta}^{\mathrm{p,ns}}) \\ &= -\mathcal{L}(r) * \big((\nabla \times \boldsymbol{\beta}^{\mathrm{p}}) * w\big) = -\mathcal{L}(r) * w * (\nabla \times \boldsymbol{\beta}^{\mathrm{p}}). \end{aligned} \tag{1.80}$$

Plugging the latter into (1.79) and using the differentiation properties of the convolution operator gives

$$\begin{aligned} \Pi &= \frac{1}{2}\int_{\Omega} \big(\mathcal{L}(r) * w * (\nabla \times \boldsymbol{\beta}^{\mathrm{p}})\big) \cdot (\boldsymbol{\beta}^{\mathrm{p}} * w) \, \mathrm{d}V \\ &= \frac{1}{2}\int_{\Omega} \big(\mathcal{L}(r) * w * w * (\nabla \times \boldsymbol{\beta}^{\mathrm{p}})\big) \cdot \boldsymbol{\beta}^{\mathrm{p}} \, \mathrm{d}V \\ &= \frac{1}{2}\int_{\Omega} \big(\mathcal{L}(r * w * w) * (\nabla \times \boldsymbol{\beta}^{\mathrm{p}})\big) \cdot \boldsymbol{\beta}^{\mathrm{p}} \, \mathrm{d}V \\ &= \frac{1}{2}\int_{\Omega} \big(\mathcal{L}(r * \tilde{w}) * (\nabla \times \boldsymbol{\beta}^{\mathrm{p}})\big) \cdot \boldsymbol{\beta}^{\mathrm{p}} \, \mathrm{d}V, \end{aligned} \tag{1.81}$$

where $\tilde{w} = w * w$. If $w = \delta$, then $\tilde{w} = \delta$ and (1.81) yields the classical result. Cai et al. (2006) choose $\tilde{w}$ in such a way that its convolution with r yields the particular simple expression

$$r_a = r * \tilde{w} = \sqrt{x_1^2 + x_2^2 + x_3^2 + a^2}, \tag{1.82}$$

where a is a scalar core spreading parameter. Therefore the stress field can be obtained from the classical solution by simply replacing r with r_a. The *effective* self-stress which acts on any point of the dislocation, i.e. the stress which appears in the Peach-Koehler force, is given by

$$\boldsymbol{\sigma}^{\mathrm{eff}} = -\mathcal{L}(r_a) * (\nabla \times \boldsymbol{\beta}^{\mathrm{p}}) = \boldsymbol{\sigma} * \tilde{w} \tag{1.83}$$

and the same holds true for the stress due to another dislocation with the same isotropic core spreading.

Despite its simplicity, pre-defining $w * w$ leaves the actual spreading function undefined a priori as remarked by Po et al. (2014).[3] Whenever the dislocation is subject to a non-homogeneous applied stress $\boldsymbol{\sigma}^{\mathrm{app}}$ (e.g. due to external boundary conditions), the complex convolution integral $\boldsymbol{\sigma}^{\mathrm{app}} * \tilde{w}$ has to be evaluated. Nevertheless, if the stress gradients are sufficiently small around the dislocation core it may be sufficient to set $\boldsymbol{\sigma}^{\mathrm{app}} * \tilde{w} \approx \boldsymbol{\sigma}^{\mathrm{app}}$. □

Example 1.5 (Additional core energy term). Although the cut-off radius $r_{\mathrm{cut}}^{\mathrm{core}}$ (or the spreading parameter a) can be used to calibrate the total energy of a dislocation, the estimated value might perturb the stress field of the dislocation. This drawback can be remedied by fixing the core cut-off radius to an educated guess which encompasses the nonlinear core region (usually $\mathcal{O}(b)$) and adding an additional core contribution according to (1.56). The total core energy Π^{core} is assumed to be an integral of the core energy per unit length W^{core} which depends only on the local line orientation (see equation (1.58)). Finding the functional structure of W^{core} is a non-trivial task. Here, a particular simple example, widely used in the DDD community (see, e.g. the works by Bulatov and Cai (2006); Arsenlis et al. (2007); Fitzgerald and Aubry (2010); Szajewski et al. (2015)) is discussed which closely resembles the elasticity part. This model is derived in the following.

Assume a system containing a single dislocation γ. Recall that the elastic energy per unit length of a dislocation with character angle ϑ within a hollow disk with inner radius $r_{\mathrm{cut}}^{\mathrm{core}}$ and outer radius R is given by (Hirth and Lothe, 1982)

$$W^{\mathrm{e}} = k(\mathbb{C};\vartheta)\ln\left(\frac{R}{r_{\mathrm{cut}}^{\mathrm{core}}}\right), \tag{1.84}$$

where $k(\mathbb{C};\vartheta)$ is the *energy factor* which depends on the elastic constants and the character angle of the dislocation. Under the assumption that the character angle varies smoothly along γ the total energy Π can be approximated as a line integral over γ (c.f. Bacon et al., 1980)

$$\Pi \approx \int_\gamma W^{\mathrm{e}}(\boldsymbol{s})\,\mathrm{d}C = \int_\gamma k(\mathbb{C};\vartheta(\boldsymbol{s}))\ln\left(\frac{R}{r_{\mathrm{cut}}^{\mathrm{core}}}\right)\mathrm{d}C. \tag{1.85}$$

---

[3] An analytical approximation of $\tilde{w}$ is given in (Cai et al., 2006)

In the following the special case of isotropic solids is considered (for a discussion on anisotropic solids see Fitzgerald and Aubry, 2010). The energy factor then reads

$$\begin{aligned} k(\mathbb{C};\vartheta) = k(\mu,\nu;\vartheta) &= \frac{\mu b^2}{4\pi}\left(\frac{\sin^2\vartheta}{1-\nu} + \cos^2\vartheta\right) \\ &= \frac{\mu}{4\pi}\left(\frac{\|\boldsymbol{b}^{\perp}\|^2}{1-\nu} + \|\boldsymbol{b}^{\|}\|^2\right), \end{aligned} \tag{1.86}$$

with the shear modulus μ and the Poisson ratio ν; the vectors $\boldsymbol{b}^{\perp}$ and $\boldsymbol{b}^{\|}$ represent the edge and screw component of the Burgers vector $\boldsymbol{b}$, respectively. Now assume that the core cut-off radius is given by $r^{\text{core}}_{\text{cut}} = r$ which has been obtained from an atomistic calculation. The total energy per unit length is then written as

$$W = W^{\text{e}}(r) = k(\mu,\nu;\vartheta)\ln\left(\frac{R}{r}\right). \tag{1.87}$$

As stated above, it can be beneficial to fix the core cut-off radius to some finite value, e.g. $r^{\text{core}}_{\text{cut}} = b$,[4] such that the far-field behavior, more precisely, the stress field of the dislocation, remains unaffected. However, the elastic energy alone might not represent the true atomistic energy anymore. By adding and subtracting the elastic energy due to $r^{\text{core}}_{\text{cut}} = b$ the energy (1.87) can be rearranged as follows

$$\begin{aligned} W &= W^{\text{e}}(r) + W^{\text{e}}(b) - W^{\text{e}}(b) \\ &= k\ln\left(\frac{R}{r}\right) + k\ln\left(\frac{R}{b}\right) - k\ln\left(\frac{R}{b}\right) \\ &= k\ln(R) - k\ln(r) + k\ln(b) - k\ln(b) \\ &= k\ln\left(\frac{R}{b}\right) + k\ln\left(\frac{b}{r}\right). \end{aligned} \tag{1.88}$$

The first term is nothing but the elastic energy for $r^{\text{core}}_{\text{cut}} = b$. The second term is *independent* of R but dependent on the choice of $r^{\text{core}}_{\text{cut}}$ and b, the elastic constants and ϑ. A natural choice is thus to assume that the core energy depends on the character angle in the same way such that

$$W^{\text{core}}(E^{\text{core}};\nu;\vartheta) = E^{\text{core}}\left(\frac{\|\boldsymbol{b}^{\perp}\|^2}{1-\nu} + \|\boldsymbol{b}^{\|}\|^2\right), \tag{1.89}$$

where E^{core} replaces the term $(\mu/4\pi)\ln(b/r^{\text{core}}_{\text{cut}})$.[5] The total energy per unit length then reads

$$W = W^{\text{e}}(b) + W^{\text{core}}(E^{\text{core}};\nu;\vartheta). \tag{1.90}$$

---

[4] this is a common assumption for compact dislocation cores

[5] This terminology is commonly used in the DDD community (e.g. Bulatov et al., 2006)

The parameter E^{core} must be calibrated to atomistic models. This will be examined in Section 1.5.4.

In order to compute the forces on the dislocation line due to the additional core energy contribution first note that a variation in the position vector $\delta \boldsymbol{s}$ causes an infinitesimal change *only* in the direction normal to the dislocation line $\boldsymbol{m}$. The only parameter in W^{core} which depends on $\boldsymbol{s}$ is the character angle ϑ and therefore $\delta \boldsymbol{s} = \partial_\vartheta \boldsymbol{s}\, \delta\vartheta = \delta\vartheta\, \boldsymbol{m}$. The variation of the total core energy then reads

$$\delta \Pi^{\text{core}} = -\int_\gamma \left((\boldsymbol{f}^{\text{core}})^\mathsf{T} \cdot \boldsymbol{m} \right) \delta\vartheta \, \mathrm{d}C, \tag{1.91}$$

where $\boldsymbol{f}^{\text{core}} = -\delta_s \Pi^{\text{core}}$. In the case of an isotropic elastic solid it can be directly deduced from (1.89), i.e.

$$\begin{aligned} \boldsymbol{f}^{\text{core}} = -\frac{\partial W^{\text{core}}(\vartheta)}{\partial \vartheta} \boldsymbol{m} &= -\left(E^{\text{core}} \frac{2\nu}{1-\nu} \|\boldsymbol{b}^\perp\| \|\boldsymbol{b}^\|\| \right) \boldsymbol{m} \\ &= -\left(E^{\text{core}} \frac{2\nu}{1-\nu} \|\boldsymbol{b}^\|\| \right) \boldsymbol{b}^\perp, \end{aligned} \tag{1.92}$$

where $\|\boldsymbol{b}^\perp\|\, \boldsymbol{m} = \boldsymbol{b}^\perp$. □

1.4.4 Informing classical plasticity models from discrete dislocations dynamics simulations

DDD models can be used to characterize the macroscopic behavior due to plastic deformation induced by a collective motion of dislocations (c.f. Figure 1.2 (b)). The output of DDD simulations can then be used to calibrate continuum/density-based plasticity models (see Section 1.3.3). To account for a physically correct behavior of the dislocations, DDD models need to be supplemented with "constitutive" laws dictated by finer-scale models, e.g. atomistics. The motion of individual dislocations and their long-range interactions is well-established in the sense that the kinematics (i.e. the slip systems), the elastic constants and the core energy are reasonably captured by DDD. However, there exist many situations where a scale-separation between the discrete dislocation and the atomic scale does not apply. This includes multiple defect interactions such as dislocation pinning effects induced by precipitation or voids (Bacon et al., 2009), dislocation-crack interactions etc. One possibility to overcome this issue are concurrent multiscale models where fully atomistic and elasticity regions exist simultaneously in order to combine the individual strengths of both models. These methods will be discussed in detail in Chapter 2 and 3.

1.5 Atomistic modeling

1.5.1 Molecular statics

Contrary to the continuum models discussed in the previous sections the topological space of an atomistic model is a discrete space. That is, instead of evolving a continuous body the atomistic model only keeps track of a *finite* number of "material points", namely the lattice sites. The properties of the lattice define the nature of the material. Here, the focus is on crystalline solids such as metals which exhibit a well-defined crystal structure (lattice structure). Attention is drawn to monoatomic lattices. The computational domain is then defined as a subset of a Bravais lattice of dimension d

$$\varLambda \subseteq \left\{ \sum_{i=1}^{d} z_i \boldsymbol{a}_i \,\middle|\, z_i \in \mathbb{Z} \right\} = \boldsymbol{A}\mathbb{Z}^d, \tag{1.93}$$

where the basis vectors $\{\boldsymbol{a}_i\}_{i=1,\dots,d}$, i.e. the column vectors of the matrix $\boldsymbol{A}$ define the lattice type. The basis vectors are linearly independent such that $\boldsymbol{A}$ is nonsingular. In two dimensions, typical examples are square and hexagonal lattices which can be defined via

$$\boldsymbol{A}^{\text{sq}} = a_0 \begin{bmatrix} 1 & 0 \\ 0 & 1 \end{bmatrix}, \qquad \boldsymbol{A}^{\text{hex}} = a_0 \begin{bmatrix} 1 & 1/2 \\ 0 & \sqrt{3}/2 \end{bmatrix}, \tag{1.94}$$

where a_0 is the lattice constant, i.e. the natural length scale of the material. In three dimensions, classical examples are face-centered cubic (fcc) and body-centered cubic (bcc) lattices which can be constructed via

$$\boldsymbol{A}^{\text{fcc}} = a_0 \begin{bmatrix} 1/2 & 0 & 1/2 \\ 0 & 1/2 & 1/2 \\ 1/2 & 1/2 & 0 \end{bmatrix}, \qquad \boldsymbol{A}^{\text{bcc}} = a_0 \begin{bmatrix} 1/2 & 1/2 & 1/2 \\ 1/2 & -1/2 & 1/2 \\ 1/2 & 1/2 & -1/2 \end{bmatrix}. \tag{1.95}$$

The unit cells for fcc and bcc lattices are shown in Figure 1.6 (a). A deformation of the lattice $\varLambda$ is described via displacements $\boldsymbol{u} \in \mathcal{U} := \{\, \boldsymbol{v} : \varLambda \to \mathbb{R}^d \,\}$ (possible boundary conditions will be specified in Section 1.5.3). Every element (atom) $\boldsymbol{\xi} \in \varLambda$ has a site energy $\mathcal{E}_\xi$. It is assumed that the site energy depends on the displacement of atom ξ relative to all other atoms within its interaction range $\mathcal{R}_\xi$ which usually extends over a few lattice spacings as shown in Figure 1.6 (b) (infinite-range interactions, e.g. Coulomb interactions, are not considered). This renders the atomistic model nonlocal — but short-range. This dependence is abbreviated according to $\{\boldsymbol{u}_\eta - \boldsymbol{u}_\xi\}_{\boldsymbol{\eta} \in \mathcal{R}_\xi \setminus \boldsymbol{\xi}} \equiv \{\boldsymbol{u}_\eta - \boldsymbol{u}_\xi\}$ such that $\mathcal{E}_\xi = \mathcal{E}_\xi(\{\boldsymbol{u}_\eta - \boldsymbol{u}_\xi\})$, where $\boldsymbol{u}_\xi = \boldsymbol{u}(\boldsymbol{\xi})$ and $\boldsymbol{u}_\eta = \boldsymbol{u}(\boldsymbol{\eta})$. Examples for $\mathcal{E}_\xi$ are given in the following section.

The total energy of the system in terms of the displacements is written as (c.f. Luskin and Ortner, 2013)

$$\varPi(\boldsymbol{u}) = \varPi_0 + \varPi^{\text{int}}(\boldsymbol{u}) + \varPi^{\text{ext}}(\boldsymbol{u}), \tag{1.96}$$

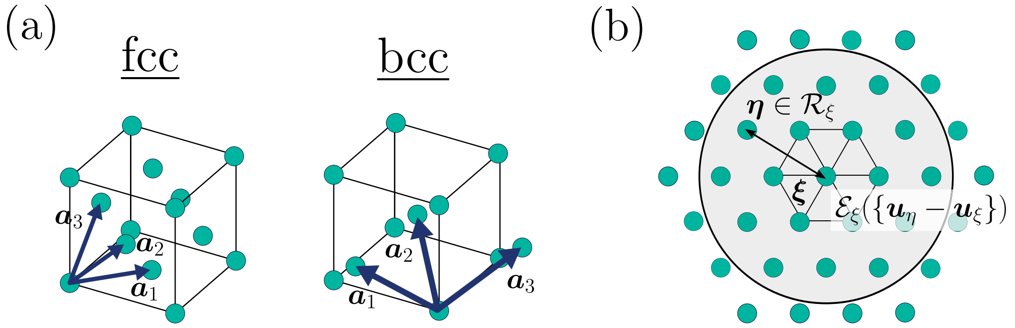
(a)
fcc
bcc
a_1
a_2
a_3
(b)
$\eta \in \mathcal{R}_\xi$
ξ
$\mathcal{E}_\xi(\{u_\eta - u_\xi\})$

Figure 1.6: (a) Unit cells for an fcc and a bcc lattice. (b) Schematic illustration of the interaction range $\mathcal{R}_\xi$ of interatomic potentials

where $\mathit{\Pi}_0$ is the energy of the ground state. For convenience $\mathit{\Pi}_0 = 0$ is assumed in the following. The internal and external contributions are then defined as

$$\mathit{\Pi}^{\text{int}}(\boldsymbol{u}) = \sum_{\boldsymbol{\xi} \in \mathit{\Lambda}} \mathcal{E}_\xi(\{\boldsymbol{u}_\eta - \boldsymbol{u}_\xi\}), \qquad \mathit{\Pi}^{\text{ext}}(\boldsymbol{u}) = -\sum_{\boldsymbol{\xi} \in \mathit{\Lambda}} (\boldsymbol{f}_\xi^{\text{ext}})^{\mathsf{T}} \cdot \boldsymbol{u}_\xi, \tag{1.97}$$

where $\boldsymbol{f}^{\text{ext}}(\boldsymbol{\xi})$ is an external force. This definition readily includes the entire class of interatomic many-body potentials. The total energy $\mathit{\Pi}$ is assumed to be nonlinear and nonconvex with respect to $\boldsymbol{u}$. Therefore the atomistic model naturally supports complex phenomena, i.e. all kinds of crystallographic defects, fracture etc. (c.f. Figure 1.7 (a)).

In molecular statics one seeks for solutions of the optimization problem

$$\boldsymbol{u} := \operatorname{Arg}\left\{ \min_{\boldsymbol{v} \in \mathcal{U}} \mathit{\Pi}(\boldsymbol{v}) \right\}. \tag{1.98}$$

In general problem (1.98) is ill-posed due to the nonconvex energy landscape, i.e. multiple solutions possibly exist. Here, a *global* optimization of $\mathit{\Pi}$ is not considered. Rather, one starts with a suitably chosen initial configuration, e.g. the ideal lattice, subject to an incrementally applied external loading. Therefore solutions $\boldsymbol{u}$ which solve (1.98) should be interpreted as *local* solutions.

The functional derivative of $\mathit{\Pi}(\boldsymbol{u})$ at $\boldsymbol{\xi}$ is given by

$$\begin{aligned} \delta_\xi \mathit{\Pi} = \delta_\xi \mathit{\Pi}^{\text{int}} + \delta_\xi \mathit{\Pi}^{\text{ext}} &= \frac{\partial \mathit{\Pi}^{\text{int}}(\boldsymbol{u})}{\partial \boldsymbol{u}_\xi} + \frac{\partial \mathit{\Pi}^{\text{ext}}(\boldsymbol{u})}{\partial \boldsymbol{u}_\xi} \\ &= \boldsymbol{f}_\xi - \boldsymbol{f}_\xi^{\text{ext}}, \end{aligned} \tag{1.99}$$

where $\boldsymbol{f}_\xi$ is the internal force on an atom. In the ground state $\delta_\xi \mathit{\Pi}^{\text{int}}(\boldsymbol{0}) = \boldsymbol{0}$ holds, i.e. in the absence of external forces. Solutions to (1.98) solve the Euler-Lagrange equation

$$\boxed{\mathcal{P}^{\text{a}} \begin{cases} \boldsymbol{f}_\xi - \boldsymbol{f}_\xi^{\text{ext}} = \boldsymbol{0} & \text{in } \mathit{\Lambda}, \\ \quad + \text{boundary conditions.} \end{cases}} \tag{1.100}$$

It is asserted that the minimizers $\boldsymbol{u}$ are strongly stable in the sense that the second variation of the energy functional is strictly positive such that

$$\forall\, \boldsymbol{v} \in \mathcal{U} \setminus \mathbf{0} \qquad \langle \delta^2 \mathit{\Pi}(\boldsymbol{u})\boldsymbol{v}, \boldsymbol{v} \rangle > 0. \tag{1.101}$$

It is then easy to see that solutions to (1.100) are also minimizers of $\mathit{\Pi}$.

1.5.2 Interatomic potentials

The choice of the interatomic potential, i.e. the site energy $\mathcal{E}_\xi$, underpins the material behavior at a fundamental level. It is thus key to find an appropriate functional form which describes the corresponding phenomena such as plasticity and failure. This process can be thought of as some kind of "constitutive modeling", similar to classical continuum mechanics. However, it might be superior to describe it as a calibration to ab initio calculations (e.g. DFT) since atomistic modeling is a direct approximation of the Schrödinger equation. The class of interatomic potentials is thus commonly referred to as *(semi-)empirical* potentials. A general form of $\mathcal{E}_\xi$ can be rigorously derived as a sequence of n-body potential functions whose size equals the total number of atoms in the system (e.g. Martin, 1975). Most of the time it is yet sufficient to consider only small numbers of n. Two examples which will be of use in this work are discussed in the following.[6]

Example 1.6 (Pair potentials). Pair potentials are the simplest type of interatomic potentials. Usually they cannot be employed solely in order to model realistic material behavior — except for noble gases. However, they are among the most popular toy models as they are cheap to compute. The site energy of an atom $\boldsymbol{\xi}$ depends only on pairwise interactions with other atoms in $\mathcal{R}_\xi$ via a potential function $\phi(\boldsymbol{u}_\eta - \boldsymbol{u}_\xi)$. The site energy is then given by $\mathcal{E}_\xi(\{\boldsymbol{u}_\eta - \boldsymbol{u}_\xi\}) = 1/2 \sum_{\boldsymbol{\eta} \in \mathcal{R}_\xi \setminus \boldsymbol{\xi}} \phi(\boldsymbol{u}_\eta - \boldsymbol{u}_\xi)$. The function ϕ usually contains an attractive and a repulsive part which becomes dominant if atoms are far apart or too close together, respectively. One simple pair potential is the Morse potential (Morse, 1929)

$$\phi(\boldsymbol{u}_\eta - \boldsymbol{u}_\xi) = De^{-2a(r(\boldsymbol{u}_\eta - \boldsymbol{u}_\xi) - r_0)} - 2De^{-a(r(\boldsymbol{u}_\eta - \boldsymbol{u}_\xi) - r_0)}, \tag{1.102}$$

where $r(\boldsymbol{u}_\eta - \boldsymbol{u}_\xi) = \|(\boldsymbol{u}_\eta - \boldsymbol{u}_\xi) + (\boldsymbol{\eta} - \boldsymbol{\xi})\|$, with D, a and r_0 being free parameters. The Morse potential is illustrated in Figure 1.7 (b). □

Example 1.7 (EAM potentials). Pair potentials predict elastic constants which satisfy the *Cauchy relation* $C_{12} - C_{44} = 0$, the so-called *Cauchy pressure*. This relation is intrinsic for pair potentials. However, for most cubic materials, that is metals, the Cauchy pressure is *non-zero*. Hence, pair potentials show their limitation already at the most fundamental

---

[6] A great introduction to (semi-)empirical atomistic models can be found in the book of Tadmor and Miller (2011) which also comprises a large set of references

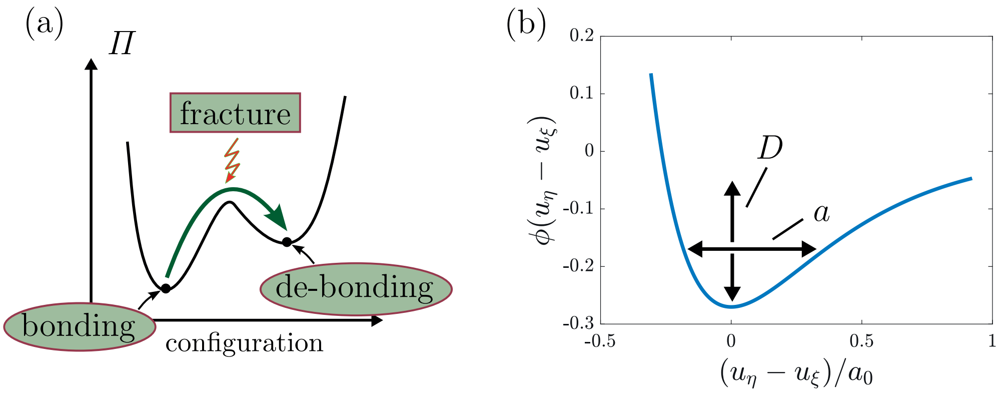

Figure 1.7: (a) Schematic illustration of the nonconvex energy landscape of atomistic models. (b) Morse potential from Example 1.6 as a function of the (here: scalar) differential displacement

level, i.e. the linear elastic regime. The embedded atom method (EAM Daw and Baskes, 1984) overcomes this limitation by adding an additional term to the site energy, i.e.

$$\mathcal{E}_\xi(\{\boldsymbol{u}_\eta - \boldsymbol{u}_\xi\}) = \frac{1}{2} \sum_{\boldsymbol{\eta} \in \mathcal{R}_\xi \setminus \boldsymbol{\xi}} \phi(\boldsymbol{u}_\eta - \boldsymbol{u}_\xi) + F\big(\rho(\{\boldsymbol{u}_\eta - \boldsymbol{u}_\xi\})\big), \tag{1.103}$$

where F is the *embedding* function which depends on the function ρ given by

$$\rho(\{\boldsymbol{u}_\eta - \boldsymbol{u}_\xi\}) = \sum_{\boldsymbol{\eta} \in \mathcal{R}_\xi \setminus \boldsymbol{\xi}} g(\boldsymbol{u}_\eta - \boldsymbol{u}_\xi), \tag{1.104}$$

where g is another function which depends on the differential displacements. The function ρ is the electron density due to atom $\boldsymbol{\xi}$ which is assumed to be given by a superposition of the pair-wise contributions $g(\boldsymbol{u}_\eta - \boldsymbol{u}_\xi)$ from its neighboring atoms in $\mathcal{R}_\xi$. The function F represents the required energy to *embed* $\boldsymbol{\xi}$ into a homogeneous electron gas. The choice of F is usually physically motivated to mimic the crucial features of the ab initio model (see Tadmor and Miller, 2011, Chapter 5 for various examples). ☐

1.5.3 Boundary conditions on atomistic problems

The boundary conditions on atomistic problems require special attention. When studying nanospecimens, e.g. nanobeams (c.f. Figure 1.2 (b)) or nanotubes, the application of boundary conditions is comparable to PDEs. That is, homogeneous Dirichlet-type conditions may be imposed to clamp the specimen or Neumann-type conditions to account for applied forces.

Contrary to classical continuum mechanics, the boundary conditions must be imposed in a *pad* region which spans *several* layers of atoms. This is due to the fact that the atomistic model is nonlocal in general and neglecting the additional layers possibly leads to artificial free surface effects. Care must be taken when choosing the size of the pad region when using many-body potentials. For the particular case of EAM potentials, the pad domain must be twice as thick as the cut-off radius of the interatomic potential since the site energy (1.103) involves an embedding function which depends on the electron density ρ, which itself depends on another function $g(\boldsymbol{u}_\eta - \boldsymbol{u}_\xi)$. To see this, consider the force on an atom $\boldsymbol{\xi}$ derived from the EAM potential from Example 1.7

$$\begin{aligned} \boldsymbol{f}_\xi &= \frac{1}{2} \sum_{\boldsymbol{\zeta} \in \mathcal{R}_\xi} \sum_{\boldsymbol{\eta} \in \mathcal{R}_\zeta \setminus \boldsymbol{\zeta}} \frac{\partial \phi(\boldsymbol{u}_\eta - \boldsymbol{u}_\zeta)}{\partial \boldsymbol{u}_\xi} + \sum_{\boldsymbol{\zeta} \in \mathcal{R}_\xi} \frac{\partial}{\partial \boldsymbol{u}_\xi} \left(F\Big(\sum_{\boldsymbol{\eta} \in \mathcal{R}_\zeta \setminus \boldsymbol{\zeta}} g(\boldsymbol{u}_\eta - \boldsymbol{u}_\zeta) \Big) \right) \\ &= \sum_{\boldsymbol{\eta} \in \mathcal{R}_\xi \setminus \boldsymbol{\xi}} \frac{\partial \phi(\boldsymbol{u}_\eta - \boldsymbol{u}_\xi)}{\partial \boldsymbol{u}_\xi} + \sum_{\boldsymbol{\zeta} \in \mathcal{R}_\xi} \frac{\partial}{\partial \boldsymbol{u}_\xi} \left(F\Big(\sum_{\boldsymbol{\eta} \in \mathcal{R}_\zeta \setminus \boldsymbol{\zeta}} g(\boldsymbol{u}_\eta - \boldsymbol{u}_\zeta) \Big) \right). \end{aligned} \tag{1.105}$$

The first term due to the pairwise interactions can be reduced to a form which only requires the derivatives of ϕ for all nearest neighbors of $\boldsymbol{\xi}$. Since the second term depends on the derivatives of the *pair functional* F, which depends on the interactions of atom $\boldsymbol{\zeta}$ with all atoms in its range $\mathcal{R}_\zeta$ via g, with respect to $\boldsymbol{u}_\xi$ for all atoms in the neighborhood of $\boldsymbol{\xi}$, the force on $\boldsymbol{\xi}$ also depends on the positions of the atoms which interact with the other atoms in its interaction range $\mathcal{R}_\xi$.

Another common application of atomistic models is the investigation of the behavior of isolated defects, e.g crack tips (brittle/ductile behavior), dislocations (core structure) etc. For an in-depth understanding of the behavior of defects it is crucial to characterize their far-field behavior, more precisely, the "regularity" of the solution. Ehrlacher et al. (2016) have shown that the far-field behavior is accurately described by the following decay hypothesis:

Hypothesis 1 (Decay hypothesis). *Assume that there exists a continuum representation Ω of Λ ($\Lambda \subset \Omega$) such that $\boldsymbol{u}$ can be continuously extended to $\boldsymbol{u} : \Omega \to \mathbb{R}^d$. Then, the far-field behavior of a defect is described by*

$$\|\nabla^i \boldsymbol{u}(\boldsymbol{x})\| \lesssim \|\boldsymbol{x}\|^{1-i-\alpha} \qquad (i = 0, 1, 2, ...), \tag{1.106}$$

where the parameter α defines the decay rate of the defect, e.g. $\alpha = 1/2$ for cracks, $\alpha = 1$ for dislocations or $\alpha = d$ for point defects.

A small α gives rise to long-range interactions which are possibly infinite-ranged. For dislocations it is therefore highly desirable to impose a good predictor of the elastic far-field on the boundary in order to minimize spurious effects. However, this is not always possible. For example, if the dislocation moves due to some remote applied stress, the highly constrained boundary imposes an artificial pinning. This is due to the fact that a dislocation moves over long distances, even when subject to rather low applied stresses.

Hence, small deviations in the boundary conditions can have a large impact on the final result. Periodic boundary conditions (e.g. Osetsky and Bacon, 2003) which provide a "softer" interface in comparison with clamped boundary conditions can overcome this problem only partially. This motivates the construction of atomistic/continuum (A/C) coupling schemes which improve the accuracy while being substantially more efficient than fully, necessarily larger atomistic calculations. Moreover, A/C coupling methods can exhibit superior convergence rates over clamped boundary conditions as shown by Ehrlacher et al. (2016).

So-called "flexible boundary conditions" which can adjust to the displacements of the atoms near the interface are discussed in detail in Chapter 2 and Chapter 3. In Section 3.8 a flexible Green function method will be introduced which updates the boundary condition according to the *current* position of the defect, thus allowing the atoms to evolve further. A more general coupling scheme is pursued in Chapter 2 where the atomistic domain is truly coupled to an elasticity problem. This makes the boundary condition independent of the placement of the defect. Numerical examples will be presented in Section 4.1.

1.5.4 Calibration of the dislocation core energy to atomistic results

As outlined in Section 1.4.4 the DDD model relies on atomistic data. For the quasi-static problem in Section 1.4.2 (no dislocation nucleation etc.) it yet suffices to calibrate the dislocation core energy to atomistics. In principle it is also necessary to determine the Peierls barrier, however, in all examples considered throughout this work the applied stress is much higher than the Peierls stress such that a calibration is not essential. In the following the continuum energy is assumed to be of the form (1.56) and the core energy density W^{core} (:= core energy per unit length) which depends on the scalar parameter E^{core} is given by (1.89). An isolated edge dislocation is chosen as a representative configuration.

For a straight dislocation the elastic energy *per unit length* in a hollow disk with a given inner radius $r_{\mathrm{cut}}^{\mathrm{core}}$ (the core cut-off radius) and outer radius R as predicted by the singular core model (Example 1.3) is given by

$$W^{\mathrm{e}}(R, r_{\mathrm{cut}}^{\mathrm{core}}) = k \ln\left(\frac{R}{r_{\mathrm{cut}}^{\mathrm{core}}}\right), \tag{1.107}$$

where k is the *energy factor*. For an edge dislocation it is given by

$$k = \frac{\mu b^2}{4\pi(1-\nu)}. \tag{1.108}$$

It is assumed that the true atomistic energy *per unit length* of the dislocation is asymptotically equivalent to the continuum energy in the sense that

$$W^{\mathrm{a}}(R) \sim W^{\mathrm{c}}(R) = W^{\mathrm{e}}(R, r_{\mathrm{cut}}^{\mathrm{core}}) + W^{\mathrm{core}}(E^{\mathrm{core}}(r_{\mathrm{cut}}^{\mathrm{core}})) \qquad \text{as } R \to \infty, \tag{1.109}$$

with

$$W^{\mathrm{core}}(E^{\mathrm{core}}(r_{\mathrm{cut}}^{\mathrm{core}})) = \frac{E^{\mathrm{core}}(r_{\mathrm{cut}}^{\mathrm{core}})b^2}{(1-\nu)}, \tag{1.110}$$

where W^{core} has an implicit dependence on the core cut-off through E^{core}. In the limiting case the core energy density is obtained as

$$W^{\mathrm{core}}(E^{\mathrm{core}}(r_{\mathrm{cut}}^{\mathrm{core}})) = \lim_{R\to\infty} \left(W^{\mathrm{a}}(R) - k \ln\left(\frac{R}{r_{\mathrm{cut}}^{\mathrm{core}}}\right)\right) \tag{1.111}$$

from which the parameter E^{core} can be deduced. In practice this is done by selecting a large enough R and computing the energy difference 1.111. For the particular case of an fcc aluminum potential E^{core} is plotted in Figure 1.8 (a) for an increasing outer radius R. For larger R the parameter becomes essentially a constant as presumed. The estimated E^{core} is then plugged into W^{core}. In Figure 1.8 (b) it is shown that the continuum energy approximates the atomistic energy very well for $R \geq 2r_{\mathrm{cut}}^{\mathrm{core}}$.

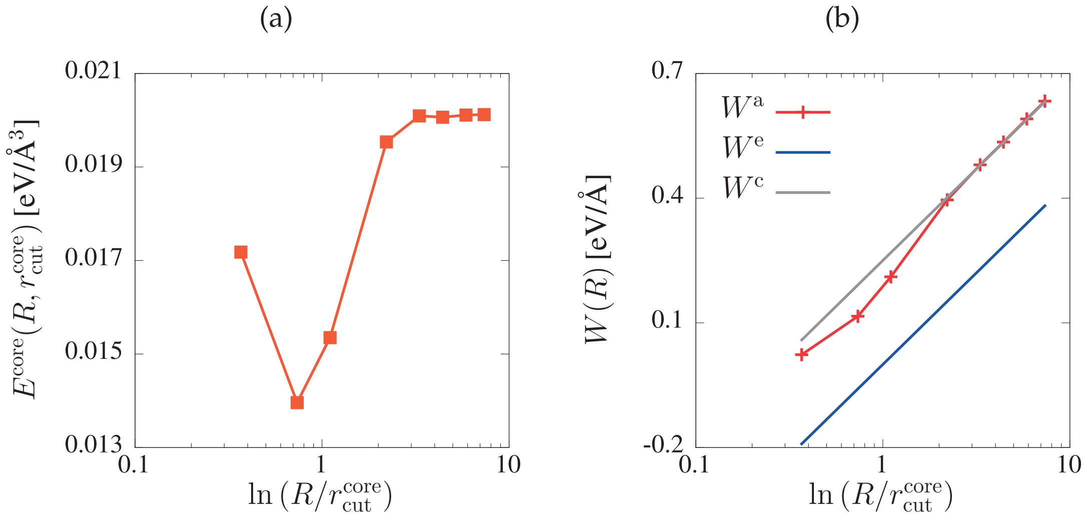

Figure 1.8: (a) E^{core} as a function of the outer radius R. (b) Total atomistic, elastic and continuum (:= elastic + core contribution) energies vs. $\ln(R/r_{\mathrm{cut}}^{\mathrm{core}})$

Note that the precise choice E^{core} is *not* unique and depends on the core cut-off radius. But, the continuum energy is *independent* of $r_{\mathrm{cut}}^{\mathrm{core}}$. At first this may suggest that the core cut-off radius is arbitrary. However, the choice of $r_{\mathrm{cut}}^{\mathrm{core}}$ influences the value of the Cauchy stress and thus the Peach-Koehler force. Choosing $r_{\mathrm{cut}}^{\mathrm{core}}$ much larger than the core radius of the *real* atomistic core, i.e. the regime where nonlinear/nonlocal interactions dominate, may perturb the far-field behavior. For partial dislocations (i.e. dislocations with a spread core) an educated choice is $r_{\text{cut}}^{\text{core}} \approx$ half the stacking fault width (c.f. Szajewski et al., 2015).

Remark 1.5.1. *The core energy model can also be used in combination with nonsingular elasticity (Example 1.4). In this case the elastic energy for an edge dislocation takes the form (Cai et al., 2006)*

$$W_{\text{ns}}^{\text{e}}(R,a) = \frac{\mu b^2}{4\pi(1-\nu)}\left(\ln\left(\frac{R}{a}\right) - \frac{(2+\nu)}{12(1-\nu)}\right) + \mathcal{O}\left(\frac{a^2}{R^2}\right). \tag{1.112}$$

For large R the elastic energy can then be written as a sum of (1.107) *and a correction*

$$W_{\text{ns}}^{\text{e}}(R,a) \sim W^{\text{e}}(R, r_{\text{cut}}^{\text{core}}) + \mathit{\Delta} W_{\text{ns}}^{\text{e}}(a, r_{\text{cut}}^{\text{core}}), \tag{1.113}$$

where

$$\begin{aligned} \mathit{\Delta} W_{\text{ns}}^{\text{e}}(a, r_{\text{cut}}^{\text{core}}) &= \lim_{R\to\infty}\left(W_{\text{ns}}^{\text{e}}(R,a) - W^{\text{e}}(R, r_{\text{cut}}^{\text{core}})\right) \\ &= \frac{\mu b^2}{4\pi(1-\nu)}\left(\ln\left(\frac{r_{\text{cut}}^{\text{core}}}{a}\right) - \frac{(2+\nu)}{12(1-\nu)}\right) \\ &= k\left(\ln\left(\frac{r_{\text{cut}}^{\text{core}}}{a}\right) - \frac{(2+\nu)}{12(1-\nu)}\right). \end{aligned} \tag{1.114}$$

The choice of a should be in the same range as $r_{\text{cut}}^{\text{core}}$, i.e. half the width of the stacking fault (Szajewski et al., 2015).

2 Flexible boundary conditions for atomistic problems

2.1 Introduction

Atomistic simulations are limited in time and size and are usually highly ill-conditioned in the sense that small errors in the input/boundary data may have large effects on the final result. One example is the propagation of defects through the material which are usually created due to rather high applied stresses but move under relatively low stresses (several orders of magnitude difference). The most widely-used approach is to restrict atomic resolution to a finite domain and apply boundary conditions (in general: free, clamped or periodic; c.f. Section 1.5.3). Many problems, however, require the atomistic problem to be independent of the precise choice of the boundary since non-negligible image forces can perturb the final results (for an example involving bowing dislocations see Szajewski and Curtin, 2015). Choosing the boundary sufficiently far away from the region of interest results in vast computational cost (e.g. Möller and Bitzek, 2015), even on state-of-the-art supercomputers.

In the 1970s Sinclair and co-workers introduced a method based on lattice Green functions (LGFs), so-called *flexible boundary conditions*, in a series of papers (Sinclair, 1971; Sinclair et al., 1978) which partitions the lattice into an anharmonic atomistic region (region 1), containing the defect(s), surrounded by a harmonic (continuum elasticity) region (region 2), as shown in Figure 2.1. In comparison with other quasicontinuum (QC) approaches (e.g. Tadmor et al., 1996; Knap and Ortiz, 2001; Miller and Tadmor, 2009; Amelang et al., 2015) it does not require an explicit discretization of the continuum domain and therefore does not introduce any error due to mesh coarsening. To date, Sinclair's method and its successors have been successfully applied to dislocation and crack problems (see Tewary, 1973; Sinclair, 1975; Sinclair et al., 1978; Gallego and Ortiz, 1993; Rao et al., 1998; Li, 2009) but not to moving defects, e.g. dislocation-obstacle interactions, crack propagation etc. These problems require large system sizes which are prohibitive due to the dense system matrices, used to update the harmonic solution in the interior and the pad region, which arise from the long-range nature of the LGF. More efficient methods have been proposed, e.g. by Yavari et al. (2007); Pastewka et al. (2012), but they require special periodicity assumptions on the geometry such that the system matrices admit a certain structure (e.g. block-Toeplitz) which can be exploited.

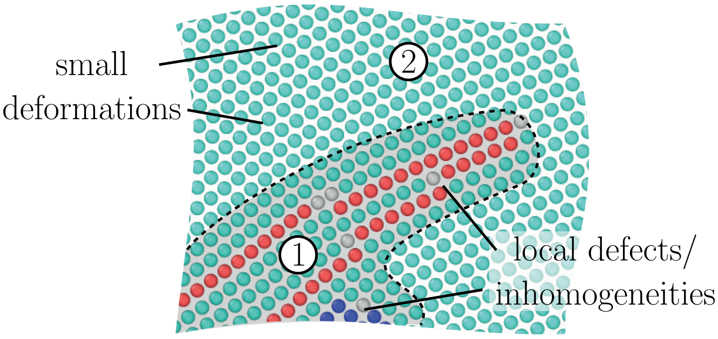

Figure 2.1: Partition of an atomistic domain in parts which contain material defects and parts which undergo small deformations

Only recently, these issues have been overcome by Hodapp et al. (2018c) who were first to observe that the harmonic solution is merely an initial guess to the atomistic problem and can be conveniently neglected since the harmonic part is already contained in the nonlinear interatomic potential. Their modified version of Sinclair's method thus requires *only* the pad atoms near the artificial interface to be updated during one iteration. The still existing bottleneck of memory consumption has been resolved using hierarchical approximations of the system matrices which admit a block-wise low-rank structure, thanks to the asymptotic smoothness of the LGF (c.f. Hackbusch, 1999). This reduces the former dense problem of quadratic complexity to one with *linear-logarithmic* complexity.

In addition, it was found in (Hodapp et al., 2018c) that Sinclair's iteration equation for the displacements leads, upon convergence, to a boundary summation equation (a discrete variant of the boundary integral equation, c.f. Brebbia, 1978). The boundary summation equation yields a **discrete boundary element method** (DBEM) which can be employed to formulate a coupled system of equations which solves simultaneously for *all* unknowns.

In the following Sinclair's method and the atomistic/DBEM coupling will be derived for infinite problems. However, an extension to bounded domains will also be presented (Section 2.5.4). Their implementation and several numerical solution algorithms, including a monolithic Newton-Krylov solver for the atomistic/DBEM coupling, are then described in detail in Section 2.6 and 2.7.

2.2 Problem statement

The fully atomistic reference problem will be defined in the following. First, assume that the computational domain is an infinite Bravais lattice $\Lambda = \boldsymbol{A}\mathbb{Z}^d$ (c.f. Section 1.5.1).

Further, it is asserted that $d = 2$ or 3 in the remainder of this Chapter. The space of admissible displacements is now defined as $\mathcal{U}^\star(\Lambda) := [l^2(\Lambda)]^d$. This definition ensures that $\boldsymbol{u}(\boldsymbol{\xi}) \to \boldsymbol{0}$ as $\|\boldsymbol{\xi}\| \to \infty$.[1] Note the equivalence relation $\boldsymbol{u} \sim \boldsymbol{u} + \boldsymbol{c}$, with $\boldsymbol{c} \in \mathbb{R}^d$, i.e. lattice properties are invariant under rigid body shifts. Otherwise the definition of the site energy and the total energy functional from Section 1.5.1 remain the same.

The optimization problem is then defined as follows

$$\boldsymbol{u} := \operatorname{Arg}\left\{ \min_{\boldsymbol{v} \in \mathcal{U}^\star} \Pi(\boldsymbol{v}) \right\}. \tag{2.1}$$

The Euler-Lagrange equation corresponding to (2.1) is given by

$$\boxed{\mathcal{P}^{\mathrm{a}}: \qquad \mathcal{L}[\boldsymbol{u}](\boldsymbol{\xi}) = \boldsymbol{f}^{\mathrm{ext}}(\boldsymbol{\xi}) \qquad \text{in } \Lambda,} \tag{2.2}$$

where the bijective nonlinear operator $\mathcal{L}$ is defined as

$$\begin{aligned} &\mathcal{L} : \mathcal{U}^\star(\Lambda) \to \mathcal{U}^\star(\Lambda) \\ &\qquad \boldsymbol{u} \mapsto \mathcal{L}[\boldsymbol{u}] \qquad \text{such that } \forall\, \boldsymbol{\xi} \in \Lambda \qquad \mathcal{L}[\boldsymbol{u}](\boldsymbol{\xi}) = \delta_\xi \Pi^{\mathrm{int}} = \boldsymbol{f}_\xi. \end{aligned} \tag{2.3}$$

In the following the arguments will be dropped if not explicit required.

In addition, the usual strong stability conditions on the minimizers $\boldsymbol{u}$ are presumed, i.e. positivity of the second variation of the energy functional such that

$$\forall\, \boldsymbol{v} \in \mathcal{U}^\star \setminus \boldsymbol{0} \qquad \langle \delta^2 \Pi^{\mathrm{int}}(\boldsymbol{u})\boldsymbol{v}, \boldsymbol{v} \rangle > 0. \tag{2.4}$$

2.3 Force-based atomistic/continuum coupling

2.3.1 Linearization of the atomistic model

The optimization problem (2.1) is infinite dimensional and usually not computable if Π is nonlinear (which is the case for all realistic interatomic potentials). A common approximation is thus to assume nonlinearity only in some finite, fully atomistic, region, e.g. around the defect core. Outside this region the crystal is assumed to behave linearly. Therefore a linearization of Π is derived which is subsequently used in Section 2.3.3 in order to define the domain partitioning.

In the following it is assumed that gradients are sufficiently small such that a linearization of Π with respect to the deformation is admissible. A Taylor expansion of Π to second order yields the *harmonic approximation*

$$\Pi(\boldsymbol{u}) \approx \Pi_{\mathrm{nle}}(\boldsymbol{u}) = \sum_{\boldsymbol{\xi} \in \Lambda} \delta_\xi \Pi(\boldsymbol{0}) \cdot \boldsymbol{u}_\xi + \frac{1}{2} \sum_{\boldsymbol{\xi} \in \Lambda} \sum_{\boldsymbol{\eta} \in \mathcal{R}_\xi} \boldsymbol{K}(\boldsymbol{\xi} - \boldsymbol{\eta}) \cdot (\boldsymbol{u}_\xi \otimes \boldsymbol{u}_\eta). \tag{2.5}$$

---

[1] This avoids further technicalities due the loss of uniqueness of the solution when $\boldsymbol{u}$ does *not* vanish at infinity

where $\boldsymbol{K}(\boldsymbol{\xi}-\boldsymbol{\eta}) = \delta^2_{\xi\eta}\mathit{\Pi}(\mathbf{0})$ is the interatomic *force constant* tensor (or *nodal stiffness* tensor in engineering notation). The quantity $\mathit{\Pi}_{\mathrm{nle}}(\boldsymbol{u})$ is denoted as the nonlocal elastic energy functional.

The Euler-Lagrange equation corresponding to the harmonic problem can then be readily obtained as

$$\mathcal{L}_{\mathrm{nle}}[\boldsymbol{u}] = \boldsymbol{f}^{\mathrm{ext}} \qquad \text{in } \mathit{\Lambda}, \qquad \text{with} \quad \mathcal{L}_{\mathrm{nle}}[\bullet] = \sum_{\boldsymbol{\eta}\in\mathcal{R}_\xi} \boldsymbol{K}(\boldsymbol{\xi}-\boldsymbol{\eta})\bullet(\boldsymbol{\eta}), \tag{2.6}$$

where $\mathcal{L}_{\mathrm{nle}}$ is a linear operator since $\boldsymbol{K}$ is evaluated in the ground state and does not depend on $\boldsymbol{u}$.

If the deformation is close to homogeneous one can consider a linearization of $\boldsymbol{u}$. Therefore it is asserted that $\boldsymbol{u}$ can be continuously extended to $\boldsymbol{u} : \mathbb{R}^d \to \mathbb{R}^d$. Further, assume that $\boldsymbol{u}(\boldsymbol{x})$ is sufficiently smooth for all $\boldsymbol{x} \in \mathbb{R}^d$ which allows to define its gradient $\nabla\boldsymbol{u}(\boldsymbol{x})$. A Taylor expansion to first order then yields

$$\boldsymbol{u}_\eta \approx \boldsymbol{u}_\xi + \nabla\boldsymbol{u}(\boldsymbol{\xi})(\boldsymbol{\eta}-\boldsymbol{\xi}) \tag{2.7}$$

which is commonly referred to as the *Cauchy-Born* approximation.

The two approaches can be combined, recognizing that the second term in (2.5) can be written as (summation by parts)

$$\sum_{\boldsymbol{\xi}\in\mathit{\Lambda}}\sum_{\boldsymbol{\eta}\in\mathcal{R}_\xi} \boldsymbol{K}(\boldsymbol{\xi}-\boldsymbol{\eta})\cdot(\boldsymbol{u}_\xi\otimes\boldsymbol{u}_\eta) = \sum_{\boldsymbol{\xi}\in\mathit{\Lambda}}\sum_{\boldsymbol{\eta}\in\mathcal{R}_\xi\backslash\boldsymbol{\xi}}\sum_{\boldsymbol{\zeta}\in\mathcal{R}_\xi\backslash\boldsymbol{\xi}} \partial^2_{\eta\zeta}\mathcal{E}_\xi(\mathbf{0})\cdot\Big((\boldsymbol{u}_\eta-\boldsymbol{u}_\xi)\otimes(\boldsymbol{u}_\zeta-\boldsymbol{u}_\xi)\Big), \tag{2.8}$$

where $\partial^2_{\eta\zeta}\mathcal{E}_\xi(\mathbf{0}) = \frac{\partial^2\mathcal{E}_\xi}{\partial\boldsymbol{u}_\eta\partial\boldsymbol{u}_\zeta}\Big|_{\mathbf{0}}$, which is obtained by expanding the site energy instead of the total energy. Using (2.7) in (2.8) one can write

$$\begin{aligned}
\mathit{\Pi}_{\mathrm{nle}}(\boldsymbol{u}) &\approx \mathit{\Pi}_{\mathrm{e}}(\boldsymbol{u}) \\
&= \frac{1}{2}\sum_{\boldsymbol{\xi}\in\mathit{\Lambda}}\sum_{\boldsymbol{\eta}\in\mathcal{R}_\xi\backslash\boldsymbol{\xi}}\sum_{\boldsymbol{\zeta}\in\mathcal{R}_\xi\backslash\boldsymbol{\xi}} \partial^2_{\eta\zeta}\mathcal{E}_\xi(\mathbf{0})\cdot\Big((\nabla\boldsymbol{u}(\boldsymbol{\xi})(\boldsymbol{\eta}-\boldsymbol{\xi}))\otimes(\nabla\boldsymbol{u}(\boldsymbol{\xi})(\boldsymbol{\zeta}-\boldsymbol{\xi}))\Big) \\
&= \frac{1}{2}\sum_{\boldsymbol{\xi}\in\mathit{\Lambda}}\left(\sum_{\boldsymbol{\eta}\in\mathcal{R}_\xi\backslash\boldsymbol{\xi}}\sum_{\boldsymbol{\zeta}\in\mathcal{R}_\xi\backslash\boldsymbol{\xi}} \partial^2_{\eta\zeta}\mathcal{E}_\xi(\mathbf{0})\,\square\Big((\boldsymbol{\eta}-\boldsymbol{\xi})\otimes(\boldsymbol{\zeta}-\boldsymbol{\xi})\Big)\right)\cdot\big(\nabla\boldsymbol{u}(\boldsymbol{\xi})\otimes\nabla\boldsymbol{u}(\boldsymbol{\xi})\big),
\end{aligned} \tag{2.9}$$

where the product $\square$ between two second order tensors $\boldsymbol{A}$, $\boldsymbol{B}$ is defined as $\boldsymbol{A}\,\square\,\boldsymbol{B} = A_{ik}B_{jl}\boldsymbol{e}_i\otimes\boldsymbol{e}_j\otimes\boldsymbol{e}_k\otimes\boldsymbol{e}_l$. Note that the term in the big parenthesis is nothing but the fourth-order elasticity tensor

$$\mathbb{C} = \sum_{\boldsymbol{\eta}\in\mathcal{R}_\xi\backslash\boldsymbol{\xi}}\sum_{\boldsymbol{\zeta}\in\mathcal{R}_\xi\backslash\boldsymbol{\xi}} \partial^2_{\eta\zeta}\mathcal{E}_\xi(\mathbf{0})\,\square\Big((\boldsymbol{\eta}-\boldsymbol{\xi})\otimes(\boldsymbol{\zeta}-\boldsymbol{\xi})\Big). \tag{2.10}$$

This yields the classical definition of the linear elastic energy

$$\varPi_{\mathrm{e}}(\boldsymbol{u}) = \frac{1}{2}\sum_{\boldsymbol{\xi}\in\varLambda} \mathbb{C}\cdot(\nabla\boldsymbol{u}(\boldsymbol{\xi})\otimes\nabla\boldsymbol{u}(\boldsymbol{\xi})) \tag{2.11}$$

similar to that of a continuous body.

In practice it is usually convenient to define a piecewise constant gradient. That is, the ideal lattice is partitioned into a periodic set of simplexes and an interpolant $\varphi_\xi \in H^1(\mathbb{R}^d)\cap C^0(\mathbb{R}^d)$ with compact support on a set $\mathcal{R}_\xi^{\mathrm{loc}} \subset \mathcal{R}_\xi$ is defined which spans to the nearest neighbors in the adjacent simplexes. Several examples for various lattice types are given in Appendix A.4.2 which will be used in Section 4.1.1 and 4.1.2. The atomic displacement field and its gradient can then be defined $\forall\,\boldsymbol{x}\in\mathbb{R}^d$ as

$$\boldsymbol{u}(\boldsymbol{x}) = \sum_{\boldsymbol{\xi}\in\mathcal{R}_\xi^{\mathrm{loc}}} \varphi_\xi(\boldsymbol{x})\boldsymbol{u}_\xi, \qquad \nabla\boldsymbol{u}(\boldsymbol{x}) = \sum_{\boldsymbol{\xi}\in\mathcal{R}_\xi^{\mathrm{loc}}} \boldsymbol{u}_\xi\otimes\nabla\varphi_\xi(\boldsymbol{x}). \tag{2.12}$$

The energy can then be written in a format similar to the pure discrete case (2.5)

$$\varPi_{\mathrm{e}}(\boldsymbol{u}) \approx \frac{1}{2}\sum_{\boldsymbol{\xi}\in\varLambda}\sum_{\boldsymbol{\eta}\in\mathcal{R}_\xi^{\mathrm{loc}}} \boldsymbol{K}^{\mathrm{e}}(\boldsymbol{\xi}-\boldsymbol{\eta})\cdot(\boldsymbol{u}_\xi\otimes\boldsymbol{u}_\eta), \tag{2.13}$$

with

$$K_{ik}^{\mathrm{e}}(\boldsymbol{\xi}-\boldsymbol{\eta}) = \sum_{\boldsymbol{\zeta}\in\mathcal{R}_\xi^{\mathrm{loc}}} C_{ijkl}\big(\nabla\varphi_\eta(\boldsymbol{x})\big)_j\big(\nabla\varphi_\zeta(\boldsymbol{x})\big)_l. \tag{2.14}$$

Thanks to the definition of the gradient the associated Euler-Lagrange reads

$$\mathcal{L}_{\mathrm{e}}[\boldsymbol{u}] = \boldsymbol{f}^{\mathrm{ext}} \quad \text{in } \varLambda, \qquad \text{with} \quad \mathcal{L}_{\mathrm{e}}[\bullet] = \sum_{\boldsymbol{\eta}\in\mathcal{R}_\xi^{\mathrm{loc}}} \boldsymbol{K}^{\mathrm{e}}(\boldsymbol{\xi}-\boldsymbol{\eta})\bullet(\boldsymbol{\eta}). \tag{2.15}$$

Generally, $\mathcal{L}_{\mathrm{h}}$ is referred to as a harmonic operator, that is to either $\mathcal{L}_{\mathrm{e}}$ or $\mathcal{L}_{\mathrm{nle}}$.

If the displacement gradient is defined via (2.12) one may think of $\varLambda$ as "continuum"-like. This definition will be liberally used in the following.

2.3.2 Lattice Green function

Consider the harmonic problem

$$\mathcal{L}_{\mathrm{h}}[\boldsymbol{u}] = \boldsymbol{f}^{\mathrm{ext}} \qquad \text{in } \varLambda. \tag{2.16}$$

If $\boldsymbol{f}^{\mathrm{ext}}$ is a unit point force, a solution to (2.16) can be computed by means of Fourier transforms (c.f. Appendix A.4.1). The displacement u_i due to a point force in direction

j is denoted as the lattice Green function G^{lgf}_{ij} which generates the lattice Green tensor $\boldsymbol{G}^{\mathrm{lgf}}(\boldsymbol{\xi}) \in \mathbb{R}^{d\times d}$. The definition of $\boldsymbol{G}^{\mathrm{lgf}}$ allows to compute the solution for *general* right hand sides $\boldsymbol{f}^{\mathrm{ext}}$. For this purpose the lattice Green operator is defined as

$$\begin{aligned} &\mathcal{G} : \mathcal{U}^\star(\mathit{\Lambda}) \to \mathcal{U}^\star(\mathit{\Lambda}) \\ &\qquad \boldsymbol{f}^{\mathrm{ext}} \mapsto \mathcal{G}[\boldsymbol{f}^{\mathrm{ext}}] \qquad \text{such that } \forall\, \boldsymbol{\xi} \in \mathit{\Lambda} \qquad \mathcal{G}[\boldsymbol{f}^{\mathrm{ext}}](\boldsymbol{\xi}) = \boldsymbol{u}_\xi, \end{aligned} \tag{2.17}$$

with

$$\mathcal{G}[\bullet] = \sum_{\boldsymbol{\eta}\in\mathit{\Lambda}} \boldsymbol{G}^{\mathrm{lgf}}(\boldsymbol{\xi}-\boldsymbol{\eta}) \bullet (\boldsymbol{\eta}). \tag{2.18}$$

Use will frequently be made of the identity relation

$$\mathcal{G} = \mathcal{L}_{\mathrm{h}}^{-1} \qquad \Rightarrow \qquad (\mathcal{G}\mathcal{L}_{\mathrm{h}})[\boldsymbol{u}] = \mathcal{I}[\boldsymbol{u}] \tag{2.19}$$

in the following sections, where $\mathcal{I}$ is the identity operator such that $\forall\, \boldsymbol{\xi} \in \mathit{\Lambda}$

$$\mathcal{I}[\boldsymbol{u}](\boldsymbol{\xi}) = \sum_{\boldsymbol{\eta}\in\mathit{\Lambda}} \delta(\boldsymbol{\xi}-\boldsymbol{\eta})\boldsymbol{u}(\boldsymbol{\eta}) = \boldsymbol{u}(\boldsymbol{\xi}), \qquad \text{with} \quad \delta(\boldsymbol{\xi}-\boldsymbol{\eta}) = \begin{cases} 1 & \text{if } \boldsymbol{\xi} = \boldsymbol{\eta}, \\ 0 & \text{else.} \end{cases} \tag{2.20}$$

Throughout the remainder of this work it is assumed that $\mathcal{G}$ is given.

2.3.3 Domain decomposition

The A/C coupling scheme will now be defined. First, the entire lattice is split into a finite inner part $\mathit{\Lambda}^{\mathrm{a}} \subset \mathit{\Lambda}$ (the atomistic domain) and an outer infinite continuum domain $\mathit{\Lambda}^{\mathrm{c}} := \mathit{\Lambda} \setminus \mathit{\Lambda}^{\mathrm{a}}$. The outermost atomic layer is denoted as the interface region $\mathit{\Lambda}^{\mathrm{i}} \subset \mathit{\Lambda}^{\mathrm{a}}$ as indicated by the continuous line in Figure 2.2. Henceforth the number of atoms in each subset $\mathit{\Lambda}^\bullet$ of $\mathit{\Lambda}$ is referred to as $N^\bullet = \#\mathit{\Lambda}^\bullet$, i.e. $N^{\mathrm{a}} = \#\mathit{\Lambda}^{\mathrm{a}}$, $N^{\mathrm{i}} = \#\mathit{\Lambda}^{\mathrm{i}}$ etc.

The energy in the atomistic domain is given by (1.96) and the linearized continuum energy relates to (2.11). *Real* atoms in $\mathit{\Lambda}^{\mathrm{a}}$ therefore possibly behave fully nonlinear and nonlocal and consequently interact with *virtual* pad atoms in $\mathit{\Lambda}^{\mathrm{p}} \subset \mathit{\Lambda}^{\mathrm{c}}$ (see Figure 2.2 ($\mathcal{P}^{\mathrm{a}}$)) which are driven by the continuum solution. On the other hand, since the continuum problem is linear and local, only the virtual atoms in $\mathit{\Lambda}^{\mathrm{i+}} \subseteq \mathit{\Lambda}^{\mathrm{p}}$ interact with real atoms, namely the interface atoms in $\mathit{\Lambda}^{\mathrm{i}}$, as shown in Figure 2.2 ($\mathcal{P}^{\mathrm{c}}$).

Remark 2.3.1. *It is explicitly noted that the proposed method is general in the sense that nonlocal harmonic interactions are not excluded per se. In fact, all following derivations translate verbatim to nonlocal elasticity — only the width of the interface regions, e.g.* $\mathit{\Lambda}^{\mathrm{i+}}$*, change. For example, if the linearized problem is fully nonlocal (i.e. excluding the Cauchy-Born approximation) the energy in* $\mathit{\Lambda}^{\mathrm{c}}$ *is given by* (2.5) *and the domains* $\mathit{\Lambda}^{\mathrm{p}}$ *and* $\mathit{\Lambda}^{\mathrm{i+}}$ *are always equivalent.*

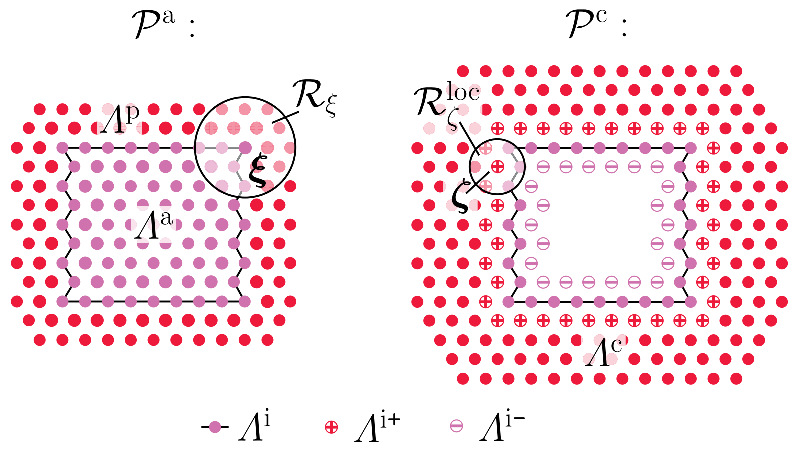

Figure 2.2: Schematic illustration of the problem decomposition (2.21) into a finite nonlocal/nonlinear atomistic region (here: third nearest neighbor interactions) and an infinite but local/linear continuum bulk region (the domain $\Lambda^{\mathrm{i-}}$ will be defined in Section 2.5.2)

A classical force-based coupling between the two domains is asserted (see e.g. Tadmor and Miller, 2011). The coupled problem can then be stated: find $\boldsymbol{u}$ such that

$$\begin{cases} \mathcal{P}^{\mathrm{a}}: \quad \mathcal{L}^{\mathrm{a}}[\boldsymbol{u}] = \boldsymbol{f}^{\mathrm{ext}} & \text{in } \Lambda^{\mathrm{a}}, \\ \mathcal{P}^{\mathrm{c}}: \quad \mathcal{L}^{\mathrm{c}}_{\mathrm{h}}[\boldsymbol{u}] = \boldsymbol{0} & \text{in } \Lambda^{\mathrm{c}} \end{cases} \tag{2.21}$$

in the absence of body forces in Λ^{c}. Problem (2.21) is still not very convenient to solve as it is infinite dimensional. In what follows, therefore, use is made of Green function techniques to reduce the solution space to finite dimensions by projecting $\boldsymbol{u}$ to the space of admissible solutions, aka. that fulfill the balance equations in $\Lambda^{\mathrm{c}} \setminus \Lambda^{\mathrm{i+}}$ (a discrete variant of the Caldéron operator).

2.4 Revisiting Sinclair's method

In the 1970s Sinclair and co-workers (Sinclair, 1971; Sinclair et al., 1978) introduced a practical method to solve (2.21) using the Green operator in order to compute a harmonic solution in the entire domain which counteracts inhomogeneous forces which build up at the artificial interface, more precisely, on the virtual pad atoms in $\Lambda^{\mathrm{i+}}$. All real *and* pad atoms are then displaced according to the harmonic solution. The steps are repeated until convergence is attained. In this section a new derivation of the method is presented which is more general and subsequently motivates the definition of a discrete boundary element method (DBEM).

First, the energy is split into a harmonic and an anharmonic contribution, i.e.

$$\Pi(\boldsymbol{u}) = \Pi_{\mathrm{h}}(\boldsymbol{u}) + \Pi_{\mathrm{ah}}(\boldsymbol{u}), \qquad \text{where} \quad \Pi_{\mathrm{ah}}(\boldsymbol{u}) = \Pi(\boldsymbol{u}) - \Pi_{\mathrm{h}}(\boldsymbol{u}). \tag{2.22}$$

A solution to (2.21) can then be obtained by optimizing $\varPi_{\mathrm{h}}$ and $\varPi_{\mathrm{ah}}$ separately. The following additive split can be admitted for the operator as well as for the displacement

$$\mathcal{L} = \mathcal{L}_{\mathrm{h}} + \mathcal{L}_{\mathrm{ah}}, \tag{2.23}$$

$$\boldsymbol{u} = \boldsymbol{u}_{\mathrm{h}} + \boldsymbol{u}_{\mathrm{ah}}. \tag{2.24}$$

For convenience, and thanks to the linearity of the harmonic operator $\mathcal{L}_{\mathrm{h}}$, one may define the following operators per subdomain

$$\mathcal{L}_{\mathrm{h}}^{\mathrm{a/a}} : \mathcal{U}^{\star}(\varLambda^{\mathrm{a}}) \to \mathcal{U}^{\star}(\varLambda^{\mathrm{a}}), \qquad \mathcal{L}_{\mathrm{h}}^{\mathrm{a/c}} : \mathcal{U}^{\star}(\varLambda^{\mathrm{c}}) \to \mathcal{U}^{\star}(\varLambda^{\mathrm{a}}), \tag{2.25}$$

$$\mathcal{L}_{\mathrm{h}}^{\mathrm{c/a}} : \mathcal{U}^{\star}(\varLambda^{\mathrm{a}}) \to \mathcal{U}^{\star}(\varLambda^{\mathrm{c}}), \qquad \mathcal{L}_{\mathrm{h}}^{\mathrm{c/c}} : \mathcal{U}^{\star}(\varLambda^{\mathrm{c}}) \to \mathcal{U}^{\star}(\varLambda^{\mathrm{c}}). \tag{2.26}$$

The coupling operators $\mathcal{L}_{\mathrm{h}}^{\mathrm{a/c}}$ and $\mathcal{L}_{\mathrm{h}}^{\mathrm{c/a}}$ satisfy the following relations $\forall\, \boldsymbol{v} \in \mathcal{U}^{\star}$

$$\mathcal{L}_{\mathrm{h}}^{\mathrm{a/c}}[\boldsymbol{v}] = \boldsymbol{0} \quad \text{in } \varLambda^{\mathrm{a}} \setminus \varLambda^{\mathrm{i}}, \qquad \mathcal{L}_{\mathrm{h}}^{\mathrm{a/c\backslash i+}}[\boldsymbol{v}] = \boldsymbol{0} \quad \text{in } \varLambda^{\mathrm{i}}, \tag{2.27}$$

$$\mathcal{L}_{\mathrm{h}}^{\mathrm{c/a}}[\boldsymbol{v}] = \boldsymbol{0} \quad \text{in } \varLambda^{\mathrm{c}} \setminus \varLambda^{\mathrm{i+}}, \qquad \mathcal{L}_{\mathrm{h}}^{\mathrm{c/a\backslash i}}[\boldsymbol{v}] = \boldsymbol{0} \quad \text{in } \varLambda^{\mathrm{i+}} \tag{2.28}$$

which follow from the domain decomposition introduced in the previous section (i.e. displacements of continuum nodes $\varLambda^{\mathrm{c}} \setminus \varLambda^{\mathrm{i+}}$ away from the interface do not exert a *harmonic* force in the atomistic region and vice versa).[2]

Using (2.23) and (2.24) one can simply re-write the coupled problem as

$$\mathcal{L}[\boldsymbol{u}] = \mathcal{L}_{\mathrm{h}}[\boldsymbol{u}_{\mathrm{h}}] + \mathcal{L}_{\mathrm{h}}[\boldsymbol{u}_{\mathrm{ah}}] + \mathcal{L}_{\mathrm{ah}}[\boldsymbol{u}] = \begin{pmatrix} \boldsymbol{f}^{\mathrm{ext}} \\ \boldsymbol{0} \end{pmatrix}. \tag{2.29}$$

This not very attractive from a computational point of view since the anharmonic operator $\mathcal{L}_{\mathrm{ah}}$ is not built in practice. Equation (2.23) permits to obtain

$$\mathcal{L}_{\mathrm{ah}}[\boldsymbol{u}] = \mathcal{L}[\boldsymbol{u}] - \mathcal{L}_{\mathrm{h}}[\boldsymbol{u}] \tag{2.30}$$

and the equivalent problem (2.21) formulation

$$\mathcal{L}_{\mathrm{h}}[\boldsymbol{u}_{\mathrm{h}}] + \mathcal{L}_{\mathrm{h}}[\boldsymbol{u}_{\mathrm{ah}}] + \mathcal{L}[\boldsymbol{u}] - \mathcal{L}_{\mathrm{h}}[\boldsymbol{u}] = \begin{pmatrix} \boldsymbol{f}^{\mathrm{ext}} \\ 0 \end{pmatrix}. \tag{2.31}$$

To obtain Sinclair's splitting, note the following notations

$$\mathcal{L}_{\mathrm{h}} = \begin{pmatrix} \mathcal{L}_{\mathrm{h}}^{\mathrm{a}} \\ \mathcal{L}_{\mathrm{h}}^{\mathrm{c}} \end{pmatrix} = \begin{pmatrix} \mathcal{L}_{\mathrm{h}}^{\mathrm{a/a}} & \mathcal{L}_{\mathrm{h}}^{\mathrm{a/c}} \\ \mathcal{L}_{\mathrm{h}}^{\mathrm{c/a}} & \mathcal{L}_{\mathrm{h}}^{\mathrm{c/c}} \end{pmatrix} \quad \Rightarrow \quad \mathcal{L}_{\mathrm{h}}[\boldsymbol{u}_{\mathrm{ah}}] = \begin{pmatrix} \mathcal{L}_{\mathrm{h}}^{\mathrm{a/a}}[\boldsymbol{u}_{\mathrm{ah}}] \\ \mathcal{L}_{\mathrm{h}}^{\mathrm{c/a}}[\boldsymbol{u}_{\mathrm{ah}}] \end{pmatrix}, \tag{2.32}$$

---

[2] The superscripts of $\mathcal{L}_{\mathrm{h}}^{\mathrm{a/c\backslash i+}}$ and $\mathcal{L}_{\mathrm{h}}^{\mathrm{c/a\backslash i}}$ after the forward slash indicate that the operator only acts on displacements in $\varLambda^{\mathrm{c}} \setminus \varLambda^{\mathrm{i+}}$ and $\varLambda^{\mathrm{a}} \setminus \varLambda^{\mathrm{i}}$

[S1] Initialize $\boldsymbol{u}^{\mathrm{a}}_1 = \boldsymbol{u}_{\mathrm{h},1}$ to a convenient analytical solution (or null if not available) and $\boldsymbol{u}_{\mathrm{ah},0} = \mathbf{0}$. Set $i = 1$.

[S2] If $i > 1$ solve the harmonic problem. Using $\boldsymbol{u}^{\mathrm{a}}_{\mathrm{ah},i-1}$, obtain forces $\mathcal{L}^{\mathrm{c/a}}_{\mathrm{h}}[\boldsymbol{u}^{\mathrm{a}}_{\mathrm{ah},i-1}]$ near the interface such that the problem reads: find $\boldsymbol{u}_{\mathrm{h},i}$ such that

$$\begin{pmatrix} \mathcal{L}^{\mathrm{a/a}}_{\mathrm{h}} & \mathcal{L}^{\mathrm{a/c}}_{\mathrm{h}} \\ \mathcal{L}^{\mathrm{c/a}}_{\mathrm{h}} & \mathcal{L}^{\mathrm{c/c}}_{\mathrm{h}} \end{pmatrix} \begin{bmatrix} \boldsymbol{u}^{\mathrm{a}}_{\mathrm{h},i} \\ \boldsymbol{u}^{\mathrm{c}}_{i} \end{bmatrix} = \begin{pmatrix} \boldsymbol{f}^{\mathrm{ext}} \\ -\mathcal{L}^{\mathrm{c/a}}_{\mathrm{h}}[\boldsymbol{u}^{\mathrm{a}}_{\mathrm{ah},i-1}] \end{pmatrix}. \tag{2.35}$$

[S3] Next, "freeze" $\boldsymbol{u}_{\mathrm{h}}$ and solve the anharmonic problem, i.e. find $\boldsymbol{u}^{\mathrm{a}}_{i}$ such that

$$\mathcal{L}^{\mathrm{a}}[\boldsymbol{u}_i] = \mathcal{L}^{\mathrm{a/a}}_{\mathrm{h}}[\boldsymbol{u}^{\mathrm{a}}_{\mathrm{h},i}] + \mathcal{L}^{\mathrm{a/c}}_{\mathrm{h}}[\boldsymbol{u}^{\mathrm{c}}_{i}] \tag{2.36}$$

and set $\boldsymbol{u}^{\mathrm{a}}_{\mathrm{ah},i} = \boldsymbol{u}^{\mathrm{a}}_{i} - \boldsymbol{u}^{\mathrm{a}}_{\mathrm{h},i}$.[3]

[S4] Check if

$$\|\mathcal{L}^{\mathrm{c/a}}_{\mathrm{h}}[\boldsymbol{u}^{\mathrm{a}}_{\mathrm{ah},i} - \boldsymbol{u}^{\mathrm{a}}_{\mathrm{ah},i-1}]\|_{\mathcal{U}^\star} < TOL. \tag{2.37}$$

If not converged → set $i = i + 1$ and go back to step **[S2]**.

Figure 2.3: Abstract formulation of Sinclair's algorithm

since $\boldsymbol{u}^{\mathrm{c}}_{\mathrm{ah}} = \mathbf{0}$, such that (2.31) can be re-arranged as follows

$$\mathcal{L}_{\mathrm{h}}[\boldsymbol{u}_{\mathrm{h}}] + \begin{pmatrix} \mathbf{0} \\ \mathcal{L}^{\mathrm{c/a}}_{\mathrm{h}}[\boldsymbol{u}_{\mathrm{ah}}] \end{pmatrix} + \mathcal{L}[\boldsymbol{u}] - \mathcal{L}_{\mathrm{h}}[\boldsymbol{u}] + \begin{pmatrix} \mathcal{L}^{\mathrm{a/a}}_{\mathrm{h}}[\boldsymbol{u}_{\mathrm{ah}}] \\ \mathbf{0} \end{pmatrix} = \begin{pmatrix} \boldsymbol{f}^{\mathrm{ext}} \\ \mathbf{0} \end{pmatrix}. \tag{2.33}$$

Using the fact that $\mathcal{L}^{\mathrm{c}}_{\mathrm{h}}[\boldsymbol{u}] = \mathbf{0}$ and grouping some terms the operator split as derived by Sinclair et al. (1978) is obtained

$$\underbrace{\begin{pmatrix} \mathcal{L}^{\mathrm{a/a}}_{\mathrm{h}} & \mathcal{L}^{\mathrm{a/c}}_{\mathrm{h}} \\ \mathcal{L}^{\mathrm{c/a}}_{\mathrm{h}} & \mathcal{L}^{\mathrm{c}}_{\mathrm{h}} \end{pmatrix} \begin{bmatrix} \boldsymbol{u}^{\mathrm{a}}_{\mathrm{h}} \\ \boldsymbol{u}^{\mathrm{c}} \end{bmatrix} - \begin{pmatrix} \boldsymbol{f}^{\mathrm{ext}} \\ -\mathcal{L}^{\mathrm{c/a}}_{\mathrm{h}}[\boldsymbol{u}^{\mathrm{a}}_{\mathrm{ah}}] \end{pmatrix}}_{\textbf{(H)}} + \underbrace{\begin{pmatrix} \mathcal{L}^{\mathrm{a}}[\boldsymbol{u}] \\ \mathbf{0} \end{pmatrix} - \begin{pmatrix} \mathcal{L}^{\mathrm{a/a}}_{\mathrm{h}}[\boldsymbol{u}^{\mathrm{a}}_{\mathrm{h}}] + \mathcal{L}^{\mathrm{a/c}}_{\mathrm{h}}[\boldsymbol{u}^{\mathrm{c}}] \\ \mathbf{0} \end{pmatrix}}_{\textbf{(AH)}} = \begin{pmatrix} \mathbf{0} \\ \mathbf{0} \end{pmatrix}, \tag{2.34}$$

where the harmonic problem **(H)** and the anharmonic problem **(AH)** are coupled through the interface and pad displacements, respectively. Note that the problems **(H)** and **(AH)** could have been equivalently deduced by differentiating the corresponding energy contributions in (2.22). This operator split was termed *flexible boundary conditions* since the boundary evolves according to linear elasticity — contrary to clamped displacements in Λ^{c}. The basic solution procedure consists of the steps given in Figure 2.3.

---

[3] The initial guess may not be exact, i.e. when using solutions to a corresponding *continuous* problem which are *not* the exact solutions to the lattice problem. Nevertheless one usually sets $\mathcal{L}^{\mathrm{a/a}}_{\mathrm{h}}[\boldsymbol{u}^{\mathrm{a}}_{\mathrm{h},i}] + \mathcal{L}^{\mathrm{a/c}}_{\mathrm{h}}[\boldsymbol{u}^{\mathrm{c}}_{i}] = \boldsymbol{f}^{\mathrm{ext}}$ in practice

This method effectively decouples the anharmonic atomistic problem from the pure harmonic problem. The atomistic problem in **[S3]** is usually solved via a nonlinear solver, e.g. a nonlinear conjugate gradient method. On the other hand, the solution of the harmonic problem in **[S2]** is obtained by application of the Green operator such that

$$\begin{pmatrix} \boldsymbol{u}^{\mathrm{a}}_{\mathrm{h},i} \\ \boldsymbol{u}^{\mathrm{c}}_{i} \end{pmatrix} = \begin{pmatrix} \mathcal{G}^{\mathrm{a/a}} & \mathcal{G}^{\mathrm{a/c}} \\ \mathcal{G}^{\mathrm{c/a}} & \mathcal{G}^{\mathrm{c/c}} \end{pmatrix} \begin{bmatrix} \boldsymbol{f}^{\mathrm{ext}} \\ -\mathcal{L}^{\mathrm{c/a}}_{\mathrm{h}}[\boldsymbol{u}^{\mathrm{a}}_{\mathrm{ah},i-1}] \end{bmatrix}. \tag{2.38}$$

However, since **[S2]** was solved in the previous step, it follows

$$\begin{pmatrix} \boldsymbol{u}^{\mathrm{a}}_{\mathrm{h},i-1} \\ \boldsymbol{u}^{\mathrm{c}}_{i-1} \end{pmatrix} = \begin{pmatrix} \mathcal{G}^{\mathrm{a/a}} & \mathcal{G}^{\mathrm{a/c}} \\ \mathcal{G}^{\mathrm{c/a}} & \mathcal{G}^{\mathrm{c/c}} \end{pmatrix} \begin{bmatrix} \boldsymbol{f}^{\mathrm{ext}} \\ -\mathcal{L}^{\mathrm{c/a}}_{\mathrm{h}}[\boldsymbol{u}^{\mathrm{a}}_{\mathrm{ah},i-2}] \end{bmatrix} \tag{2.39}$$

which allows to formulate the convenient incremental formula

$$\begin{pmatrix} \boldsymbol{u}^{\mathrm{a}}_{\mathrm{h},i} \\ \boldsymbol{u}^{\mathrm{c}}_{i} \end{pmatrix} = \begin{pmatrix} \boldsymbol{u}^{\mathrm{a}}_{\mathrm{h},i-1} \\ \boldsymbol{u}^{\mathrm{c}}_{i-1} \end{pmatrix} - \begin{pmatrix} \mathcal{G}^{\mathrm{a/a}} & \mathcal{G}^{\mathrm{a/c}} \\ \mathcal{G}^{\mathrm{c/a}} & \mathcal{G}^{\mathrm{c/c}} \end{pmatrix} \begin{bmatrix} \mathbf{0} \\ \mathcal{L}^{\mathrm{c/a}}_{\mathrm{h}}[\Delta\boldsymbol{u}^{\mathrm{a}}_{\mathrm{ah},i-2}] \end{bmatrix}. \tag{2.40}$$

Here, the notation of (Sinclair et al., 1978) is adopted, i.e. $\boldsymbol{f}^{\mathrm{c}}_{\mathrm{inh},i}$ is referred to as an *inhomogeneous* force

$$\boldsymbol{f}^{\mathrm{c}}_{\mathrm{inh},i} = \mathcal{L}^{\mathrm{c/a}}_{\mathrm{h}}[\Delta\boldsymbol{u}^{\mathrm{a}}_{\mathrm{ah},i-2}]. \tag{2.41}$$

In order explain the origin of this name, note that equation (2.35) at step $i-1$ gives in particular

$$\mathcal{L}^{\mathrm{c/a}}_{\mathrm{h}}[\boldsymbol{u}^{\mathrm{a}}_{\mathrm{h},i-1}] + \mathcal{L}^{\mathrm{c/c}}_{\mathrm{h}}[\boldsymbol{u}^{\mathrm{c}}_{i-1}] = -\mathcal{L}^{\mathrm{c/a}}_{\mathrm{h}}[\boldsymbol{u}^{\mathrm{a}}_{\mathrm{ah},i-2}] \tag{2.42}$$

and adding $\mathcal{L}^{\mathrm{c/a}}_{\mathrm{h}}[\boldsymbol{u}^{\mathrm{a}}_{\mathrm{h},i-1}]$ to (2.42), the inhomogeneous force can be rewritten as

$$\boldsymbol{f}^{\mathrm{c}}_{\mathrm{inh},i} = \mathcal{L}^{\mathrm{c/a}}_{\mathrm{h}}[\boldsymbol{u}^{\mathrm{a}}_{i-1}] + \mathcal{L}^{\mathrm{c/c}}_{\mathrm{h}}[\boldsymbol{u}^{\mathrm{c}}_{i-1}]. \tag{2.43}$$

The idea is to solve (2.35) by computing a force being equal and opposite to this inhomogeneous force which is the sum of the forces produced by atomic and continuum displacements, evaluated on the entire continuum (at convergence this force vanishes). Hence, the minus sign on the right hand side of (2.40) appears due to the fact that one seeks for displacements corresponding to a force which *counteracts* $\boldsymbol{f}^{\mathrm{c}}_{\mathrm{inh}}$.

As such the presented equations are all infinite dimensional. According to (2.28) only $\boldsymbol{f}^{\mathrm{i+}}_{\mathrm{inh},i} = \mathcal{L}^{\mathrm{i+/i}}_{\mathrm{h}}[\Delta\boldsymbol{u}^{\mathrm{i}}_{\mathrm{ah},i-2}]$ needs to be computed in practice to operate on a finite dimensional space. Furthermore, it is pointed out that the harmonic solution $\boldsymbol{u}^{\mathrm{a}}_{\mathrm{h},i}$ mainly serves as an initial guess to the atomistic problem in **[S3]**. However, the initial guess to the **harmonic** part should not affect the final solution $\boldsymbol{u}_i^{\mathrm{a}}$. Therefore it can be conveniently neglected, thus saving computational resources (c.f. Section 2.6). Hence, only the continuum displacements are updated with the iteration equation

$$\boldsymbol{u}_i^{\mathrm{p}} = \boldsymbol{u}_{i-1}^{\mathrm{p}} - \mathcal{G}^{\mathrm{p/i+}}[\boldsymbol{f}_{\mathrm{inh},i}^{\mathrm{i+}}]. \tag{2.44}$$

The convergence behavior largely depends on the quality of the initial guess (c.f. Section 4.1.1 and 4.1.2). More precisely, if $\boldsymbol{u}_{\mathrm{h}}$ is close to the full solution Sinclair's method converges rapidly within a few iterations. Otherwise, if the anharmonic contribution is large, the staggered procedure may become a bottleneck.

2.5 Discrete boundary element method for atomistic/continuum coupling

2.5.1 Rigorous derivation of a boundary summation equation for the application to monolithic solvers

Despite the simplicity of staggered algorithms, monolithic solution procedures which iterate simultaneously on all unknowns are usually preferable with respect to computational efficiency. Therefore an update of the continuum displacements $\boldsymbol{u}^{\mathrm{p}}$ that accounts for displacements on the atomistic interface Λ^{i} is sought-after. Such an update will be applied together with the iterations of the non-linear solver.

A priori, the equation (2.44) is a natural candidate as it was used to solve the harmonic subproblem **[S2]**. Furthermore, only a single matrix-vector multiplication (2.44) is necessary, and it can be computed efficiently (c.f. Section 2.6). However, it is demonstrated in this section that using (2.44) in a monolithic scheme can lead to unstable solutions because of the structure of the problem. To be convinced of this, one can consider that (2.44) optimizes Π_{h} by construction, whereas the coupled problem is *not* an energy minimization scheme (it is a *"force based"* coupling method).

What is *really* needed is an update $\boldsymbol{u}^{\mathrm{p}}$ such that the continuum problem $\mathcal{P}^{\mathrm{c}}$ is actually *solved* (i.e. an optimization of Π^{c}) for a given $\boldsymbol{u}^{\mathrm{i}}$. One straight forward possibility to solve $\mathcal{P}^{\mathrm{c}}$ could be obtained by interpreting (2.40) as a fixed point iteration. To see this, consider the expression (2.40) expanded with (2.43)

$$\boldsymbol{u}_i^{\mathrm{c}} = \boldsymbol{u}_{i-1}^{\mathrm{c}} - (\mathcal{G}^{\mathrm{c/c}}\mathcal{L}_{\mathrm{h}}^{\mathrm{c/a}})[\boldsymbol{u}_i^{\mathrm{a}}] - (\mathcal{G}^{\mathrm{c/c}}\mathcal{L}_{\mathrm{h}}^{\mathrm{c/c}})[\boldsymbol{u}_{i-1}^{\mathrm{c}}]. \tag{2.45}$$

Taking the limit $\lim\limits_{i\to\infty} \|\boldsymbol{u}_i^{\mathrm{c}} - \boldsymbol{u}_{i-1}^{\mathrm{c}}\| = 0$ will give a property satisfied at convergence

$$(\mathcal{G}^{\mathrm{c/c}}\mathcal{L}_{\mathrm{h}}^{\mathrm{c/c}})[\boldsymbol{u}^{\mathrm{c}}] = -(\mathcal{G}^{\mathrm{c/c}}\mathcal{L}_{\mathrm{h}}^{\mathrm{c/a}})[\boldsymbol{u}^{\mathrm{a}}], \tag{2.46}$$

with the fixed point $\boldsymbol{u}^{\mathrm{c}}$, which solves (2.21) since it is equivalent as saying that the inhomogeneous forces are zero, by construction. However, the composition $\mathcal{G}^{\mathrm{c/c}}\mathcal{L}_{\mathrm{h}}^{\mathrm{c/c}}$ is usually **not** symmetric and possibly indefinite for reasons that will become clear later. Hence, a fixed point algorithm based on this iteration is generally ill-posed, especially in light of the following proposition:

Proposition 1. *The incremental displacement update* (2.45) *satisfies the iteration equation of a gradient descent method, i.e.*

$$\boldsymbol{u}_i^{\mathrm{c}} = \boldsymbol{u}_{i-1}^{\mathrm{c}} - \alpha \nabla^{\mathrm{w}} \mathit{\Pi}^{\mathrm{c}}(\boldsymbol{u}_{i-1}^{\mathrm{c}}), \tag{2.47}$$

with $\alpha = 1$*, where* $\nabla^{\mathrm{w}}\bullet$ *refers to the gradient with respect to the weighted inner product space defined by*

$$\langle \bullet, \bullet \rangle_{\mathrm{w}} : \mathcal{U}^\star \times \mathcal{U}^\star \to \mathbb{R} \quad | \quad (\boldsymbol{u}, \boldsymbol{v}) = \langle \tilde{\mathcal{L}}^{\mathrm{c/c}}[\boldsymbol{u}], \boldsymbol{v} \rangle_{\mathcal{U}^\star}, \tag{2.48}$$

with $\tilde{\mathcal{L}}^{\mathrm{c/c}} = (\mathcal{G}^{\mathrm{c/c}})^{-1}$.

Proof. First, recall that the continuum energy can be written as

$$\mathit{\Pi}^{\mathrm{c}}(\boldsymbol{u}) = \frac{1}{2}\langle \mathcal{L}_{\mathrm{h}}^{\mathrm{c}}[\boldsymbol{u}^{\mathrm{c}}], \boldsymbol{u}^{\mathrm{c}} \rangle_{\mathcal{U}^\star} + \langle \mathcal{L}_{\mathrm{h}}^{\mathrm{c/a}}[\boldsymbol{u}^{\mathrm{a}}], \boldsymbol{u}^{\mathrm{c}} \rangle_{\mathcal{U}^\star}. \tag{2.49}$$

From (2.49) it follows

$$\forall\, \boldsymbol{v} \in \mathcal{U}^\star \qquad \langle \nabla \mathit{\Pi}^{\mathrm{c}}(\boldsymbol{u}^{\mathrm{c}}), \boldsymbol{v} \rangle_{\mathcal{U}^\star} = \langle \mathcal{L}_{\mathrm{h}}^{\mathrm{c/c}}[\boldsymbol{u}^{\mathrm{c}}] + \mathcal{L}_{\mathrm{h}}^{\mathrm{c/a}}[\boldsymbol{u}^{\mathrm{a}}], \boldsymbol{v} \rangle_{\mathcal{U}^\star}. \tag{2.50}$$

The definition of a gradient requires that

$$\forall\, \boldsymbol{v} \in \mathcal{U}^\star \qquad \langle \nabla \mathit{\Pi}^{\mathrm{c}}(\boldsymbol{u}^{\mathrm{c}}), \boldsymbol{v} \rangle_{\mathcal{U}^\star} = \langle \nabla^{\mathrm{w}} \mathit{\Pi}^{\mathrm{c}}(\boldsymbol{u}^{\mathrm{c}}), \boldsymbol{v} \rangle_{\mathrm{w}}. \tag{2.51}$$

Thus, the only possibility for (2.51) to hold is that

$$\nabla^{\mathrm{w}} \mathit{\Pi}^{\mathrm{c}}(\boldsymbol{u}^{\mathrm{c}}) = \mathcal{G}^{\mathrm{c/c}}[\mathcal{L}_{\mathrm{h}}^{\mathrm{c/a}}[\boldsymbol{u}^{\mathrm{a}}]] + \mathcal{G}^{\mathrm{c/c}}[\mathcal{L}_{\mathrm{h}}^{\mathrm{c/c}}[\boldsymbol{u}^{\mathrm{c}}]]. \tag{2.52}$$

Plugging the latter into (2.47) proves the stated proposition. □

Proposition 1 demonstrates that (2.45) is a gradient descent iteration. However, (2.46) is rather a root finding problem, which is linear and thus equivalent to the minimization of a quadratic form. Its structure depends on $\mathcal{G}^{\mathrm{c/c}}\mathcal{L}_{\mathrm{h}}^{\mathrm{c/c}}$: if not positive definite the quadratic form does not possess a minimum and the solution can not be obtained via a gradient descent method. A novel approach, not being based on (2.45), has to be employed to solve (2.46). This calls for more general minimal residual methods.

Therefore a practical variant of (2.46) is now developed such that the pad displacements can be obtained with an appropriate iteration method. An expression of finite dimension will be derived, aka. involving degrees of freedom in $\Lambda^{\mathrm{i+}}$ instead of the whole continuum space.

Proposition 2 (Boundary summation equation). *Assume fixed interface displacements* $\boldsymbol{u}^{\mathrm{i}}$*. Under the assumption that* $\mathcal{G}^{\mathrm{c/c}}$ *and* $\mathcal{L}_{\mathrm{h}}^{\mathrm{c/c}}$ *are nonsingular the composition* $\mathcal{G}^{\mathrm{c/c}}\mathcal{L}_{\mathrm{h}}^{\mathrm{c/c}}$ *is also nonsingular. Then a unique solution* $\boldsymbol{u}^{\mathrm{c}}$ *to* $\mathcal{P}^{\mathrm{c}}$ *exists which satisfies*

$$\boxed{\boldsymbol{u}^{\mathrm{c}}(\boldsymbol{\xi}) = \mathcal{F}^{\mathrm{c/i+}}[\boldsymbol{u}^{\mathrm{i+}}](\boldsymbol{\xi}) - \mathcal{G}^{\mathrm{c/i+}}[\boldsymbol{f}^{\mathrm{i+}}](\boldsymbol{\xi}) \qquad \textit{in } \Lambda^{\mathrm{c}},} \tag{2.53}$$

Here, $\mathcal{F}^{\mathrm{c/i+}} = \mathcal{G}^{\mathrm{c/i}}\mathcal{L}_{\mathrm{h}}^{\mathrm{i/i+}}$ *is a composition operator defined by*

$$\mathcal{F}^{\mathrm{c/i+}}[\boldsymbol{u}^{\mathrm{i+}}](\boldsymbol{\xi}) = \sum_{\boldsymbol{\eta}\in\Lambda^{\mathrm{i+}}} \boldsymbol{F}(\boldsymbol{\xi}-\boldsymbol{\eta})\boldsymbol{u}(\boldsymbol{\eta}), \qquad \boldsymbol{F}(\boldsymbol{\xi}-\boldsymbol{\eta}) = \sum_{\boldsymbol{\zeta}\in\Lambda^{\mathrm{i}}} \boldsymbol{G}^{\mathrm{lgf}}(\boldsymbol{\xi}-\boldsymbol{\zeta})\boldsymbol{K}(\boldsymbol{\zeta}-\boldsymbol{\eta}) \tag{2.54}$$

and

$$\mathcal{G}^{\mathrm{c/i+}}[\boldsymbol{f}^{\mathrm{i+}}](\boldsymbol{\xi}) = \sum_{\boldsymbol{\eta}\in\Lambda^{\mathrm{i+}}} \boldsymbol{G}^{\mathrm{lgf}}(\boldsymbol{\xi}-\boldsymbol{\eta})\boldsymbol{f}(\boldsymbol{\eta}), \qquad \boldsymbol{f}(\boldsymbol{\eta}) = \sum_{\boldsymbol{\zeta}\in\Lambda^{\mathrm{i}}} \boldsymbol{K}(\boldsymbol{\eta}-\boldsymbol{\zeta})\boldsymbol{u}(\boldsymbol{\zeta}). \tag{2.55}$$

Proof. From the definition of the Green operator and the domain decomposition the following identities are obtained

$$\begin{aligned} \mathcal{G}^{\mathrm{a/a}}\mathcal{L}_{\mathrm{h}}^{\mathrm{a/a}} + \mathcal{G}^{\mathrm{a/c}}\mathcal{L}_{\mathrm{h}}^{\mathrm{c/a}} &= \mathcal{I}, & \qquad \mathcal{G}^{\mathrm{a/a}}\mathcal{L}_{\mathrm{h}}^{\mathrm{a/c}} + \mathcal{G}^{\mathrm{a/c}}\mathcal{L}_{\mathrm{h}}^{\mathrm{c/c}} &= 0, \\ \mathcal{G}^{\mathrm{c/a}}\mathcal{L}_{\mathrm{h}}^{\mathrm{a/a}} + \mathcal{G}^{\mathrm{c/c}}\mathcal{L}_{\mathrm{h}}^{\mathrm{c/a}} &= 0, & \qquad \mathcal{G}^{\mathrm{c/a}}\mathcal{L}_{\mathrm{h}}^{\mathrm{a/c}} + \mathcal{G}^{\mathrm{c/c}}\mathcal{L}_{\mathrm{h}}^{\mathrm{c/c}} &= \mathcal{I}. \end{aligned} \tag{2.56}$$

From the last identity it follows

$$\mathcal{G}^{\mathrm{c/c}}\mathcal{L}_{\mathrm{h}}^{\mathrm{c/c}} = \mathcal{I} - \mathcal{G}^{\mathrm{c/a}}\mathcal{L}_{\mathrm{h}}^{\mathrm{a/c}}. \tag{2.57}$$

and therefore (2.46) can be re-written as

$$(\mathcal{I} - \mathcal{G}^{\mathrm{c/a}}\mathcal{L}_{\mathrm{h}}^{\mathrm{a/c}})[\boldsymbol{u}^{\mathrm{c}}] = -(\mathcal{G}^{\mathrm{c/c}}\mathcal{L}_{\mathrm{h}}^{\mathrm{c/a}})[\boldsymbol{u}^{\mathrm{a}}]. \tag{2.58}$$

The latter format acts on the entire displacement vectors, i.e. on an infinite dimensional space.

In order to reduce the continuum space to $\Lambda^{\mathrm{i+}}$, the property (2.27) can be used such that

$$(\mathcal{G}^{\mathrm{c/a}}\mathcal{L}_{\mathrm{h}}^{\mathrm{a/c}})[\boldsymbol{u}^{\mathrm{c}}] = \mathcal{G}^{\mathrm{c/a}}[\mathcal{L}_{\mathrm{h}}^{\mathrm{a/c}}[\boldsymbol{u}^{\mathrm{c}}]] = \mathcal{G}^{\mathrm{c/a}}[\mathcal{L}_{\mathrm{h}}^{\mathrm{a/i+}}[\boldsymbol{u}^{\mathrm{i+}}]] = (\mathcal{G}^{\mathrm{c/i}}\mathcal{L}_{\mathrm{h}}^{\mathrm{i/i+}})[\boldsymbol{u}^{\mathrm{i+}}]. \tag{2.59}$$

For similar reasons one can write the right hand side of (2.58) by using (2.28) as

$$(\mathcal{G}^{\mathrm{c/c}}\mathcal{L}_{\mathrm{h}}^{\mathrm{c/a}})[\boldsymbol{u}^{\mathrm{a}}] = \mathcal{G}^{\mathrm{c/c}}[\mathcal{L}_{\mathrm{h}}^{\mathrm{c/a}}[\boldsymbol{u}^{\mathrm{a}}]] = \mathcal{G}^{\mathrm{c/c}}[\mathcal{L}_{\mathrm{h}}^{\mathrm{c/i}}[\boldsymbol{u}^{\mathrm{i}}]] = (\mathcal{G}^{\mathrm{c/i+}}\mathcal{L}_{\mathrm{h}}^{\mathrm{i+/i}})[\boldsymbol{u}^{\mathrm{i}}]. \tag{2.60}$$

Now the reduced boundary equation reads

$$\mathcal{I}[\boldsymbol{u}^{\mathrm{c}}] - (\mathcal{G}^{\mathrm{c/i}}\mathcal{L}_{\mathrm{h}}^{\mathrm{i/i+}})[\boldsymbol{u}^{\mathrm{i+}}] = -(\mathcal{G}^{\mathrm{c/i+}}\mathcal{L}_{\mathrm{h}}^{\mathrm{i+/i}})[\boldsymbol{u}^{\mathrm{i}}] \qquad \text{in } \Lambda^{\mathrm{c}}. \tag{2.61}$$

With (2.54) and (2.55) the composition operator on the left hand side can be written as $\mathcal{G}^{\mathrm{c/i}}\mathcal{L}_{\mathrm{h}}^{\mathrm{i/i+}} = \mathcal{F}^{\mathrm{c/i+}}$. In addition, it holds $\mathcal{L}_{\mathrm{h}}^{\mathrm{i+/i}}[\boldsymbol{u}^{\mathrm{i}}] = \boldsymbol{f}^{\mathrm{i+}}$. Plugging $\mathcal{F}^{\mathrm{c/i+}}$ and $\boldsymbol{f}^{\mathrm{i+}}$ into (2.61) and re-arranging the terms (2.53) is obtained. □

Remark 2.5.1. *Equation* (2.53) *can be considered as a discrete equivalent of the well-known boundary integral equation (BIE)*

$$\boldsymbol{u}(\boldsymbol{x}) = \int_{\Gamma} \boldsymbol{T}^{\mathrm{cgf}}(\boldsymbol{x}-\boldsymbol{x}')\boldsymbol{u}(\boldsymbol{x}')\,\mathrm{d}A(\boldsymbol{x}') - \int_{\Gamma} \boldsymbol{G}^{\mathrm{cgf}}(\boldsymbol{x}-\boldsymbol{x}')\boldsymbol{t}(\boldsymbol{x}')\,\mathrm{d}A(\boldsymbol{x}') \tag{2.62}$$

for continuous problems. Here, $\boldsymbol{T}^{\mathrm{cgf}}$ *and* $\boldsymbol{G}^{\mathrm{cgf}}$ *refer to the fundamental tractions/displacements on the boundary* $\Gamma(\equiv \Lambda^{\mathrm{i+}})$*, respectively,* $\boldsymbol{t}$ *are the applied tractions on* Γ *and* $\boldsymbol{u}$ *are the unknowns which are sought-after. The connection between* $\boldsymbol{T}^{\mathrm{cgf}}$*,* $\boldsymbol{G}^{\mathrm{cgf}}$ *and their discrete analogs* $\boldsymbol{F}$*,* $\boldsymbol{G}^{\mathrm{lgf}}$ *is obvious.*

The boundary summation equation (BSE) permits to compute the whole displacement in Λ^{c} from the displacements and forces in $\Lambda^{\mathrm{i+}}$ under the assumption of equilibrium. In particular, it can therefore provide an expression for the displacements of the pad atoms in Λ^{p}, and as such provide the basis for a monolithic solution procedure. Recall that updating $\boldsymbol{u}^{\mathrm{p}}$ jointly within the iteration of the nonlinear atomic solver is the ultimate goal, which will be done thanks to (2.53). However, one has to provide the displacements and forces in the i+ layer. While $\boldsymbol{f}^{\mathrm{i+}} = \mathcal{L}_{\mathrm{h}}^{\mathrm{i+/i}}[\boldsymbol{u}^{\mathrm{i}}]$ depend on atomic displacements in Λ^{i}, the displacements $\boldsymbol{u}^{\mathrm{i+}}$ have to be calculated in order to employ (2.53) to compute the pad displacements. Since (2.53) also holds in $\Lambda^{\mathrm{i+}}$, it will be used to construct the linear problem that can provide $\boldsymbol{u}^{\mathrm{i+}}$. Such as procedure is summarized below:

1. Compute the displacements in $\Lambda^{\mathrm{i+}}$ due to $\boldsymbol{u}^{\mathrm{i}}$ according to

$$\tilde{\boldsymbol{u}}^{\mathrm{i+}} = \mathcal{G}^{\mathrm{i+/i+}}[\boldsymbol{f}^{\mathrm{i+}}] = \mathcal{G}^{\mathrm{i+/i+}}[\mathcal{L}_{\mathrm{h}}^{\mathrm{i+/i}}[\boldsymbol{u}^{\mathrm{i}}]]. \tag{2.63}$$

2. Compute the true displacements $\boldsymbol{u}^{\mathrm{i+}}$ by solving

$$(\mathcal{I} - \mathcal{F}^{\mathrm{i+/i+}})[\boldsymbol{u}^{\mathrm{i+}}] = -\tilde{\boldsymbol{u}}^{\mathrm{i+}} \qquad \text{in } \Lambda^{\mathrm{i+}}. \tag{2.64}$$

   The corresponding linear system comes from (2.53) *and contains* $N^{\mathrm{i+}}$ *unknowns.*

3. Determine the remaining pad displacements $\boldsymbol{u}^{\mathrm{p}\setminus\mathrm{i+}}$ using (2.53), i.e. compute

$$\boldsymbol{u}^{\mathrm{p}\setminus\mathrm{i+}} = \mathcal{F}^{\mathrm{p}\setminus\mathrm{i+/i+}}[\boldsymbol{u}^{\mathrm{i+}}] - \mathcal{G}^{\mathrm{p}\setminus\mathrm{i+/i+}}[\boldsymbol{f}^{\mathrm{i+}}] \qquad \text{in } \Lambda^{\mathrm{p}} \setminus \Lambda^{\mathrm{i+}}. \tag{2.65}$$

   This boils down to a matrix-vector multiplication with complexity of $\mathcal{O}(N^{\mathrm{p}\setminus\mathrm{i+}}N^{\mathrm{i+}})$.

The steps 1-3 provide a means to compute the pad displacements within a finite number of operations. More precisely, the linear system which has to be solved in step 2 is now *finite* dimensional in comparison with (2.46) which is *infinite*. The computation of the linear system requires further discussion. According to Remark 2.5.1 one may think of the composition operator $\mathcal{F}^{\mathrm{i+/i+}} = \mathcal{G}^{\mathrm{i+/i}}\mathcal{L}_{\mathrm{h}}^{\mathrm{i/i+}}$ as a discrete analog to the traction operator $\boldsymbol{T}^{\mathrm{cgf}}$. Noting that $\boldsymbol{G}^{\mathrm{lgf}}(\boldsymbol{\xi}-\boldsymbol{\zeta}) = \boldsymbol{G}^{\mathrm{lgf}}(\boldsymbol{\zeta}-\boldsymbol{\xi})$, the tensor $\boldsymbol{F}(\boldsymbol{\xi}-\boldsymbol{\eta})$ can be interpreted as the force (per unit force) exerted on an atom $\boldsymbol{\eta}$ by displacements in $\mathit{\Lambda}^{\mathrm{i}}$ due to a point force on $\boldsymbol{\xi}$. In general $\mathcal{F}^{\mathrm{i+/i+}}$ is not symmetric for similar reasons that $\boldsymbol{T}^{\mathrm{cgf}}$ is not symmetric in the continuous case (e.g. Bonnet et al., 1998; Sutradhar et al., 2008) in the sense that

$$\forall\, \boldsymbol{u}^{\mathrm{i+}}\ \exists\, \boldsymbol{v} \in \mathcal{U}^{\star}(\mathit{\Lambda}^{\mathrm{i+}}) \quad \text{such that} \quad \langle(\mathcal{G}^{\mathrm{i+/i}}\mathcal{L}_{\mathrm{h}}^{\mathrm{i/i+}})[\boldsymbol{u}^{\mathrm{i+}}], \boldsymbol{v}\rangle \neq \langle \boldsymbol{u}^{\mathrm{i+}}, (\mathcal{L}_{\mathrm{h}}^{\mathrm{i+/i}}\mathcal{G}^{\mathrm{i/i+}})[\boldsymbol{v}]\rangle, \tag{2.66}$$

where $\mathcal{L}_{\mathrm{h}}^{\mathrm{i+/i}}\mathcal{G}^{\mathrm{i/i+}}$ is the adjoint of $\mathcal{F}^{\mathrm{i+/i+}}$.

This lack of symmetry applies with exceptions for special geometrical cases for the fully atomistic region, e.g. with translational invariant interfaces, for instance within periodic systems. This is well-known from the classical (continuous) BEM and carries over to the discrete case. Moreover, the linear system associated with (2.64) is possibly indefinite which has direct consequences on the choice of the linear solver. For this class of problems, gradient-based methods such as gradient descent or conjugate gradient methods usually fail to converge which calls for more general minimal residual methods or direct solvers (c.f. Section 2.7.2). This lack of symmetry also explains why the simple iteration equation (2.44), which was demonstrated as a gradient descent method, cannot be used to update the continuum in a semi-monolithic scheme.

2.5.2 Symmetric discrete boundary element method

The issue of a non-symmetric operator $\mathcal{F}^{\mathrm{i+/i+}}$ can be remedied in the context of the proposed A/C coupling scheme. Instead of considering the *displacements* of the i+ atoms as the primary unknowns, one may imagine a shift of the interface such that the *forces* on the interface atoms have to be determined. This is because the matrix which defines the linear system is then associated with the symmetric Green operator $\mathcal{G}$ and not with $\mathcal{F}$. Therefore consider the BSE

$$\boxed{\boldsymbol{u}_{\mathrm{h}}(\boldsymbol{\xi}) = \mathcal{F}^{\mathrm{c\cup i/i}}[\boldsymbol{u}^{\mathrm{i}}](\boldsymbol{\xi}) - \mathcal{G}^{\mathrm{c\cup i/i}}[\tilde{\boldsymbol{f}}^{\mathrm{i}}](\boldsymbol{\xi}) \qquad \text{in } \mathit{\Lambda}^{\mathrm{c}} \cup \mathit{\Lambda}^{\mathrm{i}},} \tag{2.67}$$

where

$$\mathcal{F}^{\mathrm{c\cup i/i}}[\boldsymbol{u}^{\mathrm{i}}](\boldsymbol{\xi}) = \sum_{\boldsymbol{\eta}\in\mathit{\Lambda}^{\mathrm{i}}} \boldsymbol{F}(\boldsymbol{\xi}-\boldsymbol{\eta})\boldsymbol{u}(\boldsymbol{\eta}), \qquad \boldsymbol{F}(\boldsymbol{\xi}-\boldsymbol{\eta}) = \sum_{\boldsymbol{\zeta}\in\mathit{\Lambda}^{\mathrm{i-}}} \boldsymbol{G}^{\mathrm{lgf}}(\boldsymbol{\xi}-\boldsymbol{\zeta})\boldsymbol{K}(\boldsymbol{\zeta}-\boldsymbol{\eta}) \tag{2.68}$$

which now involves a summation over $\mathit{\Lambda}^{\mathrm{i-}}$ (see Figure 2.2). The situation is slightly different from the one depicted in Section 2.5.1. Now, the unknowns on the interface are the forces $\tilde{\boldsymbol{f}}^{\mathrm{i}}$ [4] while the displacements $\boldsymbol{u}^{\mathrm{i}}$ are known, which led to the following algorithm:

---

[4] The tilde is used here to distinguish it from the real atomic forces in $\mathit{\Lambda}^{\mathrm{i}}$

1. Compute the self-displacements induced on the interface according to

$$\tilde{\boldsymbol{u}}^{\mathrm{i}} = (\mathcal{F}^{\mathrm{i/i}} - \mathcal{I})[\boldsymbol{u}^{\mathrm{i}}]. \tag{2.69}$$

2. Determine the forces on the interface atoms $\tilde{\boldsymbol{f}}^{\mathrm{i}}$ by solving

$$\mathcal{G}^{\mathrm{i/i}}[\tilde{\boldsymbol{f}}^{\mathrm{i}}] = \tilde{\boldsymbol{u}}^{\mathrm{i}} \qquad \text{in } \Lambda^{\mathrm{i}}. \tag{2.70}$$

   The corresponding linear system contains N^{i} unknowns. It is easy to see that it is indeed symmetric due to the symmetry of the Green function.

3. Compute the pad displacements $\boldsymbol{u}^{\mathrm{p}}$ using (2.67), i.e.

$$\boldsymbol{u}^{\mathrm{p}} = \mathcal{F}^{\mathrm{p/i}}[\boldsymbol{u}^{\mathrm{i}}] - \mathcal{G}^{\mathrm{p/i}}[\tilde{\boldsymbol{f}}^{\mathrm{i}}] \qquad \text{in } \Lambda^{\mathrm{p}}. \tag{2.71}$$

   The complexity of the associated matrix-vector multiplication is of $\mathcal{O}(N^{\mathrm{p}}N^{\mathrm{i}})$.

Several remarks are in order:

Remark 2.5.2. *If more general problems are considered involving other types of boundary conditions, e.g. prescribed displacements and forces, the linear system associated with the DBEM becomes non-symmetric in any case. In the classical BEM this issue is remedied by solving a mixed problem, more precisely, a combination of the BIE and its first derivative (since the derivative of $\boldsymbol{T}^{\mathrm{cgf}}$ is again symmetric). However, a symmetric BEM seems only feasible when considering a Galerkin-type BEM since the second derivatives of $\boldsymbol{T}^{\mathrm{cgf}}$ are hypersingular according to (Bonnet et al., 1998; Sutradhar et al., 2008). Vice versa, a symmetric Galerkin-BEM comes at higher computational cost for constructing the system matrices since the equilibrium equations have to be enforced in a weak sense, thus requiring the evaluation of double integrals. This procedure will be simpler in the discrete case since the LGF is nonsingular. It is speculated that an unconditionally symmetric DBEM can be constructed similarly to the classical BEM.*

Remark 2.5.3. *The symmetric DBEM is conceptually equivalent to the method considered by Li (2009) who solved problem* (2.21) *using a staggered solution procedure (c.f. Section 2.7.1). To solve the continuum problem, the starting point in (Li, 2009) is to invert the operator $\mathcal{L}_{\mathrm{h}}^{\mathrm{c/c}}$ in $\mathcal{P}^{\mathrm{c}}$ directly and using the identity* (2.56) *subsequently to obtain*

$$\boldsymbol{u}^{\mathrm{c}} = (\mathcal{G}^{\mathrm{c/a}}(\mathcal{G}^{\mathrm{a/a}})^{-1})[\boldsymbol{u}^{\mathrm{a}}] \qquad \textit{in } \Lambda^{\mathrm{c}}. \tag{2.72}$$

In (Li, 2009) the problem was not reduced to a BSE-type formulation as shown above and is thus not practical if the problem size is large. However, the solutions of (2.72) *and* (2.67) *coincide.*

Proof of Remark 2.5.3. The idea is to rewrite (2.72) in the form of (2.67). First, an alternative expression of the inverse of $\mathcal{G}^{\mathrm{a/a}}$ denoted by $\tilde{\mathcal{L}}_{\mathrm{h}}^{\mathrm{a/a}}$is sought-after. Then $(\mathcal{G}^{\mathrm{a/a}})^{-1}$ is split into parts which act on the interface forces and the forces in the remainder $\Lambda^{a} \setminus \Lambda^{i}$, respectively, such that

$$\begin{pmatrix} \mathcal{G}^{a'/a'} & \mathcal{G}^{a'/i} \\ \mathcal{G}^{i/a'} & \mathcal{G}^{i/i} \end{pmatrix}^{-1} = \begin{pmatrix} \tilde{\mathcal{L}}_{h}^{a'/a'} & \tilde{\mathcal{L}}_{h}^{a'/i} \\ \tilde{\mathcal{L}}_{h}^{i/a'} & \tilde{\mathcal{L}}_{h}^{i/i} \end{pmatrix} \Rightarrow \begin{pmatrix} \mathcal{G}^{a'/a'} & \mathcal{G}^{a'/i} \\ \mathcal{G}^{i/a'} & \mathcal{G}^{i/i} \end{pmatrix} \begin{pmatrix} \tilde{\mathcal{L}}_{h}^{a'/a'} & \tilde{\mathcal{L}}_{h}^{a'/i} \\ \tilde{\mathcal{L}}_{h}^{i/a'} & \tilde{\mathcal{L}}_{h}^{i/i} \end{pmatrix} = \mathcal{I}. \quad (2.73)$$

Thereby, the superscript a' indicates that the domain/co-domain of the corresponding operator relates to $\Lambda^{a} \setminus \Lambda^{i}$. From (2.73) it follows

$$\begin{aligned} \mathcal{G}^{a'/a'} \tilde{\mathcal{L}}_{h}^{a'/a'} + \mathcal{G}^{a'/i} \tilde{\mathcal{L}}_{h}^{i/a'} &= \mathcal{I}, & \mathcal{G}^{a'/a'} \tilde{\mathcal{L}}_{h}^{a'/i} + \mathcal{G}^{a'/i} \tilde{\mathcal{L}}_{h}^{i/i} &= 0, \\ \mathcal{G}^{i/a'} \tilde{\mathcal{L}}_{h}^{a'/a'} + \mathcal{G}^{i/i} \tilde{\mathcal{L}}_{h}^{i/a'} &= 0, & \mathcal{G}^{i/a'} \tilde{\mathcal{L}}_{h}^{a'/i} + \mathcal{G}^{i/i} \tilde{\mathcal{L}}_{h}^{i/i} &= \mathcal{I}. \end{aligned} \quad (2.74)$$

Making use of the same splitting of $\mathcal{G}^{a/a}$ as in (2.56) leads to

$$\begin{pmatrix} \mathcal{G}^{a'/a'} & \mathcal{G}^{a'/i} & \mathcal{G}^{a'/c} \\ \mathcal{G}^{i/a'} & \mathcal{G}^{i/i} & \mathcal{G}^{i/c} \\ \mathcal{G}^{c/a'} & \mathcal{G}^{c/i} & \mathcal{G}^{c/c} \end{pmatrix} \begin{pmatrix} \mathcal{L}_{h}^{a'/a'} & \mathcal{L}_{h}^{a'/i} & 0 \\ \mathcal{L}_{h}^{i/a'} & \mathcal{L}_{h}^{i/i} & \mathcal{L}_{h}^{i/c} \\ 0 & \mathcal{L}_{h}^{c/i} & \mathcal{L}_{h}^{c/c} \end{pmatrix} = \mathcal{I}. \quad (2.75)$$

From the latter it can be deduced that

$$\mathcal{G}^{a'/a'} \mathcal{L}_{h}^{a'/a'} + \mathcal{G}^{a'/i} \mathcal{L}_{h}^{i/a'} = \mathcal{I}, \qquad \mathcal{G}^{i/a'} \mathcal{L}_{h}^{a'/a'} + \mathcal{G}^{i/i} \mathcal{L}_{h}^{i/a'} = 0. \quad (2.76)$$

Since $\mathcal{G}^{a/a}$ is nonsingular the operator $\tilde{\mathcal{L}}_{h}^{a/a}$is unique. Comparing (2.76) with the first and the third identity in (2.74) yields $\tilde{\mathcal{L}}_{h}^{a'/a'} = \mathcal{L}_{h}^{a'/a'}$ and $\tilde{\mathcal{L}}_{h}^{a'/i} = \mathcal{L}_{h}^{a'/i}$. Noting that $\mathcal{G}^{a/a}$ is symmetric it can be concluded that

$$\begin{pmatrix} \mathcal{G}^{a'/a'} & \mathcal{G}^{a'/i} \\ \mathcal{G}^{i/a'} & \mathcal{G}^{i/i} \end{pmatrix} \begin{pmatrix} \mathcal{L}_{h}^{a'/a'} & \mathcal{L}_{h}^{a'/i} \\ \mathcal{L}_{h}^{i/a'} & \tilde{\mathcal{L}}_{h}^{i/i} \end{pmatrix} = \mathcal{I}. \quad (2.77)$$

The operator $\tilde{\mathcal{L}}_{h}^{i/i}$can then be obtained from the fourth identity in (2.74) such that

$$\tilde{\mathcal{L}}_{h}^{i/i} = (\mathcal{G}^{i/i})^{-1} (\mathcal{I} - \mathcal{G}^{i/a'} \mathcal{L}_{h}^{a'/i}). \quad (2.78)$$

Now, using (2.77) and (2.78) in (2.72), it follows

$$\begin{aligned} \boldsymbol{u}^{c} &= (\mathcal{G}^{c/a} (\mathcal{G}^{a/a})^{-1})[\boldsymbol{u}^{a}] \\ &= (\mathcal{G}^{c/a'} \mathcal{L}_{h}^{a'/a'} + \mathcal{G}^{c/i} \mathcal{L}_{h}^{i/a'})[\boldsymbol{u}^{a'}] \\ &\quad + (\mathcal{G}^{c/a'} \mathcal{L}_{h}^{a'/i} + \mathcal{G}^{c/i} (\mathcal{G}^{i/i})^{-1} (\mathcal{I} - \mathcal{G}^{i/a'} \mathcal{L}_{h}^{a'/i}))[\boldsymbol{u}^{i}] \\ &\overset{(2.75)}{=} (\mathcal{G}^{c/a'} \mathcal{L}_{h}^{a'/i} + \mathcal{G}^{c/i} (\mathcal{G}^{i/i})^{-1} (\mathcal{I} - \mathcal{G}^{i/a'} \mathcal{L}_{h}^{a'/i}))[\boldsymbol{u}^{i}] \\ &= (\mathcal{F}^{c/i} + \mathcal{G}^{c/i} (\mathcal{G}^{i/i})^{-1} (\mathcal{I} - \mathcal{F}^{i/i}))[\boldsymbol{u}^{i}] \end{aligned} \quad (2.79)$$

which is nothing but (2.67). ☐

2.5.3 Computation of stresses inside the body

For many applications it is necessary to compute the stress at some (arbitrary) material point $\boldsymbol{x}$ inside the continuum domain. For example, the coupled atomistic/discrete dislocations method which is discussed in the following chapter requires the computation of the stress at any point $\boldsymbol{x}$ on the glide plane(s), in principle. Therefore the displacement gradient at $\boldsymbol{x}$ must be computed which can be done with the proposed BSE. Indeed, using (2.53) in the definition of the gradient (2.12), it follows

$$\nabla \boldsymbol{u}(\boldsymbol{x}) = \sum_{\boldsymbol{\xi} \in \mathcal{R}^{\text{loc}}_{\xi}} \big(\mathcal{F}^{\text{c/i+}}[\boldsymbol{u}^{\text{i+}}](\boldsymbol{\xi}) - \mathcal{G}^{\text{c/i+}}[\boldsymbol{f}^{\text{i+}}](\boldsymbol{\xi})\big) \otimes \nabla \varphi_{\xi}(\boldsymbol{x}). \tag{2.80}$$

Once the displacement gradient is evaluated, the Cauchy stress tensor $\boldsymbol{\sigma}(\boldsymbol{x}) \in [L^2(\Omega^{\text{c}})]^{d\times d}$ can be computed

$$\boldsymbol{\sigma}(\boldsymbol{x}) = \mathbb{C}[\nabla \boldsymbol{u}(\boldsymbol{x})], \tag{2.81}$$

noting that only the symmetric part of $\nabla \boldsymbol{u}$ enters in (2.81).

Equation (2.80) requires two algebraic operations at any $\boldsymbol{\xi} \in \mathcal{R}^{\text{loc}}_{\xi}$ (i.e. $\mathcal{F}^{\text{c/i+}}[\boldsymbol{u}^{\text{i+}}]$ and $\mathcal{G}^{\text{c/i+}}[\boldsymbol{f}^{\text{i+}}]$). With Sinclair's method the computation reduces to one operation. To see this, consider the iteration equation (2.44) but evaluated at some point $\boldsymbol{\xi} \in \Lambda^{\text{c}}$

$$\boldsymbol{u}^{\text{c}}_i(\boldsymbol{\xi}) = \boldsymbol{u}^{\text{c}}_{i-1}(\boldsymbol{\xi}) - \mathcal{G}^{\text{c/i+}}[\boldsymbol{f}^{\text{i+}}_{\text{inh},i}](\boldsymbol{\xi}). \tag{2.82}$$

Upon convergence, supposedly after N steps, the final solution reads

$$\boldsymbol{u}^{\text{c}}(\boldsymbol{\xi}) = \boldsymbol{u}^{\text{c}}_0(\boldsymbol{\xi}) - \mathcal{G}^{\text{c/i+}}[\boldsymbol{f}^{\text{i+}}_{\text{inh,tot}}](\boldsymbol{\xi}), \qquad \text{with} \quad \boldsymbol{f}^{\text{i+}}_{\text{inh,tot}} = \sum_{i=1}^{N} \boldsymbol{f}^{\text{i+}}_{\text{inh},i}, \tag{2.83}$$

where $\boldsymbol{u}^{\text{c}}_0(\boldsymbol{\xi})$ is the initial guess, which only requires to carry out the algebraic operation $\mathcal{G}^{\text{c/i+}}[\boldsymbol{f}^{\text{i+}}_{\text{inh,tot}}]$ at $\boldsymbol{\xi} \in \mathcal{R}^{\text{loc}}_{\xi}$.

Another possibility to obtain gradients of $\boldsymbol{u}^{\text{c}}$ is by Fourier interpolation (also: band-limited interpolation, c.f. Trefethen, 2000). Therefore, recall that the lattice Green tensor (Appendix A.4.1) can in principle be evaluated at *any* point $\boldsymbol{x}$ (not just on Λ^{c}). An alternative displacement *field* is then given by

$$\boldsymbol{u}^{\text{c}}(\boldsymbol{x}) = \mathcal{F}^{\text{c/i+}}[\boldsymbol{u}^{\text{i+}}](\boldsymbol{x}) - \mathcal{G}^{\text{c/i+}}[\boldsymbol{f}^{\text{i+}}](\boldsymbol{x}) = \sum_{\boldsymbol{\eta} \in \Lambda^{\text{i+}}} \sum_{\boldsymbol{\zeta} \in \Lambda^{\text{i}}} \boldsymbol{G}^{\text{lgf}}(\boldsymbol{x} - \boldsymbol{\zeta}) \boldsymbol{K}(\boldsymbol{\zeta} - \boldsymbol{\eta}) \boldsymbol{u}(\boldsymbol{\eta}) \tag{2.84}$$

or in index notation

$$u^{\text{c}}_i(\boldsymbol{x}) = \sum_{\boldsymbol{\eta} \in \Lambda^{\text{i+}}} \sum_{\boldsymbol{\zeta} \in \Lambda^{\text{i}}} G^{\text{lgf}}_{ik}(\boldsymbol{x} - \boldsymbol{\zeta}) K_{kl}(\boldsymbol{\zeta} - \boldsymbol{\eta}) u_l(\boldsymbol{\eta}). \tag{2.85}$$

The components of the gradient then follow as

$$u^{\mathrm{c}}_{i,j}(\boldsymbol{x}) = \sum_{\boldsymbol{\eta}\in\Lambda^{\mathrm{i+}}} \sum_{\boldsymbol{\zeta}\in\Lambda^{\mathrm{i}}} G^{\mathrm{lgf}}_{ik,j}(\boldsymbol{x}-\boldsymbol{\zeta}) K_{kl}(\boldsymbol{\zeta}-\boldsymbol{\eta}) u_l(\boldsymbol{\eta}). \tag{2.86}$$

This definition requires the $\boldsymbol{G}^{\mathrm{lgf}}$ *and* its gradients to be precalculated, but does not involve a summation over $\mathcal{R}^{\mathrm{loc}}_{\xi}$.

2.5.4 Bounded problems

An extension of the proposed DBEM to bounded problems is possible. Therefore consider the (pure) harmonic problem with outer boundary I in Figure 2.4 (a). For simplicity a Dirichlet problem is considered in the following, i.e. the displacements $\boldsymbol{u}^{\mathrm{I}}$ are assumed to be prescribed throughout this section.[5] It can be easily seen that the BSE (2.53) holds (yet in the reverse way) by inverting the problem description in Section 2.5.1, i.e. by considering the continuum domain as the interior (bounded) domain. The corresponding BSE then reads

$$\boxed{\boldsymbol{u}^{\mathrm{c}}(\boldsymbol{\xi}) = \mathcal{F}^{\mathrm{c/I+}}[\boldsymbol{u}^{\mathrm{I+}}](\boldsymbol{\xi}) - \mathcal{G}^{\mathrm{c/I+}}[\boldsymbol{f}^{\mathrm{I+}}](\boldsymbol{\xi}) \qquad \text{in } \Lambda^{\mathrm{c}},} \tag{2.87}$$

where $\boldsymbol{f}^{\mathrm{I+}} = \mathcal{L}^{\mathrm{I+/I}}_{\mathrm{h}}[\boldsymbol{u}^{\mathrm{I}}]$. The operators $\mathcal{F}^{\mathrm{c/I+}}$ and $\mathcal{G}^{\mathrm{c/I+}}$ are defined analogously to (2.54) and (2.55).

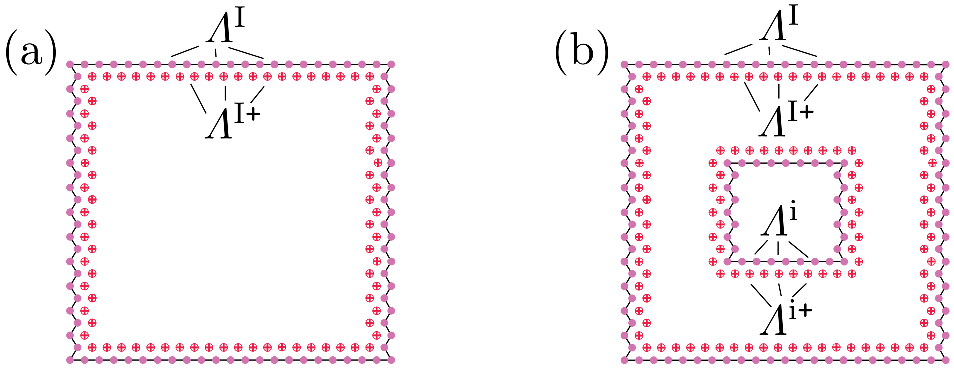

Figure 2.4: (a) Bounded domain with interface Λ^{I}. (b) Atomistic/continuum domain decomposition for bounded problems

If a coupled problem is to be considered, i.e. a finite atomistic domain surrounded by a *bounded* continuum (Figure 2.4 (b)), the corresponding BSE now involves a summation over two boundaries. This is shown in the following. Therefore assume that the additional boundary condition on the inner boundary Λ^{i} is the displacement $\boldsymbol{u}^{\mathrm{i}}$ as described in the previous sections. The corresponding continuum problem reads

---

[5] Mixed boundary conditions (i.e. Dirichlet/Neumann) are also possible but require a modification of the operator $\mathcal{F}$ and are not considered here

$$\mathcal{P}^{\mathrm{c}} \begin{cases} \mathcal{L}_{\mathrm{h}}^{\mathrm{c}}[\boldsymbol{u}] = \boldsymbol{0} & \text{in } \Lambda^{\mathrm{c}}, \\ \boldsymbol{u} = \boldsymbol{u}^{\mathrm{i}} & \text{in } \Lambda^{\mathrm{i}}, \\ \boldsymbol{u} = \boldsymbol{u}^{\mathrm{I}} & \text{in } \Lambda^{\mathrm{I}}. \end{cases} \tag{2.88}$$

Since there was no special assumption on the location of/or connectivity between the interfaces a solution to (2.88) can directly be deduced by combing (2.53) and (2.87) as follows

$$\boldsymbol{u}^{\mathrm{c}}(\boldsymbol{\xi}) = \mathcal{F}^{\mathrm{c/i+}}[\boldsymbol{u}^{\mathrm{i+}}](\boldsymbol{\xi}) - \mathcal{G}^{\mathrm{c/i+}}[\boldsymbol{f}^{\mathrm{i+}}](\boldsymbol{\xi}) + \mathcal{F}^{\mathrm{c/I+}}[\boldsymbol{u}^{\mathrm{I+}}](\boldsymbol{\xi}) - \mathcal{G}^{\mathrm{c/I+}}[\boldsymbol{f}^{\mathrm{I+}}](\boldsymbol{\xi}) \qquad \text{in } \Lambda^{\mathrm{c}}. \tag{2.89}$$

The latter form can be condensed such that the *general* BSE for bounded (Dirichlet) problems is given by

$$\boxed{\boldsymbol{u}^{\mathrm{c}}(\boldsymbol{\xi}) = \mathcal{F}^{\mathrm{c/i+\cup I+}}[\boldsymbol{u}^{\mathrm{i+\cup I+}}](\boldsymbol{\xi}) - \mathcal{G}^{\mathrm{c/i+\cup I+}}[\boldsymbol{f}^{\mathrm{i+\cup I+}}](\boldsymbol{\xi}) \qquad \text{in } \Lambda^{\mathrm{c}}.} \tag{2.90}$$

The pad displacements can subsequently be obtained analogously to the procedure from Section 2.5.1.

Remark 2.5.4. *To further clarify the proposed function space setting (see Section 2.2) consider* (2.90) *with the inner boundary* Λ^{i} *held fixed and* $\mathrm{diam}(\Lambda^{\mathrm{I}}) \to \infty$, *where* $\mathrm{diam}(\Lambda^{\mathrm{I}})$ *is the diameter of the outer boundary* Λ^{I}. *If* $\boldsymbol{u} \in \mathcal{U}^{\star}$, *then* $\boldsymbol{u}^{\mathrm{I}} \to \boldsymbol{0}$ *as* $\mathrm{diam}(\Lambda^{\mathrm{I}}) \to \infty$ *such that*

$$\begin{aligned} \lim_{\mathrm{diam}(\Lambda^{\mathrm{I}}) \to 0} \boldsymbol{u}^{\mathrm{c}} &= \lim_{\mathrm{diam}(\Lambda^{\mathrm{I}}) \to 0} \Big(\mathcal{F}^{\mathrm{c/i+}}[\boldsymbol{u}^{\mathrm{i+}}] - \mathcal{G}^{\mathrm{c/i+}}[\boldsymbol{f}^{\mathrm{i+}}] + \mathcal{F}^{\mathrm{c/I+}}[\boldsymbol{u}^{\mathrm{I+}}] - \mathcal{G}^{\mathrm{c/I+}}[\boldsymbol{f}^{\mathrm{I+}}] \Big) \\ &= \mathcal{F}^{\mathrm{c/i+}}[\boldsymbol{u}^{\mathrm{i+}}] - \mathcal{G}^{\mathrm{c/i+}}[\boldsymbol{f}^{\mathrm{i+}}] \end{aligned} \tag{2.91}$$

which is nothing but (2.53). *However, if* $\boldsymbol{u} \notin \mathcal{U}^{\star}$ *the second term does not necessarily go to zero and therefore depends on the lattice Green function (which is only unique up to a rigid body motion).*

Remark 2.5.5. *For large computational domains the outer boundary contains substantially more degrees of freedom than the inner boundary. Therefore it might be beneficial to further reduce the solution vector in* Λ^{I} *(e.g. by interpolation). However, this is not carried out here.*

Sinclair's method for bounded problems

Using the previous results Sinclair's method can be modified for the application to bounded problems. This is done by computing the solution for a bounded problem subject to the inhomogeneous (body) forces. Again, the idea is to first compute a solution of an infinite problem and subsequently superimpose the solution of an auxiliary problem which accounts for the displacements on the outer boundary. For this purpose step **[S2]** from Figure 2.3 is reconsidered in the following. To account for the outer boundary conditions the displacements due to the inhomogeneous forces, now denoted by $\boldsymbol{u}^{\infty}$ for clarity, are also computed on $\mathit{\Lambda}^{\mathrm{I}}$. Subsequently, a corrective problem is solved via (2.87) using $\boldsymbol{u}^{\mathrm{I}} - \boldsymbol{u}^{\mathrm{I},\infty}$ as boundary condition. The total pad displacements are then obtained by adding $\boldsymbol{u}^{\mathrm{p},\infty}$ and the contribution due to the corrective problem.

The steps which eventually replace step **[S2]** for bounded problems are summarized as follows:

[S2.1] First, compute the inhomogeneous forces and the displacements on the outer boundary corresponding to the infinite problem according to

$$\boldsymbol{f}^{\mathrm{i+}}_{\mathrm{inh},i} = \mathcal{L}_{\mathrm{h}}^{\mathrm{i+/i}}[\mathit{\Delta}\boldsymbol{u}^{\mathrm{i}}_{\mathrm{ah},i-2}], \qquad \boldsymbol{u}_i^{\mathrm{I},\infty} = \boldsymbol{u}_{i-1}^{\mathrm{I},\infty} - \mathcal{G}^{\mathrm{I/i+}}[\boldsymbol{f}^{\mathrm{i+}}_{\mathrm{inh},i}]. \tag{2.92}$$

[S2.2] Solve the corrective problem with boundary condition $\boldsymbol{u}^{\mathrm{I}} - \boldsymbol{u}_i^{\mathrm{I},\infty}$ in $\mathit{\Lambda}^{\mathrm{I}}$ via (2.87) with respect to $\hat{\boldsymbol{u}}_i^{\mathrm{I+}}$ and compute the pad displacements according to

$$\hat{\boldsymbol{u}}_i^{\mathrm{p}} = \mathcal{F}^{\mathrm{p/I+}}[\hat{\boldsymbol{u}}_i^{\mathrm{I+}}] - \mathcal{G}^{\mathrm{p/I+}}[\mathcal{L}_{\mathrm{h}}^{\mathrm{I+/I}}[\boldsymbol{u}^{\mathrm{I}} - \boldsymbol{u}_i^{\mathrm{I},\infty}]]. \tag{2.93}$$

[S2.3] Compute the *total* pad displacements by superimposing both solutions

$$\boldsymbol{u}_i^{\mathrm{p}} = \boldsymbol{u}_i^{\mathrm{p},\infty} + \hat{\boldsymbol{u}}_i^{\mathrm{p}}, \qquad \text{with} \quad \boldsymbol{u}_i^{\mathrm{p},\infty} = \boldsymbol{u}_{i-1}^{\mathrm{p},\infty} - \mathcal{G}^{\mathrm{p/i+}}[\boldsymbol{f}^{\mathrm{i+}}_{\mathrm{inh},i}]. \tag{2.94}$$

2.6 Implementation of the discrete boundary element method

2.6.1 Algebraic discrete boundary element method

The algebraic representation of the DBEM, introduced in the previous section, is now derived. The main purpose of this section is to give an illustration of the structure of the corresponding system matrices. Their construction comes along with prohibitive computational cost which precludes an exact representation. Nevertheless a two-level approximation is introduced in Section 2.6.2 and 2.6.3 which permits an approximative implicit representation which preserves their structure while being computationally efficient. The focus is exclusively on the symmetric DBEM for the infinite problem in the remainder of this chapter.

For the sake of clarity the following relations between the differential operators and their matrix representations are defined

$$\mathcal{L} \leftrightarrow \hat{L}, \qquad \mathcal{G} \leftrightarrow \hat{G}, \qquad \mathcal{F} \leftrightarrow \hat{F}. \tag{2.95}$$

The algebraic form of the abstract problem (2.70) then reads: find $\hat{u}^{\mathrm{i}} \in \mathbb{R}^{dN^{\mathrm{i}}}$ such that

$$(\hat{I} - \hat{F}^{\mathrm{i/i}})\hat{u}^{\mathrm{i}} = -\hat{G}^{\mathrm{i/i}}\hat{\hat{f}}^{\mathrm{i}}, \qquad \hat{\hat{f}}^{\mathrm{i}} \in \mathbb{R}^{dN^{\mathrm{i}}},\ \hat{F}^{\mathrm{i/i}} \in \mathbb{R}^{dN^{\mathrm{i}} \times dN^{\mathrm{i}}},\ \hat{G}^{\mathrm{i/i}} \in \mathbb{R}^{dN^{\mathrm{i}} \times dN^{\mathrm{i}}} \tag{2.96}$$

and the update equation for the pad displacement follows as

$$\hat{u}^{\mathrm{p}} = \hat{F}^{\mathrm{p/i}}\hat{u}^{\mathrm{i}} - \hat{G}^{\mathrm{p/i}}\hat{\hat{f}}^{\mathrm{i}}, \qquad \hat{u}^{\mathrm{p}} \in \mathbb{R}^{dN^{\mathrm{p}}},\ \hat{F}^{\mathrm{p/i}} \in \mathbb{R}^{dN^{\mathrm{p}} \times dN^{\mathrm{i}}},\ \hat{G}^{\mathrm{p/i}} \in \mathbb{R}^{dN^{\mathrm{p}} \times dN^{\mathrm{i}}}. \tag{2.97}$$

The corresponding system matrices can be written as

$$\begin{aligned}
\hat{F}^{\mathrm{i/i}} &= \begin{pmatrix} \boldsymbol{F}(\boldsymbol{\xi}_1 - \boldsymbol{\eta}_1) & \cdots & \boldsymbol{F}(\boldsymbol{\xi}_1 - \boldsymbol{\eta}_{N^{\mathrm{i}}}) \\ \vdots & \ddots & \vdots \\ \boldsymbol{F}(\boldsymbol{\xi}_{N^{\mathrm{i}}} - \boldsymbol{\eta}_1) & \cdots & \boldsymbol{F}(\boldsymbol{\xi}_{N^{\mathrm{i}}} - \boldsymbol{\eta}_{N^{\mathrm{i}}}) \end{pmatrix}, \\
\hat{G}^{\mathrm{i/i}} &= \begin{pmatrix} \boldsymbol{G}^{\mathrm{lgf}}(\boldsymbol{\xi}_1 - \boldsymbol{\eta}_1) & \cdots & \boldsymbol{G}^{\mathrm{lgf}}(\boldsymbol{\xi}_1 - \boldsymbol{\eta}_{N^{\mathrm{i}}}) \\ \vdots & \ddots & \vdots \\ \boldsymbol{G}^{\mathrm{lgf}}(\boldsymbol{\xi}_{N^{\mathrm{i}}} - \boldsymbol{\eta}_1) & \cdots & \boldsymbol{G}^{\mathrm{lgf}}(\boldsymbol{\xi}_{N^{\mathrm{i}}} - \boldsymbol{\eta}_{N^{\mathrm{i}}}) \end{pmatrix}, \\
\hat{F}^{\mathrm{p/i}} &= \begin{pmatrix} \boldsymbol{F}(\boldsymbol{\xi}_1 - \boldsymbol{\eta}_1) & \cdots & \boldsymbol{F}(\boldsymbol{\xi}_1 - \boldsymbol{\eta}_{N^{\mathrm{i}}}) \\ \vdots & \ddots & \vdots \\ \boldsymbol{F}(\boldsymbol{\xi}_{N^{\mathrm{p}}} - \boldsymbol{\eta}_1) & \cdots & \boldsymbol{F}(\boldsymbol{\xi}_{N^{\mathrm{p}}} - \boldsymbol{\eta}_{N^{\mathrm{i}}}) \end{pmatrix}, \\
\hat{G}^{\mathrm{p/i}} &= \begin{pmatrix} \boldsymbol{G}^{\mathrm{lgf}}(\boldsymbol{\xi}_1 - \boldsymbol{\eta}_1) & \cdots & \boldsymbol{G}^{\mathrm{lgf}}(\boldsymbol{\xi}_1 - \boldsymbol{\eta}_{N^{\mathrm{i}}}) \\ \vdots & \ddots & \vdots \\ \boldsymbol{G}^{\mathrm{lgf}}(\boldsymbol{\xi}_{N^{\mathrm{p}}} - \boldsymbol{\eta}_1) & \cdots & \boldsymbol{G}^{\mathrm{lgf}}(\boldsymbol{\xi}_{N^{\mathrm{p}}} - \boldsymbol{\eta}_{N^{\mathrm{i}}}) \end{pmatrix}.
\end{aligned} \tag{2.98}$$

These matrices are dense due to the long-range nature of the LGF. It is thus not practical to build them exactly, especially for larger problems, i.e. when $N^{\mathrm{i}} \in \mathcal{O}(10^4)$ or higher, which is usually the limit for the classical BEM on desktop computers. In the following two necessary and sufficient approximations are introduced to build (2.98) without losing too much accuracy. That is, approximations of (2.96) and (2.97) are sought-after such that the solution of the atomistic problem is not affected, i.e. the elasticity error dominates.

2.6.2 Approximation of the lattice Green functions

In practice, the LGF has to be computed numerically (c.f. Appendix A.4.1). With the current self-written implementation the computation of $\boldsymbol{G}^{\mathrm{lgf}}$ at ≈ 2000 lattice points takes around one day for the 3d problem from Appendix A.4.2 with an estimated relative error between 10^{-7} and 10^{-10}. It becomes immediately clear that building any of the matrices in (2.98) becomes prohibitive for larger problems. Nevertheless it is worth noting that more efficient methods to compute the LGF exist, i.e. by only meshing the irreducible part of the Brillouin zone (c.f. Monkhorst and Pack, 1976) accompanied with a partial analytic integration to eliminate increasing periodic oscillations when computing the LGF at distant points which otherwise requires a finer discretization (see Trinkle, 2008). It might also be possible to integrate the LGF partially analytically in one dimension by using the residue theorem from complex calculus (Martinsson, 2002). However, these methods are not considered in the current implementation and the author is not aware of any open-source implementations thereof.

In any case it seems simpler to replace the LGF with an analytic form which is cheap to compute outside a well-chosen cut-off radius r_{cut}. An obvious choice is the continuum Green function. Thus, the approximate LGF is defined as

$$\tilde{\boldsymbol{G}}^{\mathrm{lgf}}(\boldsymbol{\xi}-\boldsymbol{\eta}) = \begin{cases} \boldsymbol{G}^{\mathrm{lgf}}(\boldsymbol{\xi}-\boldsymbol{\eta}) & \text{if } r \leq r_{\mathrm{cut}}, \\ \boldsymbol{G}^{\mathrm{cgf}}(\boldsymbol{\xi}-\boldsymbol{\eta}) & \text{else,} \end{cases} \qquad \text{where} \quad r = \|\boldsymbol{\xi}-\boldsymbol{\eta}\|. \tag{2.99}$$

In practice the computed values of the LGF are stored within the cut-off radius in a external file such that it can be looked up during the building process and does not have to be re-computed each time when a new geometry is considered. The question then arises: what is the error introduced in (2.97) due to this approximation. To estimate the error use is made of the following result obtained by Trinkle (2008) which states that relative difference between $\boldsymbol{G}^{\mathrm{lgf}}$ and $\boldsymbol{G}^{\mathrm{cgf}}$ scales as

$$\frac{\|\boldsymbol{G}^{\mathrm{lgf}} - \boldsymbol{G}^{\mathrm{cgf}}\|_{\mathrm{fro}}}{\|\boldsymbol{G}^{\mathrm{cgf}}\|_{\mathrm{fro}}} \leq C r^{-2} \tag{2.100}$$

for some $C > 0$ which is independent of r. The error introduced in (2.97) is a direct consequence of this result and is manifested in the following proposition:

Proposition 3. *The error in the pad displacements* (2.97) *induced by the approximation* (2.99) *is bounded by*

$$\|\hat{u}^{\mathrm{p}} - \hat{\tilde{u}}^{\mathrm{p}}\| \lesssim r_{\mathrm{cut}}^{-(d+1)/2} (\log r_{\mathrm{cut}})^{3-d}. \tag{2.101}$$

Proof. The proof is subjected to Appendix A.4.3. □

Proposition 3 will prove valuable in Section 2.7.4 for the validation of the proposed method.

Numerical experiments have shown that the approximation (2.99) does not influence the structure of $\hat{G}^{\mathrm{i}/\mathrm{i}}$ with respect to symmetry and positivity such that (2.96) is unconditionally well-posed. This statement can presumably be made more rigorous but this is out of scope of the current work.

2.6.3 Data sparse approximation of the boundary matrices

Solving the linear system (2.96) requires the construction of dense matrices of the order $\mathcal{O}((N^{\mathrm{i}})^2)$ which is prohibitive for the problem sizes which are aimed for. For example, a single layered boundary matrix for a system containing $\approx$1 mio. atoms requires roughly 250 GB of memory. Moreover, the boundary matrices in (2.98) may consist of several layers (e.g. $\hat{G}^{\mathrm{p/i}}$) depending on the nonlocality of the interatomic potential such that the memory consumption can quickly increase to several terabytes. A more appropriate way to store the boundary matrices can be achieved with data-sparse low-rank representations. For this purpose the framework of hierarchical matrices (henceforth $\mathscr{H}$-matrices) by Hackbusch (1999, 2015) is used in the following. $\mathscr{H}$-matrices provide an efficient means for approximating boundary matrices for *general* interfaces with a complexity of $\mathcal{O}(\log(N)N)$. Furthermore, an "$\mathscr{H}$-arithmetic" for linear algebraic operations such as matrix-vector and matrix-matrix multiplications as well as matrix factorization is readily available. This is demonstrated in the following.

Recall that for any matrix $\hat{A} \in \mathbb{R}^{M \times N}$ there exist orthogonal matrices $\hat{U} \in \mathbb{R}^{M \times O}$ and $\hat{V} \in \mathbb{R}^{N \times O}$, with $O := \min(M, N)$, and a diagonal matrix $\hat{S} \in \mathbb{R}^{O \times O}$ such that

$$\hat{A} = \hat{U}\hat{S}\hat{V}^{\mathsf{T}} = \sum_{i=1}^{O} \sigma_i(\hat{u}_i \otimes \hat{v}_i), \tag{2.102}$$

where the σ_i's are the entries of $\hat{S}$, i.e. the singular values of $\hat{A}$, and $\hat{u}_i$ and $\hat{v}_i$ are the i-th column vectors of $\hat{U}$ and $\hat{V}$, respectively. Assume that $\sigma_i > \sigma_{i+1}$, then the best rank-k approximation (:= low-rank approximation) of $\hat{A}$ with respect to $\| \bullet \|_{\mathrm{fro}}$ is given by the Eckart-Young theorem (Eckart and Young, 1936)

$$\hat{A}^k = \sum_{i=1}^{k} \sigma_i(\hat{u}_i \otimes \hat{v}_i) \qquad \text{such that} \quad \|\hat{A} - \hat{A}^k\|_{\mathrm{fro}} = \sum_{i=k+1}^{O} \sigma_i < \epsilon. \tag{2.103}$$

Using this format, the complexity of linear algebraic operations may simplify considerably. For example, consider the matrix-vector multiplication $\hat{A}^k\hat{b}$. In order to compute the matrix-vector product the matrix $\hat{A}^k$ never has to be stored explicitly since

$$\hat{A}^k\hat{b} = \left(\sum_{i=1}^{k} \sigma_i(\hat{u}_i \otimes \hat{v}_i)\right)\hat{b} = \sum_{i=1}^{k} \sigma_i(\hat{u}_i^{\mathsf{T}} \cdot \hat{b})\hat{v}_i, \tag{2.104}$$

that is, only the k column vectors $\hat{u}_i$ and $\hat{v}_i$ have to be stored (assuming that the singular values are pre-multiplied with either $\hat{u}_i$ or $\hat{v}_i$). In addition, the necessary number of operations reduces from $\mathcal{O}(MN)$ to $\mathcal{O}(k(N + M))$ when compared to the standard representation. It can easily be seen that the representation via outer products becomes very efficient if $k \ll O$.

Usually an entire matrix can not be represented directly with a rank-k approximation, in particular matrices which define a linear system such as (2.96) — which necessarily must have full rank. Nevertheless, there exist several approaches in order to determine admissible low-rank sub-blocks in these matrices. Here, the framework of **hierarchical matrices** ($\mathscr{H}$-matrices) due to Hackbusch (1999); Bebendorf (2009) is adopted which allows for a flexible block-wise partitioning depending on a particular interface geometry, unlike other methods which impose a fixed block structure (c.f. Martinsson, 2011). This is necessary for the problem considered here because a fixed block partitioning does usually not reveal the low-rank structure of the considered matrices, except for some special cases such as rectangular geometries in two dimensions. Following Bebendorf (2009), admissible blocks can be identified using the criterion

$$\min\left(\mathrm{diam}(t), \mathrm{diam}(s)\right) \leq \eta \mathrm{dist}(t, s), \tag{2.105}$$

where η is a free parameter and t, s are subsets of Λ but also refer to the row and column indices of the matrix. Here, $\mathrm{diam}(\bullet)$ denotes the diameter of a single block and $\mathrm{dist}(\bullet)$ is the distance between them. A physical interpretation of (2.105) is given below. Suppose that the interface atoms in s and t are close-by as shown in Figure 2.5 (a). For an increasing distance between both sub-blocks the difference in the interaction of two elements in s with respect to all elements in t becomes sufficiently homogeneous for asymptotically smooth kernels (e.g. $\propto \log r$, $\propto 1/r$ etc., where r is the distance between the application and the source point). Thus, the corresponding rows of the matrix are nearly linear dependent and a good low-rank approximation is likely to exist (see Hodapp, 2017, for a two-dimensional example). Another elucidating example is given in (Bebendorf, 2009, Example 1.12, p. 22).

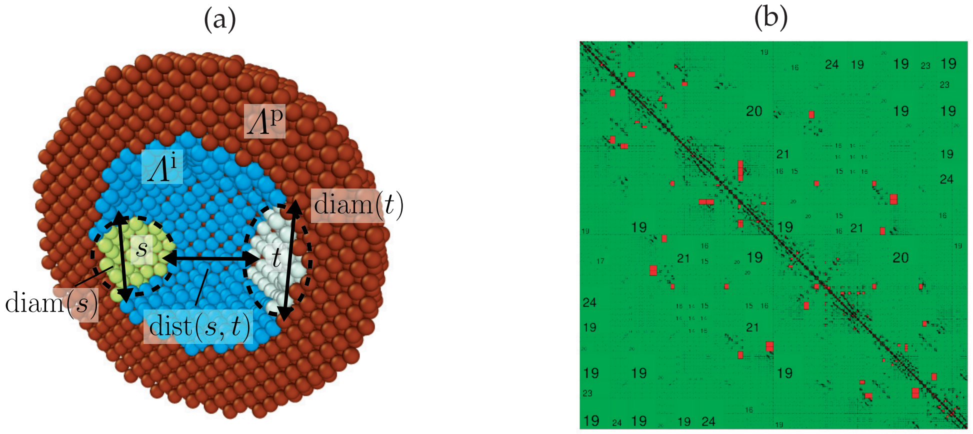

Figure 2.5: (a) Interface and pad region Λ^{i} and Λ^{p} of a spherical computational domain ($\Lambda^{\mathrm{a}} \setminus \Lambda^{\mathrm{i}}$ not shown). (b) A realistic hierarchical partitioning for the matrix corresponding to the last value in Figure 2.6, where $3N^{\mathrm{i}} = 263718$

The potential savings made by replacing a full matrix with an $\mathscr{H}$-matrix can be summarized as follows: consider a square matrix of size N defined on a regular grid. By refining the grid — or equivalently by increasing the size of the domain — the complexity of relevant matrix operations reduces as (c.f. Hackbusch, 1999; Bebendorf, 2009; Hackbusch, 2015)

$$\mathcal{O}(N^{\alpha}) \longrightarrow \mathcal{O}(N \log{(N)}^{\alpha}), \tag{2.106}$$

where the parameter α depends on the type of operation, e.g. $\alpha = 1$ for the storage requirements or matrix-vector multiplications and $\alpha = 2$ for matrix-matrix multiplications. The precise pre-factors depend largely on the geometry of the interface.

For the numerical examples *Another software library on Hierarchical Matrices for Elliptic Differential equations* (AHMED) from (Bebendorf, 2009) is used. The superior performance of the hierarchical approximation in the context of integral equations has been proven in many publications on the topic (e.g. Börm et al., 2003; Bebendorf and Kriemann, 2005; Brunner et al., 2010). For an overview of various numerical examples the reader is referred to the book of Bebendorf (2009). Here, the main focus is on the memory consumption of the matrices in (2.98) for three dimensional problems.[6] A spherically-shaped atomistic region with variable radius is selected as a representative domain (Figure 2.5 (a)). The memory consumption of the matrix $\hat{G}^{\mathrm{i/i}}$ is shown in Figure 2.6. On a desktop computer with 16 GB random-access memory (RAM), building a full matrix is only feasible up to $\approx$30000 degrees of freedom (which corresponds to $\approx$10000 real atoms) while the hierarchical memory cost shows the favorable $\log(N^{\mathrm{i}})N^{\mathrm{i}}$ scaling, thus allowing for considerably larger atomistic regions. For example, the last value in Figure 2.6 corresponds to $N^{\mathrm{a}} \approx 2.1$ mio. Of course, for the full problem the other matrices from (2.96) and (2.97) have to be built as well, though, thanks to the block-wise partitioning, $\mathscr{H}$-matrices can be distributed on several computing nodes such that the problem becomes feasible on moderate size clusters (which nowadays usually contain 64-128 GB RAM per node).

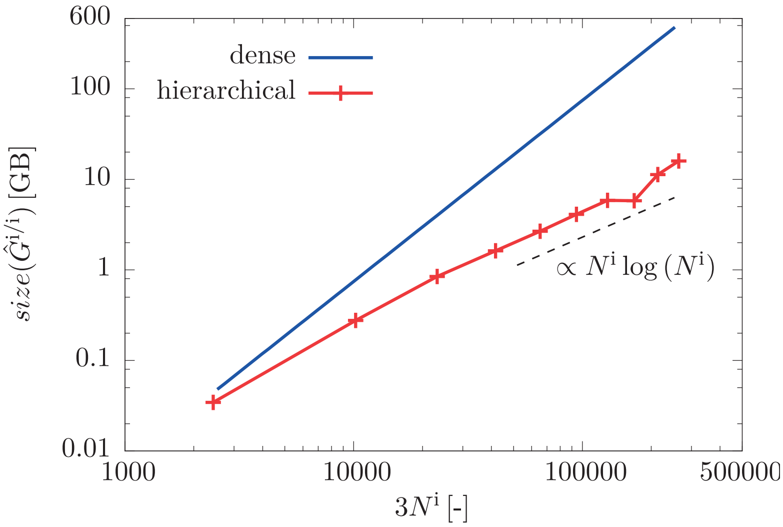

Figure 2.6: Memory consumption for the matrix $\hat{G}^{\mathrm{i/i}}$ when using the hierarchical approximation, opposed to the dense version

---

[6] In two dimensions memory consumption is usually not a problem since the number of degrees of freedom at the boundary scale approximately with $\mathcal{O}(\sqrt{N^{\mathrm{a}}})$

For the sake of clarity the hierarchical partitioning of $\hat{G}^{\mathrm{i}/\mathrm{i}}$ for the last value in Figure 2.6 ($3N^{\mathrm{i}} = 263718$) is shown in Figure 2.5 (b). The numbers in the green sub-blocks denote their rank and the red blocks in the vicinity of the diagonal denote dense parts, i.e. they do not contain any approximation. That is, the block on the lower left which has a size of roughly 20000×20000 is approximated with a matrix of rank 19. Thus the ratio of the memory consumption for the dense and the $\mathscr{H}$-matrix is ≈ 500 for this particular sub-block.

2.7 Iterative solution procedures for the coupled problem

2.7.1 Staggered schemes

In this section three algorithms to solve the coupled problem (2.21) are described. First, two staggered schemes are presented which are widely used in the A/C coupling community, mainly due to their simplicity and less time-consuming implementation.

The first algorithm which is considered is a classical multiplicative alternating Schwarz-type algorithm for Dirichlet-type problems. This algorithm has been used in (Li, 2009) to solve (2.21). Other authors, e.g. Parks et al. (2008), have used this type of algorithm for finite continuum domains, with or without overlapping subdomains. It is well-known from the theory of domain decomposition methods that this algorithm exhibits unfavorable convergence properties (c.f. Quarteroni and Valli, 1999). Usually alternating Schwarz methods are rarely used as single solvers but rather as preconditioners or, if they do, with improved interface transmission conditions ("optimized Schwarz methods"). Here, primary aim is to emphasize the need for more efficient schemes which preserve the necessary efficiency in comparison with a fully atomistic problem (see Section 2.7.4). The procedure in Algorithm 1 is standard. First, an initial guess is defined and the pad atoms are "frozen", followed by a minimization of the atomistic energy with respect to all real atoms. Subsequently the atomistic problem is held fixed and the outer problem is solved as done in Section 2.5.2 (step 1-3), that is, the linear system (2.96) is first solved with respect to $\hat{\hat{f}}^{\mathrm{i}}_{k+1}$ which is subsequently used to update the pad atoms. The previous steps are then repeated upon convergence. Convergence is obtained when force vector in Λ^{a} is minimal with respect to some properly chosen norm.

Next, a variant of Sinclair's algorithm is presented. To the author's best knowledge all implementations of this algorithm, e.g. by Rao et al. (1998); Woodward and Rao (2001), update the entire computational domain, i.e. pad **and** real atoms, using the LGF applied to the inhomogeneous point forces at the interface (Rao, 2017). While being reasonable for the considered problem sizes — the above-named authors considered primarily isolated dislocations in comparatively small domains — this becomes prohibitive for larger problems, especially in view of the analysis in Section 2.6.3. In Section 2.4 it was shown that updating the harmonic solution in the atomistic domain merely serves as an

Algorithm 1: Staggered Schwarz-type algorithm

```
Input: Initial guess $\hat{u}_0$
$k \leftarrow 1$;
repeat
    $\hat{u}^{\mathrm{a}}_{k+1} \leftarrow \min_{\hat{v}^{\mathrm{a}}} \Pi^{\mathrm{a}}(\hat{v}^{\mathrm{a}}; \hat{u}^{\mathrm{p}}_{k})$;            // solve atomistic problem
    $\hat{\hat{u}}^{\mathrm{i}}_{k+1} \leftarrow (\hat{I} - \hat{F}^{\mathrm{i/i}})\hat{u}^{\mathrm{i}}_{k+1}$;            // compute rhs of (2.96)
    $\hat{\hat{f}}^{\mathrm{i}}_{k+1} \leftarrow (\hat{G}^{\mathrm{i/i}})^{-1}\hat{\hat{u}}^{\mathrm{i}}_{k+1}$;            // solve the linear system (2.96)
    $\hat{u}^{\mathrm{p}}_{k+1} \leftarrow \hat{F}^{\mathrm{p/i}}\hat{u}^{\mathrm{i}}_{k+1} + \hat{G}^{\mathrm{p/i}}\hat{\hat{f}}^{\mathrm{i}}_{k+1}$;    // update pad atoms according to (2.97)
    if $\|\hat{f}^{\mathrm{a}}(\hat{u}_{k+1}) - \hat{f}^{\mathrm{ext}}\| < TOL$ then
        stop (repeat);
    else
        $k \leftarrow k + 1$;
    end
end
Output: Final state $\hat{u}_{k+1}$
```

initial guess and neglecting it does not alter the final solution (2.36). Omitting the initial guess has practical consequences since the matrix $\hat{G}$ corresponding to (2.44) does not need to be defined on Λ^{a}. Though the construction of the matrix $\hat{G}^{\mathrm{p/i+}}$ is still expensive, its storage requirement scales **only** with the number of boundary atoms and can further be approximated using $\mathscr{H}$-matrices as shown in the previous section. Algorithm 2 proceeds similar to the Schwarz method. After imposing an initial guess the atomistic problem is solved with respect to the real atoms. Then the inhomogeneous forces which have build up in $\Lambda^{\mathrm{i+}}$ are computed and $\hat{G}^{\mathrm{p/i+}}$ is applied to update the pad atoms. In comparison to the Schwarz method, the implementation is even simpler since only a single matrix-vector multiplication has to be computed to update the pad atoms — in comparison to a linear system which has to be solved every iteration in Algorithm 1.

In the following the alternating Schwarz and Sinclair's method are referred to as `Schwarz` and `Sinclair`, respectively.

2.7.2 Monolithic stabilized Newton-GMRes solver

Despite their simplicity, staggered algorithms usually converge rather slow. Therefore a monolithic scheme is proposed which iterates on *all* unknowns simultaneously. Recent analyses of force-based A/C coupling methods have shown that the coupled problem can be solved accurately using generalized Krylov subspace methods such as generalized minimal residual (GMRes) methods. The method was applied in (Dobson et al., 2011) for a linearized problem in one dimension and here a generalization to the three-dimensional

Algorithm 2: Staggered Sinclair-type algorithm

Input: Initial guess $\hat{u}_0$

```
$k \leftarrow 1$;
repeat
    $\hat{u}^{\mathrm{a}}_{k+1} \leftarrow \min_{\hat{v}^{\mathrm{a}}} \mathit{\Pi}^{\mathrm{a}}(\hat{v}^{\mathrm{a}}; \hat{u}^{\mathrm{p}}_k)$;          // solve atomistic problem
    $\hat{f}^{\mathrm{i+}}_{\mathrm{inh},k+1} \leftarrow \hat{L}^{\mathrm{i+/i}} \hat{u}^{\mathrm{i}}_{k+1} + \hat{L}^{\mathrm{i+/p}} \hat{u}^{\mathrm{p}}_k$;   // compute inhomogeneous forces
    $\hat{u}^{\mathrm{p}}_{k+1} \leftarrow \hat{G}^{\mathrm{p/i+}} \hat{f}^{\mathrm{i+}}_{\mathrm{inh},k+1}$;              // update pad atoms
    if $\|\hat{f}^{\mathrm{a}}(\hat{u}_{k+1}) - \hat{f}^{\mathrm{ext}}\| < TOL$ then
        stop (repeat);
    else
        $k \leftarrow k + 1$;
    end
end
```

Output: Final state $\hat{u}_{k+1}$

nonlinear case inside a Newton-Raphson iteration is presented. Nevertheless, it should be noted that a similar strategy was pursued by Shilkrot et al. (2004) in two dimensions but their solver is based on a variant of a conjugate gradient method which is likely to be unstable — even far from any physical instabilities (c.f. Dobson et al., 2011).

In general the roots $\hat{\tilde{x}}$ of a vector-valued vector function $\hat{r}(\hat{x})$ are sought-after, i.e. $\hat{r}(\hat{\tilde{x}}) = \hat{0}$. Recall that the Newton method reads in the k-th iteration as

$$\hat{J}_k \mathit{\Delta} \hat{x}_k = -\hat{r}(\hat{x}_k), \tag{2.107}$$

with the Jacobian matrix $\hat{J}_k = \nabla_x \hat{r}(\hat{x}_k)$ and $\mathit{\Delta}\hat{x}_k = \hat{x}_{k+1} - \hat{x}_k$.

For the atomistic/DBEM problem the Jacobian matrix and the solution vector are given by

$$\hat{J}_k = \left(\begin{array}{c:c:c:c} \multicolumn{2}{c:}{\hat{L}^{\mathrm{a/a}}(\hat{u}_k)} & \hat{0} & \hat{L}^{\mathrm{a/p}}(\hat{u}_k) \\ \hdashline \hat{0} & \hat{I} - \hat{F}^{\mathrm{i/i}} & \hat{G}^{\mathrm{i/i}} & \hat{0} \\ \hdashline \hat{0} & -\hat{F}^{\mathrm{p/i}} & \hat{G}^{\mathrm{p/i}} & \hat{I} \end{array}\right), \qquad \hat{x}_k = \left(\begin{array}{c} \hat{u}^{\mathrm{a\backslash i}}_k \\ \hdashline \hat{u}^{\mathrm{i}}_k \\ \hdashline \hat{\tilde{f}}^{\mathrm{i}}_k \\ \hdashline \hat{u}^{\mathrm{p}}_k \end{array}\right) \tag{2.108}$$

which can readily be deduced from (2.96) and (2.97). Here, the matrix $\hat{L}^{\mathrm{a/a}}(\hat{u}_k)$ is the linearized Hessian of the atomistic problem and $\hat{L}^{\mathrm{a/p}}(\hat{u}_k)$ is the coupling matrix. Both $\hat{L}^{\mathrm{a/a}}$ and $\hat{L}^{\mathrm{a/p}}$ depend on the current solution $\hat{x}_k$.

Instead of solving the coupled problem as it is a slightly different approach is pursued in the following which is usually more convenient for the integration into existing atomistic computer codes. In order to exploit the linearity of the continuum problem the procedure will be as follows: first, the continuum degrees of freedom (i.e. the vectors $\mathit{\Delta}\hat{\hat{f}}_k^{\mathrm{i}}$ and $\mathit{\Delta}\hat{u}_k^{\mathrm{p}}$) are condensed out such that one can write

$$\begin{aligned}
&\hat{L}^{\mathrm{a/a}}(\hat{u}_k)\mathit{\Delta}\hat{u}_k^{\mathrm{a}} + \hat{L}^{\mathrm{a/p}}(\hat{u}_k)\mathit{\Delta}\hat{u}_k^{\mathrm{p}} \\
&\qquad = \hat{L}^{\mathrm{a/a}}(\hat{u}_k)\mathit{\Delta}\hat{u}_k^{\mathrm{a}} + \hat{L}^{\mathrm{a/p}}(\hat{u}_k)(\hat{F}^{\mathrm{p/i}}\mathit{\Delta}\hat{u}_k^{\mathrm{i}} - \hat{G}^{\mathrm{p/i}}\mathit{\Delta}\hat{\hat{f}}_k^{\mathrm{i}}) \\
&\qquad = \hat{L}^{\mathrm{a/a}}(\hat{u}_k)\mathit{\Delta}\hat{u}_k^{\mathrm{a}} + \hat{L}^{\mathrm{a/p}}(\hat{u}_k)(\hat{F}^{\mathrm{p/i}} - \hat{G}^{\mathrm{p/i}}(\hat{G}^{\mathrm{i/i}})^{-1}(\hat{F}^{\mathrm{i/i}} - \hat{I}))\mathit{\Delta}\hat{u}_k^{\mathrm{i}}.
\end{aligned} \tag{2.109}$$

The reduced Jacobian matrix is then the Schur complement of the lower right 2x2 block matrix in $\hat{J}_k$. This can be written as

$$\hat{J}_k^{\mathrm{schur}} = \begin{pmatrix} \hat{L}^{\mathrm{a\backslash i'/a\backslash i}} & \hat{L}^{\mathrm{a\backslash i'/i}} \\ \hat{L}^{\mathrm{i'/a\backslash i}} & \hat{\hat{L}}^{\mathrm{i'/i}} \end{pmatrix}, \tag{2.110}$$

with

$$\hat{\hat{L}}^{\mathrm{i'/i}} = \hat{L}^{\mathrm{i'/p}}(\hat{u}_k)(\hat{F}^{\mathrm{p/i}} - \hat{G}^{\mathrm{p/i}}(\hat{G}^{\mathrm{i/i}})^{-1}(\hat{F}^{\mathrm{i/i}} - \hat{I})), \tag{2.111}$$

where the index i' refers to the set of atoms which interact with the pad atoms (note that $\mathit{\Lambda}^{\mathrm{i}} \subset \mathit{\Lambda}^{\mathrm{i}'}$). The Newton iteration for the Schur complement system can now be stated

$$\hat{J}_k^{\mathrm{schur}}\mathit{\Delta}\hat{u}_k^{\mathrm{a}} = -\hat{f}^{\mathrm{a}}(\hat{u}_k) + \hat{f}^{\mathrm{ext}}. \tag{2.112}$$

In practice, building $\hat{J}_k^{\mathrm{schur}}$ is not necessary since iterative solvers only require the action of $\hat{J}_k^{\mathrm{schur}}$ on a vector. Thereby, the matrix-vector product $\hat{\hat{L}}^{\mathrm{i'/i}}\mathit{\Delta}\hat{u}_k^{\mathrm{i}}$ requires a more detailed discussion since $\hat{\hat{L}}^{\mathrm{i'/i}}$ requires the inversion of $\hat{G}^{\mathrm{i/i}}$. In practice $(\hat{G}^{\mathrm{i/i}})^{-1}$ is never build explicitly. In lieu thereof the right hand side vector $\hat{\hat{u}} = (\hat{F}^{\mathrm{i/i}} - \hat{I})\mathit{\Delta}\hat{u}_k^{\mathrm{i}}$ is computed first. Subsequently the linear system $\hat{\hat{f}}^{\mathrm{i}} = (\hat{G}^{\mathrm{i/i}})^{-1}\hat{\hat{u}}$ is solved using a factorized representation of $\hat{G}^{\mathrm{i/i}}$ such that the solution $\hat{\hat{f}}_k^{\mathrm{i}}$ can be obtained by an efficient forward/backward substitution. Factorizing $\hat{G}^{\mathrm{i/i}}$ is possible within the framework of $\mathscr{H}$-matrices with an arithmetic complexity of $\mathcal{O}(N^{\mathrm{i}}\log{(N^{\mathrm{i}})^2})$. The pad displacements then follow by another matrix-vector multiplication (see Algorithm 1, line 6).

Furthermore, none of the $\hat{L}$-operators are built in practice. This is because these matrices would be rather large and dense (since the atomistic problem ins nonlocal). Usually the action of the Jacobian on a vector can be conveniently approximated via forward finite differences (c.f. Knoll and Keyes, 2004)

$$\hat{J}_k^{\mathrm{schur}}\mathit{\Delta}\hat{u}_k^{\mathrm{a}} \approx \frac{\hat{f}^{\mathrm{a}}(\hat{u}_k^{\mathrm{a}} + \varepsilon\mathit{\Delta}\hat{u}_k^{\mathrm{a}}; \hat{u}_k^{\mathrm{p}}) - \hat{f}^{\mathrm{a}}(\hat{u}_k)}{\varepsilon}. \tag{2.113}$$

That is, first, the pad displacements are updated using the procedure described above in order to subsequently evaluate the forces in the atomistic domain to compute the approximation (2.113).

In order to solve the linearized system (2.112) a Newton-GMRes solver is selected since the problem is nonlinear and possibly always indefinite (due to the non-symmetric force-interaction law and the atomistic-DBEM coupling). A GMRes solver has already been successfully applied for a linear one dimensional toy problem (Dobson et al., 2011). The construction of a nested Newton-Krylov solver translates verbatim to the nonlinear case which requires successive applications of the GMRes solver to the linearized problem (2.112).

The main steps are illustrated in Algorithm 3. In every k-th iteration the linear system (line 3) is formulated. The GMRes solver is confined to the inner `while`-loop. This consists of the following steps:

1. Compute the m-th basis vector $\hat{q}_m$ of the Krylov subspace
$$\mathcal{K}_{k,m} := \left\{ \hat{q}_1, \hat{J}_k^{\mathrm{schur}} \hat{q}_1, (\hat{J}_k^{\mathrm{schur}})^2 \hat{q}_1, ..., (\hat{J}_k^{\mathrm{schur}})^{m-1} \hat{q}_1 \right\}. \tag{2.114}$$
Note that this is the **only** time during the `while`-loop where atomic forces are computed to update (2.113).
2. Build the orthonormal basis vector $\hat{q}_m$ of the Krylov subspace using the Arnoldi procedure (Saad, 1980).
3. Minimize the residual over the elements of the Krylov subspace. It is emphasized that this operation does not require additional computations of the force vector (for details see Saad and Schultz, 1986).

In its current form the proposed Newton algorithm is not unconditionally stable in a physical sense. This can be made clear noting the fact that the algorithm minimizes the residual of the atomic force vector. Therefore it may converge to solutions which are *saddle points* of the atomistic Hessian which violates the stability requirement (2.4). If the problem is unstable for the current Newton step the corresponding search direction is ill-posed. To identify unsuitable search directions the algorithmic stability condition is introduced

$$\textbf{[STAB]} \quad (\Delta\hat{u}_k^{\mathrm{a}})^{\mathsf{T}} \cdot (\hat{L}^{\mathrm{a/a}}(\hat{u}_k)\Delta\hat{u}_k^{\mathrm{a}}) = -(\Delta\hat{u}_k^{\mathrm{a}})^{\mathsf{T}} \cdot (\hat{L}^{\mathrm{a/p}}(\hat{u}_k)\Delta\hat{u}_k^{\mathrm{p}} + \hat{f}^{\mathrm{a}}(\hat{u}_k) - \hat{f}^{\mathrm{ext}}) > 0. \tag{2.115}$$

which can be obtained by multiplying (2.112) with $\Delta\hat{u}_k^{\mathrm{a}}$ and isolating the inner product containing $\hat{L}^{\mathrm{a/a}}$ on the left hand side. It is easy to see that $\hat{L}^{\mathrm{a/a}}(\hat{u}_k)$ is indefinite at $\hat{u}_k$ if **[STAB]** is false. In practice the term $\hat{L}^{\mathrm{a/p}}(\hat{u}_k)\Delta\hat{u}_k^{\mathrm{p}}$ can be obtained by, e.g., applying forward finite differences akin to (2.113) with only the pad atoms being updated based on $\Delta\hat{u}_k^{\mathrm{p}}$.

In order to modify the search direction, a standard approach is to modify the atomistic Hessian by adding a stabilizing term which renders it positive definite. For an overview

Algorithm 3: Newton-Krylov algorithm

```
Input: Initial guess $\hat{u}_0$
$k \leftarrow 1$;
repeat
    define $\hat{r}_k(\hat{v}) := \hat{J}_k(\hat{u}_k + \hat{v}) + \hat{f}^{\mathrm{a}}(\hat{u}_k) - \hat{f}^{\mathrm{ext}}$;
     // residual vector
    set $\mathit{\Delta}\hat{u}_0$;
    $\hat{q}_0 \leftarrow \hat{r}(\mathit{\Delta}\hat{u}_0)/\|\hat{r}(\mathit{\Delta}\hat{u}_0)\|$;
    $m \leftarrow 1$;
    while $\|\hat{r}(\mathit{\Delta}\hat{u}_{k,m-1})\| > TOL$ do
        $\hat{\hat{q}}_m \leftarrow \hat{J}_k \hat{q}_{m-1}$;
        $\hat{q}_m \leftarrow$ Arnoldi($\hat{q}_1, ..., \hat{q}_{m-1}, \hat{\hat{q}}_m$); // compute m-th basis of $\mathcal{K}_{k,m}$ (2.114)
        $\mathit{\Delta}\hat{u}_{k,m} \leftarrow \mathrm{Arg}\left\{ \min_{\hat{v} \in \mathcal{K}_m} \|\hat{r}_k(\hat{v})\| \right\}$; // displacement update
        $m \leftarrow m + 1$;
    end
    if [STAB] is false then
        $\hat{u}_{k+1} \leftarrow$ DampedDynamics;      // do several damped dynamics steps
    else
        $\hat{u}_{k+1} \leftarrow \hat{u}_k + \alpha \mathit{\Delta}\hat{u}_{k,m-1}$;         // line search
    end
    if $\|\hat{f}^{\mathrm{a}}(\hat{u}_{k+1}) - \hat{f}^{\mathrm{ext}}\| < TOL$ then
        stop (repeat);
    else
        $k \leftarrow k + 1$;
    end
end
Output: Final state $\hat{u}_{k+1}$
```

the reader is referred to (Nocedal and Wright, 2006). Here, a simpler approach is followed: If **[STAB]** is false the system from the previous iterate is restored and several damped dynamics steps are carried out in order to overcome the instability. Here, damped dynamics relates to nothing but solving an "accelerated" version of Newton's equation of motion. This will be specified more precisely in Section 4.1.1. In all subsequent numerical examples this approach was found to work reliably. While presumably being far from optimal with respect to efficiency — when compared to the stabilized Hessian method — it currently suffices for demonstration purposes.

The standard Newton-GMRes (without checking **[STAB]**) and the stabilized version are referred to as `NT-GMRes` and `SNT-GMRes` in the following.

2.7.3 Computer implementation

The DBEM is implemented in a self-written library which contains the computations of the LGF, wrappers to AHMED and the operations needed to compute the continuum problem. These steps are shown in Figure 2.7 (offline phase). As an atomistic solver LAMMPS (Plimpton, 1995) is used which is linked with the DBEM library via a `fix`.[7] Sinclair's method and the Newton-GMRes solver are implemented using the Python interface of LAMMPS (Figure 2.7, online phase). For the Newton-GMRes solver Python's SciPy library (www.scipy.org) is used. This only requires function calls to $\hat{f}^{\mathrm{a}}$ such that the LAMMPS `fix` can be conveniently called before every force computation.

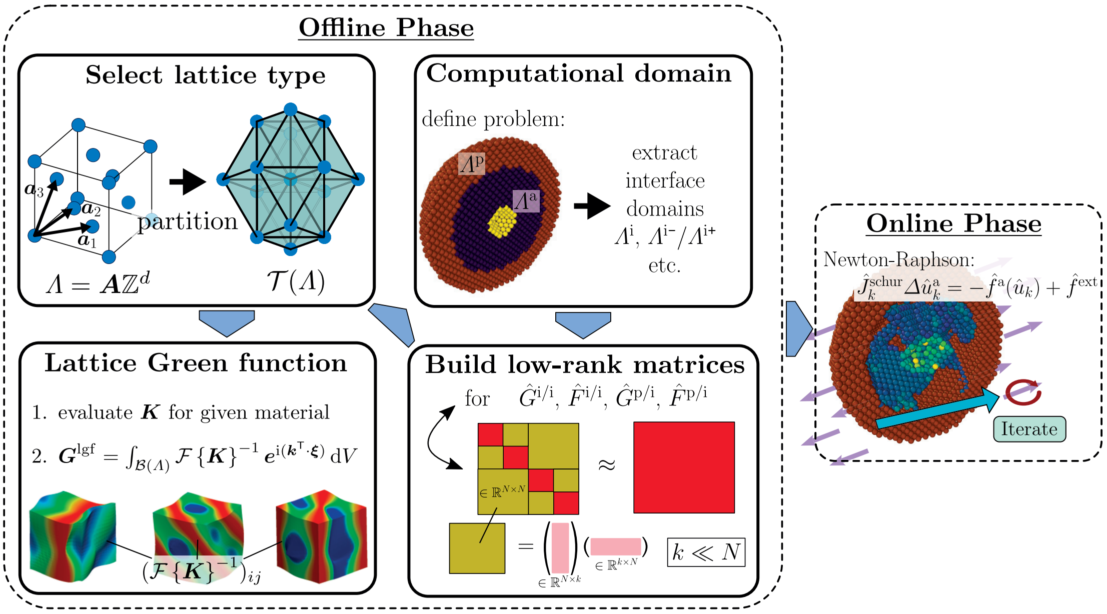
Offline Phase
Select lattice type
$\boldsymbol{a}_3$
$\boldsymbol{a}_2$
$\boldsymbol{a}_1$
partition
$\Lambda = \boldsymbol{A}\mathbb{Z}^d$
$\mathcal{T}(\Lambda)$
Computational domain
define problem:
Λ^{p}
Λ^{a}
extract interface domains
Λ^{i}, $\Lambda^{\mathrm{i-}}/\Lambda^{\mathrm{i+}}$
etc.
Lattice Green function
1. evaluate $\boldsymbol{K}$ for given material
2. $\boldsymbol{G}^{\mathrm{lgf}} = \int_{\mathcal{B}(\Lambda)} \mathcal{F}\{\boldsymbol{K}\}^{-1} e^{\mathrm{i}(\boldsymbol{k}^{\mathsf{T}}\cdot\boldsymbol{\xi})}\,\mathrm{d}V$
$(\mathcal{F}\{\boldsymbol{K}\}^{-1})_{ij}$
Build low-rank matrices
for $\hat{G}^{\mathrm{i/i}}$, $\hat{F}^{\mathrm{i/i}}$, $\hat{G}^{\mathrm{p/i}}$, $\hat{F}^{\mathrm{p/i}}$
$\in \mathbb{R}^{N\times N}$
$\approx$
$=$
$\in \mathbb{R}^{N\times k}$
$\in \mathbb{R}^{k\times N}$
$k \ll N$
Online Phase
Newton-Raphson:
$\hat{J}_k^{\mathrm{schur}}\Delta\hat{u}_k^{\mathrm{a}} = -\hat{f}^{\mathrm{a}}(\hat{u}_k) + \hat{f}^{\mathrm{ext}}$
Iterate

Figure 2.7: Data processing steps of the A/DBEM coupling. **Offline phase**: computation of the system matrices. **Online phase**: solution of the coupled problem (Algorithm 3)

Even though the aim is to reduce computational cost, solving atomistic problems on parallel machines is essential, depending on the required system size and the complexity of the interatomic potential. This requires a parallelization of the coupled problem to some degree. For the modified version of Sinclair's method this is straightforward. Due to the staggered solution procedure the parallelization of the atomistic problem is readily accomplished within the molecular dynamics program of choice. Subsequently Sinclair's method requires only one single, but large, matrix-vector multiplication in order to update the pad atoms. On a desktop computer with 16 GB RAM the limit for $\mathscr{H}$-matrices is roughly between 10^5-10^6 atoms, depending on the size of the pad region. Fortunately, efficient parallel algorithms for $\mathscr{H}$-matrices exist for shared and distributive memory systems (see e.g. Bebendorf and Kriemann, 2005). Individual low-rank matrix blocks can be distributed over the processors, thus dividing the work into smaller portions. A function for parallel matrix-vector multiplications is included in AHMED and can thus be readily accessed in the current version of the DBEM library.[8] An implementation of the monolithic solver on parallel machines is, however, far more involved and out of scope of the present work (c.f. the following remark).

---

[7] In the language of LAMMPS, a `fix` is an interface which can be called during a simulations before/after certain events, e.g. force evaluations. This interface can be used to link LAMMPS with external software packages

Remark 2.7.1. *A parallelization of the monolithic solver, as derived in the previous section, is not straight forward. This is due to the proposed computation of the pad displacements by triangular matrix inversion. More precisely, consider, e.g., the LU factorization of a matrix* $\hat{A} = \hat{L}\hat{U}$*. A solution to the linear system* $\hat{A}\hat{x} = \hat{b}$ *can then be obtained by forward-backward substitution*

$$\hat{y} = \hat{L}^{-1}\hat{b} \qquad \longrightarrow \qquad \hat{x} = \hat{U}^{-1}\hat{y} \tag{2.116}$$

which is a rather sequential algorithm and almost unparallelizable with $\hat{L}, \hat{U}$ *being* $\mathscr{H}$*-matrices due to the high communication overhead (c.f. Hackbusch, 2015). To overcome this problem Kriemann and Le Borne (2015) proposed an algorithm to obtain the factors* $\hat{W}, \hat{Z}$ *of the inverse of* $\hat{A}$*, i.e.* $\hat{A}^{-1} = \hat{W}\hat{Z}$*, using* $\mathscr{H}$*-arithmetics. The algebraic problem then comprises two matrix-vector multiplications*

$$\hat{y} = \hat{Z}\hat{b} \qquad \longrightarrow \qquad \hat{x} = \hat{W}\hat{y} \tag{2.117}$$

which can be parallelized. This approach seems promising for future application, indicated by the excellent performance reported in (Kriemann and Le Borne, 2015).

2.7.4 Algorithmic comparison

A brief algorithmic comparison between the different algorithms presented in this section is carried out to validate the accuracy of the method depending on the cut-off radius r_{cut}. Therefore let the computational domain be the square lattice $\Lambda := \mathbb{Z}^2 + \begin{pmatrix} 1/2 & 1/2 \end{pmatrix}^{\mathsf{T}}$. The atomistic domain is a square-shaped subset defined by

$$\Lambda^{\mathrm{a}} := \Lambda \cap \left([-l, l] \times [-l, l]\right), \tag{2.118}$$

with $l = 29.5$. For simplicity the atomistic problem is assumed to be linear such that both problems follow the same force interaction law. The continuous extension of the displacement field is given using the partition presented in Appendix A.4.2. As a test problem a force quadrupole is chosen. The exact solution to this problems is easy to compute numerically since the solution dies off quickly. The right hand side for this problem is then given by

---

[8] So far parallel scaling has been verified up to 48 cores using the parallel version of AHMED for matrix-vector multiplications. For further examples see (Bebendorf, 2009)

$$\boldsymbol{f}^{\text{ext}}(\boldsymbol{\xi}) = \begin{cases} \begin{pmatrix} 1 & 1 \end{pmatrix}^{\mathsf{T}} & \text{if } \boldsymbol{\xi} = \begin{pmatrix} -1/2 & -1/2 \end{pmatrix}^{\mathsf{T}}, \\ \begin{pmatrix} -1 & -1 \end{pmatrix}^{\mathsf{T}} & \text{if } \boldsymbol{\xi} = \begin{pmatrix} 1/2 & -1/2 \end{pmatrix}^{\mathsf{T}}, \\ \begin{pmatrix} 1 & 1 \end{pmatrix}^{\mathsf{T}} & \text{if } \boldsymbol{\xi} = \begin{pmatrix} 1/2 & 1/2 \end{pmatrix}^{\mathsf{T}}, \\ \begin{pmatrix} -1 & -1 \end{pmatrix}^{\mathsf{T}} & \text{if } \boldsymbol{\xi} = \begin{pmatrix} -1/2 & 1/2 \end{pmatrix}^{\mathsf{T}}, \\ \mathbf{0} & \text{else.} \end{cases} \tag{2.119}$$

The error in the solution in Λ^{a} is discussed in the following. Note that the error can be bounded from above as

$$\epsilon_{\text{rel}} = \frac{\|\boldsymbol{u}^{\text{a}} - \tilde{\boldsymbol{u}}^{\text{a}}\|_{l^2}}{\|\boldsymbol{u}^{\text{a}}\|_{l^2}} \lesssim r_{\text{cut}}^{-3/2} \log r_{\text{cut}}, \tag{2.120}$$

which follows directly from Proposition 3 and the property of bounded linear operators. The error induced by the three different solution procedures is shown in Figure 2.8. For the Sinclair method the expected scaling is observed up to a log-factor. For the Schwarz and the Newton-GMRes method a more pronounced pre-asymptotic regime is observed. Moreover, the error in the Sinclair method is slightly lower than the one induced by the other solution procedures. This is expected due to the fact that Sinclair's method does not require an intermediate step (i.e. solving a linear system). In addition, the construction of the DBEM is not exact since the algebraic representation of the identity (2.57) is only approximate. Nevertheless, for $r_{\text{cut}} \gtrsim 15\, a_0$ there is not practical difference between both methods anymore.

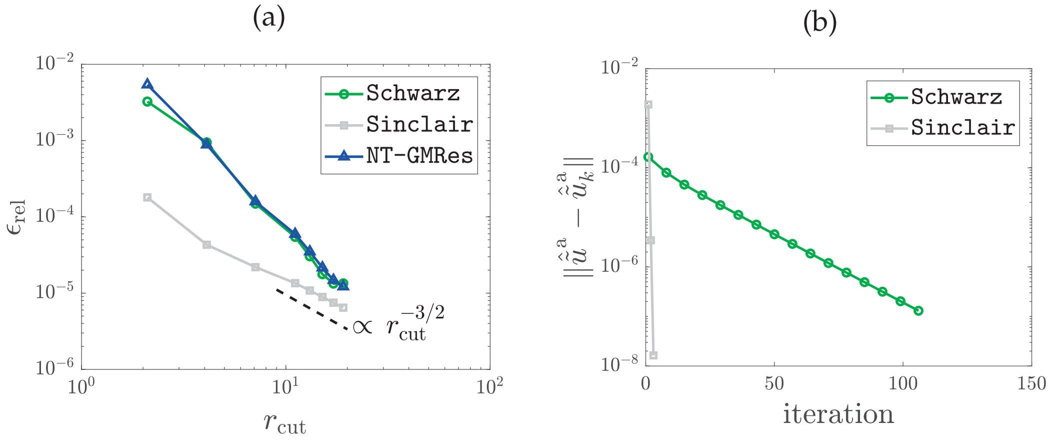

Figure 2.8: (a) Relative error (2.120) inside the atomistic domain for the force quadrupole problem defined in Section 2.7.4. (b) Residual vs. global iteration for the Schwarz and Sinclair's method for the particular case of $r_{\text{cut}} = 7$

In addition, the number of global iterations for the two staggered schemes are compared in Figure 2.8 (b). Here, The Sinclair method clearly outperforms the alternating Schwarz algorithm in reaching the desired tolerance of 10^{-7} within three iterations — as opposed to > 100 for the Schwarz method. Therefore the Schwarz algorithm is not considered in the numerical examples in Section 4.1.

3 Coupled atomistic and discrete dislocations in three dimensions

3.1 Motivation

The coupling method described in the previous chapter assumes a linear elastic bulk material. Related Quasicontinuum (QC) schemes may as well employ a Cauchy-Born model if lattice rotations are non-negligible. Both models are commonly used approximations of fully atomistic models, giving accurate results in the case of small or homogeneous deformations, respectively. However, deformations in the vicinity of defects, such as interstitials, voids, dislocations or grain boundaries, are nonlinear which cannot be captured by linearized models.

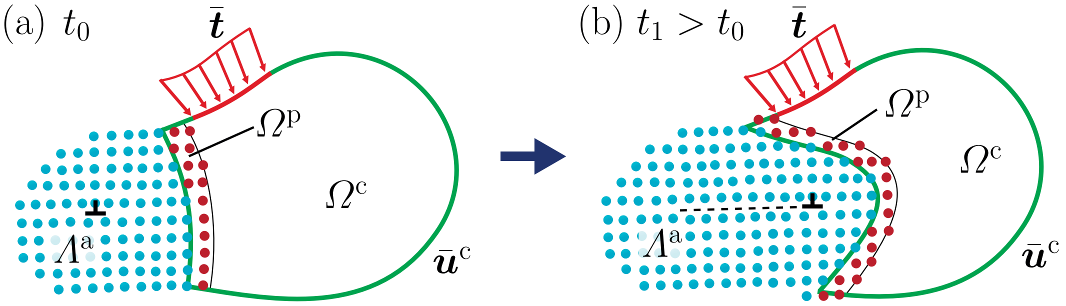
(a) t_0
$\bar{\boldsymbol{t}}$
Ω^{p}
Ω^{c}
Λ^{a}
$\bar{\boldsymbol{u}}^{\mathrm{c}}$
(b) $t_1 > t_0$
$\bar{\boldsymbol{t}}$
Ω^{p}
Ω^{c}
Λ^{a}
$\bar{\boldsymbol{u}}^{\mathrm{c}}$

Figure 3.1: (a) Domain decomposition of a material body into an atomic lattice Λ^{a} and a continuum domain Ω^{c} at time $t = t_0$. (b) Domain decomposition after the dislocation has evolved into the (former) continuum region at $t_1 > t_0$

To account for these nonlinear effects, atomistic/continuum (A/C) coupling methods use re-meshing techniques to evolve the atomistic domain with the defect, as shown in Figure 3.1 (see, e.g. Shenoy et al., 1999; Amelang and Kochmann, 2015). However, defects may travel over long distances and can induce long-range fields. Dislocations, in particular, generate stress fields which decay as $1/r$, where r is the distance to the center of the dislocation core. An evolution of the atomistic domain is thus indispensable to avoid spurious wave reflections as the dislocations approach the artificial interface. On the other hand, if plenty of dislocations have nucleated and distribute over the entire domain, desirable computational savings reduce dramatically.

Although the capability of QC methods in improving the efficiency in comparison with fully atomistic problems is indisputable, the above-mentioned trade-off between accuracy and computational cost necessitates additional approximation schemes in the coarse-grained region in order to tackle plasticity problems up to several hundreds of nanometers. But, allowing for dislocations in the coarsened region requires to permit non-homogeneous deformation in the continuum model, e.g. by means of additional internal variables.

However, up to now a simultaneous coupling of two models describing the same physical phenomena but in a different mathematical framework, i.e. a *coarse-graining of defects*, remains one of the greatest challenges in multiscale materials modeling (Curtin and Miller, 2017). Specifically for A/C coupling the problems reads: how to link internal variables of continuum models describing the plastic flow with the atomistic problem in a concurrent framework?

3.2 Coupled atomistic and discrete dislocations in two dimensions

In order to overcome the drawback of classical QC methods, Curtin and co-workers at Brown University introduced an A/C coupling scheme equipped with a non-trivial continuum model. Their seminal contribution uses the discrete dislocation dynamics (DDD) framework of Lubarda et al. (1993) and Van Der Giessen and Needleman (1995) (c.f. Section 1.4.2) allowing for discrete dislocations to exist in the continuum region. The method was consequently given the name *coupled atomistic and discrete dislocations* (CADD, Shilkrot et al., 2002a,b) method (hereafter also referred to as CADD-2d). Figure 3.2 shows a simple one-dimensional illustration of the mathematical structure of CADD. This illustration is of course not representative since dislocations do not exist in one dimension but is useful to clarify the main ideas.

Consider the evolution of a chain of atoms in Figure 3.2 a) between some initial time t_0 and $t_1 > t_0$. For the coupled problem in Figure 3.2 b), which represents the same *physical* problem, the nonlinear wave must cross the artificial interface $\mathit{\Gamma}_\mathrm{i}$ at some time $t \in (t_0, t_1)$. Beyond $\mathit{\Gamma}_\mathrm{i}$, CADD merely keeps track of the wave position neglecting the nonlinear field at the wave front while preserving the accuracy of the far-field, i.e. the displacement field and its gradient propagate in $\mathit{\Omega}^\mathrm{c}$ as a discontinuity and a δ-function, respectively. That is, *only* the position of the wave front is tracked through the continuum domain.

The motivation behind CADD is the genuine interest in the most accurate description — which is assumed to be the atomistic description — of field quantities, as displacements,

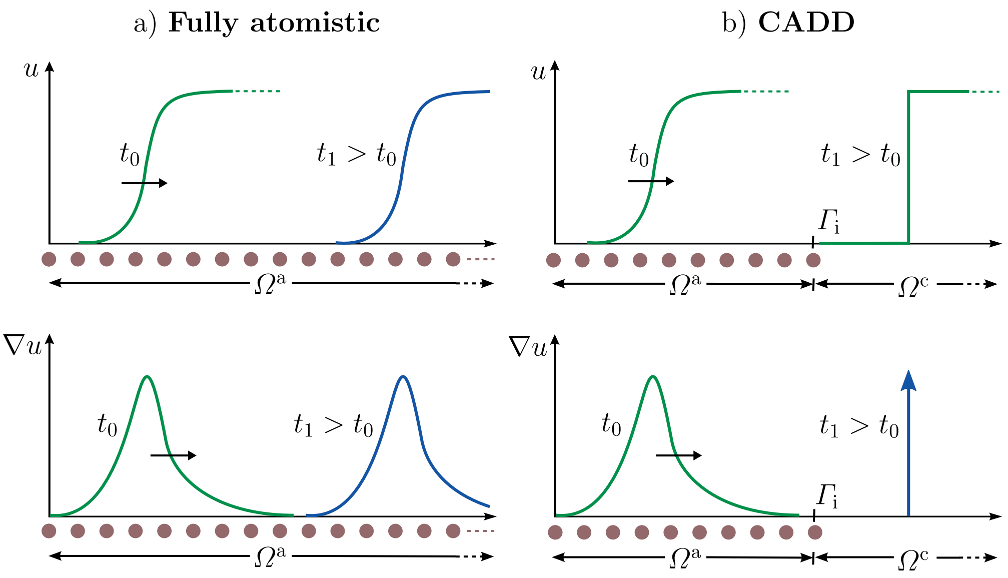

Figure 3.2: a) Schematic illustration of the evolution of one-dimensional chain of atoms. b) The equivalent CADD problem

only in some small part of the computational domain, e.g. near a crack tip or an indenter. Keeping track of all dislocations through elaborated re-meshing techniques may increase the computational cost *unnecessarily* if dislocations reside far away from the region of interest. It seems therefore sufficient to track only the positions of the dislocations in the continuum domain, disregarding the nonlinear fields around the core, and provide boundary conditions on the atomistic problem through their linear elastic far-field. CADD can thus be seen as a kind of goal-oriented multiscale method.

The most prominent quasi-static implementation of CADD by Shilkrot et al. (2004); Miller et al. (2004) uses a force-based coupling mechanism to eliminate spurious forces on the dislocations near the artificial interface which plagued an earlier energy-based version (Shilkrot et al., 2002a); see also (Tadmor and Miller, 2011) for a detailed discussion on force-based vs. energy-based methods. Later, the method was successfully extended to dynamic problems by Qu et al. (2005) and Shiari et al. (2005). The basic formalism of CADD is generically summarized in the following. Assume an initial distribution of N dislocations $\mathcal{D} := \{\boldsymbol{s}_1, ..., \boldsymbol{s}_N\}$. In two dimensions dislocations are infinite straight lines; therefore it suffices to characterize each dislocation by its position vector $\boldsymbol{s}_i \in \mathcal{D}$ with respect to the plane spanned by the glide direction $\boldsymbol{m}$ and the slip plane normal $\boldsymbol{n}$. The main algorithm can then be written as follows:

[S1] Solve the coupled atomistic/elasticity problem.

[S2] Compute the stresses $\boldsymbol{\sigma}(\boldsymbol{s}_i)$ for all $\boldsymbol{s}_i \in \mathcal{D}$ and compute $\boldsymbol{f}_i^{\mathrm{pk}}$.

[S3] Using $\boldsymbol{f}_i^{\mathrm{pk}}$, evolve $\boldsymbol{s}_i$ according to (1.71).

The steps **[S1]**-**[S3]** are repeated until convergence is attained or the final time step is reached. For quasi-static problems the physical problem in **[S1]** was solved in (Shilkrot et al., 2004) via a Schur-complement method by a priori inverting the continuum stiffness matrix. The only explicit degrees of freedom are then the positions of the real atoms. However, it should be noted that a naive (:= dense) inversion (or factorization) of the continuum stiffness matrix can *only* be done in two dimensions with tolerable effort, yet, it becomes prohibitive in three dimensions (c.f. Section 2.6.3).

In order to illustrate the characteristic feature of CADD, i.e. the transmission between atomistic and discrete dislocations, assume that a dislocation has nucleated in the atomistic domain and approaches the interface as shown in Figure 3.3. Since the motion of the dislocation line within the continuum is governed by the evolution of an internal variable, namely the *plastic strain*, it does not have a corresponding partner in the atomistic domain which prevents a direct coupling, more precisely, there exists no explicit representation of plastic deformation in an atomistic problem. In lieu thereof, an atomistic dislocation has to be interpreted as a distinct configuration of atoms within the dislocation core region where the energy of the lattice sites varies strongly from the defect-free state. In order to transmit atomistic dislocations into the bulk material, the developers of CADD introduced a heuristic scheme, referred to as *dislocation passing*. Thereby, a certain part of the atomistic domain sufficiently near the interface, the *detection band*, is triangulated to monitor the Lagrangian strain $\boldsymbol{E}$ of each element (:= triangle) as shown in Figure 3.3 (a). The measured strain is then compared to each element of a set of predefined strain tensors

$$\mathscr{E} := \left\{ \frac{1}{2}((\boldsymbol{F}^{\mathrm{p}}_i)^{\mathsf{T}}\boldsymbol{F}^{\mathrm{p}}_i - \boldsymbol{I}) \,\middle|\, i = 0, ..., N \right\}, \qquad \text{where} \qquad \boldsymbol{F}^{\mathrm{p}}_i = \frac{\boldsymbol{b}_i \otimes \boldsymbol{n}_i}{a_0} + \boldsymbol{I}. \tag{3.1}$$

Here, $\boldsymbol{F}^{\mathrm{p}}_i$ is the plastic deformation corresponding to i-th slip system and N is the total number of slip systems for the given crystal structure. Note that $i = 0$ refers to $\boldsymbol{b} = \boldsymbol{0}$, that is no slip is detected in the corresponding element. The plastic strain inside the element is then defined as the strain which minimizes the distance between $\boldsymbol{E}$ and $\mathscr{E}$ with respect to the Frobenius norm, i.e.

$$\boldsymbol{E}^{\mathrm{p}} := \operatorname{Arg} \left\{ \min_{\boldsymbol{E}^{\mathrm{p}}_i \in \mathscr{E}} \|\boldsymbol{E} - \boldsymbol{E}^{\mathrm{p}}_i\|_{\mathrm{fro}} \right\}. \tag{3.2}$$

In essence, this scheme allows for detecting plastic slip near the artificial interface which implies that a dislocation must reside in the vicinity of the element. The dislocation is then passed to the continuum as a discrete dislocation, alongside with the creation of a dipole in Ω^{a} to remove the dislocation in the atomistic domain. In order to further improve the accuracy of the passing scheme, Dewald and Curtin (2006) introduced the *template method* which enriches the displacement field $\boldsymbol{u}^{\mathrm{c}}$ within the pad region Ω^{p} in the vicinity of an atomistic dislocation with a precomputed description of the real dislocation core structure which eventually reduces spurious effects on the dislocation.

It was shown in (Dewald and Curtin, 2006) that the passing distance d (c.f. Figure 3.3) can then be reduced significantly, thus allowing for more realistic boundary conditions on the atomistic problem.

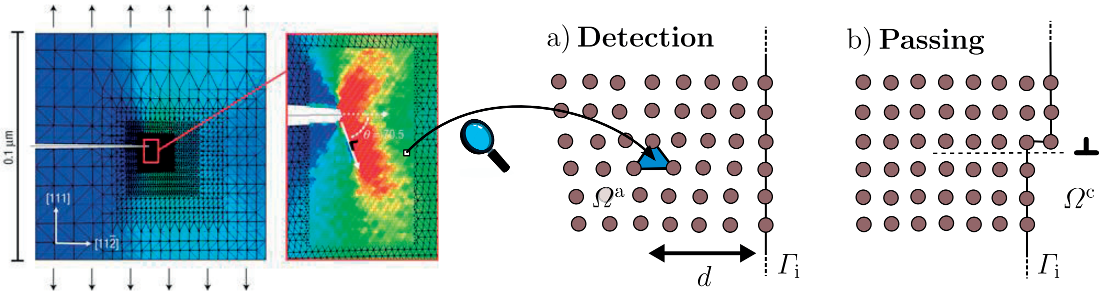

Figure 3.3: Schematic illustration of the characteristic feature of CADD: a) Detection of a dislocation in the atomistic domain. b) Passing of the detected dislocation to the continuum region as a discrete entity. The left figure is reprinted from Warner et al. (2007) with permission from Springer Nature

The CADD method has proven its capabilities in approximating large-scale fully atomistic problems with excellent accuracy, e.g. for nanoindentation (Miller et al., 2004), crack tip behavior (Warner et al., 2007) or fatigue problems (Curtin et al., 2010), at substantially lower computational cost. To date, the method has yet solely been applied to two-dimensional problems where dislocations remain straight and therefore reside either in the atomistic or in the continuum domain. In three dimensions one is usually confronted with dislocation loops which possibly span both domains. An extension of CADD to three dimensions therefore requires a reformulation of the method to allow for the evolution of dislocations residing simultaneously in both domains.

3.3 Challenges

This section serves as an introduction to the basic concepts for a three-dimensional CADD method (henceforth CADD-3d) in order to outline the main challenges of the implementation. Thereby, the dislocation detection and the core template correction will be identified as the essential prerequisites for the systematic derivation of the major assumptions and fundamental governing equations in Section 3.6.

3.3.1 Concept of hybrid dislocations

In order to illustrate this cornerstone of CADD-3d a computational domain $\Omega \subseteq \mathbb{R}^3$ is assumed in the following. The domain is decomposed into a bounded atomistic part $\Omega^{\mathrm{a}} \subset \Omega$ surrounded by a continuum elasticity region $\Omega^{\mathrm{c}} := \Omega \setminus \Omega^{\mathrm{a}}$. In order to focus on the key ideas the notation is simplified by making no formal distinction between discrete and continuous domains, including the fields defined on them, if not explicitly required. Therefore the following equivalence relations

$$\mathit{\Omega} \leftrightarrow \mathit{\Lambda}, \qquad\qquad \mathit{\Omega}^{\mathrm{a}} \leftrightarrow \mathit{\Lambda}^{\mathrm{a}}, \qquad\qquad \mathit{\Omega}^{\mathrm{c}} \leftrightarrow \mathit{\Lambda}^{\mathrm{c}} \tag{3.3}$$

are assumed in the remainder of this Chapter. The interface between the atomistic and the continuum domain is denoted by $\mathit{\Gamma}_{\mathrm{i}}$. The interface can be understood as the equivalent of the set $\mathit{\Lambda}^{\mathrm{i}}$, i.e. the layer of real atoms in $\mathit{\Omega}^{\mathrm{a}}$ which provides the boundary condition on $\mathit{\Omega}^{\mathrm{c}}$ (c.f. Section 2.3.3).

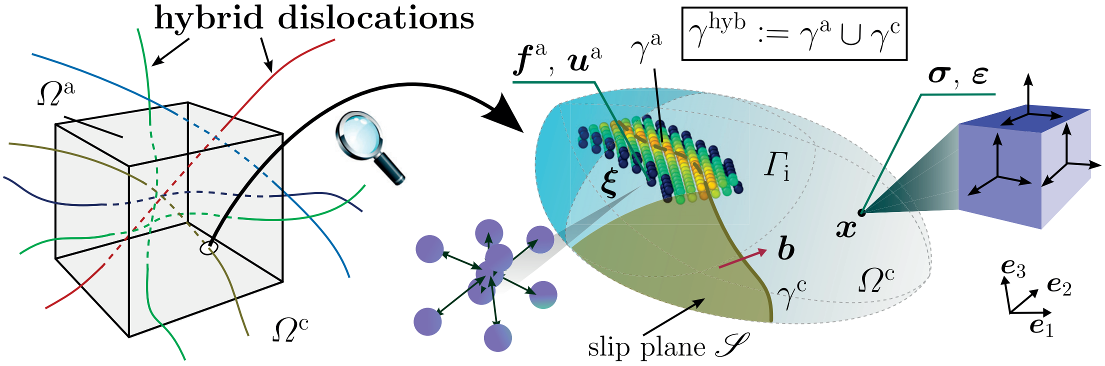
hybrid dislocations
$\mathit{\Omega}^{\mathrm{a}}$
$\mathit{\Omega}^{\mathrm{c}}$
$\boldsymbol{f}^{\mathrm{a}}$, $\boldsymbol{u}^{\mathrm{a}}$
γ^{a}
$\gamma^{\mathrm{hyb}} := \gamma^{\mathrm{a}} \cup \gamma^{\mathrm{c}}$
$\boldsymbol{\sigma}$, $\boldsymbol{\varepsilon}$
$\mathit{\Gamma}_{\mathrm{i}}$
$\boldsymbol{\xi}$
$\boldsymbol{x}$
$\boldsymbol{b}$
γ^{c}
$\mathit{\Omega}^{\mathrm{c}}$
slip plane $\mathscr{S}$
$\boldsymbol{e}_3$
$\boldsymbol{e}_2$
$\boldsymbol{e}_1$

Figure 3.4: Schematic illustration of the boundary value problem for CADD-3d

Assume now that the material body $\mathit{\Omega}$ contains a finite number of dislocations. In the atomistic domain the dislocations can be identified by means of their characteristic configuration of atoms in the vicinity of the dislocation core (see Section 1.2). In the continuum domain the dislocations are represented as discrete entities (c.f. Section 1.4). If there is no restriction on the positions of the dislocations in $\mathit{\Omega}$, a possible general configuration is schematically depicted in Figure 3.4 on the left which shows numerous dislocations piercing the A/C interface. Since a dislocation cannot end within the crystal (neglecting the possibility of dislocation junctions), its atomistic and continuum representations *must* have the same characteristics, i.e. the same Burgers vector $\boldsymbol{b}$, slip plane $\mathscr{S}$ and line orientation $\boldsymbol{t}$. This yields the following hypothesis.

Hypothesis 2 (**Discrete atomistic dislocation**). *A discrete line representation of an atomistic dislocation exists and is denoted by* γ^{a}.

From Hypothesis 2, it follows that a closed[1] line representation of the entire dislocation can be constructed which is denoted as the **hybrid dislocation** (c.f. Junge, 2014; Anciaux et al., 2018)

$$\gamma^{\mathrm{hyb}} := \gamma^{\mathrm{a}} \cup \gamma^{\mathrm{c}}, \tag{3.4}$$

where γ^{c} is the corresponding portion residing in the continuum domain. The actual detection of γ^{a} will be discussed in Section 3.4.

---

[1] Or closed *and* open if it extends to infinity

Remark 3.3.1. *If a discrete line representation γ^{a} exists it will not be unique. This can be rationalized by considering the definition of a dislocation from Section 1.2 as the incompatibility of the displacement field. In the atomistic domain the diameter of a closed path is bounded by the lattice spacing (c.f. Figure 1.2 (a)) and can therefore not be arbitrarily small — as in a continuum. The volume enclosed by the set of all smallest possible Burgers circuits represents the region of "uncertainty". This statement will be made precise in Section 3.4.2.*

Having established the notion of hybrid dislocations, the system can now be analyzed with respect to its stability properties. The atomistic system is constrained by the continuum problem through the motion of the pad atoms in Ω^{p}. Hence, the atoms in the vicinity of Γ_{i} respond to the displacements $\boldsymbol{u}^{\mathrm{p}}$, dictated by the continuum solution $\boldsymbol{u}^{\mathrm{c}}$. Far away from the defect core the continuum solution is a sufficient approximation to a solution that a fully atomistic system would attain. However, recall from Section 1.4 that $\boldsymbol{u}^{\mathrm{c}}$ may indeed be a very rough representation of the real atomistic dislocation core structure (c.f. Section 1.4.3 in particular).

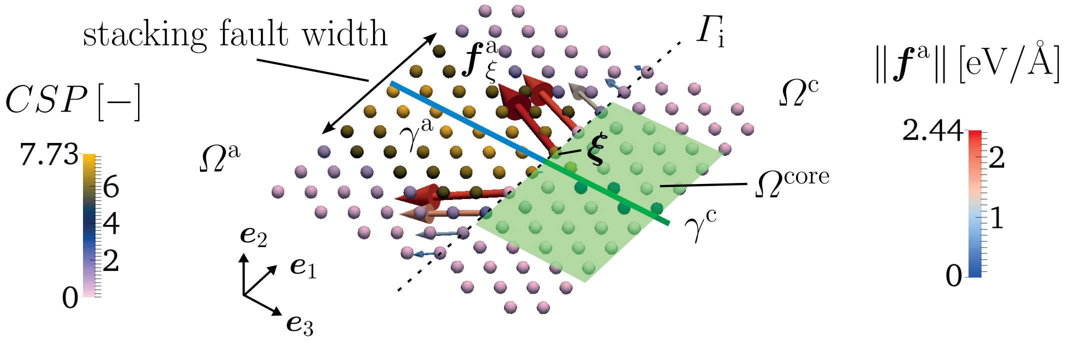

Figure 3.5: Spurious forces on boundary atoms in the vicinity of a hybrid dislocation due to a continuum solution with compact core structure; the atoms are colored according to their centrosymmetry parameter (CSP, Kelchner et al., 1998)

To illustrate the differences between the atomistic and continuum core structure, assume, for example, a relaxed edge dislocation in an infinite atomic crystal. The Burgers vector is assumed to be spread, leading to a separation of the dislocation into two Shockley partials. Now assume that the atomistic domain is cut somewhere along the glide direction. One half-crystal gets then replaced by a continuum model such that the atoms near the interface Γ_{i} around the center of the dislocation "see" the compact core corresponding to the classical Volterra solution (c.f. Appendix A.2.2). After making this replacement, spurious forces on the interface atoms arise in Ω^{core} up to the order of eV/Å, as shown in Figure 3.5. Therefore the atomistic system becomes unstable in the vicinity of the interface and the atoms relax to new, erroneous, positions to smooth out the incompatibility between the two different core structures. This leads to a "friction-like" force on γ^{hyb} which can artificially pin the hybrid dislocation. The error induced by the pinned dislocation may feed back further into the atomistic domain, thus changing the shape of the entire dislocation network.

Remark 3.3.2. *In principle the continuum solution can be improved by considering eigenstrains* $\boldsymbol{\beta}^{\mathrm{p}}$ *calibrated to atomistic results (Section 1.4.3, Example 1.4) or embedding the dislocation in a gradient continuum (c.f. Lazar, 2013). However, the DDD method may lose its strongest asset which is the simple and efficient computation of the Cauchy stress. Since the long-range interactions are well-captured by linear elasticity it seems more useful to encode the short-range interactions in the core energy term* Π^{core} *which only depends on the local line configuration such that* $\boldsymbol{f}^{\mathrm{core}}$ *is thus rather cheap to evaluate.*

3.3.2 Dislocation motion

Based on the previous discussion, CADD-3d adds two further complications regarding the motion of dislocations, as shown in Figure 3.6 (a) and (b), which are addressed in the following.

Evolution of hybrid dislocations. CADD-3d requires mutual evolving displacement boundary conditions at the A/C interface. However, the continuum solution is a rather poor representation of the dislocation core, possibly perturbing the positions of the atoms in the vicinity of the interface (c.f. Figure 3.5). Even more important, the continuum experiences similar spurious artifacts since the DD line "expects" a stress field according to a linear elastic problem. This can have drastic impacts on the evolution of γ^{c} and, as a consequence, lead to an unphysical motion of the *entire* hybrid dislocation line since the continuum solution in turn prescribes the boundary conditions on the atomistic problem. Therefore the mutual boundary conditions must be augmented with some "correction". This correction must provide the atomistic problem with the real core structure, imposed on the pad atoms in Ω^{p}, and, vice versa, the continuum problem with a description of the linear elastic core corresponding to the full DDD problem. Such an enriched boundary condition will be discussed in detail in Section 3.5.

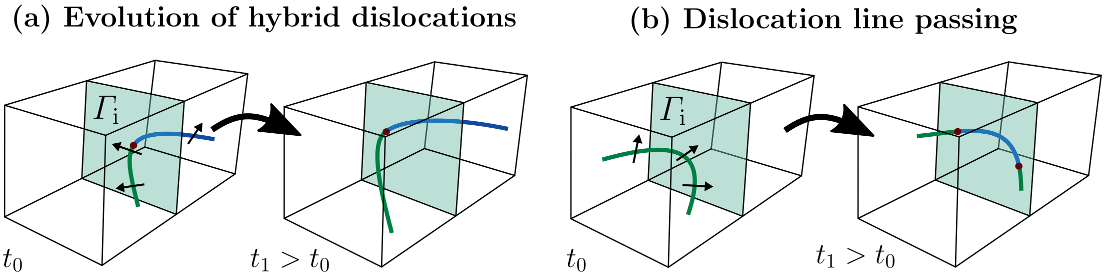

Figure 3.6: (a) Evolution of a hybrid dislocation along Γ_{i}. (b) Dislocation moving beyond Γ_{i}, thus eventually becoming a hybrid dislocation

Dislocation line passing. The second complication comes into play when a dislocation, initially contained fully in Ω^{a} *or* Ω^{c}, approaches the artificial interface. Seamless motion of dislocations between both domains is not fundamentally captured by the underlying theory of the coupled problem since their mathematical descriptions differ in the sense that a dislocation has an explicit line representation in Ω^{c}, whereas it is merely a characteristic configuration of atoms in Ω^{a}. Therefore solution algorithms for the governing equations of CADD-3d must necessarily be equipped with "exceptions" which transmit the passage of dislocations between both models akin to the two dimensional problem.

3.4 Dislocation detection in atomistic systems

To bridge the gap between atomistic and mesoscale models such as DDD, the detection of dislocation lines in atomistic systems is indispensable, especially when linking different types of models in a CADD framework. However, a unique detection of a dislocation line γ^{a} as a one-dimensional object (akin to DDD) is generally not possible (c.f. Remark 3.3.1). Fortunately, non-uniqueness is not an issue since physically relevant configurations of the discrete atomistic dislocation line are confined to a tubular region of radius $\approx b$ around a (fictitious) center of the dislocation core.

Systematic dislocation detection in atomistic systems is a rather new field. For many researchers it is sufficient to determine distorted atoms by computing their coordination numbers, e.g. using the common neighbor analysis (CNA, Honeycutt and Andersen, 1987). The demand for an explicit detection of single dislocation lines mainly stems from the motivation to utilize well-established continuum concepts for the analysis of atomistic problems, e.g. the evaluation of the plastic deformation, dislocation densities etc (e.g. Steinberger et al., 2016). To date, several methods from various research groups have been developed which can broadly be split into two categories:

- Dislocation detection based on the dislocation density tensor.
- Dislocation detection via discrete Burgers circuit analysis.

Differences and similarities between both schemes are addressed in the following by means of illustrative examples.

3.4.1 Detection based on continuum kinematics

In the following the existence of a locally incompatible elastic deformation gradient $\boldsymbol{F}^{\mathrm{e}}$ is assumed in the context of multiplicative plasticity according to Teodosiu and Sidoroff (1976); Nemat-Nasser (1979). Further it is asserted that $(\boldsymbol{F}^{\mathrm{e}})^{-1}$ pulls back from a current configuration $\mathrm{d}\boldsymbol{x}$ to a stress-free configuration $\mathrm{d}\boldsymbol{X}$ (c.f., Teodosiu and Sidoroff, 1976; Le and Stumpf, 1993; Stukowski and Arsenlis, 2012). Let C be a closed path in the current configuration. By virtue of Stokes' theorem the true Burgers vector with respect to the reference configuration for the corresponding path C_0 can then be written as

$$\boldsymbol{b} = \oint_{C_0} \mathrm{d}\boldsymbol{X} = \oint_{C} (\boldsymbol{F}^{\mathrm{e}})^{-1}\,\mathrm{d}\boldsymbol{x} = -\int_{\mathcal{A}} \nabla \times (\boldsymbol{F}^{\mathrm{e}})^{-1}\boldsymbol{n}\,\mathrm{d}A = \int_{\mathcal{A}} \boldsymbol{\alpha}\boldsymbol{n}\,\mathrm{d}A, \tag{3.5}$$

with the dislocation density tensor $\boldsymbol{\alpha} = -\nabla \times (\boldsymbol{F}^{\mathrm{e}})^{-1}$ and the unit normal vector $\boldsymbol{n}$ with respect to the area $\mathcal{A}$ which encloses C.

This derivation is based on the assumption of a continuous (possibly incompatible) body and is thus not immediately accessible to atomistic problems. Only recently, various practical techniques have been proposed which aim at extracting the elastic deformation gradient from atomistic systems (e.g. by Hartley and Mishin, 2005a,b; Begau et al., 2012). Usually a set of unique *ideal* lattice vectors corresponding to the perfect lattice is taken as a reference configuration. An ideal lattice vector is then assigned to the *current* lattice vector, e.g. by minimizing the distance between the set of ideal lattice vectors and the current lattice vector (c.f. Section 3.4.2). An average representation of $\boldsymbol{F}^{\mathrm{e}}$ may then be computed on a per-atom basis with respect to the first coordination shell (Hartley and Mishin, 2005a,b). Then, an average value for $\boldsymbol{\alpha}$ can be obtained which will be non-zero where the deformation is inhomogeneous, i.e. in the vicinity of dislocation cores. Subsequently the integral (3.5) has to be computed over a certain area around a distorted atom to obtain the Burgers vector. Note that this scheme alone will not detect a dislocation in terms of a discrete line representation. However, Begau et al. (2011) introduced a technique to construct dislocation lines via a skeletonization of the distorted regions.

Remark 3.4.1. *Note that the detection scheme used in the two-dimensional version of CADD (cf. Section 3.2) is based on continuum kinematics as well, yet in a different way. The CADD detection computes the plastic Lagrangian strain in order to identify the parts of the atomistic domain which have undergone plastic deformation. However, it does not locate the dislocation core as will be shown in Example 3.1.*

3.4.2 Detection based on discrete Burgers circuits

The second type of methods uses the classical Burgers circuit procedure. To mathematically define closed paths between (at least three) atoms, the atomistic configuration must be tessellated. A discrete Burgers loop is then defined by the path along the boundary of a facet of the tessellation. This procedure is conceptually well-known, yet, an algorithmic development with the purpose of a fully automated dislocation detection has only recently been established by Stukowski and Albe (2010b). The so-called *dislocation extraction algorithm* (DXA Stukowski and Albe, 2010a; Stukowski et al., 2012) can currently be considered as the standard visualization tool for the analysis of complex dislocation networks among the material science community. However, to the author's best knowledge, the DXA has never been applied in the context of a numerical method as it is aimed for in this work. In the following the key ideas of the algorithm are presented in a concise format.

The DXA requires the identification of reference lattice vectors corresponding to the lattice vectors in the deformed configuration, similar to the dislocation density-based method from the previous section. For this purpose a simplicial tessellation of the reference lattice is used. This choice is not unique in the sense that other types of elements could be used in almost the same manner. However, it is usually more convenient to employ a simplicial tessellation from a computational point of view since efficient existing tools for the mesh generation ("Delaunay triangulation") are available of the shelf, e.g. the *Computational Geometry Algorithms Library* (CGAL, The CGAL Project, 2017).

Since the reference lattice is translational invariant, there exists a finite set of lattice vectors $\mathcal{X}$ which correspond to the distinct edge vectors of a simplicial tessellation of the perfect lattice. The elements $\boldsymbol{v} \in \mathcal{X}$ are denoted as the *ideal lattice vectors*. Let $\mathcal{T}$ be the tessellation of a current atomistic domain Ω^{a}. Elements of $\mathcal{T}$, i.e. tetrahedra, faces and edges, are denoted t, f and e. In order to identify dislocated elements a relation between an edge vector $\mathrm{d}\boldsymbol{x}_e$ and a corresponding reference lattice vector $\mathrm{d}\boldsymbol{X}_e \in \mathcal{X}$ is sought-after. This procedure is schematically depicted in Figure 3.7 for a face-centered cubic (fcc) lattice. For the identification of the reference lattice vectors the criterion of Stukowski (2014) is adopted in the following such that

$$\forall\, \mathrm{d}\boldsymbol{x}_e \qquad \mathrm{d}\boldsymbol{X}_e := \mathrm{Arg}\left\{ \min_{\boldsymbol{v}\in\mathcal{X}} \|\, \boldsymbol{v} - \mathrm{d}\boldsymbol{x}_e \,\| \right\}. \tag{3.6}$$

An identification based on the metric properties of single bonds solely is rather simple and limited to single crystals. Other criteria have been proposed, e.g. by comparing the angles between lattice vectors (Hartley and Mishin, 2005a) but (3.6) appears to be sufficiently robust if lattice rotations remain small. For a more general identification procedure the reader is referred to (Stukowski et al., 2012).

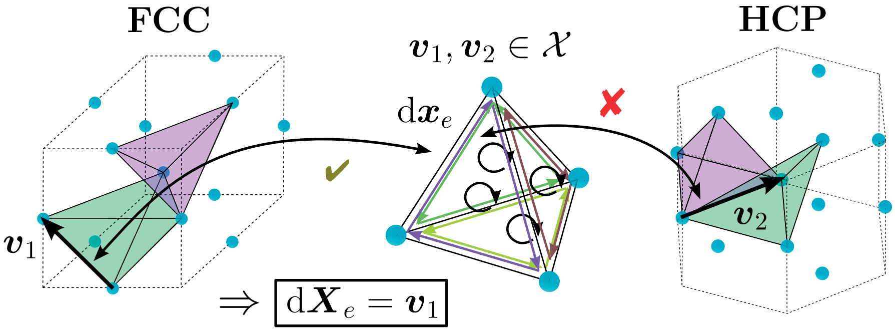
FCC
HCP
$\boldsymbol{v}_1, \boldsymbol{v}_2 \in \mathcal{X}$
$\mathrm{d}\boldsymbol{x}_e$
✓
✗
$\boldsymbol{v}_1$
$\boldsymbol{v}_2$
$\Rightarrow \boxed{\mathrm{d}\boldsymbol{X}_e = \boldsymbol{v}_1}$

Figure 3.7: Schematic illustration of the identification of the reference lattice vectors corresponding to the lattice vectors in the current configuration

In the following it is assumed that each reference lattice vector is computed via the criterion (3.6). The true Burgers vector for each face $f \in \mathcal{T}$ can then be readily identified via

$$\boldsymbol{b}_f = \sum_{e\in f} \mathrm{d}\boldsymbol{X}_e. \tag{3.7}$$

Elements with $\boldsymbol{b}_f \neq \boldsymbol{0}$ for two or more faces are consequently marked as distorted.

Remark 3.4.2. *A particular nice feature of the DXA is the fact that the Burgers vector is unconditionally conserved (c.f. Stukowski, 2014). To see this, assume a tetrahedron with vertices a-d and faces f_1-f_4. A reference lattice vector corresponding an edge e which connects, e.g., a and b is denoted $\mathrm{d}\boldsymbol{X}_e = \mathrm{d}\boldsymbol{X}_{a/b}$. Then,*

$$\begin{aligned}\boldsymbol{b}_{f_1} + \boldsymbol{b}_{f_2} + \boldsymbol{b}_{f_3} + \boldsymbol{b}_{f_4} &= \sum_{e\in f_1} \mathrm{d}\boldsymbol{X}_e + \sum_{e\in f_2} \mathrm{d}\boldsymbol{X}_e + \sum_{e\in f_3} \mathrm{d}\boldsymbol{X}_e + \sum_{e\in f_4} \mathrm{d}\boldsymbol{X}_e \\ &= \quad \mathrm{d}\boldsymbol{X}_{a/b} + \mathrm{d}\boldsymbol{X}_{b/c} + \mathrm{d}\boldsymbol{X}_{c/a} + \mathrm{d}\boldsymbol{X}_{a/c} + \mathrm{d}\boldsymbol{X}_{c/d} + \mathrm{d}\boldsymbol{X}_{d/a} \\ &\quad + \mathrm{d}\boldsymbol{X}_{a/d} + \mathrm{d}\boldsymbol{X}_{d/b} + \mathrm{d}\boldsymbol{X}_{b/a} + \mathrm{d}\boldsymbol{X}_{b/d} + \mathrm{d}\boldsymbol{X}_{d/c} + \mathrm{d}\boldsymbol{X}_{c/b} \\ &= \boldsymbol{0}\end{aligned} \tag{3.8}$$

since the edge vectors mutually cancel.

Algorithm 4 summarizes the relevant steps of the detection algorithm. The algorithm essentially iterates over all $f \in \mathcal{T}$ until a face with non-zero Burgers vector is detected. Subsequently the dislocation line is tracked through the crystal by repetitively identifying the distorted neighbor of the current tetrahedron which also contains f. For each distorted tetrahedron its center of mass is stored in a vector $\hat{p}$. The tracking process aborts if the initial tetrahedron is re-detected or the dislocation terminates at a boundary face. A continuous line representation is then constructed by connecting the elements of the point set $\hat{p}$ via piecewise linear segments. In practice it suffices to use only every N-th node from $\hat{p}$ to prevent the detection of gratuitously many small segments. An educated guess is to choose $N \in \mathcal{O}(10)$ (c.f. Chapter 4.3).

Throughout the remainder of this work Algorithm 4 is used to identify a discrete line representation of atomistic dislocations. A comparison with the algorithm of Begau et al. (2012) has not been carried out since its additional amount of post-processing steps (the computation of $\boldsymbol{F}^{\mathrm{e}}$ and $\boldsymbol{\alpha}$ etc.) seems far less efficient.

3.4.3 Examples

In the following two examples are considered to illustrate the capabilities of the DXA.

Example 3.1 (Edge dislocations in hexagonal lattices). Consider a hexagonal lattice spanned by the basis vectors $\boldsymbol{a}_1 = (a_0, 0)^{\mathsf{T}}$ and $\boldsymbol{a}_2 = \frac{1}{2}(a_0, \sqrt{a_0})^{\mathsf{T}}$, as shown in Figure 3.8. A Lennard-Jones potential is used for this test problem. A dislocation with Burgers vector $\boldsymbol{b} = \boldsymbol{a}_1$ is introduced in the center of the lattice by applying the Volterra displacements of an edge dislocation to the lattice sites (c.f. Appendix A.2.2). The total energy is then minimized and the relaxed configuration is triangulated according to Figure 3.8 (a) followed by the identification of the ideal lattice vectors. Here, the set of ideal lattice vectors $\mathcal{X}$ is the set of all possible primitive basis vectors, i.e. the six vectors shown in

Algorithm 4: Dislocation detection algorithm (**dislocDetn**)

```
Input: Atomistic domain $\Omega^{\mathrm{a}}$
$\mathcal{X} \leftarrow$ define set of ideal lattice vectors;
$\mathcal{T} \leftarrow$ tetrahedralization of $\Omega^{\mathrm{a}}$;
for all $e \in \mathcal{T}$ do
    $\mathrm{d}\boldsymbol{X}_e \leftarrow$ compute the reference lattice vector of edge $e$ using the criterion (3.6);
end
initialize:    $\hat{P} \leftarrow \{\}$;  // set containing all DD nodes
for all $f \in \mathcal{T}$ do
    $\boldsymbol{b}_f \leftarrow$ compute Burgers vector of face $f$ via (3.7);
    if $\boldsymbol{b}_f \neq \mathbf{0}$ then
        initialize:   $\hat{p} \leftarrow \{\}$;  // DD nodes belonging to the same dislocation
        while dislocation line not closed do
            $\hat{p} \leftarrow$ add center of mass of $t_f$;  // optional: project on slip plane
            $t_f \leftarrow$ identify distorted neighboring tetrahedra of $t_f$;
        end
        $\hat{P} \leftarrow$ add $\hat{p}$;
        eliminate distorted faces from $\mathcal{T}$;
    end
end
initialize:    $\mathcal{D} \leftarrow \{\}$;  // set of all dislocations
for all $\hat{p} \in \hat{P}$ do
    $\gamma^{\mathrm{a}} \leftarrow$ generate continuous line representation from the point set $\hat{p}$;
    $\mathcal{D} \leftarrow$ add $\gamma^{\mathrm{a}}$ to the set of discrete atomistic dislocations;
end
Output: Discrete atomistic dislocations $\mathcal{D} := \{\gamma^{\mathrm{a}}_1, ..., \gamma^{\mathrm{a}}_{\#\mathcal{D}}\}$
```

Figure 3.8 (b). The detection algorithm detects the dislocated cell which is highlighted in Figure 3.8 (a). Note the arbitrariness in the detection due to the non-uniqueness of the Delaunay triangulation, that is if the atoms in the vicinity of the dislocation core are slightly perturbed the algorithm may identify the adjacent face below the detected one.

In addition, Figure 3.8 illustrates the difference between the DXA and the detection used in CADD (cf. Section 3.2). The CADD detection only requires an initial triangulation as the deformation gradient $\boldsymbol{F}$ maps the reference configuration in (b) to the distorted configuration (c) and compares the Lagrangian strain $\boldsymbol{E}_e$ for each element with the ideal plastic strains from the set $\mathscr{E}$. Note that the deformed mesh in (c) is not necessarily a tessellation any more if multiple dislocations have passed the detection region. The CADD detection cannot localize the dislocation core since the method uses absolute and not relative displacements. Thus, it appears unsuitable for three dimensional problems as it detects all elements which belong to the entire slip plane as shown in Figure 3.8 (c). The CADD detection thus requires a rather complicated post-processing step in order to identify the boundary elements of $\mathscr{S}$ which belong to the dislocation line. □

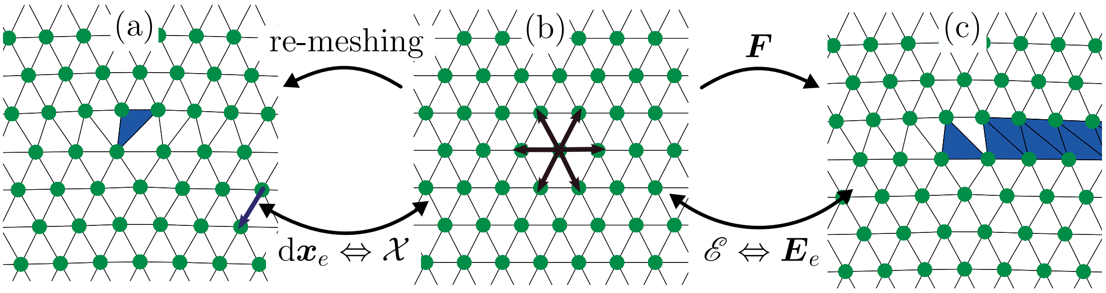
(a)
re-meshing
(b)
$\boldsymbol{F}$
(c)
$\mathrm{d}\boldsymbol{x}_e \Leftrightarrow \mathcal{X}$
$\mathscr{E} \Leftrightarrow \boldsymbol{E}_e$

Figure 3.8: (a) DXA dislocation detection. (b) Perfect lattice. (c) CADD dislocation detection

Example 3.2 (Full and partial dislocations in fcc lattices). The second example is chosen to show the capabilities of the DXA in detecting more complex core structures for three-dimensional problems. Here, an fcc lattice is considered. The interatomic potential is the EAM aluminum potential of Ercolessi and Adams (1994). Upon relaxation the dislocation core is spread over a certain distance. The corresponding stacking fault has a width of ≈ 15 Å. If the set of ideal lattice vectors contains all first and second nearest neighbors of the fcc lattice the DXA detects a full dislocation in center of the core as shown in Figure 3.9 via the green tetrahedra. Vice versa the algorithm may detect the partial dislocations if $\mathcal{X}$ is enriched with the set of ideal lattice vectors corresponding to a hexagonal closed-packed (hcp) lattice. The distorted region which corresponds to the two Shockley partial dislocations is highlighted via the dark blue tetrahedra in Figure 3.9. □

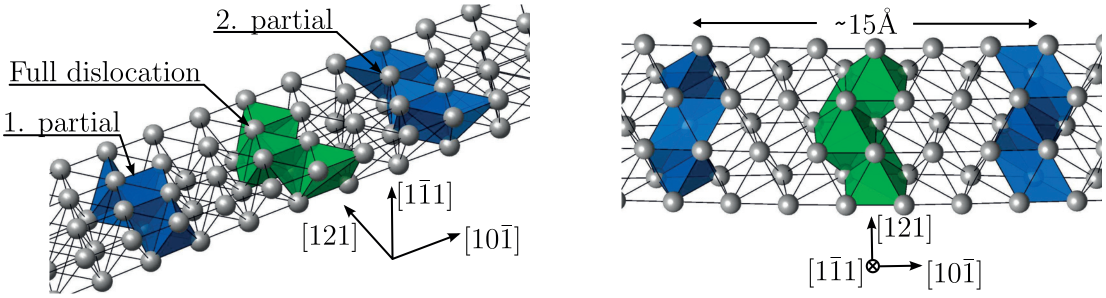

Figure 3.9: Detection of full and partial dislocations in FCC lattices

Both examples show possible applications of the proposed detection algorithm. However, the DXA can handle even more complex dislocation networks. For an impressive collection of examples involving, i.a., crystalline interfaces, grain boundaries etc. the reader is referred to Stukowski et al. (2012).

Remark 3.4.3. *The examples illustrate clearly why it can be superior to think of the dislocation as a finite core region, rather than a continuous line. For a deeper mathematical characterization of dislocations in crystalline lattices the reader is referred to work of Ariza and Ortiz (2005).*

3.5 Dislocation core templates

In this section the boundary conditions on the atomistic problem are discussed. The idea is to define a coupling that is robust in providing a correct atomistic description when the dislocations intersect the coupling interface, such that the atomistic domain responds as if embedded in an immense atomistic domain, i.e. atoms do not "know" that other parts of the material are actually treated by an entirely different method because the forces on the atoms are (almost) exactly the forces that would be generated in the immense (computationally unfeasible) atomistic simulation. This is accomplished through a "template" imposed at the A/C interface that enriches the continuum-line description with an atomistic description of the dislocation core structure. Formally the **core template correction** is defined as a (localized) field $\mathit{\Delta}\tilde{\boldsymbol{u}}^{\text{corr}}$ which is superimposed on the continuum solution such that the pad displacements read

$$\boldsymbol{u}^{\text{p}} = \boldsymbol{u}^{\text{c}} + \mathit{\Delta}\tilde{\boldsymbol{u}}^{\text{corr}}. \tag{3.9}$$

The idea of a core template correction has been originally developed by Dewald and Curtin (2006) in the context of CADD-2d. Junge (2014), Cho et al. (2015) and Anciaux et al. (2018) have shown that the same concept also applies in three dimensions under the assumption that the hybrid dislocations remain straight near the interface $\mathit{\Gamma}_{\text{i}}$ and other dislocations stay sufficiently far from γ^{hyb}. Their approach is adopted in the following.

To review the main steps for constructing $\mathit{\Delta}\tilde{\boldsymbol{u}}^{\text{corr}}$ based on infinite straight dislocations assume a coordinate system, attached to the center of the dislocation, with the usual basis $\{\boldsymbol{e}_i\}_{i=1,\dots,3}$ and axes given by ${}^*x_1$, ${}^*x_2$ and ${}^*x_3$. The axes are chosen such that ${}^*x_1$ is the glide direction, ${}^*x_2$ is the direction normal to the slip plane and ${}^*x_3$ is the line direction. A physical quantity related to this coordinate system is denoted by ${}^*\bullet$. Assume an (effectively) infinite atomic lattice $\mathit{\Lambda}^{\text{a}}$. To insert a dislocation an initial guess ${}^*\tilde{\boldsymbol{u}}$, corresponding to the continuum solution of an infinite straight dislocation (see Appendix A.2), is imposed on $\mathit{\Lambda}^{\text{a}}$. The solution ${}^*\tilde{\boldsymbol{u}}$ is not a minimizer of the atomistic energy. Therefore a *corrective* displacement is sought-after which solves

$$\mathit{\Delta}^*\tilde{\boldsymbol{u}} := \operatorname{Arg}\left\{\min_{{}^*\boldsymbol{v}\in\mathcal{U}^*} \mathit{\Pi}({}^*\tilde{\boldsymbol{u}} + {}^*\boldsymbol{v})\right\}. \tag{3.10}$$

Problem (3.10) can be efficiently solved using flexible boundary conditions or related A/C coupling schemes (c.f. Chapter 2).

In practice it is more convenient to obtain a displacement field independent of the line direction ${}^*x_3$. Therefore the lattice is projected onto the ${}^*x_1^*x_2$-plane. The corresponding projection tensor is defined as

$$\begin{aligned} \boldsymbol{P} &: \mathbb{R}^3 \to \mathbb{R}^2 \\ &{}^*\boldsymbol{x} \mapsto \boldsymbol{P}{}^*\boldsymbol{x} = {}^*\bar{\boldsymbol{x}} = \begin{pmatrix} {}^*x_1 & {}^*x_2 \end{pmatrix}^\mathsf{T} \end{aligned} \tag{3.11}$$

such that

$$\Delta^*\tilde{\boldsymbol{u}}({}^*\bar{\boldsymbol{\xi}}) = \Delta^*\tilde{\boldsymbol{u}}(\boldsymbol{P}{}^*\boldsymbol{\xi}) = \Delta^*\tilde{\boldsymbol{u}}({}^*\xi_1, {}^*\xi_2, 0). \tag{3.12}$$

Since the lattice is translational periodic in the ${}^*x_3$-direction it suffices to project only the lattice sites from the periodic supercell, denoted by $\Lambda^\mathrm{a}_\mathrm{per} \subset \Lambda^\mathrm{a}$. To make (3.12) compatible with $\boldsymbol{u}^\mathrm{c}$ it is asserted that the corrective displacement can be continuously extended to $\Delta^*\tilde{\boldsymbol{u}} : \mathbb{R}^2 \to \mathbb{R}^3$. Therefore a nodal interpolant $\phi_{{}^*\bar{\xi}} \in W^{1,\infty}(\mathbb{R}^2)$ is defined such that $\forall\, {}^*\bar{\boldsymbol{x}} \in \mathbb{R}^2$ it follows

$$\Delta^*\tilde{\boldsymbol{u}}({}^*\bar{\boldsymbol{x}}) = \sum_{{}^*\bar{\boldsymbol{\xi}} \in \boldsymbol{P}\Lambda^\mathrm{a}_\mathrm{per}} \phi_{{}^*\bar{\xi}}({}^*\bar{\boldsymbol{x}}) \Delta^*\tilde{\boldsymbol{u}}({}^*\bar{\boldsymbol{\xi}}). \tag{3.13}$$

A convenient choice is to assume a piecewise linear displacement field. The function $\Delta^*\tilde{\boldsymbol{u}}$ can then be constructed by triangulating $\boldsymbol{P}\Lambda^\mathrm{a}_\mathrm{per}$, as shown in Figure 3.10 (a), and $\phi_{{}^*\bar{\xi}}$ then denotes the standard P1 interpolant. This construction will be used in all numerical experiments in Section 4.3.5.

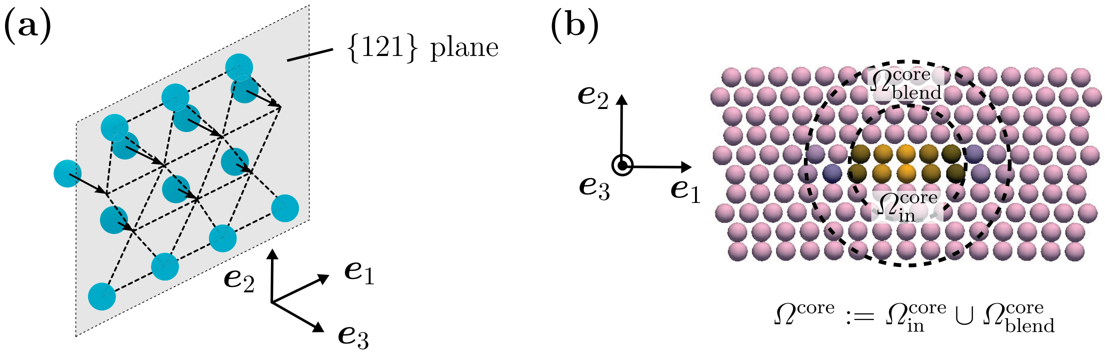
(a)
{121} plane
e_2
e_1
e_3
(b)
e_2
e_3
e_1
$\Omega^\mathrm{core}_\mathrm{blend}$
$\Omega^\mathrm{core}_\mathrm{in}$
$\Omega^\mathrm{core} := \Omega^\mathrm{core}_\mathrm{in} \cup \Omega^\mathrm{core}_\mathrm{blend}$

Figure 3.10: (a) Projection of the lattice sites according to (3.11) for an fcc lattice. (b) Application range of the core template

In practice it suffices to superimpose $\Delta^*\tilde{\boldsymbol{u}}$ on the continuum solution only in some small domain around the dislocation core. This domain is denoted as the *core region* Ω^core. For simplicity Ω^core is assumed to be a cylindrical region, centered on the dislocation line (Figure 3.10 (b)). To ensure a smooth transition, the core region is divided into in an inner region $\Omega^\mathrm{core}_\mathrm{in}$ with radius $r^\mathrm{core}_\mathrm{in}$, where $\Delta^*\tilde{\boldsymbol{u}}$ is fully applied, and a blending region

$\varOmega^{\text{core}}_{\text{blend}}$ with inner radius $r^{\text{core}}_{\text{in}}$ and outer radius $r^{\text{core}} > r^{\text{core}}_{\text{in}}$, given by

$$\varOmega^{\text{core}}_{\text{in}} := \left\{ {}^{*}\bar{\boldsymbol{x}} \in \mathbb{R}^2 \,\middle|\, {}^{*}x_1^2 + {}^{*}x_2^2 < (r^{\text{core}}_{\text{in}})^2 \right\}, \tag{3.14}$$

$$\varOmega^{\text{core}}_{\text{blend}} := \left\{ {}^{*}\bar{\boldsymbol{x}} \in \mathbb{R}^2 \,\middle|\, {}^{*}x_1^2 + {}^{*}x_2^2 < (r^{\text{core}})^2 \right\} \setminus \varOmega^{\text{core}}_{\text{in}}. \tag{3.15}$$

Appropriate choices for $r^{\text{core}}_{\text{in}}$ are discussed below. The smooth "step function" $\lambda \in C^0(\mathbb{R}^2)$, compactly supported on $\varOmega^{\text{core}}$, is defined as

$$\lambda({}^{*}\bar{\boldsymbol{x}}) := \begin{cases} 1 & \text{if } {}^{*}\bar{\boldsymbol{x}} \in \varOmega^{\text{core}}_{\text{in}}, \\ (0,1] & \text{if } {}^{*}\bar{\boldsymbol{x}} \in \varOmega^{\text{core}}_{\text{blend}}, \\ 0 & \text{on else.} \end{cases} \tag{3.16}$$

The (localized) core template correction is then defined $\forall\, {}^{*}\bar{\boldsymbol{x}} \in \mathbb{R}^2$ as

$$\varDelta^{*}\tilde{\bar{\boldsymbol{u}}}^{\text{corr}}(\bar{\boldsymbol{x}}) = \lambda({}^{*}\bar{\boldsymbol{x}})\varDelta^{*}\tilde{\bar{\boldsymbol{u}}}({}^{*}\bar{\boldsymbol{x}}). \tag{3.17}$$

The goal is now to express the core template correction with respect to the general $x_1x_2x_3$-space. For this purpose an orthonormal basis $\{\boldsymbol{e}'_i\}$ is defined as

$$\boldsymbol{e}'_1 = \boldsymbol{m}, \qquad \boldsymbol{e}'_2 = \boldsymbol{n}, \qquad \boldsymbol{e}'_3 = \boldsymbol{t} \tag{3.18}$$

for some glide direction $\boldsymbol{m}$, slip plane normal $\boldsymbol{n}$ and line orientation $\boldsymbol{t}$. A relation between a vector $\boldsymbol{v}'$ with respect to $\{\boldsymbol{e}'_i\}$ and a vector $\boldsymbol{v}$ with respect to $\{\boldsymbol{e}_i\}$ is given by the rotation tensor $\boldsymbol{R} \in SO(3)$, defined by

$$R_{ij} = \boldsymbol{e}'_i \cdot \boldsymbol{e}_j, \qquad \Rightarrow \qquad \boldsymbol{R} = \begin{pmatrix} \boldsymbol{m} & \boldsymbol{n} & \boldsymbol{t} \end{pmatrix} \tag{3.19}$$

such that

$$\boldsymbol{v}' = \boldsymbol{R}\boldsymbol{v}. \tag{3.20}$$

A material point ${}^{*}\boldsymbol{x}$ can then be equivalently expressed in terms of $\boldsymbol{x}$ via a rotation by $\boldsymbol{R}$ and a translation

$${}^{*}\boldsymbol{x} = \boldsymbol{R}\boldsymbol{x} + \boldsymbol{c} \tag{3.21}$$

for some $\boldsymbol{c} \in \mathbb{R}^2$. The core template correction is then generally defined $\forall\, \boldsymbol{x} \in \mathbb{R}^3$ as

$$\varDelta\tilde{\boldsymbol{u}}^{\text{corr}}(\boldsymbol{x}) = \lambda(\boldsymbol{P}\boldsymbol{R}\boldsymbol{x} + \boldsymbol{P}\boldsymbol{c})\boldsymbol{R}^{\mathsf{T}}\varDelta^{*}\tilde{\bar{\boldsymbol{u}}}^{\text{corr}}(\boldsymbol{P}\boldsymbol{R}\boldsymbol{x} + \boldsymbol{P}\boldsymbol{c}). \tag{3.22}$$

Equation (3.22) is now in a suitable form to be superimposed on a general continuum solution $\boldsymbol{u}^{\text{c}}$ in the pad domain in the vicinity of a dislocation core. This application will be made precise in the following section.

As a hybrid dislocation traverses the crystal, its character angle ϑ at the artificial interface $\mathit{\Gamma}_\mathrm{i}$ may evolve. It is not practical to compute $\mathit{\Delta}\tilde{\boldsymbol{u}}^\mathrm{corr}$ on-the-fly for each new ϑ. The strategy proposed in (Anciaux et al., 2018), which is adopted here, is to precompute the core template correction for a given set of N character angles. Given precomputed solutions for some $\vartheta_i \in [0^\circ, ..., 90^\circ]$, $i = 1, ..., N$, the core template correction for *any* $\vartheta \in (0^\circ, ..., 90^\circ)$, where $\vartheta_i < \vartheta < \vartheta_{i+1}$, is obtained by blending the solutions due to its neighboring angles as follows

$$\mathit{\Delta}\tilde{\boldsymbol{u}}^\mathrm{corr}(\boldsymbol{x};\vartheta) = \alpha \mathit{\Delta}\tilde{\boldsymbol{u}}^\mathrm{corr}(\boldsymbol{x};\vartheta_i) + (1-\alpha)\mathit{\Delta}\tilde{\boldsymbol{u}}^\mathrm{corr}(\boldsymbol{x};\vartheta_{i+1}), \qquad \text{with } \alpha = \frac{\vartheta - \vartheta_{i+1}}{\vartheta_i - \vartheta_{i+1}} \tag{3.23}$$

In the remainder of this work it is tacitly assumed that $\mathit{\Delta}\tilde{\boldsymbol{u}}^\mathrm{corr}$ is known for arbitrary character angles.

An adequate size of the core region $\mathit{\Omega}^\mathrm{core}$ can be estimated by analyzing the error between the fully atomistic and the continuum solutions $\boldsymbol{u}^\mathrm{a}$ and $\tilde{\boldsymbol{u}}$, respectively. According to (Ehrlacher et al., 2016, Theorem 5) the pointwise error decays as

$$\|\boldsymbol{u}^\mathrm{a} - \tilde{\boldsymbol{u}}\| \lesssim r^{-1}\log r, \qquad \|\nabla\boldsymbol{u}^\mathrm{a} - \nabla\tilde{\boldsymbol{u}}\|_\mathrm{fro} \lesssim r^{-2}\log r, \tag{3.24}$$

where r is the distance to the center of the dislocation core. Equation (3.24) holds generally for straight dislocations and has been verified in (Anciaux et al., 2018) for various character angles. According to (Anciaux et al., 2018) it suffices in practice to choose an $r^\mathrm{core}_\mathrm{cut}$ slightly beyond the pre-asymptotic regime, which usually comprises the stacking fault of the dislocation. For straight interfaces the error in the gradient of the boundary condition (3.9) can then be readily deduced by integrating $\|\nabla\boldsymbol{u}^\mathrm{a} - \nabla(\tilde{\boldsymbol{u}} - \mathit{\Delta}\tilde{\boldsymbol{u}}^\mathrm{corr})\|_\mathrm{fro}$ over the entire space and using the result (3.24) such that

$$\|\nabla\boldsymbol{u}^\mathrm{a} - \nabla(\boldsymbol{u}^\mathrm{c} - \mathit{\Delta}\tilde{\boldsymbol{u}}^\mathrm{corr})\|_{L^2} = \left(\int_{\mathbb{R}^2} \|\nabla\boldsymbol{u}^\mathrm{a} - \nabla(\boldsymbol{u}^\mathrm{c} - \mathit{\Delta}\tilde{\boldsymbol{u}}^\mathrm{corr})\|^2_\mathrm{fro}\,\mathrm{d}A\right)^{1/2} \tag{3.25}$$

$$\lesssim \left(\int_0^{2\pi}\int_{r^\mathrm{core}_\mathrm{in}}^\infty r^{-4}\log{(r)}^2 r\,\mathrm{d}r\mathrm{d}\theta\right)^{1/2} \tag{3.26}$$

$$\lesssim (r^\mathrm{core}_\mathrm{in})^{-1}\log r. \tag{3.27}$$

As a matter of fact, this decay rate is the same as the one obtained in (Ehrlacher et al., 2016) for various A/C coupling schemes (clamped, QC etc.) up to a log-factor, when interpreting $r^\mathrm{core}_\mathrm{in}$ as the size of the fully atomistic region. Therefore there is (at least theoretically) no advantage of using a costly QC scheme in the bulk material over the CADD-3d boundary condition, yet, it is remarked that this estimate only holds for straight and isolated hybrid dislocations.

Remark 3.5.1. *It would be interesting to know if (and how) a solution based on a generalized continuum can improve the convergence rates* (3.24). *A fully three-dimensional DDD model* *using gradient elasticity has been proposed only recently by Po et al. (2014) which could then possibly replace the classical model used in the present work.*

Remark 3.5.2. *Further, it would be highly desirable to characterize the behavior of the error ϵ induced in the atomistic region due to the boundary condition* (3.9) *as a function of the distance d to the artificial interface $\mathit{\Gamma}_{\mathrm{i}}$. Error estimates of the form*

$$\epsilon(d) \lesssim d^{-\beta}, \tag{3.28}$$

for some $\beta > 0$, could then be used to analyze any spurious effects on the dislocation(s) in $\mathit{\Omega}^{\mathrm{a}}$.

Another possibility to apply a corrective displacement field to the continuum solution which was originally suggested by Junge (2014) is discussed in the following. In (Junge, 2014) a set of N dislocation loops is initially assumed. The continuum solution can then be obtained by a superposition of the solutions due to the individual dislocation lines $\tilde{\boldsymbol{u}}_i$ (c.f. Appendix A.1.3)

$$\boldsymbol{u}^{\mathrm{c}} = \sum_{i=1}^{N} \tilde{\boldsymbol{u}}_i. \tag{3.29}$$

Now assume that the j-th dislocation is a hybrid dislocation. The idea of Junge (2014) is to replace $\tilde{\boldsymbol{u}}_j$ with the atomistic solution $\boldsymbol{u}^{\mathrm{a}} = \tilde{\boldsymbol{u}}_j + \mathit{\Delta}\tilde{\boldsymbol{u}}^{\mathrm{corr}}$ for an infinite straight dislocation, obtained from the optimization problem (3.10), in the sense that

$$\boldsymbol{u}^{\mathrm{c}} = \begin{cases} \displaystyle\sum_{\substack{i=1\\ i\neq j}}^{N} \tilde{\boldsymbol{u}}_i + \boldsymbol{u}^{\mathrm{a}} & \text{in } \mathit{\Omega}^{\mathrm{core}}, \\ \displaystyle\sum_{i=1}^{N} \tilde{\boldsymbol{u}}_i & \text{else.} \end{cases} \tag{3.30}$$

However, this method is generally ill-posed. This can be rationalized, considering the fact that the solution $\tilde{\boldsymbol{u}}_j$ shows a logarithmic divergence with an increasing diameter of the dislocation loop (Appendix A.3.1). This is shown rigorously in Proposition 4. This divergence is *not* contained in $\boldsymbol{u}^{\mathrm{a}}$. Therefore, as the loop expands, a mismatch develops between the displacements in the core region and the remainder of the pad. Therefore this approach is not pursued further in the following.

3.6 Problem formulation

3.6.1 Assumptions

In this section the quasi-static boundary value problem for CADD-3d is formulated. Based on the previous considerations made in Section 3.3-3.5, and to formally define the range of application of the proposed method, the following assumptions are postulated:

Assumption 1. *A geometric linearization in the continuum domain is appropriate, that is*

$$\|\nabla \boldsymbol{u}^{\mathrm{c}}\|_{\mathrm{fro}} \approx 0 \qquad \textit{in } \mathit{\Omega}^{\mathrm{c}}. \tag{3.31}$$

Assumption 2. *The evolution of the entire material body $\mathit{\Omega} := \mathit{\Omega}^{\mathrm{a}} \cup \mathit{\Omega}^{\mathrm{c}}$ is sufficiently slow such that the second time derivative of the displacement becomes negligible small*

$$\left\| \frac{\partial^2 \boldsymbol{u}}{\partial t^2} \right\| \approx 0 \qquad \textit{in } \mathit{\Omega}. \tag{3.32}$$

Therefore a (quasi-)static problem description will be presumed.

Assumption 3. *The dislocation line γ^{a} in the atomistic domain can be unambiguously detected in $\mathit{\Omega}^{\mathrm{a}}$ using Algorithm 4 in the sense that γ^{a} and γ^{c} share the same Burgers vector and the same slip plane with normal $\boldsymbol{n}$. The line direction $\boldsymbol{t}$ of γ^{a} is implicitly defined through γ^{c}.*

Assumption 4. *The core template correction $\mathit{\Delta}\tilde{\boldsymbol{u}}^{\mathrm{corr}}$* (3.23) *is a sufficient approximation to the exact (hypothetical) fully atomistic solution*

$$\boldsymbol{u}^{\mathrm{exact}} = \boldsymbol{u}^{\mathrm{a}} \approx \boldsymbol{u}^{\mathrm{c}} + \mathit{\Delta}\tilde{\boldsymbol{u}}^{\mathrm{corr}} \qquad \textit{in } \mathit{\Omega}^{\mathrm{p}}. \tag{3.33}$$

Equation (3.33) *holds if the following conditions on the hybrid dislocation line γ^{hyb} in the vicinity of the interface $\mathit{\Gamma}_{\mathrm{i}}$ are satisfied:*

- **[C1]** *The hybrid dislocation line remains sufficiently straight such that $\vartheta(\boldsymbol{s}) \approx$ const.*
- **[C2]** *Non-glide components of the shear stress acting on the hybrid dislocation, e.g. Escaig stresses (which are the driving forces for cross-slip; e.g. Escaig, 1968), are negligible such that the core configuration is consistent with the precomputed $\mathit{\Delta}\tilde{\boldsymbol{u}}^{\mathrm{corr}}$, more precisely, the dislocation dissociation remains constant.*
- **[C3]** *Individual hybrid dislocation are clearly separated such that junction formation does not occur.*

Assumption 5. *The motion of γ^{c}, governed by the DDD model, accurately reproduces that of a (hypothetical) fully atomistic dislocation in $\mathit{\Omega}^{\mathrm{c}}$.*

According to Assumption 1 the continuum body behaves linear elastic. A formulation of CADD-3d for geometric nonlinear problems is conceptually possible; research in this direction has been conducted by Deshpande et al. (e.g. 2003); Irani et al. (e.g. 2015) who developed a DDD framework at large deformations for plane strain problems. However, the author is currently not aware of any implementation of a finite strain DDD for three-dimensional problems.

Assumption 2 may be weakened in the sense that real dynamics can in principle be considered in the atomistic domain. A version of CADD-3d at finite temperature, using a fully dynamic atomistic problem, has been developed by Cho (2017); Cho et al. (2018) alongside the present work. On the other hand, a *fully* dynamic problem is unstable in general due to the force-based coupling mechanism (c.f. Dobson et al., 2010; Junge et al., 2015) but possible for certain problems with appropriate thermostatting (c.f. Shiari et al., 2005). However, this requires artificially high damping parameters as shown by Junge et al. (2015). Thus, if real dynamics must be considered, a different coupling mechanism based on a well-defined energy functional has to be employed presumably (see e.g. Dupuy et al., 2005).

With Assumption 1, it follows that the assumption of small deformations presumably hold in parts of atomistic domain which are close to the artificial interface — except in regions where the dislocation lines crosses $\mathit{\Gamma}_{\mathrm{i}}$, that is in $\mathit{\Omega}^{\mathrm{core}}$. The influence of lattice rotations in this region can thus safely be neglected which emphasizes that Algorithm 4 should satisfy Assumption 3.

Further, it is noteworthy that the DXA detects a representation of the atomistic dislocation line in the *current* configuration, a fact which has been left aside so far. However, the continuum problem necessitates a description of the dislocation line in the *reference* configuration as the Peach-Koehler force is a force per reference unit length (since the Eshelby stress tensor is defined with respect to the material frame; c.f. Section 1.4.1). Hence, in order to identify the reference placement γ_0^{a} corresponding to γ^{a} it is assumed that a bijective mapping $\chi : \gamma_0^{\mathrm{a}} \to \gamma^{\mathrm{a}}$ must exist such that

$$\gamma_0^{\mathrm{a}} := \left\{ \chi^{-1}(\boldsymbol{s}) = \boldsymbol{s} - \boldsymbol{u}^{\mathrm{a}}(\chi^{-1}(\boldsymbol{s})) \,|\, \boldsymbol{s} \in \gamma^{\mathrm{a}} \right\}, \tag{3.34}$$

Due to Assumption 1 the displacement gradient is small but *displacements* themselves can still be large if the net Burgers vector is large. On the other hand, Assumption 1 also excludes the potential occurrence of large net Burgers vectors which is manifested in the following remark:

Remark 3.6.1. *Statement* (3.35) *can indeed be justified by considering Assumption 1. Recall that lattice rotations become negligible if displacement gradients are small. The density of geometric necessary dislocations (GNDs), which is the measure of lattice curvature*[2] *and depends linearly on the net Burgers vector, is therefore insignificant. Hence, the net displacement should be small around some control volume at the A/C interface such that differences between reference and current configurations* γ^{a} *and* γ_0^{a}*, respectively, can be safely neglected.*

Therefore

$$\gamma^{\mathrm{a}} \approx \gamma_0^{\mathrm{a}} \tag{3.35}$$

is asserted to hold throughout the remainder of this work.

---

[2] This is due to the fact that an edge dislocation introduces a bending moment with respect to the center of the dislocation core

3.6.2 Governing equations

Anciaux et al. (2018) were first to present a general methodology for the coupling of a finite atomistic domain $\varOmega^{\mathrm{a}}$ to a (possibly infinite) continuum domain $\varOmega^{\mathrm{c}}$ described by DDD, for systems containing dislocations spanning both domains, i.e. hybrid dislocations formed by the intersection of the two lines γ^{a} and γ^{c}. At any instant or increment of loading, the atomistic problem involves the interactions of atoms via interatomic potentials subjected to boundary conditions on a surrounding atomistic pad region $\varOmega^{\mathrm{p}} \subset \varOmega^{\mathrm{c}}$ whose atomic positions are dictated by the solution of the continuum dislocations problem. The associated continuum problem involves a small-strain elasticity solution of a DDD problem subjected to the displacement boundary conditions associated with atomic positions at the A/C interface plus any boundary conditions applied on the external boundaries. For hybrid dislocations, the continuum displacement field in the pad region is enriched by the addition of a corrective displacement field $\varDelta\tilde{\boldsymbol{u}}^{\mathrm{corr}}(\boldsymbol{x}) = \varDelta\tilde{\boldsymbol{u}}^{\mathrm{corr}}(\boldsymbol{x}; \vartheta^{\mathrm{p}}, \boldsymbol{b})$ that approximates the true atomistic core structure of the hybrid dislocation at the interface with character angle ϑ^{p} and Burgers vector $\boldsymbol{b}$. An algorithm for the simultaneous evolution of both atomistic and continuum domains was then presented for the case of full quasi-dynamic coupling (quasi-static evolution of the dislocation dynamics problem).

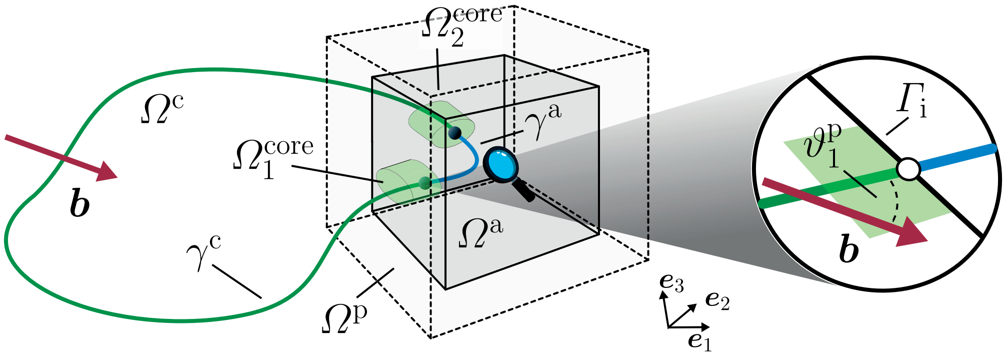

Figure 3.11: Schematic illustration of the boundary value problem for CADD-3d

A formulation of CADD-3d for fully quasi-static problems has been presented by Hodapp et al. (2018a) which is considered in the following. Without loss of generality attention is drawn to systems containing a single hybrid dislocation γ^{hyb}. This can be a closed loop, as shown in Figure 3.11, or a line which pierces the continuum region with both ends on the outer boundary. Using Assumption 4, **[C3]**, the framework can be generalized directly to an arbitrary number of (hybrid) dislocations by merely changing the notation (i.e. by a summation over all hybrid dislocations in the system).

Here, the creation of hybrid dislocations by the impingement of dislocations onto the interface region, whether originating from the atomistic or continuum domains, is not addressed. It is emphasized that a dislocation passing between both domains is fundamentally an algorithmic question and is thus not relevant for the definition of the boundary value problem. To be more precise, assume for a moment that the dislocation loop resides solely in one region. If a portion of the loop is now passed to the other domain it becomes a hybrid dislocation by construction, i.e. the generic state (Figure 3.11) is then recovered. For a recent discussion on dislocation passing in the context of CADD-3d the reader is referred to (Cho, 2017; Cho et al., 2018).

In accordance with Assumption 4, **[C1]** it is appropriate to prescribe the parts of γ^{c} in the pad region with *straight segments* such that the character angle in $\varOmega^{\mathrm{p}}$ is uniquely defined. In Figure 3.11 the dislocation loop passes the interface $\varGamma_{\mathrm{i}}$ two times. The Burgers vector remains constant over the whole loop but the character angles may differ, i.e. $\vartheta_1^{\mathrm{p}} \neq \vartheta_2^{\mathrm{p}}$. The total core correction with respect to $\varOmega^{\mathrm{core}} := \varOmega_1^{\mathrm{core}} + \varOmega_2^{\mathrm{core}}$ must then be defined as

$$\varDelta\tilde{\boldsymbol{u}}^{\mathrm{corr}}(\boldsymbol{x}) = \varDelta\tilde{\boldsymbol{u}}^{\mathrm{corr}}(\boldsymbol{x};\vartheta_1^{\mathrm{p}}) + \varDelta\tilde{\boldsymbol{u}}^{\mathrm{corr}}(\boldsymbol{x};\vartheta_2^{\mathrm{p}}), \tag{3.36}$$

with $\varDelta\tilde{\boldsymbol{u}}_i^{\mathrm{corr}}(\boldsymbol{x};\vartheta_i^{\mathrm{p}})$ given

$$\forall\,\boldsymbol{x} \in \varOmega^{\mathrm{p}} \qquad \varDelta\tilde{\boldsymbol{u}}_i^{\mathrm{corr}}(\boldsymbol{x};\vartheta_i^{\mathrm{p}}) = \begin{cases} \boldsymbol{R}^{\mathsf{T}}\varDelta^{*}\tilde{\tilde{\boldsymbol{u}}}^{\mathrm{corr}}(\boldsymbol{P}\boldsymbol{R}\boldsymbol{x} + \boldsymbol{P}\boldsymbol{c};\vartheta_i) & \text{in } \varOmega_i^{\mathrm{core}}, \\ \hfill \boldsymbol{0} & \text{else}, \end{cases} \tag{3.37}$$

according to (3.22)/(3.23). The (precomputed) core correction (3.36) is then added to the continuum elasticity solution. Vice versa, the core correction has to be *subtracted* from the interface displacements $\boldsymbol{u}^{\mathrm{i}}$, which provide the physical boundary condition on the continuum problem. More precisely, since the atomic displacements $\boldsymbol{u}^{\mathrm{i}}$ correspond to the *real* core structure, the core correction has to be considered in the reverse way in order to avoid spurious forces on γ^{c} in the vicinity of the artificial interface due to the fact that the DDD problem “expects” Peach-Koehler forces in response to the continuum elasticity solution (c.f. Section 3.3.2).

Given the Assumptions 1-5 and the above schematic background of the method, the solution of the *quasi-static* coupled problem can now more carefully be defined as the fields $\boldsymbol{u}^{\mathrm{a}}$, $\boldsymbol{u}^{\mathrm{c}}$ and γ^{c} that solve

$$\boxed{\mathcal{P}^{\mathrm{cadd}} \quad \left\{ \begin{array}{ll} \underline{\text{Atomistic problem } \mathcal{P}^{\mathrm{a}}}\text{:} & \\ \qquad \boldsymbol{f}^{\mathrm{a}} - \boldsymbol{f}^{\mathrm{ext}} = \boldsymbol{0} & \text{in } \varOmega^{\mathrm{a}}, \\ \qquad \boldsymbol{u}^{\mathrm{a}} = \boldsymbol{u}^{\mathrm{c}} + \varDelta\tilde{\boldsymbol{u}}^{\mathrm{corr}} & \text{in } \varOmega^{\mathrm{p}}, \\ \underline{\text{Continuum problem } \mathcal{P}^{\mathrm{c}}}\text{:} & \\ \nabla\cdot\boldsymbol{\sigma} + \boldsymbol{f}^{\mathrm{body}} = \boldsymbol{0} & \text{in } \varOmega^{\mathrm{c}}, \\ \qquad \boldsymbol{u}^{\mathrm{c}} = \boldsymbol{u}^{\mathrm{a}} - \varDelta\tilde{\boldsymbol{u}}^{\mathrm{corr}} & \text{on } \varGamma_{\mathrm{i}}, \\ \quad \boldsymbol{f}^{\mathrm{pk}} + \boldsymbol{f}^{\mathrm{core}} = \boldsymbol{0} & \text{on } \gamma^{\mathrm{c}}, \\ \qquad \gamma^{\mathrm{c}} = \gamma^{\mathrm{a}} & \text{on } \varGamma_{\mathrm{i}}, \end{array} \right.} \tag{3.38}$$

where $\mathcal{P}^{\mathrm{c}} := \mathcal{P}^{\mathrm{c/p}} \wedge \mathcal{P}^{\mathrm{c/dd}}$, as defined in Section 1.4.2. Note that the natural boundary conditions (displacements/tractions) on the outer boundary $\partial\Omega^{\mathrm{c}} \setminus \Gamma_{\mathrm{i}}$ are omitted for compactness.

Remark 3.6.2. *The definition of the boundary condition $\gamma^{\mathrm{c}} = \gamma^{\mathrm{a}}$ on Γ_{i} is not a necessary condition by any means. As a matter of fact, it could have likewise been omitted. However, evolving discrete dislocations along surfaces may be cumbersome (c.f. Crone et al., 2014). Using this boundary condition, γ^{c} evolves implicitly through the motion of the atoms in the vicinity of Γ_{i}.*

The physical subproblem $\mathcal{P}^{\mathrm{p}} := \mathcal{P}^{\mathrm{a}} \wedge \mathcal{P}^{\mathrm{c/p}}$ is nothing but a standard force-based coupling (c.f. Section 2.3.3). However, the *fully* coupled problem $\mathcal{P}^{\mathrm{cadd}}$ is non-standard due to the boundary condition $\gamma^{\mathrm{c}} = \gamma^{\mathrm{a}}$ on Γ_{i}. The definition of such a boundary condition suggests that there exists a coupling operator which relates the displacement of the atoms to a displacement of the discrete dislocation. However, this *cannot* be a differential operator since the dislocation detection, which maps the atomic lattice to a set of discrete dislocations, is essentially an *algorithmic* operator. Thus, problem (3.38) cannot be easily written as a (global) linearized system of equations to analyze its stability properties. Thus, a fully monolithic solution procedure to $\mathcal{P}^{\mathrm{cadd}}$, which requires such a global stability analysis, is not considered. Rather, an efficient *semi-monolithic* algorithm will be constructed in the following section which circumvents a fully concurrent motion.

3.7 Semi-monolithic solution procedure

In this section an iterative solution procedure for $\mathcal{P}^{\mathrm{cadd}}$ is presented. A related algorithm has been proposed by Hodapp et al. (2018a), however, their method is based on a nested *three-way* staggered scheme which iterates between the atomistic problem $\mathcal{P}^{\mathrm{a}}$ and the continuum problem $\mathcal{P}^{\mathrm{c}}$, wherein $\mathcal{P}^{\mathrm{c}}$ itself is solved via an alternating procedure between the physical problem $\mathcal{P}^{\mathrm{c/p}}$ and the DDD problem $\mathcal{P}^{\mathrm{c/dd}}$. Despite its simplicity and excellent stability properties it seems counterproductive to employ such a staggered scheme for CADD-3d, especially in light of Section 2.7.4, since much of its potential efficiency is likely to be lost. Therefore a semi-monolithic approach using a *two-way* staggered solution procedure is proposed in the following, which iterates between the *entire* physical problem and the DDD problem.

Preparation

Applying a fully coupled solver to the physical problem $\mathcal{P}^{\mathrm{p}}$ requires some initial discussion of the problem $\mathcal{P}^{\mathrm{c/p}}$. Allowing for discrete dislocations in the continuum domain imposes a distributive source term (:= the plastic strain) on the momentum balance which renders the solution $\boldsymbol{u}^{\mathrm{c}}$ discontinuous on the slip plane, i.e. $\boldsymbol{u} \notin \mathcal{V}(\Omega^{\mathrm{c}})$. At this point classical numerical methods, such as the finite element method (FEM), usually fail. More advanced methods have been proposed by various research groups, i.a. the extended FEM (XFEM, Moës et al., 1999) which uses special enrichment functions accounting for the discontinuity of the solution vector (e.g. Gracie et al., 2007, 2008).

Another common approach, which is pursued here, is the *superposition method* (c.f. Appendix A.1.3; see also Lubarda et al., 1993; Weygand et al., 2002, in the context of DDD). The superposition method splits $\mathcal{P}^{\mathrm{c/p}}$ into a homogeneous problem (the $\tilde{\bullet}$ fields) in $\mathbb{R}^3$ which accommodates the discontinuity induced by the presence of a dislocation line γ (:= $\partial\mathscr{S}$) and is solved exactly (see below), and a corrective problem (the $\hat{\bullet}$ fields) which accounts for the boundary conditions on $\partial\Omega^{\mathrm{c}}$. The problem then reads: find $\tilde{\boldsymbol{u}}(\gamma) \in [C(\Omega^{\mathrm{c}} \setminus \mathscr{S})]^3$ and $\hat{\boldsymbol{u}}(\gamma) \in [H^2(\Omega^{\mathrm{c}})]^3$ such that

$$\mathcal{P}^{\mathrm{c/p}} \quad \begin{cases} \underline{\text{Infinite problem } \tilde{\mathcal{P}}^{\mathrm{c/p}}\text{:}} & \\ \qquad \nabla\cdot\tilde{\boldsymbol{\sigma}}(\gamma) = \boldsymbol{0} & \text{in } \mathbb{R}^3, \\ \underline{\text{Corrective problem } \hat{\mathcal{P}}^{\mathrm{c/p}}\text{:}} & \\ \nabla\cdot\hat{\boldsymbol{\sigma}}(\gamma) + \boldsymbol{f}^{\mathrm{body}} = \boldsymbol{0} & \text{in } \Omega^{\mathrm{c}}, \\ \qquad \hat{\boldsymbol{u}}(\gamma) = \bar{\boldsymbol{u}}^{\mathrm{c}} - \tilde{\boldsymbol{u}}(\gamma) & \text{on } \partial_{\mathrm{u}}\Omega^{\mathrm{c}}, \\ \qquad \hat{\boldsymbol{t}}(\gamma) = \bar{\boldsymbol{t}} - \tilde{\boldsymbol{t}}(\gamma) & \text{on } \partial_{\mathrm{t}}\Omega^{\mathrm{c}}. \end{cases} \tag{3.39}$$

The full solution and the stress field are then given by

$$\boldsymbol{u}^{\mathrm{c}} = \tilde{\boldsymbol{u}}(\gamma) + \hat{\boldsymbol{u}}(\gamma), \qquad \boldsymbol{\sigma} = \tilde{\boldsymbol{\sigma}}(\gamma) + \hat{\boldsymbol{\sigma}}(\gamma). \tag{3.40}$$

A general analytical solution $\tilde{\boldsymbol{u}}(\gamma)$ to $\tilde{\mathcal{P}}^{\mathrm{c/p}}$ can be obtained by means of the Burgers equation for anisotropic media (c.f. Appendix A.3.1). The Burgers equation is a representation of $\tilde{\boldsymbol{u}}(\gamma)$ as a line integral over γ. In what follows use is made of the fact that, given two segments $\gamma_1 \subset \gamma$ and $\gamma_2 = \gamma \setminus \gamma_1$, the total solution can be obtained by summing up the individual contributions $\tilde{\boldsymbol{u}}(\gamma_1)$ and $\tilde{\boldsymbol{u}}(\gamma_2)$

$$\tilde{\boldsymbol{u}}(\gamma) = \tilde{\boldsymbol{u}}(\gamma_1) + \tilde{\boldsymbol{u}}(\gamma_2). \tag{3.41}$$

However, it should be noted that $\tilde{\boldsymbol{u}}(\gamma_1)$ and $\tilde{\boldsymbol{u}}(\gamma_2)$ alone do not have a physical meaning since a dislocation cannot end within the domain.

The superposition method requires explicit knowledge of the hybrid dislocation in order to obtain the solution $\tilde{\boldsymbol{u}}(\gamma^{\mathrm{hyb}})$. In principle γ^{hyb} can be reconstructed by a dislocation detection of γ^{a} in the entire atomistic domain (another algorithm based thereon will in fact be proposed in the following section). However, this adds gratuitous computational effort to the problem due to the fact that, even though the solution $\tilde{\boldsymbol{u}}$ depends on γ^{a}, the full solution $\boldsymbol{u}^{\mathrm{c}}$ does *not* depend on the precise location of the discrete atomistic dislocation since the boundary condition on $\partial\Omega^{\mathrm{c}}$ is unconditionally satisfied due to the corrective problem $\hat{\mathcal{P}}^{\mathrm{c/p}}$. It is thus more practical to detect the dislocation only in some small part Ω^{detn} in the vicinity of the artificial interface (Figure 3.12) to ensure that the location of the discontinuity is properly captured by $\gamma^{\mathrm{detn}} \subset \gamma^{\mathrm{a}}$. In the remainder of the atomistic domain the dislocation can be artificially closed by a composition of virtual segments $\gamma^{\mathrm{a}}_{\mathrm{v}}$ (c.f. Anciaux et al., 2018). The "fictitious" dislocation line in the atomistic domain is the given by $\tilde{\gamma}^{\mathrm{a}} := \gamma^{\mathrm{detn}} \cup \gamma^{\mathrm{a}}_{\mathrm{v}}$ and the entire loop, used to compute the $\tilde{\bullet}$ fields, will be denoted $\tilde{\gamma}^{\mathrm{hyb}} := \tilde{\gamma}^{\mathrm{a}} \cup \gamma^{\mathrm{c}}$.

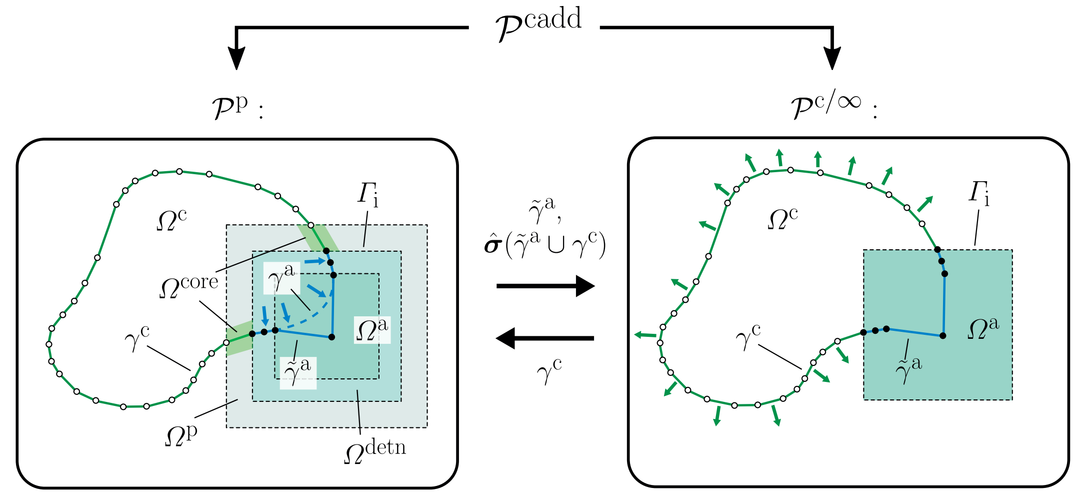
$\mathcal{P}^{\mathrm{cadd}}$
$\mathcal{P}^{\mathrm{p}}$:
$\mathcal{P}^{\mathrm{c}/\infty}$:
Ω^{c}
Γ_{i}
Ω^{core}
γ^{a}
Ω^{a}
γ^{c}
$\tilde{\gamma}^{\mathrm{a}}$
Ω^{p}
Ω^{detn}
$\tilde{\gamma}^{\mathrm{a}}$,
$\hat{\boldsymbol{\sigma}}(\tilde{\gamma}^{\mathrm{a}} \cup \gamma^{\mathrm{c}})$
γ^{c}
Ω^{c}
Γ_{i}
γ^{c}
Ω^{a}
$\tilde{\gamma}^{\mathrm{a}}$

Figure 3.12: Schematic illustration of the problem decomposition of $\mathcal{P}^{\mathrm{cadd}}$ (3.38) corresponding to the semi-monolithic solution procedure from Section 3.7

Description of the algorithm

Before formulating the actual algorithm the two subproblems are discussed as they are shown in Figure 3.12. Here, the hybrid dislocation line $\tilde{\gamma}^{\mathrm{hyb}}$ is composed of straight segments. Further, it is assumed that the motion of the straight segment in Ω^{core} is constrained such the outer node (in Ω^{c}) cannot enter the pad region. Therefore the core template correction is consistently well-defined. Hence, given $\tilde{\gamma}^{\mathrm{hyb}}$, the physical subproblem reads: find $\boldsymbol{u}^{\mathrm{a}}$ and $\boldsymbol{u}^{\mathrm{c}}$ such that

$$\mathcal{P}^{\mathrm{p}} \quad \left\{ \begin{array}{lll} \underline{\text{Atomistic problem } \mathcal{P}^{\mathrm{a}}}: & & \\ \qquad \boldsymbol{f}^{\mathrm{a}} - \boldsymbol{f}^{\mathrm{ext}} &= \boldsymbol{0} & \text{in } \Omega^{\mathrm{a}}, \\ \qquad \boldsymbol{u}^{\mathrm{p}} &= \tilde{\boldsymbol{u}} + \Delta\tilde{\boldsymbol{u}}^{\mathrm{corr}} + \hat{\boldsymbol{u}} & \text{in } \Omega^{\mathrm{p}}, \\ \underline{\text{Physical continuum problem } \mathcal{P}^{\mathrm{c/p}}}: & & \\ \qquad \nabla \cdot \tilde{\boldsymbol{\sigma}} &= \boldsymbol{0} & \text{in } \mathbb{R}^3, \\ \nabla \cdot \hat{\boldsymbol{\sigma}} + \boldsymbol{f}^{\mathrm{body}} &= \boldsymbol{0} & \text{in } \Omega^{\mathrm{c}}, \\ \qquad \hat{\boldsymbol{u}} &= \boldsymbol{u}^{\mathrm{a}} - \tilde{\boldsymbol{u}} - \Delta\tilde{\boldsymbol{u}}^{\mathrm{corr}} & \text{on } \Gamma_{\mathrm{i}}, \end{array} \right. \tag{3.42}$$

omitting the external boundary conditions. The physical problem consists of three balance equations, namely (1) the atomistic force balance $\mathcal{P}^{\mathrm{a}}$, (2) the balance of linear momentum in $\mathbb{R}^3$ $\tilde{\mathcal{P}}^{\mathrm{c/p}}$ due to the presence of the dislocation $\tilde{\gamma}^{\mathrm{hyb}}$ and (3) the corrective problem $\hat{\mathcal{P}}^{\mathrm{c/p}}$ which accounts for the prescribed boundary conditions. The solution $\tilde{\boldsymbol{u}}$ and the stress field $\tilde{\boldsymbol{\sigma}}$ are assumed to be known at any instant in the remainder of this chapter (c.f. Appendix A.3.1). Thus, the only unknowns which have to be determined numerically are the atomic displacements $\boldsymbol{u}^{\mathrm{a}}$ and the corrective solution $\hat{\boldsymbol{u}}$. Since weak solutions to $\hat{\mathcal{P}}^{\mathrm{c/p}}$ are in $\mathcal{V}(\Omega^{\mathrm{c}})$ the atomistic/DBEM coupling, introduced in Chapter 2, is particularly suited to solve $\mathcal{P}^{\mathrm{a}} \wedge \hat{\mathcal{P}}^{\mathrm{c/p}}$; but any other conventional atomistic/FEM scheme could be used likewise.

Using a (temporary) output of the physical problem, i.e. the location of $\tilde{\gamma}^{\mathrm{a}}$ and the stress field $\boldsymbol{\sigma}$, The DDD problem evolves the dislocation line γ^{c} in the continuum domain. Here, the DDD problem is assumed to be solved together with $\tilde{\mathcal{P}}^{\mathrm{c/p}}$ due to the fact that the stress field $\tilde{\boldsymbol{\sigma}}$ on γ^{c} has to be recomputed as the dislocation line advances in search of equilibrium. Thus, it is more adequate to use the stress field due to the momentary position of γ^{c}, rather than the stress field due its initial location. Then, given $\tilde{\gamma}^{\mathrm{a}}$ and $\hat{\boldsymbol{\sigma}}$, the problem reads: find γ^{c} such that

$$\mathcal{P}^{\mathrm{c}/\infty} \quad \begin{cases} \underline{\text{Infinite problem } \tilde{\mathcal{P}}^{\mathrm{c/p}}}: & \\ \qquad \nabla \cdot \tilde{\boldsymbol{\sigma}} = \boldsymbol{0} & \text{in } \mathbb{R}^3, \\ \underline{\text{DDD problem } \mathcal{P}^{\mathrm{c/dd}}}: & \\ \boldsymbol{f}^{\mathrm{pk}} + \boldsymbol{f}^{\mathrm{core}} = \boldsymbol{0} & \text{on } \gamma^{\mathrm{c}}, \\ \qquad\quad \gamma^{\mathrm{c}} = \tilde{\gamma}^{\mathrm{a}} & \text{on } \Gamma_{\mathrm{i}}. \end{cases} \tag{3.43}$$

If the dislocation line is discretized into straight segments, the force on the dislocation line is usually interpolated between the nodes. The problem $\mathcal{P}^{\mathrm{c/dd}}$ is then solved in a weak sense with respect to the nodal positions. The precise details on the numerical treatment can be found elsewhere (e.g. Hirth and Lothe, 1982; Weygand et al., 2002; Cai et al., 2006; Arsenlis et al., 2007).

The entire solution procedure, designated as Algorithm 5, is presented in detail in the following. The algorithm is formulated in a multiplicative way, yet an additive procedure may also be possible. An iteration between the different subproblems is referred to as a *global* iteration k. Quantities in the k-th step are consequently denoted $\bullet_k$. A *local* iteration, i.e. an iteration of the nonlinear solver corresponding one of the subproblems, is specified with the index j and a quantity at global iteration k and local iteration j, i.e. at (k, j), is consequently denoted as $\bullet_{k,j}$. To make the entire solution procedure precise, an initial configuration for the entire system is selected first. A schematic illustration is shown in Figure 3.14 (a) for a dislocation segment in the vicinity of the interface spanning both domains. This configuration at iteration k is specified by the displacements of both real atoms in Ω^{a}_k and pad atoms in Ω^{p}_k as well as the nodal positions of the discrete hybrid

1. Compute the DDD displacements $\tilde{\boldsymbol{u}}(\gamma^{\mathrm{c}}_{k})$ in $\Omega^{\mathrm{p}} \cup \Gamma_{\mathrm{i}}$. **[Pre-processing]**

2. Assemble the DDD displacements for the *closed* loop $\tilde{\gamma}^{\mathrm{hyb}}_{k,j-1} := \tilde{\gamma}^{\mathrm{a}}_{k,j-1} \cup \gamma^{\mathrm{c}}_{k}$, i.e. compute

$$\tilde{\boldsymbol{u}}(\tilde{\gamma}^{\mathrm{hyb}}_{k,j-1}) = \tilde{\boldsymbol{u}}(\tilde{\gamma}^{\mathrm{a}}_{k,j-1}) + \tilde{\boldsymbol{u}}(\gamma^{\mathrm{c}}_{k}) \qquad \text{in } \Omega^{\mathrm{p}} \cup \Gamma_{\mathrm{i}};\,. \tag{3.44}$$

3. **Boundary condition on $\mathcal{P}^{\mathrm{a}}$.** Set

$$\boldsymbol{u}^{\mathrm{p}}_{k,j} = \boldsymbol{u}^{\mathrm{c}}_{k,j-1} + \Delta\tilde{\boldsymbol{u}}^{\mathrm{corr}}_{k,j} \qquad \text{in } \Omega^{\mathrm{p}}, \tag{3.45}$$

where the continuum displacements are given by

$$\boldsymbol{u}^{\mathrm{c}}_{k,j-1} = \tilde{\boldsymbol{u}}(\tilde{\gamma}^{\mathrm{hyb}}_{k,j-1}) + \hat{\boldsymbol{u}}(\tilde{\gamma}^{\mathrm{hyb}}_{k,j-1}), \tag{3.46}$$

with the corrective displacement $\hat{\boldsymbol{u}}(\tilde{\gamma}^{\mathrm{hyb}}_{k,j-1})$ from iteration $j-1$.

Boundary condition on $\hat{\mathcal{P}}^{\mathrm{c/p}}$. Set

$$\hat{\boldsymbol{u}}_{k,j} = \boldsymbol{u}^{\mathrm{a}}_{k,j-1} - \tilde{\boldsymbol{u}}(\tilde{\gamma}^{\mathrm{hyb}}_{k,j-1}) - \Delta\tilde{\boldsymbol{u}}^{\mathrm{corr}}_{k,j} \qquad \text{on } \Gamma_{\mathrm{i}}. \tag{3.47}$$

Figure 3.13: Artificial boundary conditions on the physical subproblem $\mathcal{P}^{\mathrm{p}}$ from Algorithm 5, line 4, at any iteration j of the numerical solver

dislocation $\tilde{\gamma}^{\mathrm{hyb}}_{k}$. The defined physical problem $\mathcal{P}^{\mathrm{c/p}}$ is then solved up to a prescribed tolerance. This problem requires as an input the discrete dislocation γ^{c} from the previous iteration in order to compute the boundary conditions. The boundary conditions that are imposed on $\mathcal{P}^{\mathrm{c/p}}$ in every iteration (k, j) are described in Figure 3.13. Note that γ^{c}_{k} is held fixed such that the corresponding displacement field $\tilde{\boldsymbol{u}}(\gamma^{\mathrm{c}}_{k})$ can be computed a priori. On the other hand, the contribution $\tilde{\boldsymbol{u}}(\tilde{\gamma}^{\mathrm{a}}_{k,j})$ due to $\tilde{\gamma}^{\mathrm{a}}_{k,j}$ has to updated in every j-th step. However, the associated computational cost is assumed to be negligible, compared to an evaluation of the atomic force vector, since the detection domain Ω^{detn} is only a small portion of Ω^{a}.[3] As a result the dislocation in the atomistic domain evolves as shown in Figure 3.14 (b). Subsequently the discrete dislocation problem $\mathcal{P}^{\mathrm{c/dd}}$ is solved to evolve the dislocation nodes residing in the continuum domain, as shown in Figure 3.14 (c). With the new continuum dislocation line, the boundary conditions on Ω^{p} and Γ_{i} are then updated using the new displacement field of the dislocation network. The above steps are performed iteratively until convergence is obtained, e.g. when the incremental differences between two iterates of the solution falls below some tolerance.

---

[3] In practice it may actually suffice to recompute $\tilde{\gamma}^{\mathrm{a}}_{k,j}$ only every (k, N)-th step, where $N \in \mathcal{O}(10)$, but this remains to be verified

Algorithm 5: Semi-monolithic algorithm for CADD-3d

```
Input: Initial state $(\boldsymbol{u}^{\mathrm{a}}, \boldsymbol{u}^{\mathrm{c}}, \tilde{\gamma}^{\mathrm{hyb}})_0$
$k \leftarrow 0$;
repeat
    /* Physical problem $\mathcal{P}^{\mathrm{c/p}}$ */
    $\tilde{\boldsymbol{u}}(\gamma^{\mathrm{c}}_k) \leftarrow$ compute the DDD displacements due to $\gamma^{\mathrm{c}}_k$ in $\Omega^{\mathrm{p}} \cup \Gamma_{\mathrm{i}}$;
    $(\boldsymbol{u}^{\mathrm{a}}, \boldsymbol{u}^{\mathrm{c}}, \tilde{\gamma}^{\mathrm{a}})_{k+1} \leftarrow$ solve (3.42);
    /* Infinite problem $\mathcal{P}^{\mathrm{c}/\infty}$ */
    initialize: $j \leftarrow 0$, $\gamma^{\mathrm{c}}_{k,j} \leftarrow \gamma^{\mathrm{c}}_k$, $\tilde{\gamma}^{\mathrm{hyb}}_{k+1/2,j} \leftarrow \tilde{\gamma}^{\mathrm{a}}_{k+1} \cup \gamma^{\mathrm{c}}_{k,j}$;
    while $\|\boldsymbol{f}^{\mathrm{pk}} + \boldsymbol{f}^{\mathrm{core}}\|_{L^2(\gamma^{\mathrm{c}})} < TOL$ do
        compute on $\gamma^{\mathrm{c}}_{k,j}$: $\boldsymbol{\sigma}(\tilde{\gamma}^{\mathrm{hyb}}_{k+1/2,j}) \leftarrow \tilde{\boldsymbol{\sigma}}(\tilde{\gamma}^{\mathrm{hyb}}_{k+1/2,j}) + \hat{\boldsymbol{\sigma}}(\tilde{\gamma}^{\mathrm{a}}_{k+1} \cup \gamma^{\mathrm{c}}_k)$;
        compute on $\gamma^{\mathrm{c}}_{k,j}$: $\boldsymbol{f}^{\mathrm{pk}} \leftarrow (\boldsymbol{\sigma}(\tilde{\gamma}^{\mathrm{hyb}}_{k+1/2,j})\boldsymbol{b}) \times \boldsymbol{t}$, $\boldsymbol{f}^{\mathrm{core}}$;
        $\gamma^{\mathrm{c}}_{k,j+1} \leftarrow$ evolve DD line;
        $j \leftarrow j+1$, $\tilde{\gamma}^{\mathrm{hyb}}_{k+1/2,j} \leftarrow \tilde{\gamma}^{\mathrm{a}}_{k+1} \cup \gamma^{\mathrm{c}}_{k,j}$;
    end
    $\gamma^{\mathrm{c}}_{k+1} \leftarrow \gamma^{\mathrm{c}}_{k,j}$, set $k \leftarrow k+1$;
until convergence;
Output: Final state $(\boldsymbol{u}^{\mathrm{a}}, \boldsymbol{u}^{\mathrm{c}}, \tilde{\gamma}^{\mathrm{hyb}})_k$
```

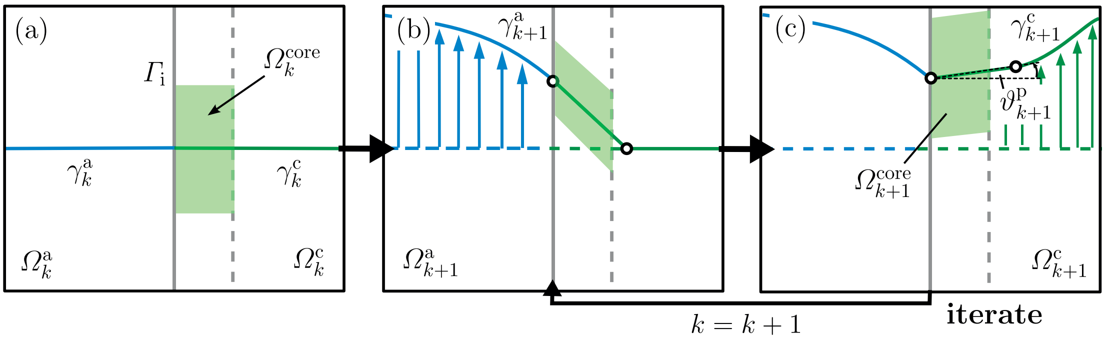
(a)
Γ_{i}
Ω^{core}_k
γ^{a}_k
γ^{c}_k
Ω^{a}_k
Ω^{c}_k
(b)
$\gamma^{\mathrm{a}}_{k+1}$
$\Omega^{\mathrm{a}}_{k+1}$
(c)
$\gamma^{\mathrm{c}}_{k+1}$
$\vartheta^{\mathrm{p}}_{k+1}$
$\Omega^{\mathrm{core}}_{k+1}$
$\Omega^{\mathrm{c}}_{k+1}$
$k = k+1$
iterate

Figure 3.14: Schematic illustration of the semi-monolithic algorithm for CADD-3d

3.8 Simplified solution procedure

3.8.1 Approximation of the coupled problem

In the previous section a general semi-monolithic scheme for CADD-3d has been developed. At its basis, the proposed algorithm offers the possibility to apply a fully coupled solver to the physical problem $\mathcal{P}^{\mathrm{p}}$ which iterates simultaneously on the atomic and the corrective displacements $\boldsymbol{u}^{\mathrm{a}}$ and $\hat{\boldsymbol{u}}$, respectively. For many problems the outer boundary of Ω^{c} mainly serves to apply far-field conditions, thus embedding the atomistic region in an effectively infinite bulk material in order to avoid spurious image effects due to defect-boundary interactions. The solution for the $\hat{\boldsymbol{u}}$ fields is numerical, and normally accomplished using the FEM, which can in three dimensions be computationally very expensive due to the vast amount of degrees of freedom in a (discretized) Ω^{c} (c.f. Pavia and Curtin, 2015). For this class of problems boundary element techniques, such as the one established in Chapter 2 become useful, as they allow for the computation of exterior problems using *only* the degrees of freedom on the boundary. Fully coupled solvers are yet difficult to implement and, to the author's best knowledge, a publicly available high-performance implementation is still lacking. For this purpose a simplified solution procedure is proposed which does not require to solve for the $\hat{\bullet}$ fields numerically and is, moreover, relatively simple to integrate into existing molecular dynamics (MD) codes.

The subclass of possible dislocation problems involving dislocations and atoms embedded in an infinite homogeneous elastic domain and subjected to a far-field applied stress state is considered in the following. This subclass of problems still involves the mechanical coupling at the A/C interface. To eliminate the need to compute the corrective $\hat{\bullet}$ fields *numerically* due to the direct A/C coupling, the following additional assumption is essential:

Assumption 6. *The atomistic domain does not contain other defects than dislocations, e.g cracks, voids or grain boundaries etc.*[4]

Assumption 6 is not yet the suggested approximation, merely a characterization of the entire problem in terms of the existing dislocation network, which is a prerequisite for the simplified solution procedure.

Henceforth, it is assumed that the atomistic dislocation line (γ^{a}) is detected throughout the *entire* atomistic domain, as shown schematically in Figure 3.15. The entire dislocation network $\gamma^{\mathrm{hyb}} := \gamma^{\mathrm{a}} \cup \gamma^{\mathrm{c}}$ is then used to define a "fully-continuum" problem $\mathcal{P}^{\mathrm{c}}$ within the infinite continuum elastic domain $\Omega^{\mathrm{a}} \cup \Omega^{\mathrm{c}} \equiv \mathbb{R}^3$; that is, the portion of the dislocation, residing in the atomistic domain, passed to the continuum problem is now $\tilde{\gamma}^{\mathrm{a}} = \gamma^{\mathrm{a}}$. The solution of this continuum problem is thus the analytic $\tilde{\bullet}$ fields plus the analytic $\hat{\bullet}$ fields, *linear* in $\boldsymbol{x}$, due to the constant remote applied stress. There are no other corrective $\hat{\bullet}$ fields. From the displacement field $\boldsymbol{u}^{\mathrm{c}} = \tilde{\boldsymbol{u}}(\gamma^{\mathrm{hyb}}) + \hat{\boldsymbol{u}}$, the displacement field of the pad atoms in Ω^{p} is then computed including the template correction field for the hybrid dislocations; these displacements then serve, as in the full problem, as the boundary conditions for the atomistic problem.

---

[4] Technically it *is* possible to incorporate other defects in the atomistic region, provided that their stress field is self-equilibrated, but this is not considered here

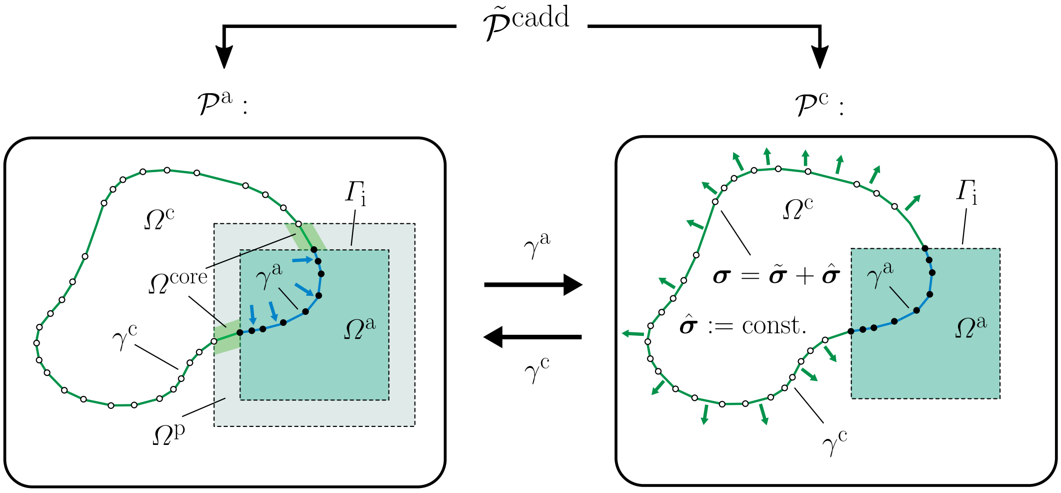
$\tilde{\mathcal{P}}^{\mathrm{cadd}}$
$\mathcal{P}^{\mathrm{a}}$:
$\mathcal{P}^{\mathrm{c}}$:
Ω^{c}
Γ_{i}
Ω^{core}
γ^{a}
γ^{c}
Ω^{a}
Ω^{p}
γ^{a}
γ^{c}
Ω^{c}
Γ_{i}
$\boldsymbol{\sigma} = \tilde{\boldsymbol{\sigma}} + \hat{\boldsymbol{\sigma}}$
γ^{a}
$\hat{\boldsymbol{\sigma}} := \text{const.}$
Ω^{a}
γ^{c}

Figure 3.15: Schematic illustration of the problem decomposition of the *approximate* problem $\tilde{\mathcal{P}}^{\mathrm{cadd}}$ (3.38) corresponding to the solution procedure from Section 3.8.1

The reduced problem can then be stated as: find $\boldsymbol{u}^{\mathrm{a}}$ and γ^{c} such that

$$\tilde{\mathcal{P}}^{\mathrm{cadd}} \left\{ \begin{array}{lr} \underline{\text{Atomistic problem } \mathcal{P}^{\mathrm{a}}:} & \\ \qquad \boldsymbol{f}^{\mathrm{a}} = \boldsymbol{0} & \text{in } \Omega^{\mathrm{a}}, \\ \qquad \boldsymbol{u}^{\mathrm{a}} = \boldsymbol{u}^{\mathrm{c}} + \Delta\tilde{\boldsymbol{u}}^{\mathrm{corr}} & \text{in } \Omega^{\mathrm{p}}, \\ \underline{\text{Continuum problem } \mathcal{P}^{\mathrm{c}}:} & \\ \nabla \cdot \tilde{\boldsymbol{\sigma}}(\gamma^{\mathrm{hyb}}) = \boldsymbol{0} & \text{in } \mathbb{R}^3, \\ \nabla \cdot \hat{\boldsymbol{\sigma}} = \boldsymbol{0} & \text{in } \mathbb{R}^3, \\ \boldsymbol{f}^{\mathrm{pk}} + \boldsymbol{f}^{\mathrm{core}} = \boldsymbol{0} & \text{on } \gamma^{\mathrm{c}}, \\ \gamma^{\mathrm{c}} = \gamma^{\mathrm{a}} & \text{on } \Gamma_{\mathrm{i}} \end{array} \right. \tag{3.48}$$

in the absence of external/body forces. The incremental evolution of the coupled problem (motion of the DDD nodes in Ω^{c} and motion of the atoms in Ω^{a}) is discussed below.

3.8.2 Updated Green function method

In the following the notation from Section 3.7 is adopted, that is, a physical quantity at a global iteration k is referred to as $\bullet_k$; if the quantity is furthermore evaluated at a local iteration j it is denoted $\bullet_{k,j}$. To solve (3.48) numerically for quasistatic equilibrium problems, Algorithm 5 can be simplified considerably. Following Algorithm 6 *only* the atomistic problem is solved in the first step. The boundary condition on $\mathcal{P}^{\mathrm{a}}$ at step k is obtained by a superposition of DDD displacements $\tilde{\boldsymbol{u}}(\gamma_k^{\mathrm{hyb}})$ and the (linear) displacement field $\hat{\boldsymbol{u}}$ due to the constant applied stress

$$\boldsymbol{u}^{\mathrm{p}}_k = \tilde{\boldsymbol{u}}(\gamma^{\mathrm{hyb}}_k) + \hat{\boldsymbol{u}} \qquad \text{in } \Omega^{\mathrm{p}}. \tag{3.49}$$

Assume again an initial hybrid dislocation as depicted in Figure 3.16 (a). Solving the atomistic problem evolves the dislocation line in Ω^{a}, shown in Figure 3.16 (b). Note that the boundary is now held fixed and the dislocation core does not evolve in the pad. Using the updated atomic positions, a new dislocation may be detected based on some convergence condition which will be specified in the following paragraph. Assume now that a new dislocation line is detected in the atomistic domain and the hybrid dislocation is updated according to Figure 3.16 (b). Subsequently the continuum problem $\mathcal{P}^{\mathrm{c}}$ is solved. Since $\hat{\boldsymbol{\sigma}}(\gamma^{\mathrm{hyb}})$ is known analytically at any instant and a numerical evaluation of $(\hat{\boldsymbol{u}}, \hat{\boldsymbol{\sigma}})$ is not required due to the constant applied stress, only $\gamma^{\mathrm{c}}_{k+1}$ is computed iteratively. These steps are repeated until convergence is attained.

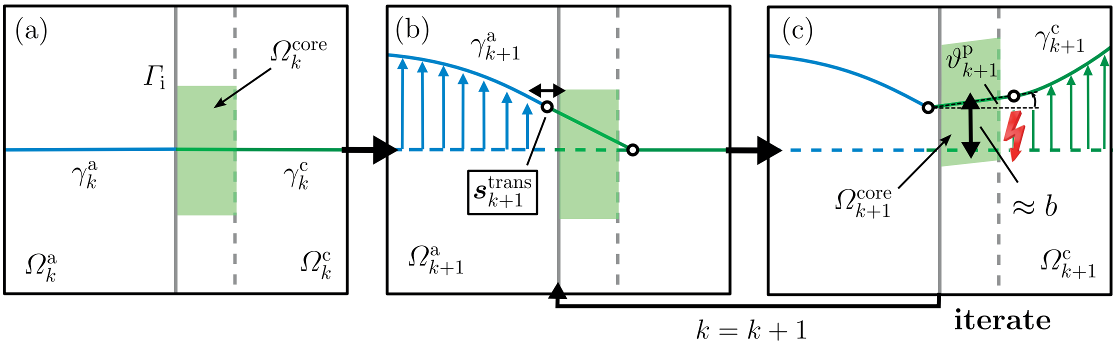
(a)
Γ_{i}
Ω^{core}_k
γ^{a}_k
γ^{c}_k
Ω^{a}_k
Ω^{c}_k
(b)
$\gamma^{\mathrm{a}}_{k+1}$
$\boldsymbol{s}^{\mathrm{trans}}_{k+1}$
$\Omega^{\mathrm{a}}_{k+1}$
(c)
$\vartheta^{\mathrm{p}}_{k+1}$
$\gamma^{\mathrm{c}}_{k+1}$
$\Omega^{\mathrm{core}}_{k+1}$
$\approx b$
$\Omega^{\mathrm{c}}_{k+1}$
$k = k + 1$
iterate

Figure 3.16: Schematic illustration of the updated Green function algorithm for CADD-3d

Recall that the atomistic discrete dislocation, generated by the dislocation detection algorithm, is *not* continuous in the displacements $\boldsymbol{u}^{\mathrm{a}}$ (cf. Section 3.4.2). Therefore the algorithm may oscillate around the equilibrium state, more precisely between two subsequent states $(\boldsymbol{u}^{\mathrm{a}}, \gamma^{\mathrm{hyb}})_{k-1}$ and $(\boldsymbol{u}^{\mathrm{a}}, \gamma^{\mathrm{hyb}})_k$. Hence, the weaker convergence criterion with respect to the subsequence

$$\forall \text{ odd } k > 2 \qquad \left(\boldsymbol{u}^{\mathrm{a}}_{k_l}\right)_{l\in\mathbb{N}} = \left(\boldsymbol{u}^{\mathrm{a}}_1, \boldsymbol{u}^{\mathrm{a}}_3, ..., \boldsymbol{u}^{\mathrm{a}}_{k-2}, \boldsymbol{u}^{\mathrm{a}}_k\right) \tag{3.50}$$

is defined. That is, the current state is compared with the state two iterations previous. Convergence is then attained when

$$\|\boldsymbol{u}^{\mathrm{a}}_l - \boldsymbol{u}^{\mathrm{a}}_{l-1}\|_{l^2(\Omega^{\mathrm{a}})} < TOL^{\mathrm{detn}}, \tag{3.51}$$

where TOL^{detn} is some pre-defined tolerance. If the criterion (3.51) is fulfilled it is easy to see that the algorithm is converged since the hybrid dislocation line does not get updated and therefore the pad atoms remain the same as in the previous step. The criterion (3.51) appeared to be very robust in the conducted numerical experiments in Section 4.3. The proposed algorithm may suggest a rather slow convergence due to the iterative

Algorithm 6: Updated Green function method for CADD-3d

```
Input: Initial state $(\boldsymbol{u}^{\mathrm{a}}, \boldsymbol{u}^{\mathrm{c}}, \gamma^{\mathrm{hyb}})_0$
$k \leftarrow 0$;
repeat
    /* Atomistic problem $\mathcal{P}^{\mathrm{a}}$ */
    $\tilde{\boldsymbol{u}}(\gamma_k^{\mathrm{hyb}}) \leftarrow$ compute the DDD displacements due to $\gamma_k^{\mathrm{hyb}}$ in $\Omega^{\mathrm{p}}$;
    $\boldsymbol{u}_{k+1}^{\mathrm{a}} \leftarrow$ solve $\mathcal{P}^{\mathrm{a}}$ (3.48);
    /* Continuum problem $\mathcal{P}^{\mathrm{c}}$ */
    if convergence criterion (3.51) not satisfied then
        $\gamma_{k+1}^{\mathrm{a}} \leftarrow$ dislocDetn($\Omega_{k+1}^{\mathrm{a}}$); // (re-)detect dislocation line in $\Omega^{\mathrm{a}}$
        initialize:    $j \leftarrow 0$,    $\gamma_{k,j}^{\mathrm{c}} \leftarrow \gamma_k^{\mathrm{c}}$,    $\gamma_{k+1/2,j}^{\mathrm{hyb}} \leftarrow \gamma_{k+1}^{\mathrm{a}} \cup \gamma_{k,j}^{\mathrm{c}}$;
        while $\|\boldsymbol{f}^{\mathrm{pk}} + \boldsymbol{f}^{\mathrm{core}}\|_{L^2(\gamma^{\mathrm{c}})} < TOL$ do
            compute on $\gamma_{k,j}^{\mathrm{c}}$:    $\boldsymbol{\sigma}(\gamma_{k+1/2,j}^{\mathrm{hyb}}) \leftarrow \tilde{\boldsymbol{\sigma}}(\gamma_{k+1/2,j}^{\mathrm{hyb}}) + \hat{\boldsymbol{\sigma}}$;
            compute on $\gamma_{k,j}^{\mathrm{c}}$:    $\boldsymbol{f}^{\mathrm{pk}} \leftarrow (\boldsymbol{\sigma}(\gamma_{k+1/2,j}^{\mathrm{hyb}})\boldsymbol{b}) \times \boldsymbol{t}$,    $\boldsymbol{f}^{\mathrm{core}}$;
            $\gamma_{k,j+1}^{\mathrm{c}} \leftarrow$ evolve DD line;
            $j \leftarrow j+1$,    $\gamma_{k+1/2,j}^{\mathrm{hyb}} \leftarrow \gamma_{k+1}^{\mathrm{a}} \cup \gamma_{k,j}^{\mathrm{c}}$;
        end
        $\gamma_{k+1}^{\mathrm{c}} \leftarrow \gamma_{k,j}^{\mathrm{c}}$,    set $k \leftarrow k+1$;
    else
        stop (repeat);
    end
until convergence;
Output: Final state $(\boldsymbol{u}^{\mathrm{a}}, \boldsymbol{u}^{\mathrm{c}}, \gamma^{\mathrm{hyb}})_k$
```

procedure and the sharp interface coupling. However, note that the physical problem $\mathcal{P}^{\mathrm{c/p}}$ is effectively solved in the **entire** domain. Therefore the discrete dislocation in the continuum can advance much further than if it would "see" a fixed boundary. The algorithm has therefore analogies with respect to overlapping domain decomposition methods. In all numerical tests the updated Green function method was found to remain reasonably fast. Computational savings will be briefly discussed in Section 4.3.5.

There is some freedom in choosing the *transmission node* $\boldsymbol{s}^{\mathrm{trans}}$ that merges γ^{a} and γ^{c}, corresponding to the uncertainty in the definition of γ^{a} due to the non-unique continuum representation of Ω^{a}. The choice of $\boldsymbol{s}^{\mathrm{trans}}$ affects the evolution — the dislocation line may advance rather slowly in the neighborhood of the interface Γ_{I} if $\boldsymbol{s}^{\mathrm{trans}}$ is too close to the artificial interface. Loosely speaking, the atomistic dislocation in Figure 3.16 (b) cannot introduce a "discontinuity" with respect to the discrete dislocation in the continuum region. Hence, the dislocation segment in the pad may not advance by more than $\approx b$ — unlike in the general solution procedure where the pad displacements are updated on-the-fly (c.f. Figure 3.14). This reveals a possible source for pre-mature convergence, in particular when the system is close to equilibrium. In the Section 4.3.5 it will be shown how different choices of $\boldsymbol{s}^{\mathrm{trans}}$ can influence the equilibrium shape of the hybrid dislocation.

3.9 Computational complexity compared to related methods

To estimate the computational complexity of CADD-3d in terms of the degrees of freedom, consider the decomposition of a domain Ω into an atomistic domain Ω^{a} and a continuum domain Ω^{c}. The region Ω^{a} is assumed to be the *irreducible* atomistic domain (meaning no change in size) where nonlinear deformation (e.g. dislocation nucleation) ought to happen. In the QC method the atomistic region is allowed to grow as defects expand into the bulk material, whereas in CADD-3d a dislocation becomes discrete beyond the A/C interface.

In general, the computational complexity of a linear numerical problem can be written as

$$C \propto N, \tag{3.52}$$

where N is the number of degrees of freedom (precise prefactors are usually strongly implementation dependent and not considered in the following). For the considered class of A/C coupling problems the computational complexity reads

$$C^{\mathrm{a/c}} = C^{\mathrm{a}} + C^{\mathrm{cg}} + C^{\mathrm{core}}, \tag{3.53}$$

where C^{a} is due to the irreducible atomistic domain Ω^{a}, C^{cg} is the computational complexity of the coarse-grained region $\Omega \setminus (\Omega^{\mathrm{a}} \cup \Omega^{\mathrm{core}})$ and C^{core} is due to the dislocation core region(s) Ω^{core} outside Ω^{a}. In the following (almost) linear complexity (3.52) is tacitly assumed for *all* coefficients in (3.53) (in the case of CADD-3d this requires special accelerated solvers as discussed below).

The first term in (3.53) is the same for both methods by construction and is thus not considered in the following. The parameter C^{cg} is assumed to be comparable for both methods if CADD-3d uses a standard FEM discretization in the bulk material (c.f. Pavia and Curtin, 2015). Additional speed-ups can be obtained when using CADD-3d with the boundary element method developed in the previous chapter due to the reduced number of degrees of freedom (c.f. Table 3.1; only the interface and pad atoms are considered which are assumed to be $\ll N^{\mathrm{cg}}$). For large dislocation densities C^{cg} is assumed to be dominated by C^{core}. For this case C^{core} is estimated in the following.

	QC	CADD-3d (w/ FEM)	CADD-3d (w/ DBEM)
Ω^{a}	N^{a}	N^{a}	N^{a}
Ω^{c}	$N^{\mathrm{cg}} + N^{\mathrm{core}}$	$N^{\mathrm{cg}} + N^{\mathrm{seg}} \log N^{\mathrm{seg}}$	$N^{\mathrm{i}} \log N^{\mathrm{i}} + N^{\mathrm{p}} \log N^{\mathrm{i}}$ $+ N^{\mathrm{seg}} \log N^{\mathrm{seg}} + N^{\mathrm{seg}} \log N^{\mathrm{i}}$

Table 3.1: Complexity estimates for the QC method and CADD-3d (with FEM or DBEM); it is assumed that CADD-3d uses fast summation methods

Assume a dislocation loop with radius R outside Ω^{a}. The third contribution in (3.53) can then be written as (Anciaux, 2018)

$$C^{\mathrm{core}} \propto NR, \tag{3.54}$$

where N is now the total number of degrees of freedom *per unit length* in Ω^{core}. For the QC method N corresponds to the number of real atoms N^{core} per unit length around the dislocation core[5] and for CADD-3d it is the number of DD segments N^{seg} per unit length.

First, the complexity of the QC method is estimated. The total number of atoms in the vicinity of the dislocation is given by

$$N^{\mathrm{core}} R = \frac{2\pi^2 (r^{\mathrm{core}})^2 R}{V_0} \qquad \Rightarrow \qquad N^{\mathrm{core}} = \frac{2\pi^2 (r^{\mathrm{core}})^2}{V_0}, \tag{3.55}$$

where r^{core} is the radius of the core region and V_0 is the volume per atom. Writing r^{core} and V_0 in terms of b, e.g. for the particular case of an fcc lattice $V_0 = 0.741 a_0^3 = 0.741 \cdot 2\sqrt{2} b \approx 2b$ and $r^{\mathrm{core}} = N_b^{\mathrm{core}} b$ ($N_b^{\mathrm{core}} \in \mathbb{Z}^+$), one obtains

$$N^{\mathrm{core}} \approx \frac{\pi^2 (N_b^{\mathrm{core}})^2}{b}. \tag{3.56}$$

Next, the complexity of CADD-3d is considered. By assuming an average dislocation segment length l, the total number of DD segments is

$$N^{\mathrm{seg}} R = \frac{2\pi R}{l} \qquad \Rightarrow \qquad N^{\mathrm{seg}} = \frac{2\pi}{l}. \tag{3.57}$$

Again, writing $l = N_b^{\mathrm{seg}} b$ ($N_b^{\mathrm{seg}} \in \mathbb{Z}^+$), it follows

$$N^{\mathrm{seg}} = \frac{2\pi}{N_b^{\mathrm{seg}} b}. \tag{3.58}$$

---

[5] This is yet an optimistic estimate since efficient adaptive mesh coarsening in QC implementations, restricting fully atomistic resolution to the defect core, still remains an open research problem (Tembhekar et al., 2017)

The ratio between the number of degrees of freedom for the QC method and CADD-3d can then readily be deduced as

$$\frac{N^{\mathrm{core}}}{N^{\mathrm{seg}}} \approx \frac{\pi}{2}(N_b^{\mathrm{core}})^2 N_b^{\mathrm{seg}}. \tag{3.59}$$

Note that the $(N_b^{\mathrm{core}})^2 N_b^{\mathrm{seg}}$ proportionality is in fact general and applies to arbitrarily curved dislocations.

To illustrate the potential savings which can possibly be obtained in practice, consider the activation of a Frank-Read source in fcc aluminum centered in a cubic domain, as exemplified in Figure 3.17. The box size is $\approx 2\times2\times2\,\mu\mathrm{m}^3$ and the diameter of the outermost loop is $\approx 1\,\mu$m. The average segment length of a representative DDD simulation for this problem is $\approx 150b$, i.e. $N_b^{\mathrm{seg}} = 150$. For fcc aluminum the stacking fault width is ≈ 15 Å. With $b = 2.851$ Å, it follows $(N_b^{\mathrm{core}})^2 \approx$ 7-10. These values yield a complexity estimate of $\mathcal{O}(10^2)$-$\mathcal{O}(10^3)$ for C^{core}, which is still conservative since only a single dislocation is considered.

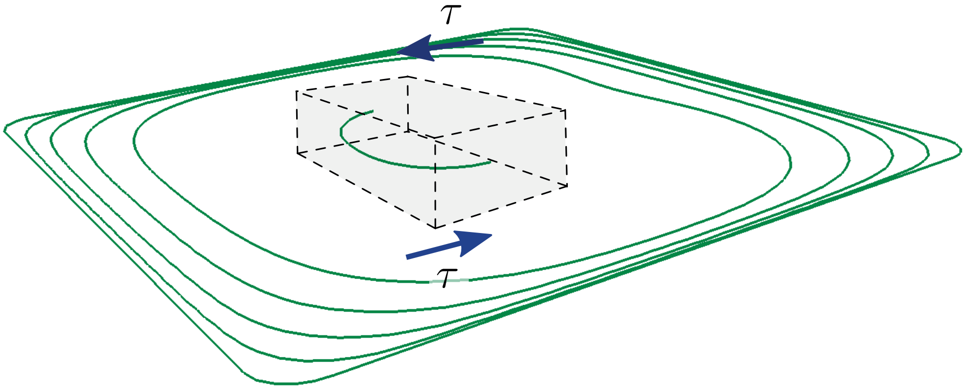

Figure 3.17: DDD simulation of a Frank-Read source which is subjected to an applied shear stress τ; the figure is used by courtesy of Dr. Markus Stricker

The outstanding potential of CADD-3d can be rationalized by considering a coupled problem where atomic resolution is restricted to the region confined by the dashed box. If the ratio between the size of Ω^{c} and Ω^{a} is large (in the figure it is roughly 100), $C^{\mathrm{a}}, C^{\mathrm{cg}} \ll C^{\mathrm{core}}$ if many dislocations have passed the A/C interface and propagated far into the bulk crystal, as shown in Figure 3.17. In this case CADD-3d becomes highly favorable.

However, it should be noted that this advantage does not come for free. More precisely, the DDD problem suffers from quadratic complexity due to the interactions between all segments which may extinguish much of the potential efficiency if implemented naively. This necessitates accelerated, fast-multipole-based algorithms (c.f. Greengard and Rokhlin, 1987) to solve the problem with (almost) linear complexity (see below).

3.10 Computer implementation

The implementation of CADD-3d, i.e. Algorithm 5 and Algorithm 6, is accomplished in the in-house C++ library libMultiscale (LM, Anciaux et al., 2006, lsms.epfl.ch/libmultiscale). Its key features are summarized below:

- LM was tailored for the purpose of a generic interface between heterogeneous parts of source code to incorporate extrinsic software in a single parallel computing framework using collective communication via the Message Passing Interface (MPI, www.mpich.org) and has been successfully employed for several A/C coupling problems, e.g. for studying problems in contact mechanics (e.g. Anciaux and Molinari, 2009). Therefore the effort of writing own code can be significantly reduced by making use of existing, optimized implementations for each subproblem.
- Data exchange in LM between external software is realized via template interfaces. This is not only efficient for replacing old/adding new source code, but also simplifies the pre- and post-processing due to the unifying structure.

CADD-3d harnesses the atomistic code LAMMPS (Plimpton, 1995, lammps.sandia.gov) and the DDD code ParaDis (paradis.stanford.edu) which have been integrated into the LM environment by Anciaux and Molinari (2009); Junge (2014). In particular, ParaDis uses the fast multipole method to compute the elastic far-field interactions such that the forces on the DD nodes can be computed with linear complexity (Arsenlis et al., 2007).

The library has been extended by the author (Hodapp et al., 2018a) and others (e.g. Anciaux et al., 2018; Cho et al., 2018) with additional self-written routines to compute the displacement boundary conditions due to the discrete dislocation network, accompanied with the dislocation core template correction, and to compute the discrete atomistic dislocation(s) according to Algorithm 4. The integration of the A/DBEM solver (Chapter 2) is ongoing work and results will be reported in a future publication (Hodapp et al., 2018b).

4 Computational results

4.1 Validation of the discrete boundary element method

The goal of this section is to validate the flexible boundary conditions which have been proposed in Chapter 2. Thereby, special emphasize is given to the total error in the atomistic region

$$\epsilon = \epsilon_{\mathrm{h}} + \epsilon_{\mathrm{lgf}} + \epsilon_{\mathrm{mat}}, \tag{4.1}$$

where ϵ_{lgf} is due to the transition between the LGF and the CGF (Section 2.6.2) and ϵ_{mat} is the error committed by the approximation of the system matrices via $\mathscr{H}$-matrices (Section 2.6.3). The error ϵ_{h} is the best possible approximation in the harmonic limit. It is thus of practical importance that the total error is dominated by ϵ_{h}. Fortunately ϵ_{lgf} and ϵ_{mat} can be controlled but choosing them too low increases the computational cost.

In section 4.1.1 the influence of ϵ_{lgf} solely is investigated. For the three-dimensional test problems in Section 4.1.2 some guidance on choosing an optimal ϵ_{mat} without a priori knowledge of ϵ will be given by fixing an appropriate cut-off radius, estimating the error ϵ_{lgf} and choosing the accuracy of the $\mathscr{H}$-matrices in the same range.

4.1.1 Two-dimensional test cases for hexagonal lattices

A hexagonal lattice $\varLambda$ is considered whose basis vectors are given by

$$\boldsymbol{v}_1 = \begin{pmatrix} a_0 & 0 \end{pmatrix}^{\mathsf{T}}, \qquad \boldsymbol{v}_2 = 1/2 \begin{pmatrix} a_0 & \sqrt{3}a_0 \end{pmatrix}^{\mathsf{T}}, \tag{4.2}$$

where a_0 is the associated lattice constant. For this class of test problems a Morse potential is selected (Morse, 1929). The corresponding site energy is given by

$$\mathcal{E}_\xi(\boldsymbol{u}_\eta - \boldsymbol{u}_\xi) = \sum_{\boldsymbol{\eta} \in \mathcal{R}_\xi} De^{-2a(r(\boldsymbol{u}_\eta - \boldsymbol{u}_\xi) - r_0)} - 2De^{-a(r(\boldsymbol{u}_\eta - \boldsymbol{u}_\xi) - r_0)}, \tag{4.3}$$

where $r(\boldsymbol{u}_\eta - \boldsymbol{u}_\xi) = \|(\boldsymbol{u}_\eta - \boldsymbol{u}_\xi) + (\boldsymbol{\eta} - \boldsymbol{\xi})\|$, with D, a and r_0 being free parameters.

Approximations via $\mathscr{H}$-matrices are not considered in this section as the boundary matrices introduce negligible computational cost in two dimensions.

4.1.1.1 Vacancy relaxation

As a first test problem a vacancy embedded in the atomistic region is considered. The atomistic domain is assumed to be a disk with radius r, i.e.

$$\Lambda^{\mathrm{a}} := (\{\, \boldsymbol{x} \in \mathbb{R}^2 \,|\, \|\boldsymbol{x}\| \leq r \,\} \cap \Lambda) \setminus \boldsymbol{0} \tag{4.4}$$

as shown in Figure 4.1 (a). The parameters of the Morse potential (4.3) are chosen as follows

$$D_0 = 1\,\mathrm{eV}, \qquad a = 4.4\,/\text{Å}, \qquad r_0 = 1\,\text{Å}. \tag{4.5}$$

Note that these parameters are not based on a specific material. The same set of parameters has been used in other benchmark studies for A/C coupling schemes (e.g. Van Koten et al., 2012). In the numerical tests a cut-off radius which comprises six nearest neighbor interactions is used. The corresponding lattice constant is given by $a_0 = 0.978$, i.e. the atomistic model is slightly non-local.

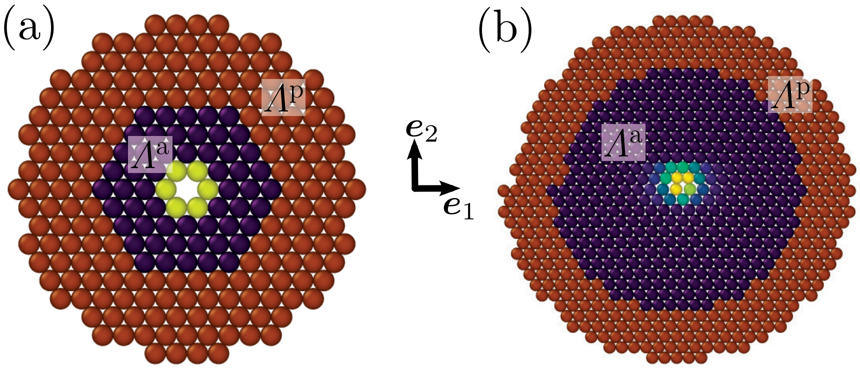

Figure 4.1: Schematic illustration of the domain decomposition for (a) the vacancy problem, (b) the dislocation problem

Discussion (accuracy). The decay of error in the total energy as $r \to \infty$ is analyzed in the following. Theoretical decay rates were derived in (Ehrlacher et al., 2016) for clamped and flexible boundary conditions which read

$$\textbf{clamped:} \quad |\Pi - \tilde{\Pi}| \lesssim (N^{\mathrm{a}})^{-1}, \qquad \textbf{flexible:} \quad |\Pi - \tilde{\Pi}| \lesssim (N^{\mathrm{a}})^{-2}. \tag{4.6}$$

Note that this estimate is not necessarily sharp for the current problem due to the underlying assumption on the atomistic model which includes nearest neighbor many-body interactions only. However, the upper bound must be satisfied. For the clamped boundary conditions the precise scaling as predicted by (4.6) is observed. Indeed, for the atomistic-DBEM coupling a faster decay rate is observed which is proportional to $(N^{\mathrm{a}})^{-3}$.[1] Also the pre-factor is much larger for the clamped boundary conditions outlining the superior performance of the flexible boundary conditions. As expected, the accuracy for the atomistic-DBEM coupling is slightly lower than for the Sinclair method if the cut-off radius is too small (here: $r_{\mathrm{cut}} = 3a_0$). For $r_{\mathrm{cut}} \geq 5a_0$ the results are essentially the same.

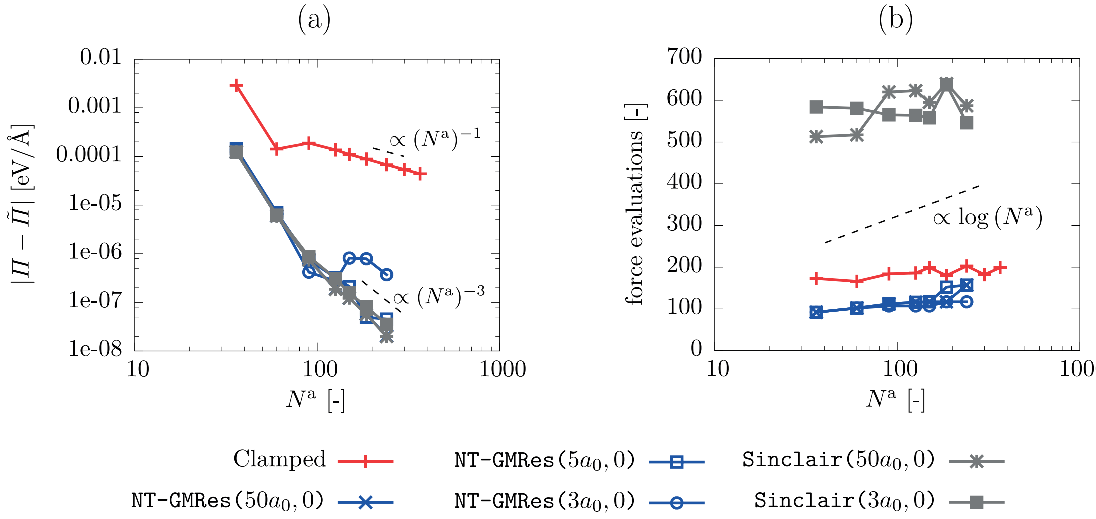

Figure 4.2: (a) Energy error vs. number of real atoms N^{a} for the vacancy problem for clamped and flexible boundary conditions. (b) Number of force evaluations corresponding to each data point in (a)

Discussion (efficiency). In addition, the number of force evaluations for each solution procedure is shown in Figure 4.2 (b). As a solver for the atomistic problem, employed for the clamped boundary conditions and Sinclair's method, it is decided on FIRE (Bitzek et al., 2006) which was found comparable to other available solvers (i.a. nonlinear conjugate gradients, Hessian-free Newton-Raphson) with respect to the speed of convergence for the considered problems. FIRE is a damped-dynamics method which requires an initial timestep. In (Bitzek et al., 2006) it was recommended to set the timestep ≈ 1 order of magnitude higher than in a usual molecular dynamics calculation. Therefore the timestep is chosen 0.01 ps. The number of force evaluations scales very weakly with total number of real atoms in the system. This confirms a similar observation from Dobson et al. (2011) who have defined a macro-stretch on a one dimensional chain of atoms which eventually causes bond-breaking. For an increased macro-stretch the system gets closer to an instability and the required number of iterations approaches a $\log N^{\mathrm{a}}$-scaling.

---

[1] The same decay rate was also observed in the numerical experiments from (Ehrlacher et al., 2016)

Since the atomistic configuration in the vicinity of the vacancy is far from an instability this observation seems reasonable. The total number of force evaluations is $\approx$5-6 times higher for Sinclair's method due to the alternating solution procedure. Surprisingly the Newton-GMRes solver outperforms the clamped boundary conditions for the same system size in this respect. Note however that one force computation is slightly higher for the Newton-GMRes solver. The average cost over all simulations from Figure 4.2 for a single force computation is 0.014 ms for `NT-GMRes` and 0.0041 ms for `Sinclair`. Thus, `NT-GMRes` is *effectively* 1.5-2 times faster than `Sinclair` with the current implementation. The time ratio between updating the pad atoms and one computation of the atomic force vector is approximately between 1/3 and 1/6. The increased computational cost for `NT-GMRes` is therefore mainly due to the higher complexity of a Newton iteration (compared to a FIRE iteration). This can potentially be optimized using high performance libraries, e.g PETSc (www.mcs.anl.gov/petsc).

4.1.1.2 Dislocation core relaxation

Now a single edge dislocation embedded in the atomic crystal, as shown in Figure 4.1 (b), is considered. Since a dislocation has infinite energy the problem description has to be modified since the displacements are unbounded and therefore $\boldsymbol{u} \notin \mathcal{U}^\star(\varLambda)$. For this purpose the initial configuration is pre-strained using an initial guess $\boldsymbol{u}_0$, i.e. $\varLambda + \boldsymbol{u}_0$. Subsequently, the finite *energy difference functional* $\varDelta\varPi(\varDelta\boldsymbol{u}) = \varPi(\boldsymbol{u}_0 + \varDelta\boldsymbol{u}) - \varPi(\boldsymbol{u}_0)$ is defined with respect to a correction $\varDelta\boldsymbol{u} \in \mathcal{U}^\star$ (c.f. Ehrlacher et al., 2016). That is, minimizers of $\varDelta\varPi$ are now sought-after, i.e.

$$\varDelta\boldsymbol{u} := \mathrm{Arg}\left\{\min_{\boldsymbol{v}\in\mathcal{U}^\star} \varDelta\varPi(\boldsymbol{v})\right\}. \tag{4.7}$$

which renders the problem well-posed. The definition of the coupled problem follows

$$\begin{cases} \mathcal{P}^{\mathrm{a}}: \quad \mathcal{L}^{\mathrm{a}}[\varDelta\boldsymbol{u}] = \mathbf{0} & \text{in } \varLambda^{\mathrm{a}}, \\ \mathcal{P}^{\mathrm{c}}: \quad \mathcal{L}^{\mathrm{c}}_{\mathrm{h}}[\varDelta\boldsymbol{u}] = \mathbf{0} & \text{in } \varLambda^{\mathrm{c}}, \end{cases} \tag{4.8}$$

with $\mathcal{L}^{\mathrm{a}}$ and $\mathcal{L}^{\mathrm{c}}_{\mathrm{h}}$ being now defined with respect to $\varDelta\varPi^{\mathrm{a}}(\varDelta\boldsymbol{u})$ and $\varDelta\varPi^{\mathrm{c}}(\varDelta\boldsymbol{u})$.

Since the material stiffness tensor $\mathbb{C}$, obtained from the linearization of the atomistic model, is isotropic the classical Volterra solution is employed

$$\tilde{u}_1(\boldsymbol{\xi}) = \frac{b}{2\pi}\left(\frac{(\xi_1 - \varDelta\xi_1)(\xi_2 - \varDelta\xi_2)}{2(1-\nu)\|\boldsymbol{\xi} - \varDelta\boldsymbol{\xi}\|^2} + \arctan\frac{\xi_2 - \varDelta\xi_2}{\xi_1 - \varDelta\xi_1}\right), \tag{4.9}$$

$$\tilde{u}_2(\boldsymbol{\xi}) = \frac{b}{2\pi}\left(\frac{(\xi_2 - \varDelta\xi_2)^2 - (\xi_1 - \varDelta\xi_1)^2}{4(1-\nu)\|\boldsymbol{\xi} - \varDelta\boldsymbol{\xi}\|^2} - \frac{1-2\nu}{4(1-\nu)}\ln\|\boldsymbol{\xi} - \varDelta\boldsymbol{\xi}\|^2\right), \tag{4.10}$$

with $r = \|\boldsymbol{\xi} - \Delta\boldsymbol{\xi}\|$, $b = a_0$ and $\nu = 0.25$. The dislocation is placed slightly off-center at $\Delta\boldsymbol{\xi} = b/4 \begin{pmatrix} 1 & \sqrt{3} \end{pmatrix}^\mathsf{T}$ due to the singularity of $\tilde{\boldsymbol{u}}$ at $\boldsymbol{\xi} = \boldsymbol{0}$. The final solution is then given by $\boldsymbol{u} = \boldsymbol{u}_0 + \Delta\boldsymbol{u}$, with $\boldsymbol{u}_0 = \tilde{\boldsymbol{u}}$.

Discussion (accuracy). Again, the error in the total energy is investigated. The theoretical decay rate for both the clamped and the flexible boundary conditions from (Ehrlacher et al., 2016) reads

$$|\varPi - \tilde{\varPi}| \lesssim (N^\mathrm{a})^{-1}. \tag{4.11}$$

Slightly faster decay rates for all boundary conditions are observed which might also be due to the fact that the energy difference is only considered up to a certain radius r around the dislocation core. The elasticity error clearly dominates such that $r_\mathrm{cut} = 3a_0$ was found to be sufficient. For the flexible boundary conditions the error shows an alternating behavior as r is increased by $a_0/2$. This is indicated by the separated error curves in Figure 4.3 (a) associated with the two possible types of boundaries. Since the two curves show approximately the same scaling and the upper bound is satisfied in both cases this might indicate a more subtle issue, especially in light of the final results corresponding to the Sinclair method and the Newton-GMRes scheme which differ slightly. Several modifications were investigated, e.g. by choosing a different initial guess or imposing small perturbations of real atoms upon convergence to overcome a possibly unstable minimum. However, the final result remained unchanged. This gives rise to the conclusion that the Volterra solution might not be a suitable far-field predictor, i.e. $\Delta\boldsymbol{u} \neq \mathcal{U}^\star(\varLambda)$. However, other solutions are not investigated and a definite answer cannot be given at this point.

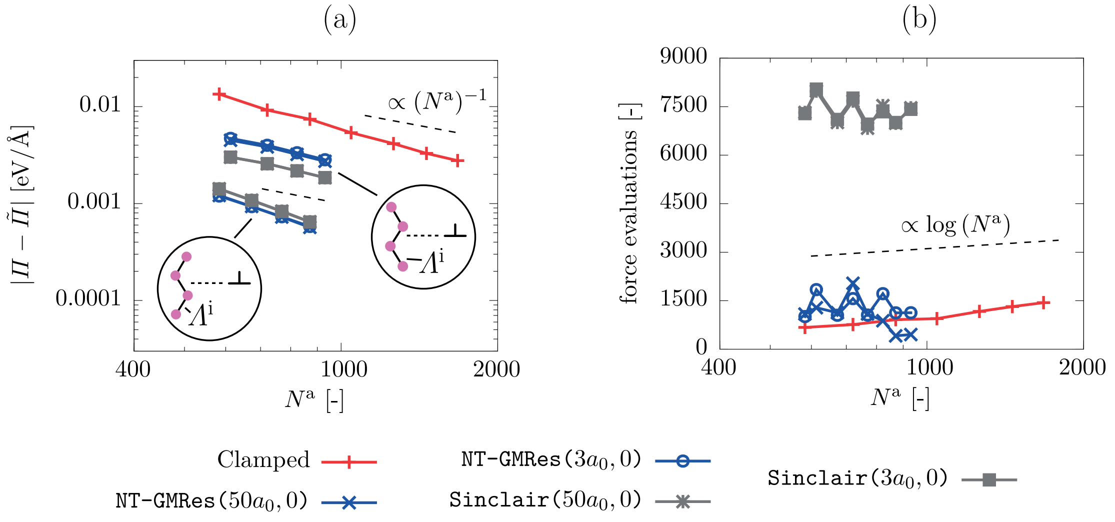

Figure 4.3: (a) Energy error vs. number of real atoms N^a for the dislocation problem for clamped and flexible boundary conditions. (b) Number of force evaluations corresponding to each data point in (a)

In the present case the Volterra dislocation is already a rather good predictor as the dislocation core is compact. Thus, a distinctive performance of flexible over clamped boundary conditions is not observed. Nevertheless, severe differences for dislocations with spread cores are expected (especially in view of Section 4.1.1.3).

Discussion (efficiency). In Figure 4.3 (b) the corresponding number force evaluations is shown. It is observed that Sinclair's method requires roughly between 5-15 times more force evaluations due to a larger number of outer iterations when compared to the vacancy problem. The clamped and the flexible boundary conditions are approximately in the same range which is remarkable. Here, a slightly larger increase of the required number of total force evaluations is observed which is most likely due to the fact that the atomistic configuration around the dislocation core is naturally much closer to an instability, as opposed to the vacancy case. The average cost over all simulations from Figure 4.3 for a single force computation is 0.004 ms for `NT-GMRes` and 0.0021 ms for `Sinclair`. The reduced cost in comparison with the vacancy problem is most likely due to the fact that the sample sizes are much larger, thus reducing the influence of setup times etc. Therefore `NT-GMRes` is effectively 2.5-5 times faster than `Sinclair` for this problem and is expected to be higher for more complex dislocation core structures.

4.1.1.3 Spurious stresses on dislocations near interfaces

In practice, a classical limitation of clamped boundary conditions is their stiff reaction to atomic fluctuations. When considering defects, subject to an applied loading, the highly constrained interface reveals a severe issue as defects nucleate and propagate through the crystal lattice. Since defects move under rather low applied stresses the final result may be highly perturbed by undesired image effects. Periodic boundary conditions overcome this problem only partially.

A test problem for probing the "softness" of artificial interfaces was introduced by Dewald and Curtin (2006) for moving dislocations. Thereby the dislocation is subject to an applied shear stress $\sigma_{12}^{\mathrm{app}}$ which eventually moves the dislocation towards the interface (see Figure 4.4 (a)). The spurious stress $\sigma_{12}^{\mathrm{sp}}(d) = \sigma_{12}^{\mathrm{app}}(d) - \sigma_{12}^{\mathrm{peierls}}$, where $\sigma_{12}^{\mathrm{peierls}}$ is the Peierls stress for the given interatomic potential, as a function of the distance to the interface d can then be used as a measure for the quality of the continuum solution since the dislocation must necessarily continue gliding in a perfect infinite crystal. Further studies have revealed that linear elasticity can substantially improve the accuracy over clamped boundary conditions as shown by Pavia and Curtin (2015) and Hodapp et al. (2018a). Here, their setting is adopted as a reference test case for the flexible boundary conditions.

A rectangular atomistic domain given by

$$\Lambda^{\mathrm{a}} := [-l, l]^2 \cap \Lambda, \qquad \text{with} \quad l = 22.5b \tag{4.12}$$

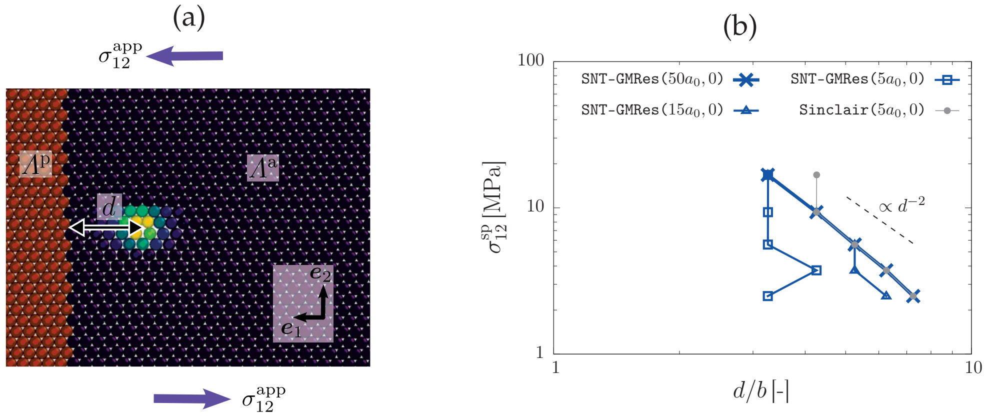

Figure 4.4: (a) Schematic view of the dislocation halting at a distance d from the artificial interface. (b) Spurious stress $\sigma_{12}^{\mathrm{sp}}(d) = \sigma_{12}^{\mathrm{app}}(d) - \sigma_{12}^{\mathrm{peierls}}$ as a function of d

is considered. The influence of the domain size has been investigated to ensure that the results do not change qualitatively for larger l. The setup remains the same as in the previous section, though the parameters of the Morse potential are now chosen to mimic those of aluminum (Girifalco and Weizer, 1959)

$$D_0 = 0.2703\,\mathrm{eV}, \qquad a = 1.1646\,/\mathrm{\mathring{A}}, \qquad r_0 = 3.253\,\mathrm{\mathring{A}}. \tag{4.13}$$

The reasoning behind this is to obtain physically realistic estimates of the spurious stress. The initial guess is modified accordingly, i.e.

$$\boldsymbol{u}_0(\boldsymbol{\xi}) = \tilde{\boldsymbol{u}}(\boldsymbol{\xi}) + \boldsymbol{u}^{\mathrm{app}}(\boldsymbol{\xi}), \qquad \text{where} \quad \boldsymbol{u}^{\mathrm{app}}(\boldsymbol{\xi}) = \frac{\sigma_{12}^{\mathrm{app}}}{\mu}\xi_2 \boldsymbol{e}_1. \tag{4.14}$$

The second term accounts for the applied shear stress $\sigma_{12}^{\mathrm{app}}$.

In this test the stability condition **[STAB]** becomes inevitable since the lattice becomes unstable as the dislocation "hops" from one to the next position by one Burgers vector. The choice of the number of FIRE iterations is a delicate question. If this value is chosen too low the dislocation cannot overcome a local saddle point and may subsequently be driven backwards by the Newton-GMRes method. On the other hand, a too large number slows down the convergence of the solver. It was found that a number of ≈ 1000 ensures rapid convergence for this test problem.

Discussion (accuracy). For the Morse potential with parameters given by (4.13) the Peierls stress is $\sigma_{12}^{\mathrm{peierls}} = 5.6\,\mathrm{MPa}$. Various applied stresses above the Peierls barrier were chosen, i.e. $\sigma_{12}^{\mathrm{app}} \in \{8.1, 9.3, 11.2, 14.9, 22.4\}\,\mathrm{MPa}$. From Figure 4.4 (b) one can see that the final result is rather sensitive to the boundary condition. For a lower cut-off radius of $5a_0$ the boundary reaction is much softer such that the dislocation can propagate very close to the interface, even for the lowest applies stress. For an increasing cut-off radius the final position converges to that of a reference calculation with $r_{\mathrm{cut}} = 50a_0$.

As expected, the accuracy of the Sinclair method is slightly better in the sense that for $r_{\text{cut}} = 5a_0$ the same results as for `NT-GMRes`$(50a_0, 0)$ are already obtained, except for the highest applied stress. Moreover, the same scaling d^{-2} was observed that has already been obtained in other publications (Pavia and Curtin, 2015; Hodapp et al., 2018a), as will be shown in Section 4.2 where the same test case is used to validate the updated Green function method. Moreover this scaling is similar to the recent error estimates for isolated dislocations in a finite computational domain embedded in an effectively infinite medium for various artificial boundary conditions (Ehrlacher et al., 2016). The results in Section 4.2.2 are obtained with an fcc aluminum potential with a spread core, thus it is expected that the spurious effects are approximately in the same range. Indeed, by comparing the results of Figure 4.4 (b) with those obtained by (Pavia and Curtin, 2015) (Figure 4.9, ref. calculation) it is observed that for an applied stress of 22.4 MPa the spurious stress is $\approx$ 17 MPa and $d = 3b$. In (Pavia and Curtin, 2015) the distance of the full dislocation was found to be roughly between 3 and $4b$ for approximately the same spurious stress.

Discussion (efficiency). In Table 4.1 the number of force evaluations for `NT-GMRes`$(15a_0, 0)$ and `Sinclair`$(5a_0, 0)$ are presented. Sinclair's method requires only $\approx$ 5-7 times more force evaluations. The average speedup of `NT-GMRes` compared to `Sinclair` is then $\approx$ 2.5-3.5 due to the higher complexity of the Newton iteration (c.f. Section 4.1.1.2). This is remarkable for a staggered method for this class of problems. However, it is pointed out that switching between different solvers is far from being optimal and therefore a stabilized Newton-GMRes may improve the convergence considerably.

	$\sigma^{\text{app}} = 11.2\,\text{MPa}$ / $\sigma^{\text{sp}} = 5.6\,\text{MPa}$	
	distance to interface d/b [-]	force evaluations [-]
`NT-GMRes`$(15a_0, 0)$	5.3	30557
`Sinclair`$(5a_0, 0)$	5.3	134652
	$\sigma^{\text{app}} = 14.9\,\text{MPa}$ / $\sigma^{\text{sp}} = 9.3\,\text{MPa}$	
	distance to interface d/b [-]	force evaluations [-]
`NT-GMRes`$(15a_0, 0)$	4.2	22747
`Sinclair`$(5a_0, 0)$	4.2	132645
	$\sigma^{\text{app}} = 22.4\,\text{MPa}$ / $\sigma^{\text{sp}} = 16.8\,\text{MPa}$	
	distance to interface d/b [-]	force evaluations [-]
`NT-GMRes`$(15a_0, 0)$	3.2	15284
`Sinclair`$(5a_0, 0)$	4.3	81851

Table 4.1: Number of force evaluations corresponding to the Newton-GMRes and Sinclair's method for the moving dislocation problem from Figure 4.4

4.1.2 Three-dimensional test cases for face-centered cubic lattices

As a three dimensional test case a face-centered cubic (fcc) lattice is selected. The basis vectors are given by

$$\boldsymbol{v}_1 = 1/2\begin{pmatrix}0 & a_0 & a_0\end{pmatrix}^{\mathsf{T}}, \quad \boldsymbol{v}_2 = 1/2\begin{pmatrix}a_0 & 0 & a_0\end{pmatrix}^{\mathsf{T}}, \quad \boldsymbol{v}_2 = 1/2\begin{pmatrix}a_0 & a_0 & 0\end{pmatrix}^{\mathsf{T}}. \tag{4.15}$$

Atomic interactions are prescribed via a homogenized embedded atom model (Varvenne et al., 2016). Its site energy is given by

$$\mathcal{E}_\xi(\{\boldsymbol{u}_\eta - \boldsymbol{u}_\xi\}) = \sum_{\eta\in\mathcal{R}_\xi} \phi^{\mathrm{avg}}(\boldsymbol{u}_\eta - \boldsymbol{u}_\xi) + \sum_X c_X F_X(\bar{\rho}_\xi(X, \{\boldsymbol{u}_\eta - \boldsymbol{u}_\xi\})), \tag{4.16}$$

where ϕ^{avg} is a pair potential of the average atom, c_X is the concentration of atom type X and F_X is the embedding function of the average electron density of atom ξ which itself depends on the concentration and the differential displacements between the atoms. In principle, any multiple-element EAM potential can be converted to (4.16). Here the aluminum-magnesium potential from (Liu et al., 1996) is selected with $c_{\mathrm{Mg}} = 14.7$, intentionally chosen, which yields an effectively isotropic interatomic potential. The reasoning behind this approach is the fact that the fully anisotropic continuum solution is not implemented at present. Nevertheless it is emphasized that this is rather a convenient choice and not a limitation in the sense that it preserves all requirements on realistic EAM potentials with respect to nonlinearity, nonlocality and the Cauchy relations. That is, any qualitative changes of the numerical estimates for other, physically motivated, EAM potentials are not expected.

The numerical parameters remain the same as in the previous section except for the initial time step which is now set to 0.08 ps which led to an overall faster convergence of FIRE.

4.1.2.1 Void relaxation

Consider a spherical void centered in the origin of the atomistic domain, possibly subject to a remote applied stress σ_{22}, as shown in Figure 4.5. The atomistic domain is given by

$$\mathit{\Lambda}^{\mathrm{a}} := (\{\, \boldsymbol{x} \in \mathbb{R}^3 \mid \|\boldsymbol{x}\| \le r \,\} \cap \mathit{\Lambda}) \setminus \mathit{\Lambda}^{\mathrm{void}}, \tag{4.17}$$

where $\mathit{\Lambda}^{\mathrm{void}} = \{\, \boldsymbol{x} \in \mathbb{R}^3 \mid \|\boldsymbol{x}\| \le r_{\mathrm{c}} \,\} \cap \mathit{\Lambda}$ is the region is excluded from the computational domain.

Discussion (accuracy). First, consider the case $\sigma_{22} = 0$. This problem is similar to the vacancy case but a slightly slower decay of the error is expected for the coupled problem as a void generates a field which has a longer range. The method is tested for various choices of the accuracy of the $\mathscr{H}$-matrices prescribed by the parameter ϵ. In general it

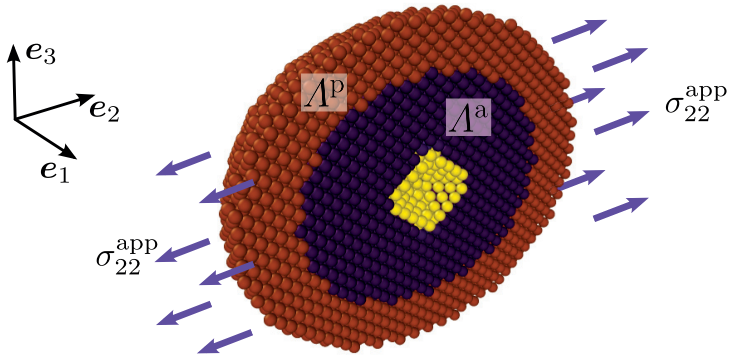

Figure 4.5: Illustration of an fcc lattice containing a void subject to a uniaxial remote tensile stress

can be quite difficult to estimate a proper ϵ which is accurate enough to satisfy the user demands while preserving optimal efficiency. Here, the following approach is taken. From the two-dimensional test cases it can be observed that a cut-off radius of $5a_0$ is sufficient. If the relative error depends only weakly on the shape of the domain and the solution on the boundary, in comparison with the void problem, the necessary accuracy may be estimated from the force quadrupole problem in Section 2.7.4. For this example the relative error in the pad displacements is of $\mathcal{O}(10^{-4})$ for $r_{\mathrm{cut}} = 5a_0$ (c.f. Figure 2.8 (a)). Indeed, in Figure 4.6 (a) it can be observed that an accuracy of $\epsilon = 10^{-4}$ is sufficient to predict a smooth decay proportional to $(N^{\mathrm{a}})^{-2}$ for both the Newton-GMRes and the Sinclair method. An accuracy of $\epsilon = 10^{-3}$ was found to give almost no decay of the error for $N^{\mathrm{a}} > 2000$, yet it should be noted that it is still much more accurate than the clamped boundary conditions. In total the error in the energy is always several orders of magnitude smaller, similarly to the vacancy problem.

Discussion (efficiency). The number of force evaluations is ≈ 10 times higher for `Sinclair(`$5a_0, 10^{-4}$`)` when compared to `NT-GMRes(`$5a_0, 10^{-4}$`)`. It was found that the number of force evaluations for the flexible boundary conditions does not increase with the number of atoms in the system while for the clamped boundary conditions it increases slightly. This might be due to the fact that the problem is closer to an instability than the vacancy but still much further than in the case of a pre-existing dislocation. For this problem the cost per single force computation is 0.0087 ms for `Sinclair(`$5a_0, 10^{-4}$`)` and 0.053 ms for `NT-GMRes(`$5a_0, 10^{-4}$`)`, i.e. a single force computation is ≈ 6 times more expensive for `NT-GMRes(`$5a_0, 10^{-4}$`)`. The increase by a factor of ≈ 3 in comparison with the two-dimensional problem stems from the fact that the ratio between updating the pad atoms and one computation of the entire atomic force vector is now significantly higher. More precisely, the cost for solving the algebraic problem (c.f. Section 2.6.1) is now ≈ 2.5-3 times higher than the subsequent evaluation of the atomic forces. Thus, an overall speedup of ≈ 1.5-2 is obtained by dividing the ratio between the number of force evaluations and the ratio of the cost per single force computation.

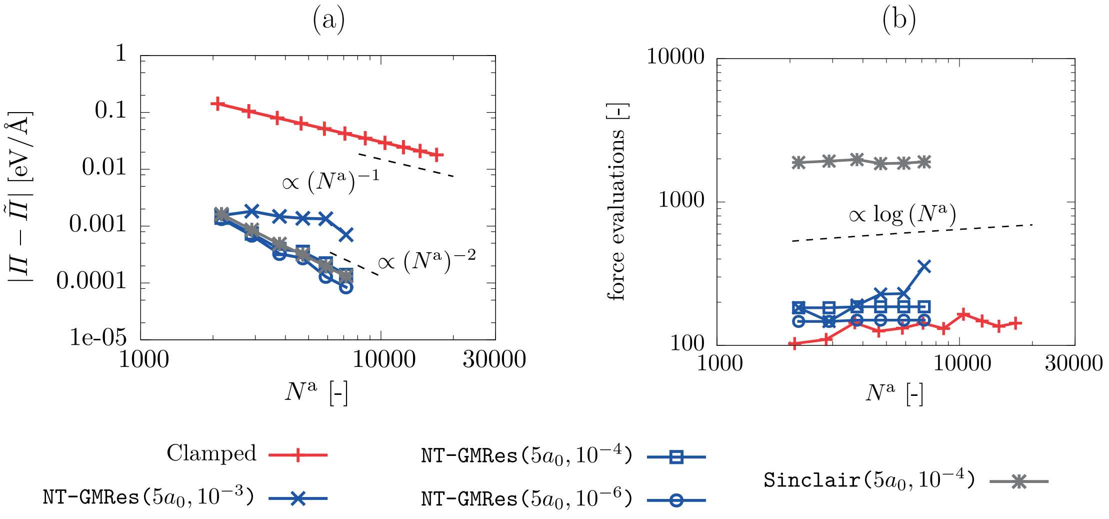

Figure 4.6: (a) Energy error vs. number of real atoms N^{a} for the void problem for clamped and flexible boundary conditions. (b) Number of force evaluations corresponding to each data point in (a)

The matrix-vector multiplication (2.97) has been identified as the most time consuming part. Future research should thus be devoted to an optimization of the pre-factors of the scaling law (2.106) to further improve the performance of the $\mathscr{H}$-matrices for three dimensional problems.

4.1.2.2 Void growth under uniaxial tension

Now, a uniaxial applied stress $\sigma_{22} > 0$ is considered upon relaxation according to Figure 4.5. Therefore the stress is increased up to a strain of $\varepsilon_{22} \approx 2.5\,\%$. At this stress level, both clamped and flexible boundary conditions predict an instability of the lattice. However, comparing the two converged solutions in Figure 4.7 reveals a much richer microstructure for the flexible boundary conditions as shown in Figure 4.7 (a). Dislocations have nucleated from the void as predicted by the dislocation extraction algorithm (Stukowski et al., 2012, DXA). The microstructure for the clamped boundary conditions in 4.7 (b) is far less evolved as it shows only small lattice distortions around the void. This test is mainly carried out to outline the benefits of flexible boundary conditions for practical applications. As an example consider plastic shielding of crack tips. This requires dislocations to nucleate from the crack and to propagate inside the atomistic domain. If the dislocation motion is perturbed upon nucleation the ductile behavior of the material might not be predicted correctly.

It is noted explicitly that the intention here is *not* to model a realistic scenario. Rather, it is emphasized that the method could also be applied to problems which involve highly distorted atomistic systems. Moreover, the numerical solver was properly converging to a residual of $\|\hat{f}^{\mathrm{a}}\| < 10^{-4}$ outlining the robustness of the proposed method.

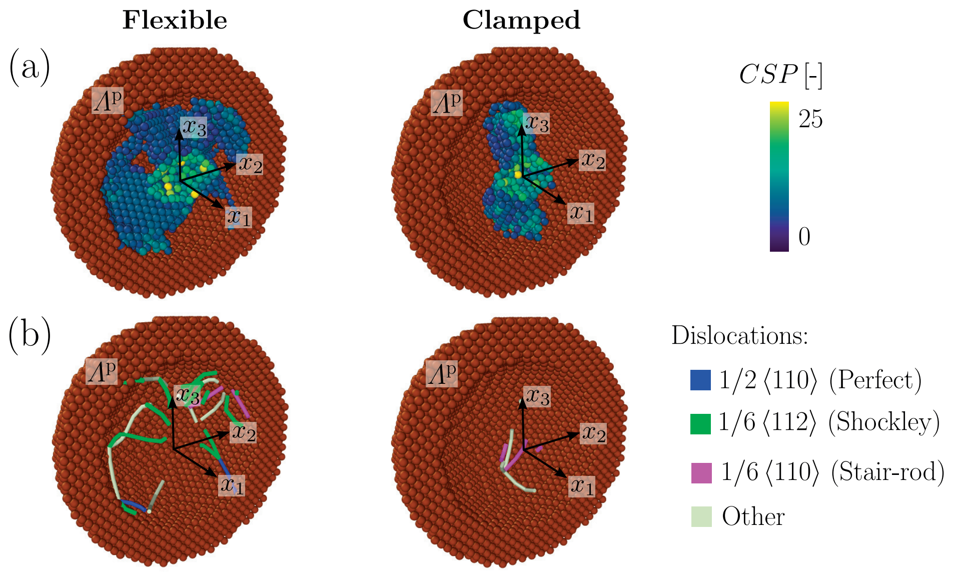

Figure 4.7: (a) Converged microstructure of a nanovoid under uniaxial tension when using flexible and clamped boundary conditions; the coloring of the real atoms is according to the centro-symmetry parameter CSP (Kelchner et al., 1998) (only atoms with $CSP > 5$ are shown in the fully atomistic domain). (b) Corresponding dislocation network as predicted by the DXA within Ovito (Stukowski, 2010, `www.ovito.org`)

4.2 Validation of the updated Green function method

4.2.1 Reference problem

The updated Green function method (Algorithm 6, Section 3.8) involves two approximations. First, it assumes that the forces on the continuum DDD nodes due to the atomistic dislocations can be accurately computed by representing the atomistic dislocations via the DDD method. Second, it assumes that the displacement fields on the pad atoms due to the atomistic dislocations can accurately be represented by elastic DDD fields. Use of the DDD method for both aspects implies that linear elasticity (and, usually, isotropic linear elasticity) is sufficiently accurate for these fields. Errors can thus arise, relative to a fully coupled solution, due to the inadequacy of linear, isotropic elasticity.

The DDD method also usually treats dislocations as having compact cores, whereas dislocations in fcc and hcp metals dissociate into partial dislocations separated by stacking faults. The DDD method can handle partial dislocations and stacking faults (see e.g. Shenoy et al., 2000) but this adds to the computational load since it doubles the number of segments and nodes, and greatly reduces the time increments, and hence is not usually considered in full DDD problems. In CADD-3d, the atomistic dislocation may be dissociated. The use of the core template mitigates the serious difference between the continuum line solution and the atomistic solution in the core of the hybrid dislocations but the far-field interactions between dissociated atomistic dislocations and continuum line dislocations remains approximate.

All of the above approximate aspects are expected to create only small errors for dislocation segments that are sufficiently far from the atomistic/continuum interface. Here, these errors are assessed quantitatively in terms of any spurious Peach-Koehler forces as a function of the distance of an atomistic dislocation from the A/C interface. To do so, following Dewald and Curtin (2006) and Pavia and Curtin (2015), a *straight edge dislocation* residing in a semi-periodic fcc atomistic domain is considered which approaches the atomistic/continuum interface; there are no hybrid dislocations in this problem.

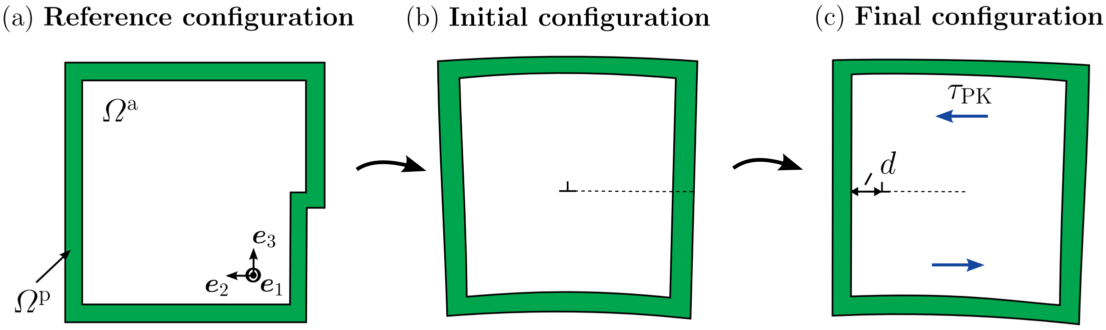

Figure 4.8: Schematic illustration of the numerical test to determine the spurious stress exerted on an edge dislocation near artificial interfaces. The reference configuration is given in (a). Subsequently a predictor for an edge dislocation is applied to the reference configuration in (b). An applied shear stress τ^{app} will eventually move the dislocation to the stable position in (c)

The problem is initialized by placing one dislocation at the center of a large box by displacing all atoms according to the continuum Volterra field as shown in Figure 4.8 (a) and (b). A sufficient in-plane size (240 Å × 240 Å) is validated ex post facto by observing that the initial dislocation motion starts at precisely the Peierls stress measured independently in a much larger atomistic cell. The box is periodic in the line direction of the dislocation, enabling use of a minimum periodic distance defined by the atomic unit cell. The initial box also includes a step consisting of two extra planes of atoms on the upper half of the box. The $\tilde{\boldsymbol{u}}$ field of the dislocation is then imposed, with the jump in the displacement across the glide plane eliminating the step to leave a smooth boundary. With the pad atoms held fixed, the atomistic system is then fully relaxed, during which the dislocation dissociates naturally into two partial dislocations separated by a stacking fault. For the large box size used here, this relaxation is independent of the $\tilde{\boldsymbol{u}}$ field.

A uniform shear stress is then applied to the entire system. The dislocation commences glide at the Peierls stress τ_{P}. In an infinite atomistic system, the dislocation would glide continuously at the Peierls stress. In the coupled method, errors in the coupling method give rise to spurious forces τ_{SP} on the dislocation; these are found to repel the dislocation from the boundary. Thus, under an applied stress τ_{PK} above the Peierls stress, the dislocation will glide until it reaches an equilibrium position (position of the center of mass of the dislocation) at distance d from the interface at which the total driving force $\tau_{\mathrm{PK}} - \tau_{\mathrm{P}} - \tau_{\mathrm{SP}} = 0$ (see Figure 4.8). The spurious force at d is then measured directly as $\tau_{\mathrm{SP}}(d) = \tau_{\mathrm{PK}} - \tau_{\mathrm{P}}$.

The spurious stresses are analyzed corresponding to the three relevant approximate solutions for $\tilde{\boldsymbol{u}}$ that could be used in CADD-3d:

(i) **Isotropic undissociated** (Appendix A.2.2, equation (A.25))

$$\tilde{\boldsymbol{u}}(\boldsymbol{x}) = \tilde{\boldsymbol{u}}^{\mathrm{edge2}}(\boldsymbol{x}) = \frac{b}{2\pi}\begin{pmatrix} \frac{x_2 x_3}{2(1-\nu)r^2} + \arctan\frac{x_3}{x_2} \\ \frac{x_3^2 - x_2^2}{4(1-\nu)r^2} - \frac{1-2\nu}{4(1-\nu)}\ln r^2 \\ 0 \end{pmatrix}, \quad r = \sqrt{x_2^2 + x_3^2}. \tag{4.18}$$

(ii) **Anisotropic undissociated** (Appendix A.2.4)

$$\begin{aligned} \tilde{\boldsymbol{u}}(\boldsymbol{x}) &= \tilde{\boldsymbol{u}}^{\mathrm{aiso}}(\boldsymbol{x}; \boldsymbol{b}) \\ &= \frac{1}{2}\sum_{i=1}^{3} \ln\left((x_2 + r_i x_3)^2 + (q_i x_3)^2\right)\boldsymbol{c}_i - \arctan\left(\frac{q_i x_3}{x_2 + r_i x_3}\right)\boldsymbol{d}_i. \end{aligned} \tag{4.19}$$

The real quantities $\boldsymbol{c}_i$, $\boldsymbol{d}_i$, r_i and q_i for $\boldsymbol{b} = \begin{pmatrix} 0 & b & 0 \end{pmatrix}^{\mathsf{T}}$ are computed using the procedure described in (Hirth and Lothe, 1982, page 444-445).

(iii) **Anisotropic partial dislocations**

$$\tilde{\boldsymbol{u}}(\boldsymbol{x}) = \tilde{\boldsymbol{u}}^{\mathrm{aiso}}(x_1, x_2 + \Delta^{\mathrm{split}}, x_3; \boldsymbol{b}_{\mathrm{le}}) + \tilde{\boldsymbol{u}}^{\mathrm{aiso}}(x_1, x_2 - \Delta^{\mathrm{split}}, x_3; \boldsymbol{b}_{\mathrm{tr}}), \tag{4.20}$$

where $2\Delta^{\mathrm{split}}$ is the atomistic spacing between the leading and trailing partial dislocations having Burgers vectors $\boldsymbol{b}_{\mathrm{le}}$, $\boldsymbol{b}_{\mathrm{tr}}$, respectively,

$$\boldsymbol{b}_{\mathrm{le}} = \frac{1}{2}b\begin{pmatrix} \frac{1}{\sqrt{3}} & 1 & 0 \end{pmatrix}^{\mathsf{T}}, \qquad \boldsymbol{b}_{\mathrm{tr}} = \frac{1}{2}b\begin{pmatrix} -\frac{1}{\sqrt{3}} & 1 & 0 \end{pmatrix}^{\mathsf{T}}. \tag{4.21}$$

To be clear, Algorithm 6 is used for each of the above approximate displacement fields. There is no discrete dislocation in the continuum domain and so only the atomistic problem is solved. At each applied stress, the atomistic system is relaxed, the new position of the dislocation is detected (averaged of the centers of mass of the detected tetrahedra representing the full dislocation), and the pad atom displacements are updated according to the new positions according to the approximate displacement field (equation (4.18), (4.19) or (4.20)). Convergence is obtained when the criterion (3.51) is satisfied with $TOL^{\mathrm{detn}} = 10^{-6}\,b$.

4.2.2 Comparison with a fully coupled scheme

Aluminum as described by the EAM potential of Ercolessi and Adams (1994) is used as a reference material which is slightly anisotropic ($2C_{44}/(C_{11} - C_{12}) = 1.315$). The partial spacing of the dissociated edge dislocation is $2\Delta^{\text{split}} = 15$ Å and the Peierls stress is $\tau_{\text{P}} = 3$ MPa. This problem was studied for this same material using the full CADD atomistic/continuum coupling wherein the linearly elastic continuum domain is coupled to the fully non-linear atomistic domain (Dewald and Curtin, 2006; Pavia and Curtin, 2015). The results are compared to these full results as a measure of the error of using the linear elasticity solution.

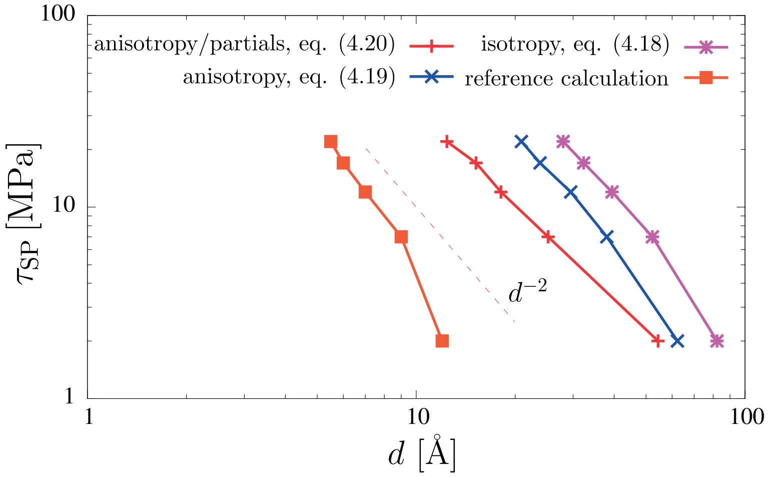

Figure 4.9: Spurious stress τ_{SP} on a stable edge dislocation as a function of its distance to the artificial interface d

Figure 4.9 shows the spurious stress vs. distance d to the interface for the successively better approximations to $\tilde{\boldsymbol{u}}$. In all cases, including the fully non-linear solution, the spurious stresses scale as $\approx\ d^{-2}$ as for the test problem considered in Section 4.1.1.3. The magnitude of the error decreases with increasing accuracy of the approximation for $\tilde{\boldsymbol{u}}$. The isotropic compact core solution is least accurate while the anisotropic dissociated core is the most accurate when using elasticity, and the full coupled solution is overall most accurate. The magnitude of the spurious stresses shown here remain small, on the order of 10 MPa, with an error of 12 MPa reached at distances of 40, 30, 18, and 7 Å with increasing fidelity of the numerical method. To further support these results, the initial dislocation was placed at 10 Å from the interface and Algorithm 6 was applied in the same way. The final positions of the relaxed dislocation are in agreement with the results from Figure 4.9 up to $\approx b$ due to the direction-dependent Peierls stress (which acts opposite to the direction of motion) and to the non-uniqueness of the dislocation detection. Overall, these results show that the typical distances over which moderate spurious coupling errors (>5 MPa) occur is on the order of 30-60 Å when using the various linear elasticity approximations to $\tilde{\boldsymbol{u}}$. Testing of local details of the hybrid dislocation coupling in CADD-3d must therefore, when using these approximations, ensure that the dislocations remain at these distances or further (see below). For the CADD-3d methodology described in Section 3.6 and 3.7 with full coupling, the spurious forces are those corresponding to the reference solution (Dewald and Curtin, 2006; Pavia and Curtin, 2015), which are negligible at distances beyond 10 Å.

Finally, these tests serve as guidance for the determination of a necessary "passing" distance, or size of any overlap zone between atomistic and continuum regions, that must be developed for full operation of CADD-3d to treat dislocations moving in and out of the atomistic and continuum domains. The approximate updated Green function method (with spurious forces as shown in Figure 4.9) enables the use of a passing methodology. However, if the stress on the dislocations in the vicinity of the interface is rather low, the passing distance may become impracticably large as shown in Figure 4.9. Fortunately, this may not be an issue for many problems where dislocations mainly glide off into the bulk material (e.g. cracks under tensile loading). Another practical example is presented in (Cho, 2017) for a Frank-Read source, subject to a constant applied shear stress. The stresses on the dislocations approaching the interface are high enough such that the passing distance can be kept to practical limits, i.e. a few Angstroms of the leading partial dislocation from the interface. For the fully coupled problem (c.f. Algorithm 5) a universal passing distance is expected to be in the range 5-10 Å as demonstrated by Pavia and Curtin (2015) and in many other works on CADD-2d.

4.3 Validation of CADD-3d for hybrid dislocations

4.3.1 Reference problem

As a test problem to assess the accuracy of the CADD-3d treatment of hybrid dislocations, the quasistatic bow-out of an initially straight planar periodic array of edge dislocations in an infinite box under an applied resolved shear stress τ^{app} is examined. A schematic of the problem is shown in Figure 4.10 (a). This problem can be studied accurately in a full atomistic simulation in a suitable large but finite size box and in a full discrete dislocation dynamics simulation (see below), which enables (i) careful comparison of the predictions of the CADD-3d method to the fully atomistic results and (ii) calibration of DDD to atomistics (see Figure 4.10 (b) and (c)).

A single periodic spacing of the pinning points of $l_1 \approx 200$ Å,[2] is chosen which is then the periodic length of the simulation cell along x_1. A finite box size, l_2 along the glide direction and l_3 normal to the slip plane, is used with periodicity in x_2 and traction boundary conditions on the x_3 surfaces. Following Szajewski and Curtin (2015) for exactly this problem, the dimensions are chosen $l_2 \approx l_3 \approx 400$ Å. This size is sufficient to ensure that image effects, due to the traction-free x_3 surfaces, of the non-straight

---

[2] Note that the real box dimensions can vary slightly from the given values according to the periodic interatomic spacing

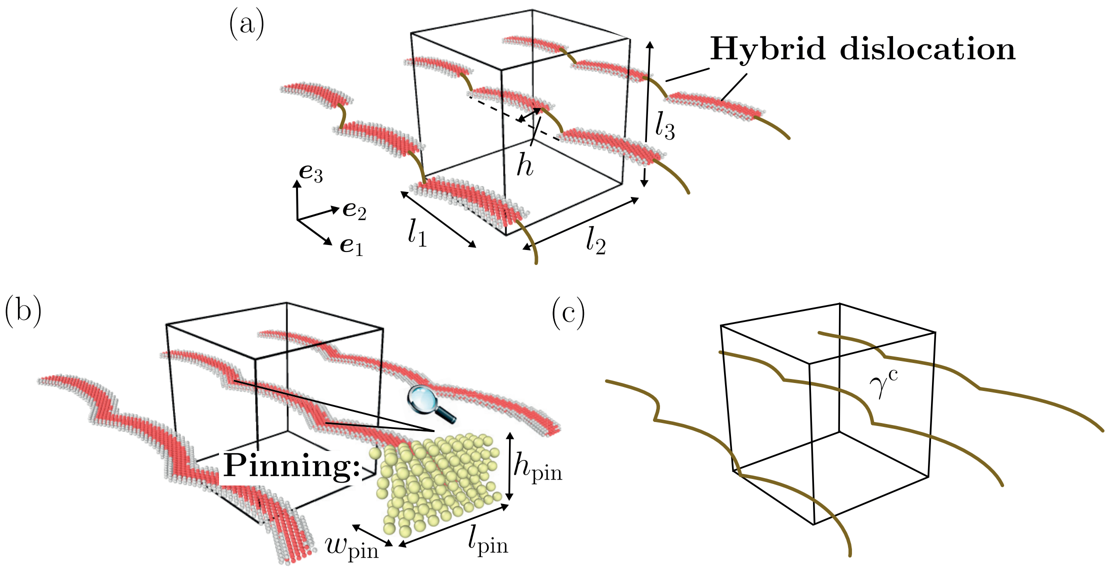

Figure 4.10: Schematic illustration of the bow-out of a nominal straight dislocation for (a) the coupled CADD-3d problem, (b) the fully atomistic model (only the atoms in the core region are visualized), and (c) the continuum DDD model

bowed-out dislocations are minimal and can be neglected relative to the applied loads. Pinning of the dislocation follows (Szajewski and Curtin, 2015; Szajewski et al., 2015) and is described in more detail below.

In accordance with the validation study in Section 4.2.2, Aluminum is used, modeled by an EAM potential (Ercolessi and Adams, 1994). Material parameters needed for the isotropic continuum DDD simulation are the lattice constant $a_0 = 4.032\,\text{Å}$, Burgers vector $b = 2.851\,\text{Å}$, approximate isotropic Poisson ratio $\nu = 0.35$ and shear modulus $\mu = 30.8\,\mathrm{GPa}$. For this quasistatic problem, results are independent of the dislocation mobility, although a value for the mobility is used for incrementing the DDD solution toward equilibrium. Also required is a calibrated dislocation core energy to supplement the non-singular dislocation field solution in the DDD code ParaDis; this is discussed below.

Before describing the full test problem in more detail, it is convenient to present the two corresponding reference problems, the fully atomistic and fully DDD models of the same test problem geometry. The fully atomistic solution provides the base for assessment of the CADD-3d algorithms. The fully DDD solution is used to calibrate the DDD core energy parameter to the fully atomistic solution.

4.3.2 Line tension model

First, an analytical model is used to estimate the stability region of the problem, i.e. the maximum applied shear stress under which an equilibrium solution exists. In order to simplify the problem the influence of the periodic images are neglected. The external energy due to the applied shear stress is then given by

$$\Pi^{\mathrm{ext}} = \int_{-l_1/2}^{l_1/2} \tau^{\mathrm{app}} b \, s_2(x_1) \, \mathrm{d}x_1. \tag{4.22}$$

The dislocation tries to minimize its slip surface due to its line tension T which is assumed to be constant over the entire line. The associated internal energy is therefore given by

$$\Pi^{\mathrm{int}} = T \int_{-l_1/2}^{l_1/2} \sqrt{1 + s_2'(x_1)^2} \, \mathrm{d}x_1, \tag{4.23}$$

where $s_2'(x_1) = \partial_{x_1} s_2(x_1)$. The total energy thus reads

$$\Pi^{\mathrm{tot}} = \Pi^{\mathrm{int}} + \Pi^{\mathrm{ext}} = \int_{-l_1/2}^{l_1/2} \left(T \sqrt{1 + s_2'(x_1)^2} + \tau^{\mathrm{app}} b \, s_2(x_1) \right) \mathrm{d}x_1. \tag{4.24}$$

Minimizers $s_2(x_1)$ to (4.24) solve the Euler-Lagrange equation

$$T \frac{\partial}{\partial x_1} \frac{s_2'(x_1)}{\sqrt{1 + s_2'(x_1)^2}} + \tau^{\mathrm{app}} b = 0. \tag{4.25}$$

Following Shenoy and Phillips (1997), it is assumed that the final configuration γ has the form of a catenary. The relationship between the applied stress τ^{app} and the maximal bow-out h is then given by (see Shenoy and Phillips, 1997)

$$\tau^{\mathrm{app}}(h) = \frac{8hT}{b l_1^2}. \tag{4.26}$$

Atomistic models are usually assumed to be stable only up to a bow-out of $\approx 1/4 l_1$, e.g. due to interactions between the partial dislocations not considered in the continuum model. Hence, the necessary applied stress producing $h = 1/4 l_1$ is sought-after. For the tension factor T the common assumption from the literature (see e.g. Hirth and Lothe, 1982) is used, i.e. that $T \approx \mu b^2/4$. The required applied stress for a bowout of $1/4$ of the distance between the pinning points is then

$$\tau^{\mathrm{app}}|_{h=50\,\mathrm{\AA}} = 219.527\,\mathrm{MPa}. \tag{4.27}$$

4.3.3 Atomistic and discrete dislocation dynamics reference solutions

Schematic illustrations of the two reference problems are shown in Figure 4.10 (b) and (c). The fully atomistic box dimensions l_1, l_2 and l_3 are those given above, with ≈ 2 million atoms and therefore ≈ 6 million degrees of freedom. The introduction of the periodic array of straight dislocations in the initial structure is accomplished using the known elastic displacement fields of the so-called periodic array of dislocations (PAD, see Appendix A.2.5) given by

$$\begin{aligned}\tilde{u}_1^{\mathrm{PAD}}(\boldsymbol{x}) =& 0,\\ \tilde{u}_2^{\mathrm{PAD}}(\boldsymbol{x}) =& -\frac{b}{4\pi(1-\nu)}\frac{Cx_3\sin(2Cx_2)}{(\cos(2Cx_2)-\cosh(2Cx_3))}\\ &+\frac{b}{2\pi}\arctan(\coth(Cx_3)\tan(Cx_2)),\\ \tilde{u}_3^{\mathrm{PAD}}(\boldsymbol{x}) =& -\frac{b}{4\pi(1-\nu)}\frac{Cx_3\sin(2Cx_3)}{(\cos(2Cx_2)-\cosh(2Cx_3))}\\ &-\frac{b(1-2\nu)}{8\pi(1-\nu)}\ln(|\cos(2Cx_2)-\cosh(2Cx_3)|),\end{aligned} \tag{4.28}$$

where $C = \pi/l_2$. Note that (4.28) is not truly periodic since it contains the slip step but, as in the previous section, a reference configuration is chosen that includes the same slip step so that the deformed configuration has the required in-plane periodicity.

The atom positions are then relaxed to equilibrium subject to the periodic boundary conditions in x_1- and x_2-directions and free surfaces on the top and bottom x_3 boundaries. The Hessian-free Newton-Raphson algorithm in LAMMPS is used, with the convergence criterion $\|\boldsymbol{f}^{\mathrm{a}}\|_{l^2(\Omega^{\mathrm{a}})} < 10^{-4}\,\mathrm{eV/Å}$.

After the initial relaxation, the "pinning points" for the subsequent bow-out (see Figure 4.10 (b)) are established as follows. Atoms in a small rectangle (dimensions: $l_{\mathrm{pin}} = 24\,\mathrm{Å}$, $w_{\mathrm{pin}} = 12\,\mathrm{Å}$, $h_{\mathrm{pin}} = 6\,\mathrm{Å}$) centered on the core of the dislocation and at one end of the periodic box along x_1 are identified. These atoms are then held fixed (zero subsequent displacement) during subsequent loading of the simulation cell. Forces are then applied to the atoms on the top along x_3 corresponding to a desired applied shear stress τ^{app} as $\boldsymbol{f}^{\mathrm{ext}} = \frac{A}{N}\tau^{\mathrm{app}}\boldsymbol{e}_2$ where $A = l_1 l_2$ is the area of the top surface and N the number of atoms in the surface layer, with forces of opposite sign applied on the bottom surface atoms. The entire system is then again allowed to relax to equilibrium, during which the dislocation core bows out between the periodic pinning points to reach an equilibrium configuration characterized by the bow-out height h at the center of the box.

In the corresponding full DDD continuum problem, the pinning points are defined by fixed segments or length $w_{\mathrm{pin}}/2$ on each end of the dislocation line along x_1. The initial dislocation line is discretized into 16 piecewise linear segments of lengths between $5b - 8b$. The DDD methodology in ParaDis is employed, which uses a nonsingular theory (Cai et al., 2006) with parameter a to regularize the singular core. An additional core energy per unit length is introduced with a dependence on the character angle according to linear elastic theory

$$W^{\mathrm{core}}(E^{\mathrm{core}};\vartheta) = E^{\mathrm{core}}\left(\frac{\sin^2\vartheta}{1-\nu} + \cos^2\vartheta\right)b^2, \tag{4.29}$$

as defined in Section 1.4.3, Example 1.5. Since the non-singular theory includes some core energy through the regularization parameter a, the parameter $E^{\text{core}} = E^{\text{core}}(a)$ has an implicit dependence on a if the total DDD core energy is intended to agree with the true atomistic core energy. Usually W^{core} is calibrated with respect to a representative atomistic configuration, e.g. straight dislocations in infinite domains. For the bow-out problem, Szajewski et al. (2015) were calibrating W^{core} for a given amount of bowout and showed good agreement between fully atomistic and fully DDD solutions in ParaDis by varying the periodic length l_1 between the pinning points. The parameters used in (Szajewski et al., 2015) are

$$a = 7.714\,\text{Å}, \qquad\qquad E^{\text{core}}(a) = 5\,\text{GPa}. \tag{4.30}$$

An alternative calibration with respect to an infinite straight edge dislocation, as described in Section 1.5.4, gives

$$E^{\text{core}}(a) = 6.4\,\text{GPa} \tag{4.31}$$

for the same a.

Solution of the DDD bow-out problem within ParaDis is achieved by computing the velocities for nodes $\boldsymbol{s} \in \gamma^{\text{c}}$ using the overdamped mobility law

$$\boldsymbol{v} = \boldsymbol{M}(\boldsymbol{f}^{\text{pk}} + \boldsymbol{f}^{\text{core}}). \tag{4.32}$$

where $\boldsymbol{M}$ is the mobility tensor. Here, the motion is restricted to gliding on the defined glide plane and quasistatic solutions are sought-after. The numerical solution of (4.32) is reduced, using a forward-Euler integration scheme with time step Δt, to a steepest descent method

$$\boldsymbol{v}_k \approx \frac{\boldsymbol{s}_{k+1} - \boldsymbol{s}_k}{\Delta t} \qquad \Rightarrow \qquad \boldsymbol{s}_{k+1} = \boldsymbol{s}_k + \Delta t \boldsymbol{M}(\boldsymbol{f}_k^{\text{pk}} + \boldsymbol{f}_k^{\text{core}}), \tag{4.33}$$

where $\Delta t\boldsymbol{M}$ acts as a constrained line search. The steepest descent method is known to converge rather slowly but here the number of nodes is small and the computational cost of solving the DDD problem is negligible as compared to the cost of solving the atomistic problem. Convergence is achieved when the total force on the dislocation line is

$$\|\boldsymbol{f}^{\text{pk}} + \boldsymbol{f}^{\text{core}}\|_{L^2(\gamma^{\text{c}})} < 10^{-3}\,\text{N}. \tag{4.34}$$

Figure 4.11 (a)-(c) show the fully-atomistic and fully DDD configurations with the core parameters given by (4.30) obtained at applied shear stresses of 50, 100 and 150 MPa which are below the critical value as predicted by the line tension model. The good agreement confirms that the choice of the core energy parameter in ParaDis is sufficiently accurate. At 150 MPa, there is a slight deviation in the maximum bow-out between the two models ($\approx 34\,\text{Å}$ for DDD vs. $\approx 30\,\text{Å}$ for atomistics), which most likely arises because the core parameters (4.30) were calibrated using different box sizes than those used here[3] but given the simplicity of the approach which only requires the calibration of one *single parameter*, the results seem remarkable. As a matter of fact, an almost perfect match between both models is obtained when using E^{core} according to (4.31) as shown in Figure 4.11 (d).

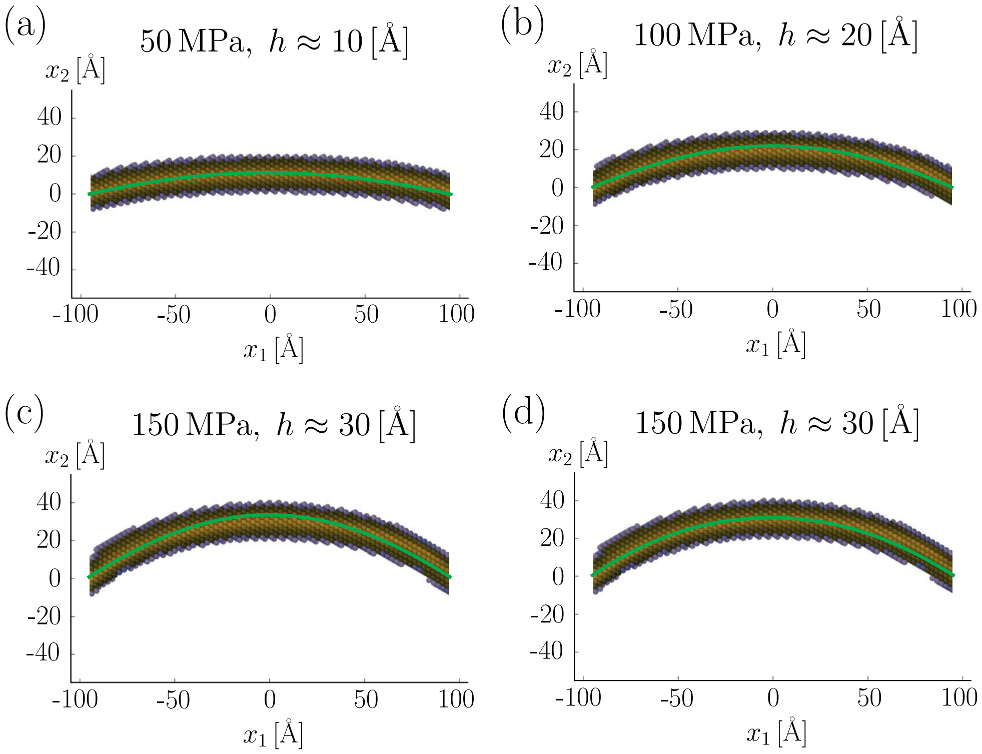

Figure 4.11: Comparison between fully atomistic calculations and the continuum model (solid line) for different applied shear stresses

In order to validate CADD-3d the DDD model with $E^{\text{core}} = 5\,\text{GPa}$ is used in the following sections since a perfect match between both models is not essential to test crucial features of the coupled problem. In practice small deviations between atomistic and DDD models are always expected.

4.3.4 CADD-3d problem

Since the atomistic domain does not contain other defects than dislocations the coupled problem can be approximated with $\tilde{\mathcal{P}}^{\text{cadd}}$ (3.48) which can be conveniently solved using the updated Green function method presented in Section 3.8.2. Corresponding results

---

[3] This is expected and was also observed in the work by Szajewski et al. (2015) (c.f. Figure 6 (a) and (b) in Szajewski et al., 2015)

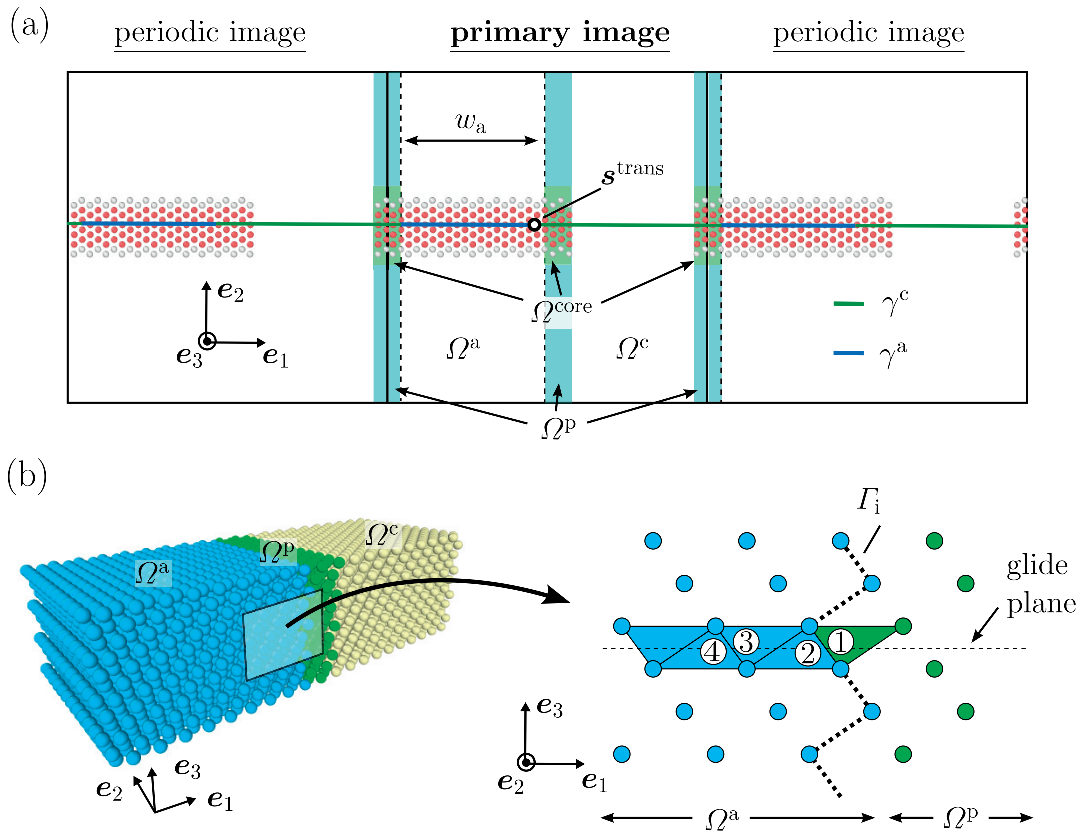
(a)
periodic image
primary image
periodic image
w_a
s^{trans}
e_2
e_3
e_1
Ω^{core}
Ω^a
Ω^c
γ^c
γ^a
Ω^p
(b)
Ω^a
Ω^p
Ω^c
Γ_i
glide plane
④
③
②
①
e_3
e_2
e_1
Ω^a
Ω^p

Figure 4.12: Schematic top view of the domain decomposition for the PAD geometry (a). A side view along the dislocation line direction is shown in (b) to illustrate where the detection algorithm generates nodal positions of γ^a (the interface node is located in region 1, its neighboring node in region 2 etc.)

obtained with the general solution procedure will be reported in a future publication (Hodapp et al., 2018b).

For the CADD-3d study of the bow-out problem, the entire domain is divided into atomistic and continuum regions along the x_1-direction (see Figure 4.10 (a)). The width of the atomistic domain is denoted w_a. A schematic top view of the coupled problem is shown in Figure 4.12 (a). The width of the pad domain is conveniently set to the width of the pinning points w_{pin} which is slightly greater than two times the cut-off radius $r_{cut} = 5.56\,\text{Å}$ of the interatomic potential. The initial displacements of the atomistic domain are taken as the relaxed configuration of the periodic array of straight dislocations from the previous subsection. The initial hybrid dislocation is a straight line along the origin.

A homogeneous shear stress at infinity is applied, which generates displacements of the pad atoms given

$$\forall \boldsymbol{\xi} \in \Omega^p \qquad \hat{\boldsymbol{u}}(\boldsymbol{\xi}) = \frac{\tau^{app}}{\mu} \xi_3 \, \boldsymbol{e}_2. \tag{4.35}$$

As the dislocation bows out, the additional displacements of the pad atoms are computed as the sum of the elastic displacements for the periodic array of straight edge dislocations $\tilde{\boldsymbol{u}}^{\mathrm{PAD}}$ (4.28) plus a correction $\varDelta\tilde{\boldsymbol{u}}^{(i,j)}$ due to curved segments for the primary and periodic images (i, j). The correction is computed using the Barnett formalism (Barnett, 1985; Barnett and Balluffi, 2007) as described in Appendix A.3.2. Including the core template correction, the displacements of the pad atoms are thus given

$$\forall\, \boldsymbol{\xi} \in \varOmega^{\mathrm{p}} \qquad \boldsymbol{u}^{\mathrm{a}}(\boldsymbol{\xi}) = \tilde{\boldsymbol{u}}^{\mathrm{PAD}}(\boldsymbol{\xi}) + \sum_{j=-N_2}^{N_2} \sum_{i=-N_1}^{N_1} \varDelta\tilde{\boldsymbol{u}}^{(i,j)}(\boldsymbol{\xi}) + \varDelta\tilde{\boldsymbol{u}}^{\mathrm{corr}}(\boldsymbol{\xi}) + \hat{\boldsymbol{u}}(\boldsymbol{\xi}), \tag{4.36}$$

where N_1, N_2 are the number of periodic images considered in the x_1- and x_2-direction, respectively. For the application of the core template (Anciaux et al., 2018), a core region $\varOmega^{\mathrm{core}}$ is used with $r^{\mathrm{core}} = 16\,\text{Å}$ which covers the stacking fault of the chosen interatomic potential. The core region comprises a blending region of width $\approx 4\,\text{Å}$ to guarantee a smooth transition of $\varDelta\tilde{\boldsymbol{u}}^{\mathrm{corr}}$ to zero at $\partial\varOmega^{\mathrm{core}}$ (c.f. Section 3.5). Tests with larger core templates gave no qualitative change in the results. Throughout the simulations, the displacements of atoms in the pinning regions are held fixed.

After each relaxation of the atomistic system, the discrete dislocation γ^{a} is re-detected. Following the approximate approach (see Section 3.8), the full DDD line $\gamma^{\mathrm{a}} + \gamma^{\mathrm{c}}$ is used to compute the forces on γ^{c} and the pad displacements. The DDD line γ^{c} is then evolved according to the PK forces on the nodes within ParaDis. The new DDD line is then used to update the pad displacement field, and the atomistic system is then relaxed again.

As indicated in Section 3.8.2 the choice of the transmission node $\boldsymbol{s}^{\mathrm{trans}}$ is not unique and may influence the final converged solution. The algorithms presented in Chapter 3 state that $\boldsymbol{s}^{\mathrm{trans}}$ should reside in the atomistic domain, and here the effect of $\boldsymbol{s}^{\mathrm{trans}}$ on the final solution is demonstrated explicitly. For the selection of the transmission node a simple scheme is employed which does not require additional efforts with regard to the implementation. Recall that the dislocation detection algorithm identifies successive tetrahedral units in the atomistic domain, schematically depicted by the filled triangles in Figure 4.12 (b). These units are then used to discretize the dislocation into nodes and segments. The transmission node is then the first node in the atomistic domain, which could be in the first tetrahedron, the second, the third, etc. Assume for a moment that $\boldsymbol{s}^{\mathrm{trans}}$ is in the first tetrahedron (i.e. region 1 in Figure 4.12 (b)). As a consequence γ^{a} would only advance in very small increments in the vicinity of the interface. As a result, the algorithm may suffer from premature convergence leaving artificial kinks at the interface. Therefore it might be favorable to ignore the interface node and set $\boldsymbol{s}^{\mathrm{trans}}$ to be equal to the detected node in region 2, 3 or even farther in the atomistic domain.

4.3.5 Assessment of CADD-3d

The coupled problem is applied to study the bow-out process at an applied shear stress of 150 MPa. At this stress level, the reference atomistic and DDD dislocation lines do not match perfectly but are sufficiently close to enable assessment of the coupled problem. Convergence is attained when the criterion (3.51) is satisfied with $TOL^{\mathrm{detn}} = 10^{-2}\,b$. For all numerical simulations here, convergence is reached after 15-25 global iterations.

In order to judge the accuracy of the coupled problem, the bow-out of the hybrid dislocation is compared with the atomistic reference calculation. More precisely, the difference in the displacements $\varDelta s_{\mathrm{hyb},2}$ and $\varDelta s^{\mathrm{ref}}_{\mathrm{a},2}$ is measured along the glide direction (x_2-direction). In practice one is only interested in the error in $\varOmega^{\mathrm{a}}$. Defining $\mathcal{A}(w) = (-l_1/2 + w_{\mathrm{pin}}, -l_1/2 + w_{\mathrm{pin}} + w)$ as an interval along the x_1-direction which encompasses a length $w \leq w_{\mathrm{a}}$, the relative error with respect to w is then defined as

$$e_{\mathrm{rel}}(w) = \frac{\|\varDelta s_{\mathrm{hyb},2} - \varDelta s^{\mathrm{ref}}_{\mathrm{a},2}\|_{L^2(\mathcal{A}(w))}}{\|\varDelta s^{\mathrm{ref}}_{\mathrm{a},2}\|_{L^2(\mathcal{A}(w))}}. \tag{4.37}$$

The coupled problem is analyzed for two different domain decompositions, $w_{\mathrm{a}} \approx l_1/4$ and $w_{\mathrm{a}} \approx l_1/2$, and various choices of the transmission node position. The relative errors are presented in Table 4.2.

First, the width of the atomistic domain is chosen to be $w_{\mathrm{a}} \approx l_1/4$ of the width of the domain. This problem represents a crucial test case for the core template approximation since the character angle must evolve and eventually reach the equilibrium value $0° < \vartheta_{\mathrm{p}} < 90°$ near the atom/continuum interface. The discrete dislocation γ^{c} is discretized into eleven segments (including the one crossing the pad region) such that the segment length is approximately the same as for the reference DDD problem. The coarsening of the discrete atomistic dislocation is chosen to match this segment length approximately such that the total number of segments remains between 14-16 during one simulation. Tests were then performed using different locations of the transmission node $\boldsymbol{s}^{\mathrm{trans}}$. The final equilibrium configurations are shown in Figure 4.13 (a)-(c). The choice of the transmission node has a clear influence on the convergence. As stated in Section 3.8, when the transmission node is at or near the atom/continuum interface, namely in region 1 or 2 (c.f. Figure 4.12 (b)), the algorithm converges pre-maturely to leave a small kink at the A/C interface. When the transmission node is further from the A/C interface (region 3), the converged solution is in excellent agreement with the fully-atomistic solution. Specifically, the hybrid dislocation line coincides nearly perfectly with the atomistic/continuum descriptions in $\varOmega^{\mathrm{a}}$ and with the DDD description in $\varOmega^{\mathrm{c}}$, as shown quantitatively in Table 4.2 by the small error, which is on the order of the difference between fully atomistic and fully DDD problems. When the transmission node lies deeper into the atomistic domain (region 4), the results do not change notably. It can be concluded that it is necessary to choose the transmission node to lie a few atomic layers inside the atom/continuum interface to obtain accurate results.

More broadly, the result in Figure 4.13 (c) demonstrates the high fidelity of the proposed CADD-3d treatment of hybrid dislocations. A close inspection of the atomic displacements near the atom/continuum interface shows a very slight shift in the visualized

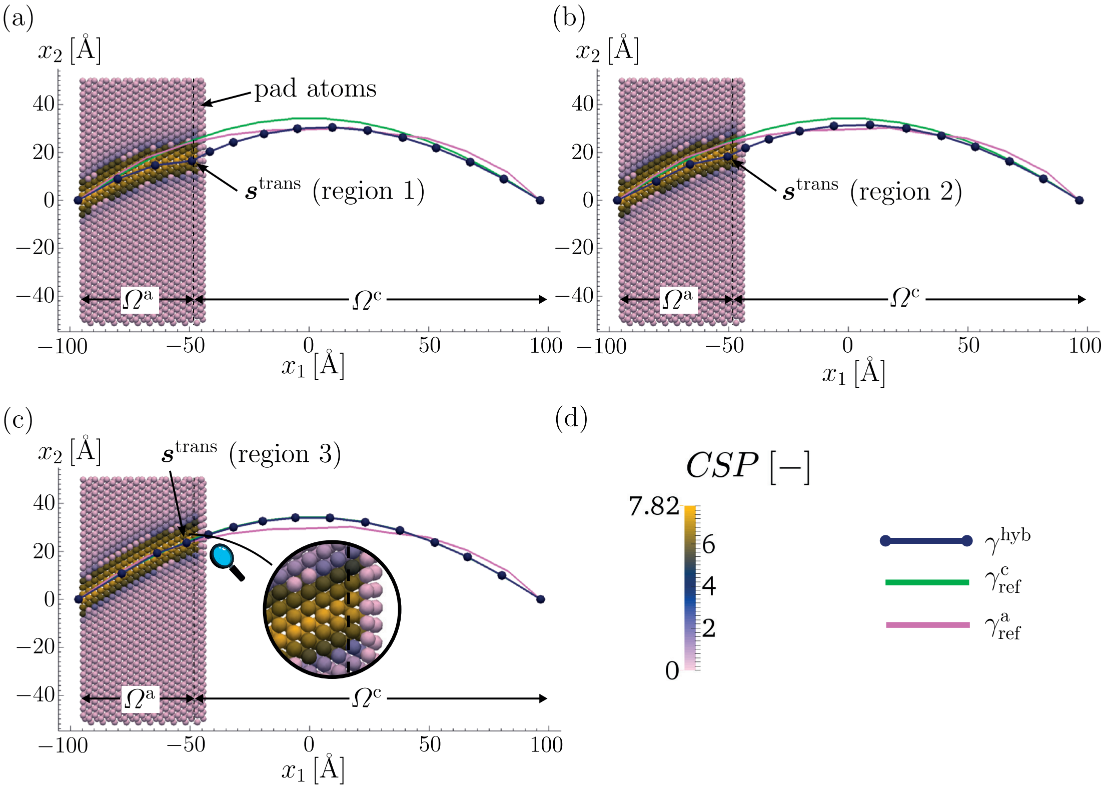

Figure 4.13: Solution of the coupled problem for $w_{\text{a}} = l_1/4$ for different choices of the transmission node s^{trans} (a)-(c). Real and pad atoms are highlighted with respect to the centrosymmetry parameter (CSP Kelchner et al., 1998) according to (d)

atomic core structure, but the overall level of agreement is excellent. The atomistic dislocation away from the interface is experiencing no spurious stresses that cause a measurable disturbance, so the atomistic system does not know that the dislocation is represented by DDD in another large portion of the domain. Such atomistic fidelity is precisely the goal of CADD-3d.

To further validate CADD-3d, the same problem is examined with an atomistic domain that is approximately the same size as the continuum domain. This captures the region of the bow-out where the atomistic and DDD reference problems show the largest differences in equilibrium positions. Seven segments are used to discretize the continuum dislocation line in Ω^{c} and the transmission node is chosen to be in region 3. Otherwise the problem remains the same as above. The final configuration at 150 MPa is shown in Figure 4.14. The hybrid dislocation line now resides between the solution for the individual problems, with an error (c.f. Table 4.2) of approximately half of the error of the full DDD reference problem in half of the total domain. Moreover, the analysis shows that, considering only the error in $\mathcal{A}(l_1/4)$, improved results are obtained in comparison with the coupled problem where the width of the atomistic domain was $l_1/4$.

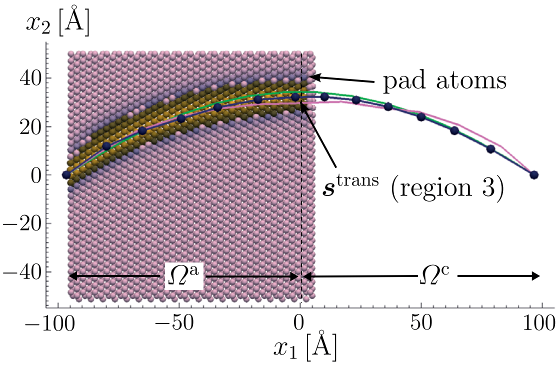

Figure 4.14: Solution of the coupled problem for $w_{\text{a}} = l_1/2$. Real and pad atoms are highlighted with respect to the centrosymmetry parameter (CSP Kelchner et al., 1998) according to Figure 4.13 (d)

To demonstrate the benefits of the atomistic core template approximation, simulations have been performed using solely the Volterra solution in the entire pad region. Results at 150 MPa are shown in Figure 4.15 for two different positions of the transmission node. For the transmission node in region 3, there is an artificial pinning of the dislocation leading to a kink that should not exist. The atoms in region 3 experience the constraint of the incorrect core template and cannot adjust suitably. Away from the kink, however, the solution is in reasonable agreement with the previous results. The use of the Volterra core retains knowledge of the Burgers vector and correct slip displacements, and so the differences between the Volterra core and the full dissociated core are limited to short-range fields, and thus cause short-range disturbances. However, those disturbances do extend into the atomistic region and thus generate unwanted spurious stress fields that may drive unphysical atomistic behavior even though the atomic displacement differences are localized.

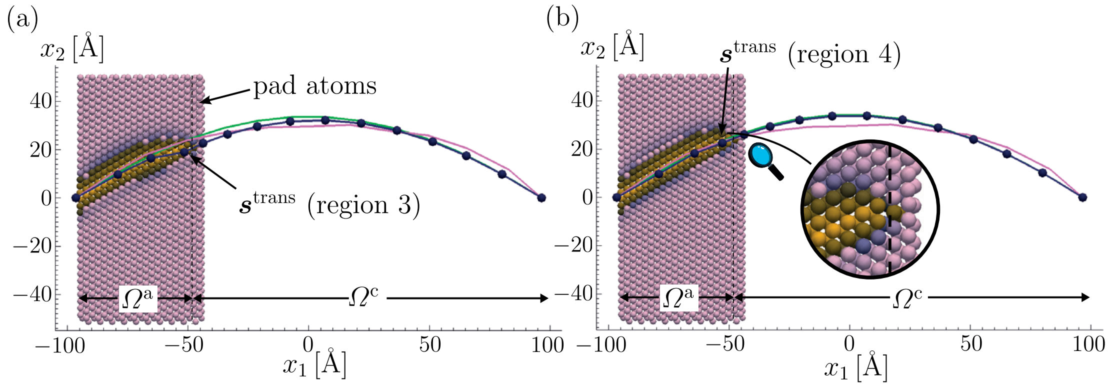

Figure 4.15: Solution of the coupled problem for $w_{\text{a}} = l_1/4$ using the classical Volterra solution in the core region. Real and pad atoms are highlighted with respect to the centrosymmetry parameter (CSP Kelchner et al., 1998) according to Figure 4.13 (d)

width w_{a} of Ω^{a}	region of $\boldsymbol{s}^{\mathrm{trans}}$	w	$e_{\mathrm{rel}}(w)$ [%]
$l_1/4$	1	$l_1/4$	26.9
$l_1/4$	2	$l_1/4$	21.4
$l_1/4$	3	$l_1/4$	5.2
$l_1/2$	3	$l_1/2$	5.8
$l_1/2$	3	$l_1/4$	4.1
full DDD	⁄	$l_1/4$	5.7
full DDD	⁄	$l_1/2$	9.9

Table 4.2: Error in the bow-out between the hybrid dislocation and the detected atomistic dislocation from the reference calculation. The third column specifies the width w of the domain over which the error is measured

In the present approximate model that uses DDD fields to inform the pad atoms, the atomic disturbances caused by the Volterra solution are not fed back into the pad - there is no full coupling - and hence the disturbances are likely *underestimated* when using the current approximate model. Interestingly, if the transmission node is moved slightly further from the interface (region 4), then the final hybrid dislocation line is largely unaffected by the use of the Volterra core. In region 4, the atoms are able to correct slightly better for the Volterra field error, and the segment connecting the transmission node to the first DDD node spans across the Volterra solution, smoothening out the DDD description. While the Volterra solution is attractive for simplicity, the core template approximation yields a smoother transition between the two descriptions of the dislocation and a far better description of the atomistic displacements inside the atomistic region near the atom/continuum interface. The smoother transition can be visualized by comparing the close-up views in Figure 4.15 (b) and Figure 4.13 (c); the dislocation core becomes significantly more compact from $\approx 3b$ to the interface.

A detailed comparison of computational efficiency of the coupled problem is not presented at this stage of the CADD-3d development. The test problems here are very small in size, especially the DDD regions, and so CADD-3d is not expected to be notably faster than a full atomistic solution. Nonetheless, the computational time for the results in Figure 4.14 ($w_{\mathrm{a}} = l_1/2$) were comparable to those for the fully atomistic problem and the computational time for the results in Figure 4.13 ($w_{\mathrm{a}} = l_1/4$) were ≈ 3.5 less than the fully atomistic problem, thus approaching perfect scaling with the atomistic size. Thus, even these preliminary tests indicate the high possible efficiency of CADD-3d for problems when the entire domain is much much larger than the atomistic domain alone.

5 Conclusions

Summary

In this work computational methods for coupled atomistic/continuum (A/C) problems, with emphasize on efficiency and practical application, have been developed. Thereby, the focus has been set on the systematic derivation of the underlying mathematical concepts and implementation aspects in order to provide a solid foundation for the construction of sophisticated numerical algorithms which can potentially lead to a complexity reduction by several orders of magnitude, compared to (computational prohibitive) fully atomistic models.

A thorough evaluation of flexible elasticity boundary conditions for atomistic problems has been presented in Chapter 2. The most widely used scheme for this class of problems is the method by Sinclair (1971). However, to date it has never been applied to problems beyond the scope of isolated defects due to practical limitations regarding efficiency and memory requirements for larger atomistic domains since the pad and the real atoms must be updated after every equilibration of the atomistic region. The operator split presented in Section 2.4 revealed that the second step is not necessary and rather serves as an initial guess to the anharmonic atomistic problem. Nevertheless, the problem still contains a tremendous amount of atoms near the boundary which is prohibitive for larger problems due to the quadratic complexity, except on supercomputers. Using the framework of $\mathscr{H}$-matrices a significant reduction in necessary memory capacity for the boundary matrices can be obtained as shown in Section 2.6.3 and 4.1.2. This representation admits a linear-logarithmic scaling for the memory requirements and the algebraic operations, thus opening the door for large-scale three-dimensional applications.

A second outcome of the analysis of Sinclair's method has led to the development of a discrete variant of the boundary element method (DBEM). This has enabled the construction a monolithic Newton-GMRes solver for the coupled problem presented in Section 2.7.2. Monolithic solvers are usually preferable over staggered schemes as they require fewer function evaluations and converge faster in general. It is verified with numerical examples that the monolithic solver requires fewer force evaluations than Sinclair's method, yet at the cost of a much more involved implementation. Especially for the two-dimensional problems Sinclair's method was found remarkably efficient, especially when compared to the classical alternating Schwarz method commonly used in the A/C coupling community which is found to be unsuitable for the considered class of problems.

The method has been analyzed for various types of test problems in Section 4.1.1 and 4.1.2. An overall excellent accuracy and improved scaling of the error was found in comparison with clamped boundary conditions — at substantially reduced computational cost. Further, the softer interface allows to study problems involving moving defects which usually require substantially bigger atomistic systems. In addition, the common approximation of the LGF, i.e. by replacing it with the CGF outside a cut-off radius, has been investigated. It was shown that choosing a cut-off radius of a few lattice spacings is usually enough not to effect the final result qualitatively which yields a reduction of the offline phase.

To further allow parts of the continuum domain to undergo dislocation-based plasticity the three-dimensional coupled atomistic/discrete dislocation (CADD-3d, Anciaux et al., 2018; Hodapp et al., 2018a; Cho et al., 2018) method has been selected. The key concepts of the method for the intimate coupling of a fully atomistic domain to a surrounding domain described by a discrete dislocation dynamics (DDD) domain in three dimensions have been thoroughly reviewed. In particular, the focus was set on the treatment of hybrid dislocations, with a careful description of the dislocation detection in the atomistic system, the core template correction for minimizing spurious forces on atoms near the interface and the formulation of the quasi-static boundary value problem. A semi-monolithic algorithm for evolving the entire system by iterating between the physical and the DDD problem has been presented. Thereby, the DBEM developed in Chapter 2 has been identified as highly suitable for solving the associated elasticity problem. In addition, an approximation of the fully coupled problem has been derived in Section 3.8.1 for infinite problems and when the atomistic region contains only dislocations. Using the updated Green function method presented in Section 3.8.2 the need to execute three dimensional finite-element (or related) solutions can then be eliminated through a fully-DDD representation of the dislocation network at any instant to compute the boundary conditions on the atomistic domain. Even with this approximation, the atomistic domain still evolves according to atomistic forces, and so the main new features of the A/C coupling are preserved here. The accuracy of this approximation has been quantitatively assessed in Section 4.2.

The validation of CADD-3d is finally presented in Section 4.3. Specifically, it has been shown that CADD-3d can handle hybrid dislocations that span the atomistic and continuum domains with high fidelity, approaching the exact fully atomistic solution. The quasi-static CADD-3d method has been tested by studying the problem of the bow-out of a dislocation that is pinned periodically along its length. By comparing CADD-3d predictions to a fully atomistic solution of the same problem, the accuracy of the method is demonstrated in all important aspects. It is further shown that two algorithmic details (the use of the core template correction to accurately represent the true atomistic core structure of the dislocation and the choice of the transmission node connecting the continuum and atomistic portions of a hybrid dislocation) are essential for achieving high accuracy.

The present methodology, including the elasticity approximation for obtaining atomistic boundary conditions, can be used to enrich the fidelity of existing DDD studies. That is, during the evolution of a full DDD simulation, a fully-atomistic domain can be inserted into any region of the DDD simulation in which one wishes to interrogate the atomistic details specifically. The DDD network is used to define the boundary conditions of the atomistic domain, and then the CADD-3d algorithm is used to evolve the coupled problem and resolve atomistic behavior in the selected region. The problem can revert to a full DDD simulation automatically because the current CADD-3d method can always restore the entire dislocation network. CADD-3d is therefore the computational nanoscope that enables on-the-fly atomistic study of any domain of interest as a DDD system evolves in time.

Outlook

The author thinks that the proposed methodology has promising potential in addressing and/or supporting novel materials science research. In particular, the proposed modified version of Sinclair's method (Section 2.7.1) and the updated Green function method for the approximate CADD-3d problem (Section 3.8) can in principle be directly applied to actual research problems. However, covering the entire scope of possible applications requires further generalizations and new developments with respect to high-performance implementations.

Regarding the implementation of the DBEM the following topics have to be addressed shortly:

Parallelization. The parallelization of the A/DBEM coupling is involved. Using a matrix factorization as proposed in Section 2.7.2 might not be suitable since triangular systems are not parallelizable due to the high communication overhead for $\mathscr{H}$-matrices (Kriemann, 2017). However, other approaches exist, e.g. by factorizing the *inverse* matrix directly (Kriemann and Le Borne, 2015). If the factors of the inverse are known the linear system reduces to two matrix-vector multiplications, essentially. Another possibility is to solve the coupled problem (2.107) with respect to all unknowns which only requires matrix-vector multiplications. Both approaches have to be tested thoroughly in prospective future work.

Bounded problems. The current implementation of the A/DBEM coupling is restricted to unbounded problems. Therefore it can only be applied in situations where one seeks for the quasi-static evolution of defects (or arrangements of defects) in an infinite medium. This is a drastic restriction as in many practical cases the problem might not admit a solution at all. It was found inevitable for testing purposes, however, if far-field conditions must be prescribed an additional outer boundary needs to be considered. An extension of the formulation to bounded domains for a Dirichlet problem has been discussed in Section 2.5.4. The therefrom derived variant of Sinclair's method for bounded problems will, moreover, possibly prove useful for future applications. However, additional reduction in the number of degrees of freedom might be necessary if the boundary is far from the artificial interface, possibly spanning to several hundred nanometers, thus potentially leading to variants of multigrid methods.

Dynamics. Another important application are dynamic problems at finite temperature. Approximating the dynamics of fully atomistic systems usually comes along with severe challenges. Statistical ensembles usually require the Hamiltonian of the system to be preserved. A known issue of force-based A/C coupling is the lack of a Hamiltonian for the coupled system which requires artificial damping to ensure stability (Shiari et al., 2005). Nevertheless, in (Dobson et al., 2010; Junge et al., 2015) it is shown that a dynamical system is stable, provided that one of the subproblems — in the present case the continuum problem — is static, that is, it responds instantaneously to atomic fluctuations. This is supported by the numerical experiments in Section 4.1 in the sense that damped dynamics is nothing but solving Newton's equation of motion — with artificial trajectories. Therefore the author sees no immediate obstacle in applying the A/DBEM coupling to this class of problems. Moreover, similar ideas as presented here may be used in combination with other energy-based coupling schemes.

Further, it is emphasized that, even though it has been proposed in the context of A/C coupling, the method is general in the sense that it can be applied to any kind of discrete problem which have an underlying repetitive lattice structure which allows for an efficient computation of the LGF. The method may thus also be applicable to other types of discrete problems, e.g. trusses, beams or foams (c.f. Beex et al., 2014).

In addition, for the implementation of CADD-3d there remain some current operational limits to the coupling of atomistics to discrete dislocation dynamics with full atomistic fidelity due to the existing open-source DDD methodologies:

DDD model. First, real crystalline materials are elastically anisotropic, and the computation of both stress fields and, moreover, displacement fields of dislocations in anisotropic materials remains challenging. Second, real atomistic dislocations have a character-dependent core energy that may be difficult to represent within continuum DDD models. Here, the edge dislocation bow-out was calibrated by adjusting the core energy model in ParaDis (Cai et al., 2006). Recent work (Szajewski et al., 2015) suggests this may be insufficient, and so new models may be needed.

Full problem. The numerical solution of the full coupled boundary value problem remains necessary to solve many problems of interest wherein (i) the atomistic domain contains other defects (cracks, voids, inclusions, etc.), (ii) the boundary conditions are essential to the solution of the problem or (iii) stresses on dislocations in the vicinity of the interface introduce non-negligible spurious forces such that the passing distance becomes impracticably large with the approximate method. Ongoing research is devoted to the integration of the DBEM library into libMultiscale and results will soon be reported (Hodapp et al., 2018b).

Dislocation passing. The passing of dislocations in and out of the atomistic domain, i.e. the *creation* of hybrid dislocations, has not been discussed. In Section 3.6 dislocation passing has been identified as a mere algorithmic problem. Therefore it could be neglected for the validation of the artificial boundary condition. A method that is suitable for the approximate CADD-3d problem has been introduced in (Cho et al., 2018). This limit is quite useful in many cases but more general passing algorithms need to be discussed in future work.

With the development of the general theoretical and algorithmic framework in Chapter 2 and 3 the author is confident that the preceding tasks can be successfully addressed within a short period of time, thus opening the possibility for studying forthcoming problems in materials physics.

A Appendix

A.1 Green functions in anisotropic media

In the following linear elasticity is presumed. A Green function (fundamental solution) for the balance of linear momentum is a displacement $\boldsymbol{u}^k : \mathbb{R}^d \setminus \boldsymbol{0} \to \mathbb{R}^d$, which solves

$$\forall\, k = 1, ..., d \qquad \nabla \cdot \boldsymbol{\sigma}^k = \boldsymbol{f}^k \qquad \text{in } \mathbb{R}^d, \qquad \text{with} \quad f_i^k = \begin{cases} \delta(\boldsymbol{x}) & \text{if } i = k, \\ \boldsymbol{0} & \text{else.} \end{cases} \tag{A.1}$$

In index notation this is written as

$$\sigma_{ij,j}^k = \left(C_{ijlm} u_{l,m}^k\right)_{,j} = C_{ijlm} u_{l,mj}^k. \tag{A.2}$$

Equivalently, one may write (A.1) as

$$\mathcal{L}[\boldsymbol{G}^{\text{cgf}}] = \delta \boldsymbol{I} \qquad \text{in } \mathbb{R}^d, \qquad \text{with } (\mathcal{L}[\bullet])_{lk} = C_{ijlm} \bullet_{lk,mj}, \tag{A.3}$$

where $\boldsymbol{G}^{\text{cgf}}$ is refereed to as the *continuum Green tensor* ($G_{ik}^{\text{cgf}} = u_i^k$).

Problem (A.3) is useful as it can be used to compute the solution for arbitrary right hand sides, provided that the Green tensor is available. For an arbitrary body force $\boldsymbol{f}^{\text{body}}$ the balance of linear momentum is given by

$$\nabla \cdot \boldsymbol{\sigma} = \boldsymbol{f}^{\text{body}} \qquad \text{in } \mathbb{R}^d. \tag{A.4}$$

Assume that $\boldsymbol{G}^{\text{cgf}}$ is known. The body force is then convolved with (A.3) such that

$$\mathcal{L}[\boldsymbol{G}^{\text{cgf}}] * \boldsymbol{f}^{\text{body}} = \int_{\mathbb{R}^d} \mathcal{L}[\boldsymbol{G}^{\text{cgf}}](\boldsymbol{x} - \boldsymbol{x}') \boldsymbol{f}^{\text{body}}(\boldsymbol{x}') \, \mathrm{d}V' = \delta \boldsymbol{I} * \boldsymbol{f}^{\text{body}} = \boldsymbol{f}^{\text{body}}. \tag{A.5}$$

The differential operator $\mathcal{L}$ only acts on $\boldsymbol{x}$ and can therefore be pulled out of the integrand such that

$$\nabla_x \cdot \left(\mathbb{C}\left[\nabla_x\left(\int_{\mathbb{R}^d} \boldsymbol{G}^{\mathrm{cgf}}(\boldsymbol{x}-\boldsymbol{x}')\boldsymbol{f}^{\mathrm{body}}(\boldsymbol{x}')\,\mathrm{d}V'\right)\right]\right) = \boldsymbol{f}^{\mathrm{body}} = \nabla_x \cdot \mathbb{C}[\nabla_x \boldsymbol{u}]. \tag{A.6}$$

By comparing the terms in the square brackets the solution follows as

$$\boldsymbol{u}(\boldsymbol{x}) = \int_{\mathbb{R}^d} \boldsymbol{G}^{\mathrm{cgf}}(\boldsymbol{x}-\boldsymbol{x}')\boldsymbol{f}^{\mathrm{body}}(\boldsymbol{x}')\,\mathrm{d}V'. \tag{A.7}$$

A.1.1 General solution

A standard procedure to obtain the components of the continuum Green tensor is to solve (A.3) in Fourier space. The final solution from (Lifshits and Rozentsveig, 1947; Mura, 1982) is restated here

$$G_{ij}^{\mathrm{cgf}}(\boldsymbol{x}) = (2\pi)^{-3}\int_{\mathbb{R}^d} \frac{\tilde{g}_{ij}}{k^2}\boldsymbol{e}^{\mathrm{i}(\boldsymbol{k}^{\mathsf{T}}\cdot\boldsymbol{x})}\,\mathrm{d}V(\boldsymbol{k}), \tag{A.8}$$

with

$$k = \sqrt{\sum_{i=1}^{d} k_i^2}, \qquad \tilde{g}_{ij} = (C_{ijkl}k_jk_l)^{-1}. \tag{A.9}$$

In general the integral in (A.8) cannot be solved analytically, except if special symmetry conditions hold (see below). To compute $\boldsymbol{G}^{\mathrm{cgf}}$ in practice, the integral (A.8) is further simplified using polar (2d) or spherical (3d) coordinates and then solved numerically using standard techniques (Mura, 1982).

A.1.2 Isotropic solution

For the special case of isotropic elasticity a closed-form analytical solution exists. The components of $\boldsymbol{G}^{\mathrm{cgf}}$ for $d=2$ and $d=3$ are given as follows (e.g. Mura, 1982)

$$\textbf{(2d)} \qquad G_{ij}^{\mathrm{cgf}}(\boldsymbol{x}) = \frac{1}{8\pi\mu(1-\nu)}\left(\frac{x_ix_j}{r^2} - (3-4\nu)\ln(r)\delta_{ij}\right), \tag{A.10}$$

$$\textbf{(3d)} \qquad G_{ij}^{\mathrm{cgf}}(\boldsymbol{x}) = \frac{1}{16\pi\mu(1-\nu)}\left(\frac{x_ix_j}{r^3} + \frac{(3-4\nu)\delta_{ij}}{r}\right), \tag{A.11}$$

where $r = \sqrt{\sum_{i=1}^{d} x_i^2}$.

A.1.3 Principle of superposition

Let $\boldsymbol{f}^{\text{body}} = \boldsymbol{f}_1^{\text{body}} + \boldsymbol{f}_2^{\text{body}}$. By linearity, a solution to (A.4) can be obtained by solving the individual subproblems with respect to $\boldsymbol{u}_1$ and $\boldsymbol{u}_2$

$$\nabla \cdot \boldsymbol{\sigma}_1 = \boldsymbol{f}_1^{\text{body}} \qquad \text{in } \mathbb{R}^d, \qquad\qquad \nabla \cdot \boldsymbol{\sigma}_2 = \boldsymbol{f}_2^{\text{body}} \qquad \text{in } \mathbb{R}^d. \tag{A.12}$$

If a finite body $\Omega \subset \mathbb{R}^d$, subjected to the same body force, is considered, external boundary conditions can be taken into account by solving the following corrective problem which does not contain the source term

$$\begin{cases} \nabla \cdot \hat{\boldsymbol{\sigma}} = \boldsymbol{0} & \text{in } \Omega, \\ \hat{\boldsymbol{u}} = \bar{\boldsymbol{u}} - \boldsymbol{u}_1 - \boldsymbol{u}_2 & \text{on } \partial_{\mathrm{u}}\Omega, \\ \hat{\boldsymbol{t}} = \bar{\boldsymbol{t}} - \boldsymbol{t}_1 - \boldsymbol{t}_2 & \text{on } \partial_{\mathrm{t}}\Omega. \end{cases} \tag{A.13}$$

The total solution $\boldsymbol{u}$ can then be obtained by superimposing the individual solutions

$$\boldsymbol{u} = \boldsymbol{u}_1 + \boldsymbol{u}_2 + \hat{\boldsymbol{u}}, \qquad\qquad \boldsymbol{\sigma} = \boldsymbol{\sigma}_1 + \boldsymbol{\sigma}_2 + \hat{\boldsymbol{\sigma}}. \tag{A.14}$$

The superposition principle will be heavily used in the following sections in the context of dislocations.

A.2 Green functions for straight dislocations

A discrete dislocation is defined via a plastic strain

$$\boldsymbol{\varepsilon}^{\mathrm{p}}(\boldsymbol{x}) = \begin{cases} \dfrac{\boldsymbol{b} \otimes \boldsymbol{n} + \boldsymbol{n} \otimes \boldsymbol{b}}{2} & \text{on } \mathscr{S}, \\ \boldsymbol{0} & \text{else} \end{cases} \tag{A.15}$$

which is confined on the slip plane $\mathscr{S}$. In the elastic regime the strains are additive such that $\boldsymbol{\varepsilon} = \boldsymbol{\varepsilon}^{\mathrm{e}} + \boldsymbol{\varepsilon}^{\mathrm{p}}$. The Cauchy stress thus becomes

$$\boldsymbol{\sigma} = \mathbb{C}[\boldsymbol{\varepsilon} - \boldsymbol{\varepsilon}^{\mathrm{p}}]. \tag{A.16}$$

By linearity of the divergence operator one has

$$\begin{aligned} \nabla \cdot \boldsymbol{\sigma} &= \nabla \cdot \mathbb{C}[\boldsymbol{\varepsilon} - \boldsymbol{\varepsilon}^{\mathrm{p}}] \\ &= \nabla \cdot \mathbb{C}[\boldsymbol{\varepsilon}] - \nabla \cdot \mathbb{C}[\boldsymbol{\varepsilon}^{\mathrm{p}}]. \end{aligned} \tag{A.17}$$

Since the plastic strain is defined a priori according to (A.15) a general solution for a discrete dislocation is a displacement $\boldsymbol{u} : \mathbb{R}^3 \setminus \mathscr{S} \to \mathbb{R}^3$ which solves

$$\nabla \cdot \mathbb{C}[\boldsymbol{\varepsilon}] = \nabla \cdot \mathbb{C}[\boldsymbol{\varepsilon}^{\mathrm{p}}] \qquad \text{in } \mathbb{R}^3, \tag{A.18}$$

where $\boldsymbol{\varepsilon} = \nabla^{\mathrm{sym}}\boldsymbol{u}$.

If the Green tensor $\boldsymbol{G}^{\mathrm{cgf}}$ is known analytically (which is the case for isotropic problems) a solution to (A.18) can directly be given by convolving (A.3) with $\nabla \cdot \mathbb{C}[\boldsymbol{\varepsilon}^{\mathrm{p}}]$ such that

$$\tilde{\boldsymbol{u}}(\boldsymbol{x}) = \int_{\mathbb{R}^3} \boldsymbol{G}^{\mathrm{cgf}}(\boldsymbol{x} - \boldsymbol{x}')\big(\nabla_{x'} \cdot \mathbb{C}[\boldsymbol{\varepsilon}^{\mathrm{p}}(\boldsymbol{x}')]\big)\,\mathrm{d}V'. \tag{A.19}$$

Using the product rule and Gauss' theorem one can write

$$\tilde{\boldsymbol{u}}(\boldsymbol{x}) = -\int_{\mathbb{R}^3} \nabla_{x'}\big(\boldsymbol{G}^{\mathrm{cgf}}(\boldsymbol{x} - \boldsymbol{x}')\big)\mathbb{C}[\boldsymbol{\varepsilon}^{\mathrm{p}}(\boldsymbol{x}')]\,\mathrm{d}\mathscr{S}'. \tag{A.20}$$

That is, in order to compute a solution $\tilde{\boldsymbol{u}}$ one has to evaluate the partial derivatives of $\boldsymbol{G}^{\mathrm{cgf}}$ followed by an integration over the slip plane (as $\boldsymbol{\varepsilon}^{\mathrm{p}}$ is zero elsewhere).

The solutions for straight dislocations in elastic continua are presented in the following.

A.2.1 Isotropic solution for screw dislocations

In the following it is assumed that the slip plane is given by $\mathscr{S} := \{\, \boldsymbol{x} \in \mathbb{R}^3 \,|\, x_1 < 0, x_2 = 0 \,\}$. Hence, the dislocation line is $\gamma := \{\, \boldsymbol{x} \in \mathbb{R}^3 \,|\, x_1 = x_2 = 0 \,\}$. For a screw dislocation the Burgers vector is given by $\boldsymbol{b} = \begin{pmatrix} 0 & 0 & b \end{pmatrix}^{\mathsf{T}}$. The plastic strain tensor then reads

$$\boldsymbol{\varepsilon}^{\mathrm{p}} = \frac{b\delta(x_2)H(-x_1)}{2} \begin{pmatrix} 0 & 0 & 0 \\ 0 & 0 & 1 \\ 0 & 1 & 0 \end{pmatrix}. \tag{A.21}$$

Using (A.21) in (A.20) one obtains (c.f. Hirth and Lothe, 1982; Mura, 1982)

$$\begin{aligned} \tilde{u}_1^{\mathrm{screw}}(\boldsymbol{x}) = \tilde{u}_2^{\mathrm{screw}}(\boldsymbol{x}) &= 0, \\ \tilde{u}_3^{\mathrm{screw}}(\boldsymbol{x}) &= \frac{b}{2\pi} \arctan\left(\frac{x_2}{x_1}\right). \end{aligned} \tag{A.22}$$

A.2.2 Isotropic solution for edge dislocations

The definition of $\mathscr{S}$ and γ is adopted from the previous section. For an edge dislocation the Burgers vector is given by $\boldsymbol{b} = \begin{pmatrix} b & 0 & 0 \end{pmatrix}^{\mathsf{T}}$. The plastic strain tensor then reads

$$\boldsymbol{\varepsilon}^{\mathrm{p}} = \frac{b\delta(x_2)H(-x_1)}{2} \begin{pmatrix} 0 & 1 & 0 \\ 1 & 0 & 0 \\ 0 & 0 & 0 \end{pmatrix}. \tag{A.23}$$

Using (A.23) in (A.20) one obtains (c.f. Nabarro, 1967)

$$\begin{aligned}
\tilde{u}_1^{\mathrm{edge}}(\boldsymbol{x}) &= \frac{b}{4\pi(1-\nu)} \frac{x_1 x_2}{x_1^2 + x_2^2} + \frac{b}{2\pi} \arctan \frac{x_2}{x_1}, \\
\tilde{u}_2^{\mathrm{edge}}(\boldsymbol{x}) &= \frac{b}{4\pi(1-\nu)} \frac{x_2^2}{x_1^2 + x_2^2} - \frac{(1-2\nu)b}{8\pi(1-\nu)} \ln\left(x_1^2 + x_2^2\right), \\
\tilde{u}_3^{\mathrm{edge}}(\boldsymbol{x}) &= 0.
\end{aligned} \tag{A.24}$$

This solution is referred to as the Nabarro solution. Another solution which can often be found in literature is the solution by Hirth and Lothe (1982) given by

$$\begin{aligned}
\tilde{u}_1^{\mathrm{edge2}}(\boldsymbol{x}) &= \tilde{u}_1^{\mathrm{edge}}(\boldsymbol{x}), \\
\tilde{u}_2^{\mathrm{edge2}}(\boldsymbol{x}) &= -\frac{b}{8\pi(1-\nu)} \frac{x_1^2 - x_2^2}{x_1^2 + x_2^2} - \frac{(1-2\nu)b}{8\pi(1-\nu)} \ln(x_1^2 + x_2^2), \\
\tilde{u}_3^{\mathrm{edge2}}(\boldsymbol{x}) &= 0
\end{aligned} \tag{A.25}$$

which can be obtained by applying certain boundary conditions before evaluating the integral in (A.20).

A.2.3 Isotropic solution for mixed dislocations

If the character angle of the dislocation is $0^\circ < \vartheta < 90^\circ$, the Burgers vector of the dislocation has a screw and an edge component, i.e. $\boldsymbol{b} = b \begin{pmatrix} \sin(\vartheta) & 0 & \cos(\vartheta) \end{pmatrix}^{\mathsf{T}}$. Thanks to principle of superposition, the plastic strains due to the screw and the edge components can be separated and the solution of a mixed dislocation can directly be given as

$$\tilde{u}^{\mathrm{mixed}}(\boldsymbol{x}; \vartheta) = \cos(\vartheta) \tilde{u}^{\mathrm{screw}}(\boldsymbol{x}) + \sin(\vartheta) \tilde{u}^{\mathrm{edge}}(\boldsymbol{x}). \tag{A.26}$$

A.2.4 General solution

In the general anisotropic case a closed form expression of (A.20) does not exist. However, for straight dislocations an analytic formula can be obtained by exploiting certain symmetry conditions. Then general solution reads (Eshelby et al., 1953)

$$\tilde{u}_i^{\mathrm{aiso}}(\boldsymbol{x}; \boldsymbol{b}) = \mathrm{Re} \left\{ \sum_{j=1}^{3} A_{ij} \ln\left(\eta_j(\boldsymbol{x})\right) \right\}, \qquad \text{with} \quad \eta_j(\boldsymbol{x}) = x_1 + p_j x_2, \tag{A.27}$$

where the coefficients $A_{ij}, p_j \in \mathbb{C}$ have to be determined numerically. Equation (A.27) can be re-written as

$$\tilde{u}_i^{\mathrm{aiso}}(\boldsymbol{x}; \boldsymbol{b}) = \frac{1}{2} \sum_{j=1}^{3} C_{ij} \ln\left((x_1 + r_j x_2)^2 + (q_j x_2)^2\right) - D_{ij} \arctan\left(\frac{q_j x_2}{x_1 + r_j x_2}\right), \tag{A.28}$$

with

$$C_{ij} = \mathrm{Re}\{A_{ij}\}, \qquad D_{ij} = \mathrm{Im}\{A_{ij}\}, \qquad r_j = \mathrm{Re}\{p_j\}, \qquad q_j = \mathrm{Im}\{p_j\}. \tag{A.29}$$

A.2.5 Periodic arrays of straight dislocations

In what follows a closed-form analytical expression for the displacement field of an infinite array of isotropic edge dislocations is sought-after. The approach carries over almost verbatim to the general anisotropic case which is omitted for compactness. Under certain assumptions infinite sums can be conveniently evaluated via the Residue theorem from complex analysis:

Theorem A.2.1 (Residue theorem). *Let $\mathcal{A}$ be an open set containing $\{w_1, ..., w_p\}$ and let further g be holomorphic in $\mathcal{A} \setminus \{w_1, ..., w_p\}$. Then*

$$\frac{1}{2\pi \mathrm{i}} \int_{\partial \mathcal{A}} g(x)\,\mathrm{d}x = \sum_{k=1}^{p} \mathrm{res}(g(x), w_k), \tag{A.30}$$

where for an n-th order pole

$$\mathrm{res}(g(x), w_k) = \frac{1}{(n-1)!} \lim_{x \to w_k} \frac{\partial^{n-1}}{\partial x^{n-1}} \Big((x - w_k)^n g(x) \Big). \tag{A.31}$$

In order to evaluate infinite sums the function $g(x)$ is multiplied with a function $h(x) = \pi \cot \pi x$. Using the fact that $h(x)$ has simple poles $\forall\, x \in \mathcal{A} = \mathbb{N}$ yields

$$\frac{1}{2\pi \mathrm{i}} \int_{\partial \mathcal{A}} g(x) h(x)\,\mathrm{d}x = \sum_{k=1}^{p} \mathrm{res}(g(x)h(x), w_k) + \sum_{k=-\infty}^{\infty} g(k). \tag{A.32}$$

It is assumed that the function $g(x)$ goes to zero as $x \to \infty$. Therefore the left hand side of (A.32) is essentially zero. Thus,

$$\sum_{k=-\infty}^{\infty} g(k) = -\sum_{k=1}^{p} \mathrm{res}(g(x)h(x), w_k). \tag{A.33}$$

In order to evaluate infinite sums it therefore suffices to determine the poles of $g(x)$ and compute the residues of $g(x)h(x)$.

Consider a periodic array of infinite straight edge dislocations with $\boldsymbol{e}_2, \boldsymbol{e}_3$ being the glide direction and slip plane normal, respectively. The separation between the dislocations is $\mathit{\Delta} x_2 = l_2$. The position of the dislocations is thus

$$\forall\, i \in \mathbb{N} \qquad \boldsymbol{x}_i = \begin{pmatrix} 0 \\ i \mathit{\Delta} x_2 \\ 0 \end{pmatrix} = \begin{pmatrix} 0 \\ \mathit{\Delta} x_2^i \\ 0 \end{pmatrix}. \tag{A.34}$$

The isotropic displacement field induced by each dislocation is then given by

$$\begin{aligned}
\tilde{u}_1^i(\boldsymbol{x}) &= 0,\\
\tilde{u}_2^i(\boldsymbol{x}) &= \frac{b}{2\pi}\left(\frac{(x_2-\varDelta x_2^i)x_3}{2(1-\nu)((x_2-\varDelta x_2^i)^2+x_3^2)}+\arctan\left(\frac{x_2-\varDelta x_2^i}{x_3}\right)\right),\\
\tilde{u}_3^i(\boldsymbol{x}) &= -\frac{b}{2\pi}\left(\frac{(x_2-\varDelta x_2^i)^2-x_3^2}{4(1-\nu)((x_2-\varDelta x_2^i)^2+x_3^2)}+\frac{1-2\nu}{4(1-\nu)}\ln\left((x_2-\varDelta x_2^i)^2+x_3^2\right)\right).
\end{aligned} \tag{A.35}$$

Henceforth the following compact notation is used

$$\begin{aligned}
\tilde{u}_2^i(\boldsymbol{x}) &= a_1 f_{11}^i(\boldsymbol{x}) + b_1 f_{12}^i(\boldsymbol{x}),\\
\tilde{u}_3^i(\boldsymbol{x}) &= a_2 f_{21}^i(\boldsymbol{x}) + b_2 f_{22}^i(\boldsymbol{x}),
\end{aligned} \tag{A.36}$$

where

$$a_1 = \frac{b}{4\pi(1-\nu)}, \qquad a_2 = -\frac{1}{2}a_1 \qquad b_1 = \frac{b}{2\pi}, \qquad b_2 = (1-2\nu)a_2 \tag{A.37}$$

and

$$\begin{aligned}
f_{11}^i(\boldsymbol{x}) &= \frac{(x_2-\varDelta x_2^i)x_3}{(x_2-\varDelta x_2^i)^2+x_3^2}, & f_{12}^i(\boldsymbol{x}) &= \arctan\left(\frac{x_2-\varDelta x_2^i}{x_3}\right),\\
f_{21}^i(\boldsymbol{x}) &= \frac{(x_2-\varDelta x_2^i)^2-x_3^2}{(x_2-\varDelta x_2^i)^2+x_3^2}, & f_{22}^i(\boldsymbol{x}) &= \ln\left((x_2-\varDelta x_2^i)^2+x_3^2\right).
\end{aligned} \tag{A.38}$$

The total displacement field follows by summing the contributions from the individual dislocations, that is

$$\begin{aligned}
\tilde{u}_2^{\mathrm{PAD}}(\boldsymbol{x}) &= a_1 \sum_{i=-\infty}^{+\infty} f_{11}^i(\boldsymbol{x}) + b_1 \sum_{i=-\infty}^{+\infty} f_{12}^i(\boldsymbol{x}),\\
\tilde{u}_3^{\mathrm{PAD}}(\boldsymbol{x}) &= a_2 \sum_{i=-\infty}^{+\infty} f_{21}^i(\boldsymbol{x}) + b_2 \sum_{i=-\infty}^{+\infty} f_{22}^i(\boldsymbol{x}).
\end{aligned} \tag{A.39}$$

It is easy to see that the displacement $\tilde{u}_3^{\mathrm{PAD}}$ diverges with respect to the second term f_{22}^i as $\varDelta x_2^i \to \infty$. The divergent term is effectively associated with a rigid body shift — since the Green function lacks the definition of boundary conditions.

Hence, the sums of the partial derivatives of $f_{22}^i(\boldsymbol{x})$, given by

$$\frac{\partial f_{22}^i(\boldsymbol{x})}{\partial x_2} = \frac{2(x_2+\varDelta x_2^i)}{(x_2+\varDelta x_2^i)+x_3^2}, \qquad \frac{\partial f_{22}^i(\boldsymbol{x})}{\partial x_3} = \frac{2x_3}{(x_2+\varDelta x_2^i)+x_3^2}, \tag{A.40}$$

converge as sums $\sum_{i=-\infty}^{\infty} 1/r$ **converge** (whereas $\sum_{i=0}^{\infty} 1/r$ **does not**). In the following the derivation of the closed-form solution for the infinite sum $\sum_{i=-\infty}^{+\infty} \partial_{x_2} f_{22}^i(\boldsymbol{x})$ is exemplified.

First note that the function $\partial_{x_2} f^i_{22}(\boldsymbol{x})$ has two poles

$$w_1 = \frac{-x_2 + \mathrm{i}x_3}{l_2}, \qquad w_2 = \frac{-x_2 - \mathrm{i}x_3}{l_2}. \tag{A.41}$$

Applying the residue theorem leads to

$$\begin{aligned}\sum_{i=-\infty}^{+\infty} \frac{\partial f^i_{22}(\boldsymbol{x})}{\partial x_2} &= -\sum_{k=1}^{2} \operatorname{res}(\partial_{x_2} f^i_{22}(\boldsymbol{x}) h(k), w_k) \\ &= C \ \operatorname{Re}\left\{\cot\left[C(x_2 - \mathrm{i}x_3)\right] + \cot\left[C(x_2 - \mathrm{i}x_3)\right]\right\} \\ &= -\frac{2C\sin(2Cx_2)}{(\cos(2Cx_2) - \cosh(2Cx_3))},\end{aligned} \tag{A.42}$$

with $C = \pi/l_2$. The infinite sum may then be written as

$$\sum_{i=-\infty}^{+\infty} f^i_{22}(\boldsymbol{x}) \equiv \int \left(\sum_{i=-\infty}^{+\infty} \frac{\partial f^i_{22}(\boldsymbol{x})}{\partial x_2} \right) \mathrm{d}x_2 + I(x_3) < \infty. \tag{A.43}$$

But $I(x_3) = 0$ since

$$\int \frac{\partial f^i_{22}(\boldsymbol{x})}{\partial x_2} \,\mathrm{d}x_2 = \int \frac{\partial f^i_{22}(\boldsymbol{x})}{\partial x_3} \,\mathrm{d}x_3. \tag{A.44}$$

Therefore it follows

$$\begin{aligned}\sum_{i=-\infty}^{+\infty} f^i_{22}(\boldsymbol{x}) &\equiv \int \left(-\frac{2C\sin(2Cx_2)}{(\cos(2Cx_2) - \cosh(2Cx_3))} \right) \mathrm{d}x_2 \\ &= \ln(|\cos(2Cx_2) - \cosh(2Cx_3)|).\end{aligned} \tag{A.45}$$

To compute the remaining infinite sums one can proceed in a similar way. Note that the residue theorem can be applied directly to $\sum_{i=-\infty}^{+\infty} f^i_{11}(\boldsymbol{x})$ since the series is convergent and consists of rational terms.

On the other hand, the sum $\sum_{i=-\infty}^{+\infty} f^i_{12}(\boldsymbol{x})$ which accounts for the plastic slip is obviously divergent. Again, its partial derivatives can be used in order to omit the rigid body shift as for the logarithmic term. In summary,

$$\sum_{i=-\infty}^{+\infty} f^i_{11}(\boldsymbol{x}) \equiv -\frac{Cx_3\sin(2Cx_2)}{(\cos(2Cx_2) - \cosh(2Cx_3))}, \tag{A.46}$$

$$\sum_{i=-\infty}^{+\infty} f^i_{12}(\boldsymbol{x}) \equiv -\arctan(\coth(Cx_3)\tan(Cx_2)), \tag{A.47}$$

$$\sum_{i=-\infty}^{+\infty} f^i_{21}(\boldsymbol{x}) \equiv \frac{2Cx_3\sinh(2Cx_3)}{(\cos(2Cx_2) - \cosh(2Cx_3))}. \tag{A.48}$$

The closed-form expression of (A.39) therefore reads

$$
\begin{aligned}
\tilde{u}_2^{\mathrm{PAD}}(\boldsymbol{x}) &= -a_1 \frac{C x_3 \sin(2 C x_2)}{(\cos(2 C x_2) - \cosh(2 C x_3))} - b_1 \arctan(\coth(C x_3) \tan(C x_2)), \\
\tilde{u}_3^{\mathrm{PAD}}(\boldsymbol{x}) &= a_2 \frac{2 C x_3 \sinh(2 C x_3)}{(\cos(2 C x_2) - \cosh(2 C x_3))} + b_2 \ln(|\cos(2 C x_2) - \cosh(2 C x_3)|).
\end{aligned}
\tag{A.49}
$$

A.3 Green functions for curved dislocations

A.3.1 Triangular dislocation loops

A general expression of the displacement field as a line integral over some arbitrarily-shaped dislocation loop γ for anisotropic media has been derived in (Indenbom and Lothe, 1992). Here, only the isotropic solution is presented which is used in Section 4.3.5. The displacement field (A.20) can then be written as

$$
\begin{aligned}
\tilde{\boldsymbol{u}}(\boldsymbol{x}) = &-\mu \int_{\mathscr{S}} \nabla \boldsymbol{G}^{\mathrm{cgf}}(\boldsymbol{x}-\boldsymbol{x}')(\boldsymbol{b} \otimes \boldsymbol{n})\,\mathrm{d}A' - \mu \int_{\mathscr{S}} \nabla \boldsymbol{G}^{\mathrm{cgf}}(\boldsymbol{x}-\boldsymbol{x}')(\boldsymbol{n} \otimes \boldsymbol{b})\,\mathrm{d}A' \\
&- \lambda \int_{\mathscr{S}} (\boldsymbol{b}^{\mathsf{T}} \cdot \boldsymbol{n}) \nabla \cdot \boldsymbol{G}^{\mathrm{cgf}}(\boldsymbol{x}-\boldsymbol{x}')\,\mathrm{d}A',
\end{aligned}
\tag{A.50}
$$

with the Lamé constant λ. Using (A.11) in (A.50) and rearranging the terms, the displacement field can then be transformed into the following line integral representation by virtue of Stokes' theorem (e.g. Balluffi, 2012)

$$
\tilde{\boldsymbol{u}}(\boldsymbol{x}) = \frac{\Omega_{\mathrm{s}}(\boldsymbol{x})}{4\pi} \boldsymbol{b} + \boldsymbol{f}(\boldsymbol{x}) + \boldsymbol{g}(\boldsymbol{x}), \tag{A.51}
$$

with

$$
\boldsymbol{f}(\boldsymbol{x}) = -\frac{1}{4\pi} \int_{\gamma} \frac{\boldsymbol{b} \times \boldsymbol{t}(\boldsymbol{x})}{\|\boldsymbol{x}-\boldsymbol{x}'\|}\,\mathrm{d}C', \tag{A.52}
$$

$$
\boldsymbol{g}(\boldsymbol{x}) = -\frac{1}{8\pi(1-\nu)} \nabla \left(\int_{\gamma} \frac{\big(\boldsymbol{b} \times (\boldsymbol{x}-\boldsymbol{x}')\big)^{\mathsf{T}} \cdot \boldsymbol{t}(\boldsymbol{x})}{\|\boldsymbol{x}-\boldsymbol{x}'\|}\,\mathrm{d}C' \right) \tag{A.53}
$$

and the solid angle $\Omega_{\mathrm{s}}(\boldsymbol{x})$ (see Balluffi, 2012, Chapter 12, for details).

Barnett (1985) and Barnett and Balluffi (2007) introduced a particular convenient formalism to obtain a closed-form expression of (A.51) by considering piecewise linear dislocations composed of triangular loops. Consider a triangular $\gamma^{\triangle}$loop with nodes A, B and C. The vector-valued vector functions $\boldsymbol{f}(\boldsymbol{x})$ and $\boldsymbol{g}(\boldsymbol{x})$ for the segment A $\rightarrow$ B are

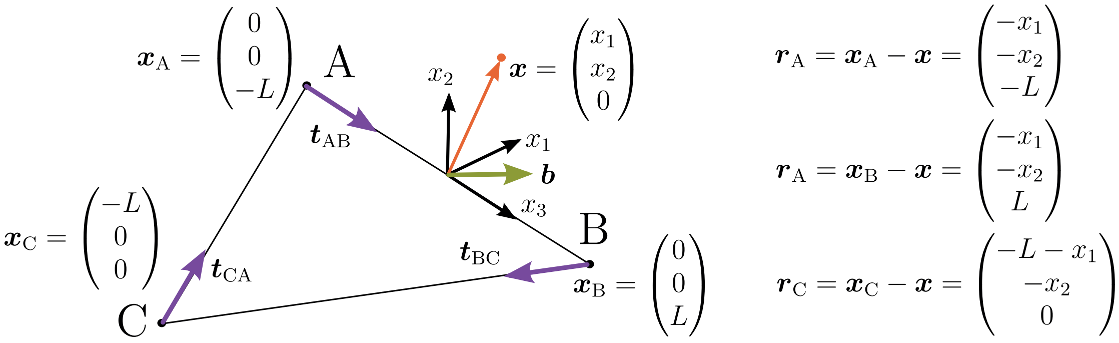
$\boldsymbol{x}_\mathrm{A} = \begin{pmatrix} 0 \\ 0 \\ -L \end{pmatrix}$
A
x_2
$\boldsymbol{x} = \begin{pmatrix} x_1 \\ x_2 \\ 0 \end{pmatrix}$
$\boldsymbol{r}_\mathrm{A} = \boldsymbol{x}_\mathrm{A} - \boldsymbol{x} = \begin{pmatrix} -x_1 \\ -x_2 \\ -L \end{pmatrix}$
$\boldsymbol{t}_\mathrm{AB}$
x_1
$\boldsymbol{b}$
$\boldsymbol{r}_\mathrm{A} = \boldsymbol{x}_\mathrm{B} - \boldsymbol{x} = \begin{pmatrix} -x_1 \\ -x_2 \\ L \end{pmatrix}$
x_3
$\boldsymbol{x}_\mathrm{C} = \begin{pmatrix} -L \\ 0 \\ 0 \end{pmatrix}$
B
$\boldsymbol{t}_\mathrm{BC}$
$\boldsymbol{t}_\mathrm{CA}$
$\boldsymbol{x}_\mathrm{B} = \begin{pmatrix} 0 \\ 0 \\ L \end{pmatrix}$
$\boldsymbol{r}_\mathrm{C} = \boldsymbol{x}_\mathrm{C} - \boldsymbol{x} = \begin{pmatrix} -L - x_1 \\ -x_2 \\ 0 \end{pmatrix}$
C

Figure A.1: Example for a triangular dislocation loop

then given by

$$\begin{aligned} \boldsymbol{f}_\mathrm{AB}(\boldsymbol{x}) &= -\frac{1}{4\pi}(\boldsymbol{b}\times\boldsymbol{t}_\mathrm{AB})\int_\mathrm{A}^\mathrm{B}\frac{1}{\|\boldsymbol{x}-\boldsymbol{x}'\|}\,\mathrm{d}C' \\ &= -\frac{1}{4\pi}(\boldsymbol{b}\times\boldsymbol{t}_\mathrm{AB})\ln\left(\frac{r_\mathrm{A}}{r_\mathrm{B}}\left(\frac{1+\boldsymbol{\lambda}_\mathrm{B}^\mathsf{T}\cdot\boldsymbol{t}_\mathrm{AB}}{1+\boldsymbol{\lambda}_\mathrm{A}^\mathsf{T}\cdot\boldsymbol{t}_\mathrm{AB}}\right)\right), \end{aligned} \tag{A.54}$$

$$\begin{aligned} \boldsymbol{g}_\mathrm{AB}(\boldsymbol{x}) &= -\frac{1}{8\pi(1-\nu)}(\boldsymbol{b}\times\boldsymbol{t}_\mathrm{AB})\int_\mathrm{A}^\mathrm{B}\frac{1}{\|\boldsymbol{x}-\boldsymbol{x}'\|}\,\mathrm{d}C' \\ &\quad -\int_\mathrm{A}^\mathrm{B}\frac{(\boldsymbol{b}\times\boldsymbol{t}_\mathrm{AB})^\mathsf{T}\cdot(\boldsymbol{x}-\boldsymbol{x}')}{\|\boldsymbol{x}-\boldsymbol{x}'\|}(\boldsymbol{x}-\boldsymbol{x}')\,\mathrm{d}C' \\ &= -\frac{1}{8\pi(1-\nu)}\left(\boldsymbol{f}_\mathrm{AB}(\boldsymbol{x}) - \frac{\boldsymbol{b}^\mathsf{T}\cdot(\boldsymbol{\lambda}_\mathrm{A}\times\boldsymbol{\lambda}_\mathrm{B})}{1+\boldsymbol{\lambda}_\mathrm{A}^\mathsf{T}\cdot\boldsymbol{\lambda}_\mathrm{B}}(\boldsymbol{\lambda}_\mathrm{A}+\boldsymbol{\lambda}_\mathrm{B})\right), \end{aligned} \tag{A.55}$$

where

$$\begin{aligned} &\boldsymbol{r}_\mathrm{A} = \boldsymbol{x}_\mathrm{A} - \boldsymbol{x}, \qquad r_\mathrm{A} = \|\boldsymbol{r}_\mathrm{A}\|, \qquad \boldsymbol{r}_\mathrm{B} = \boldsymbol{x}_\mathrm{B} - \boldsymbol{x}, \qquad r_\mathrm{B} = \|\boldsymbol{r}_\mathrm{B}\|, \\ &\boldsymbol{\lambda}_\mathrm{A} = \frac{1}{r_\mathrm{A}}\boldsymbol{r}_\mathrm{A}, \qquad \boldsymbol{\lambda}_\mathrm{B} = \frac{1}{r_\mathrm{B}}\boldsymbol{r}_\mathrm{B} \end{aligned} \tag{A.56}$$

from which the remaining terms follow verbatim. The displacement field of a triangular loop is then given by

$$\tilde{\boldsymbol{u}}^\triangle(\boldsymbol{x}) = \frac{\Omega_\mathrm{s}(\boldsymbol{x})}{4\pi}\boldsymbol{b} + \big(\boldsymbol{f}'_\mathrm{AB}(\boldsymbol{x}) + \boldsymbol{f}'_\mathrm{BC}(\boldsymbol{x}) + \boldsymbol{f}'_\mathrm{CA}(\boldsymbol{x})\big) + \big(\boldsymbol{g}'_\mathrm{AB}(\boldsymbol{x}) + \boldsymbol{g}'_\mathrm{BC}(\boldsymbol{x}) + \boldsymbol{g}'_\mathrm{CA}(\boldsymbol{x})\big), \tag{A.57}$$

with

$$\boldsymbol{f}'_\mathrm{AB}(\boldsymbol{x}) = -\frac{3-2\nu}{8\pi(1-\nu)}(\boldsymbol{b}\times\boldsymbol{t}_\mathrm{AB})\ln\left(\frac{r_\mathrm{A}}{r_\mathrm{B}}\left(\frac{1+\boldsymbol{\lambda}_\mathrm{B}^\mathsf{T}\cdot\boldsymbol{t}_\mathrm{AB}}{1+\boldsymbol{\lambda}_\mathrm{A}^\mathsf{T}\cdot\boldsymbol{t}_\mathrm{AB}}\right)\right), \tag{A.58}$$

$$\boldsymbol{g}'_\mathrm{AB}(\boldsymbol{x}) = \frac{1}{8\pi(1-\nu)}\frac{\boldsymbol{b}^\mathsf{T}\cdot(\boldsymbol{\lambda}_\mathrm{A}\times\boldsymbol{\lambda}_\mathrm{B})}{1+\boldsymbol{\lambda}_\mathrm{A}^\mathsf{T}\cdot\boldsymbol{\lambda}_\mathrm{B}}(\boldsymbol{\lambda}_\mathrm{A}+\boldsymbol{\lambda}_\mathrm{B}) \qquad \text{etc.} \tag{A.59}$$

The isotropic solution for an infinite straight edge dislocation should be recovered in the limit when the diameter of $\gamma^{\triangle}$tends to infinity, more precisely, when the x_3 coordinate of the nodes A and B as well as the x_1 coordinate of the node C become very large compared to $\boldsymbol{x}$. This is shown in the following.

Proposition 4. *Assume that* $\tilde{\boldsymbol{u}}^{\triangle}$*is a solution to* (A.50) *for the triangular loop* $\gamma^{\triangle}$*shown in Figure A.1. Then, in the limiting case when* $L \to \infty$*, i.e. for*

$$x_{\mathrm{A},3} \to -\infty, \qquad x_{\mathrm{B},3} \to \infty, \qquad x_{\mathrm{C},1} \to -\infty, \tag{A.60}$$

the isotropic solution (A.26) *is recovered. That is, for* $\boldsymbol{b} = \begin{pmatrix} 0 & 0 & b \end{pmatrix}^{\mathsf{T}}$

$$\textbf{(1)} \qquad \lim_{L\to\infty} \tilde{\boldsymbol{u}}^{\triangle}(\boldsymbol{x}; L) = \tilde{\boldsymbol{u}}^{\mathrm{screw}} \tag{A.61}$$

and for $\boldsymbol{b} = \begin{pmatrix} b & 0 & 0 \end{pmatrix}^{\mathsf{T}}$

$$\textbf{(2)} \qquad \lim_{L\to\infty} \left(\tilde{\boldsymbol{u}}^{\triangle}(\boldsymbol{x}; L) - \tilde{\boldsymbol{f}}'_{\mathrm{AB}}(L) \right) = \tilde{\boldsymbol{u}}^{\mathrm{edge}}, \tag{A.62}$$

with $\tilde{\boldsymbol{f}}'_{\mathrm{AB}}(L) = \frac{1-2\nu}{8\pi(1-\nu)} \ln\left(4L^2\right) \begin{pmatrix} 0 & b & 0 \end{pmatrix}^{\mathsf{T}}$.

Proof. The proof of statement **(1)** can be found (Balluffi, 2012, Exercise 12.10).

To proof statement **(2)** the limiting case for $\tilde{\boldsymbol{u}}^{\triangle}$is obtained first. It can be readily checked that

$$\lim_{L\to\infty} \Omega_{\mathrm{s}} = \frac{b}{2\pi} \arctan \frac{x_2}{x_1}, \tag{A.63}$$

$$\lim_{L\to\infty} \boldsymbol{f}'_{\mathrm{AB}} = \lim_{L\to\infty} \left(\frac{1-2\nu}{8\pi(1-\nu)} \ln\left(\frac{r_{\mathrm{A}}+L}{r_{\mathrm{A}}-L}\right) \begin{pmatrix} 0 \\ b \\ 0 \end{pmatrix} \right) = \infty, \tag{A.64}$$

$$\lim_{L\to\infty} \boldsymbol{f}'_{\mathrm{BC}} = \boldsymbol{0}, \tag{A.65}$$

$$\lim_{L\to\infty} \boldsymbol{f}'_{\mathrm{CB}} = \boldsymbol{0}, \tag{A.66}$$

$$\lim_{L\to\infty} \boldsymbol{g}'_{\mathrm{AB}} = \frac{b}{4\pi(1-\nu)} \frac{x_2}{x_1^2 + x_2^2} \begin{pmatrix} x_1 \\ x_2 \\ 0 \end{pmatrix}, \tag{A.67}$$

$$\lim_{L\to\infty} \boldsymbol{g}'_{\mathrm{BC}} = \boldsymbol{0}, \tag{A.68}$$

$$\lim_{L\to\infty} \boldsymbol{g}'_{\mathrm{CB}} = \boldsymbol{0}. \tag{A.69}$$

The precise derivations are left to the interested reader.

It can be immediately seen that $\lim_{L\to\infty} \tilde{u}_1^{\triangle} = \tilde{u}_1^{\text{edge}}$. The logarithmic term in (A.64) is divergent and therefore another divergent term must be subtracted in order to obtain a converged result. Therefore the asymptotic behavior of (A.64) needs to be analyzed. Since $r_{\text{A}} = \sqrt{x_1^2 + x_2^2 + L^2}$ one may re-write the logarithmic term as a function

$$f(u) = \ln\left(\frac{\sqrt{r^2u^2+1}+1}{\sqrt{r^2u^2+1}-1}\right) = \ln\left(\sqrt{r^2u^2+1}+1\right) - \ln\left(\sqrt{r^2u^2+1}-1\right), \quad \text{(A.70)}$$

with $r = \sqrt{x_1^2 + x_2^2}$ and $u = 1/L$. A Taylor expansion of $\sqrt{r^2u^2+1}$ around $u = 0$ yields

$$\sqrt{r^2u^2+1} = 1 + \frac{1}{2}r^2u^2 + \mathcal{O}(u^3). \quad \text{(A.71)}$$

For small u the higher order terms can be neglected such that f can be written as

$$f(u) \approx \ln\left(1 + \frac{1}{2}r^2u^2 + 1\right) - \ln\left(1 + \frac{1}{2}r^2u^2 - 1\right) \quad \text{(A.72)}$$

$$= \ln 2 - \ln\left(\frac{1}{2}r^2u^2\right) \quad \text{(A.73)}$$

$$= \ln\frac{4}{u^2} - \ln r^2, \quad \text{(A.74)}$$

where $\ln 4/u^2 = \ln 4L^2$. Hence, subtracting $\tilde{\boldsymbol{f}}'_{\text{AB}}$ from $\boldsymbol{f}'_{\text{AB}}$ in (A.64) leads to

$$\lim_{L\to\infty}\left(\boldsymbol{f}'_{\text{AB}} - \tilde{\boldsymbol{f}}'_{\text{AB}}\right) = -\frac{(1-2\nu)}{8\pi(1-\nu)}\ln\left(x_1^2 + x_2^2\right)\begin{pmatrix}0\\ b\\ 0\end{pmatrix}. \quad \text{(A.75)}$$

which proves the stated proposition. ☐

A.3.2 Periodic arrays of bowing dislocations

The previous results can be efficiently used to facilitate the computation of the elastic displacement field of periodic arrays of curved dislocations. Due to the linearity of the problem the analytic, closed-form expression (A.49) can be used in order to compute the displacement field of infinite edge dislocations. Subsequently the displacement field of the closed loops $\Delta\tilde{\boldsymbol{u}}^{(i,j)}$ for a periodic image (i, j) is superimposed which account for the bowed components of the dislocations as shown in Figure A.2. Note that only the computation of the contributions from the surface segments and the solid angle are necessary as the inner segments cancel each other out.

The displacement field converges approximately linearly with respect to the number of periodic images. Fortunately this is not an issue since a great portion of the full solution is already captured analytically via $\tilde{\boldsymbol{u}}^{\text{PAD}}$. If this scheme should be adopted to larger problems, e.g. to visualize the displacement field in PAD domains containing numerous

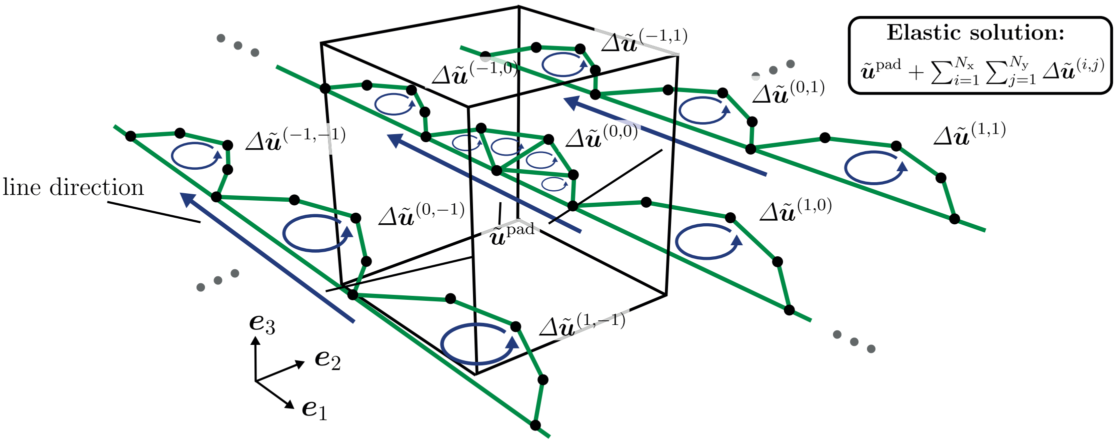
$\Delta\tilde{\boldsymbol{u}}^{(-1,1)}$
Elastic solution:
$\tilde{\boldsymbol{u}}^{\mathrm{pad}} + \sum_{i=1}^{N_{\mathrm{x}}} \sum_{j=1}^{N_{\mathrm{y}}} \Delta\tilde{\boldsymbol{u}}^{(i,j)}$
$\Delta\tilde{\boldsymbol{u}}^{(-1,0)}$
$\Delta\tilde{\boldsymbol{u}}^{(0,1)}$
$\Delta\tilde{\boldsymbol{u}}^{(-1,-1)}$
$\Delta\tilde{\boldsymbol{u}}^{(0,0)}$
$\Delta\tilde{\boldsymbol{u}}^{(1,1)}$
line direction
$\Delta\tilde{\boldsymbol{u}}^{(0,-1)}$
$\tilde{\boldsymbol{u}}^{\mathrm{pad}}$
$\Delta\tilde{\boldsymbol{u}}^{(1,0)}$
$\boldsymbol{e}_3$
$\Delta\tilde{\boldsymbol{u}}^{(1,-1)}$
$\boldsymbol{e}_2$
$\boldsymbol{e}_1$

Figure A.2: Schematic illustration of the summation scheme for the computation of the elastic displacement field of periodic arrays of curved dislocations

dislocations, more efficient summation schemes would have to be developed. However, this scheme was mainly aimed for the computation of the boundary conditions on the atomistic problem for the specific test case considered in Section 4.3.

A.4 Lattice Green functions

A.4.1 Construction of G^{lgf}

Theorem A.4.1 (Semi-discrete Fourier transform). *For any function $f(\boldsymbol{\xi}) \in \mathcal{U}^{\star}(\Lambda)$ its semi-discrete Fourier transform (SDFT), which belongs to $L^2(\mathcal{B})$, is given*

$$\forall\, \boldsymbol{k} \in \mathcal{B} \qquad \mathcal{F}\left\{f\right\}(\boldsymbol{k}) = \sum_{\boldsymbol{\xi}\in\Lambda} f_{\xi} e^{-\mathrm{i}(\boldsymbol{k}^{\mathsf{T}}\cdot\boldsymbol{\xi})}, \tag{A.76}$$

where $\mathcal{B}$ is the Brillouin zone of Λ. The function f can be recovered using the inverse SDFT as

$$f(\boldsymbol{\xi}) = \mathcal{F}^{-1}\left\{\mathcal{F}\left\{f\right\}\right\}(\boldsymbol{\xi}) = \frac{1}{|\mathcal{B}|}\int \mathcal{F}\left\{f\right\}(\boldsymbol{k}) e^{\mathrm{i}(\boldsymbol{k}^{\mathsf{T}}\cdot\boldsymbol{\xi})}\,\mathrm{d}\mathcal{B} \tag{A.77}$$

To compute the lattice Green function the following problem is defined: find $\boldsymbol{u}^k : \Lambda \to \mathbb{R}^d$ which solves $\forall\, k = 1, \ldots, d$

$$\mathcal{L}_{\mathrm{h}}[\boldsymbol{u}^k](\boldsymbol{\xi}) = \sum_{\boldsymbol{\eta}\in\mathcal{R}_{\xi}^{\mathrm{loc}}} \boldsymbol{K}(\boldsymbol{\xi}-\boldsymbol{\eta})\boldsymbol{u}^k(\boldsymbol{\eta}) = \boldsymbol{f}^k(\boldsymbol{\xi}) \qquad \text{in } \Lambda, \tag{A.78}$$

with

$$f_i^k(\boldsymbol{\xi}) = \delta_{ik}\delta(\boldsymbol{\xi}) = \begin{cases} 1 & \text{if } (i=k)\wedge(\boldsymbol{\xi}=\boldsymbol{0}), \\ 0 & \text{else.} \end{cases} \tag{A.79}$$

First, problem (A.78) is written component-wise, i.e.

$$\forall\, k = 1, ..., d \qquad \delta_{ik}\delta(\boldsymbol{\xi}) = \sum_{\boldsymbol{\xi}\in\mathcal{R}_{\xi}^{\mathrm{loc}}} K_{ij}(\boldsymbol{\xi}-\boldsymbol{\eta})u_j^k(\boldsymbol{\eta}) = K_{ij} * u_j^k, \tag{A.80}$$

where $*$ is the convolution operator. Now the SDFT is applied on both sides such that

$$\mathcal{F}\left\{\delta_{ik}\delta(\boldsymbol{\xi})\right\} = \delta_{ik} = \mathcal{F}\left\{K_{ij} * u_j^k\right\} = \mathcal{F}\left\{K_{ij}\right\}\cdot\mathcal{F}\left\{u_j^k\right\}. \tag{A.81}$$

Note that the convolution operation reduces to a simple multiplication in Fourier space. The remaining steps are exemplified for $d = 2$. Rewriting in matrix-vector notation gives

$$\begin{bmatrix}\mathcal{F}\left\{K_{11}\right\} & \mathcal{F}\left\{K_{12}\right\}\\ \mathcal{F}\left\{K_{21}\right\} & \mathcal{F}\left\{K_{22}\right\}\end{bmatrix}\begin{bmatrix}\mathcal{F}\left\{u_1^1\right\} & \mathcal{F}\left\{u_1^2\right\}\\ \mathcal{F}\left\{u_2^1\right\} & \mathcal{F}\left\{u_2^2\right\}\end{bmatrix} = \hat{I}. \tag{A.82}$$

Inverting the Fourier stiffness matrix gives

$$\begin{bmatrix}\mathcal{F}\left\{u_1^1\right\} & \mathcal{F}\left\{u_1^2\right\}\\ \mathcal{F}\left\{u_2^1\right\} & \mathcal{F}\left\{u_2^2\right\}\end{bmatrix} = \frac{1}{det}\begin{bmatrix}\mathcal{F}\left\{K_{11}\right\} & -\mathcal{F}\left\{K_{12}\right\}\\ -\mathcal{F}\left\{K_{21}\right\} & \mathcal{F}\left\{K_{22}\right\}\end{bmatrix}, \tag{A.83}$$

with $det = \mathcal{F}\left\{K_{11}\right\}\mathcal{F}\left\{K_{22}\right\} - \mathcal{F}\left\{K_{12}\right\}\mathcal{F}\left\{K_{21}\right\}$. Transforming $\mathcal{F}\left\{u_i^k\right\}$ back to the real space gives the components of the lattice Green tensor

$$G_{11}(\boldsymbol{\xi}) = u_1^1(\boldsymbol{\xi}) = \mathcal{F}^{-1}\left\{(1/det)\mathcal{F}\left\{K_{11}\right\}\right\}(\boldsymbol{\xi}) \qquad \text{etc.} \tag{A.84}$$

A.4.2 Lattice Green function for linear elasticity

In the numerical examples in Section 2.6, 2.7 and 4.1 the interpolation function φ_ξ is the classical P1 interpolant often used in finite elements (see e.g. (Bathe and Zimmermann, 2002)). An LGF for linear elasticity can then be obtained by periodically partitioning the lattice into simplices (triangles in 2d and tetrahedrons in 3d). Such a partition is usually not unique but results are not qualitatively impacted. For the square, hexagonal and the fcc lattice a possible partitioning is shown in Figure A.3 (a)-(c).

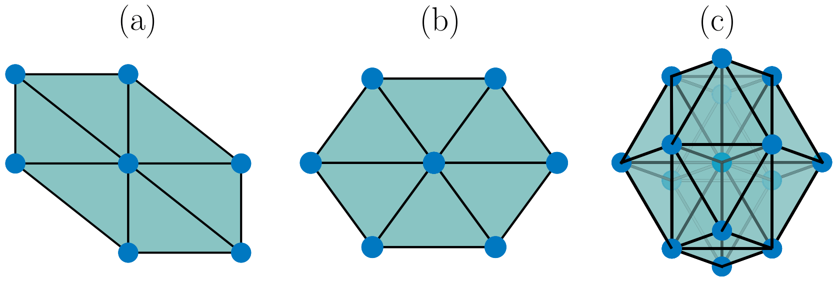

Figure A.3: Simplicial partitioning of various Bravais lattice types

A.4.3 Error estimates

Preparation

Below, use will be made of the following inequalities, that is for all $\hat{A} \in \mathbb{R}^{N\times M}$, $\hat{B} \in \mathbb{R}^{M\times O}$ and $\hat{x} \in \mathbb{R}^{M}$ it holds

$$\|\hat{A}\hat{B}\|_{\text{fro}} \leq \|\hat{A}\|_{\text{fro}}\|\hat{B}\|_{\text{fro}}, \qquad \|\hat{A}\hat{x}\| \leq \|\hat{A}\|_{\text{fro}}\|\hat{x}\| \tag{A.85}$$

which both follow from the Cauchy-Schwarz inequality.

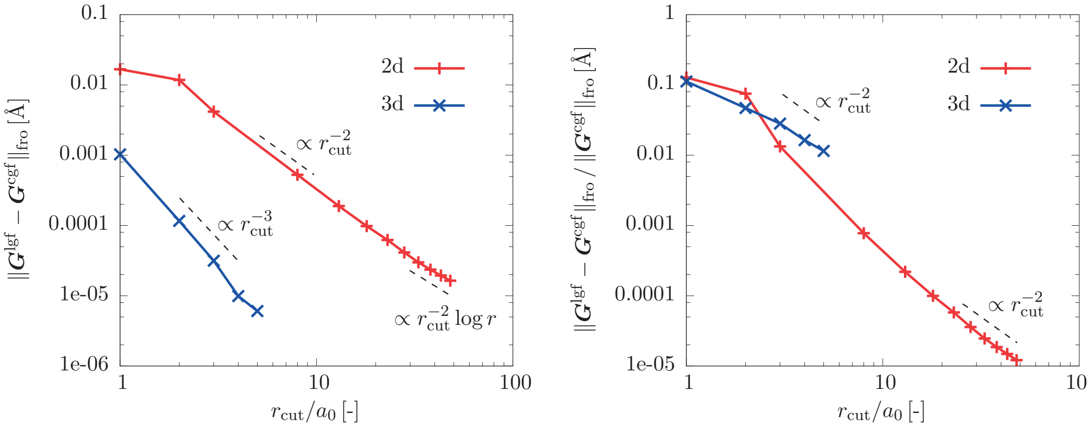

Figure A.4: Absolute and relative errors of the CGF when compared to the LGF

In (Trinkle, 2008) the difference between the LGF and the CGF $\boldsymbol{\epsilon}(\boldsymbol{\xi}) \in \mathbb{R}^{d\times d}$ was defined as

$$\boldsymbol{G}^{\text{lgf}}(\boldsymbol{\xi}) - \boldsymbol{G}^{\text{cgf}}(\boldsymbol{\xi}) = \boldsymbol{G}^{\text{cgf}}(\boldsymbol{\xi})\boldsymbol{\epsilon}(\boldsymbol{\xi}). \tag{A.86}$$

Taking norms on both sides one can write

$$\|\boldsymbol{G}^{\text{lgf}} - \boldsymbol{G}^{\text{cgf}}\|_{\text{fro}} = \|\boldsymbol{G}^{\text{cgf}}\boldsymbol{\epsilon}\|_{\text{fro}} \leq \|\boldsymbol{G}^{\text{cgf}}\|_{\text{fro}}\|\boldsymbol{\epsilon}\|_{\text{fro}}. \tag{A.87}$$

The total error then reads

$$\|\boldsymbol{\epsilon}\|_{\text{fro}} = \frac{\|\boldsymbol{G}^{\text{lgf}} - \boldsymbol{G}^{\text{cgf}}\|_{\text{fro}}}{\|\boldsymbol{G}^{\text{cgf}}\|_{\text{fro}}}. \tag{A.88}$$

In (Trinkle, 2008) it was shown that, under certain assumptions, $\|\boldsymbol{\epsilon}\|_{\text{fro}} \propto r^{-2}$ for $d = 3$. It is presumed that the same result holds also for the 2d case. This can be made rigorous considering the fact that $\forall\, \boldsymbol{\xi} \neq \boldsymbol{0}\ \lim\limits_{a_0\to 0} \boldsymbol{G}^{\text{lgf}}(\boldsymbol{\xi}) = \boldsymbol{G}^{\text{cgf}}(\boldsymbol{\xi})$ and using the fact that the scaling only differs by a log-factor but this is not carried out. Using the fact that $\|\boldsymbol{G}^{\text{cgf}}\|_{\text{fro}} \propto \log r$ for $d = 2$ and $\|\boldsymbol{G}^{\text{cgf}}\|_{\text{fro}} \propto r^{-1}$ for $d = 3$ the asymptotic decay rates for the absolute errors are obtained

$$\textbf{2d:}\quad \|\boldsymbol{G}^{\mathrm{lgf}} - \boldsymbol{G}^{\mathrm{cgf}}\|_{\mathrm{fro}} \lesssim r^{-2}\log r, \qquad \textbf{3d:}\quad \|\boldsymbol{G}^{\mathrm{lgf}} - \boldsymbol{G}^{\mathrm{cgf}}\|_{\mathrm{fro}} \lesssim r^{-3}. \tag{A.89}$$

The estimates are verified with numerical experiments in Figure A.4 for the potentials used in Section 4.1.1 and 4.1.2.

In order to prove Proposition 3 the following preliminary result is required:

Proposition 5. *Using the approximation* $\tilde{\boldsymbol{G}}^{\mathrm{lgf}}$(2.99) *the scaling of the error for any matrix* $\hat{G} = \hat{G}^{\bullet/\bullet}$ *and* $\hat{F} = \hat{F}^{\bullet/\bullet}$ *defined in Section 2.6 which acts on two interface domains* Λ_1 *and* Λ_2 [1] *can directly be given as*

$$\|\hat{G} - \hat{\tilde{G}}\|_{\mathrm{fro}} \lesssim r_{\mathrm{cut}}^{-(d+1)/2}(\log r_{\mathrm{cut}})^{3-d}, \qquad \|\hat{F} - \hat{\tilde{F}}\|_{\mathrm{fro}} \lesssim r_{\mathrm{cut}}^{-(d+1)/2}(\log r_{\mathrm{cut}})^{3-d} \tag{A.90}$$

as $\mathrm{diam}(\Lambda_1) \to \infty$ *or* $\mathrm{diam}(\Lambda_2) \to \infty$, *where* $\mathrm{diam}(\bullet)$ *is the diameter of the corresponding domain.*

Sketch of the proof. Choose Λ_1 as the set of application points and Λ_2 as the set of source points. Hence, the norm of the error in $\hat{G}$ is given by

$$\begin{aligned} &\|\hat{G} - \hat{\tilde{G}}\|_{\mathrm{fro}} \\ &= \left(\sum_{\boldsymbol{\xi}\in\Lambda_1} \sum_{\substack{\boldsymbol{\eta}\in\Lambda_2,\\ r>r_{\mathrm{cut}}}} \Big(\boldsymbol{G}^{\mathrm{lgf}}(\boldsymbol{\xi}-\boldsymbol{\eta}) - \tilde{\boldsymbol{G}}^{\mathrm{lgf}}(\boldsymbol{\xi}-\boldsymbol{\eta})\Big) \cdot \Big(\boldsymbol{G}^{\mathrm{lgf}}(\boldsymbol{\xi}-\boldsymbol{\eta}) - \tilde{\boldsymbol{G}}^{\mathrm{lgf}}(\boldsymbol{\xi}-\boldsymbol{\eta})\Big) \right)^{1/2} \end{aligned} \tag{A.91}$$

Since

$$\begin{aligned} &\Big(\boldsymbol{G}^{\mathrm{lgf}}(\boldsymbol{\xi}-\boldsymbol{\eta}) - \tilde{\boldsymbol{G}}^{\mathrm{lgf}}(\boldsymbol{\xi}-\boldsymbol{\eta})\Big) \cdot \Big(\boldsymbol{G}^{\mathrm{lgf}}(\boldsymbol{\xi}-\boldsymbol{\eta}) - \tilde{\boldsymbol{G}}^{\mathrm{lgf}}(\boldsymbol{\xi}-\boldsymbol{\eta})\Big) \\ &\qquad\qquad = \|\boldsymbol{G}^{\mathrm{lgf}} - \tilde{\boldsymbol{G}}^{\mathrm{lgf}}\|_{\mathrm{fro}}^2 \lesssim r^{-2d}(\log r)^{2(3-d)} \end{aligned} \tag{A.92}$$

one can write

$$\|\hat{G} - \hat{\tilde{G}}\|_{\mathrm{fro}} \lesssim \left(\sum_{\boldsymbol{\xi}\in\Lambda_1} \sum_{\substack{\boldsymbol{\eta}\in\Lambda_2,\\ r>r_{\mathrm{cut}}}} r^{-2d}(\log r)^{2(3-d)} \right)^{1/2}. \tag{A.93}$$

The inner sum is now approximated as an integral over a surface Γ which includes all lattice points in Λ_2, i.e.

$$\sum_{\substack{\boldsymbol{\eta}\in\Lambda_2,\\ r>r_{\mathrm{cut}}}} r^{-2d}(\log r)^{2(3-d)} \approx \frac{1}{A_0} \int_{\Gamma\setminus B_{r_{\mathrm{cut}}}} r^{-2d}(\log r)^{2(3-d)}\,\mathrm{d}\,A, \tag{A.94}$$

---

[1] More precisely, Λ_1/Λ_2 refer to Λ^{i}, Λ^{p}, $\Lambda^{\mathrm{i+}}$ or $\Lambda^{\mathrm{i-}}$ as defined in Section 2.3.3

where A_0 is some reference area and $B_{r_{\mathrm{cut}}} = \{\, \boldsymbol{x}' \in \mathbb{R}^d \mid \|\boldsymbol{\xi} - \boldsymbol{x}'\| \le r_{\mathrm{cut}} \,\}$ is the closed ball with radius r_{cut}.

First, the integral is estimated for $d = 2$. Therefore, pick one application point $\boldsymbol{\xi} \in \Lambda_1$. Since the integrand is always positive the right hand side of (A.94) can be bound by an integral over the surface of a *square* domain $\Gamma_{\square}$ which encloses Γ such that

$$\int_{\Gamma \setminus B_{r_{\mathrm{cut}}}} r^{-4} (\log r)^2 \mathrm{d}\, A \le \int_{\Gamma_{\square} \setminus B_{r_{\mathrm{cut}}}} r^{-4} (\log r)^2 \mathrm{d}\, A. \tag{A.95}$$

As $\operatorname{diam}(\Gamma_{\square}) \to \infty$ this integral becomes proportional to $r_{\mathrm{cut}}^{-3} (\log r_{\mathrm{cut}})^2$. Plugging this result into (A.93) and proceeding similarly for the other application points it follows

$$\|\hat{G} - \hat{\hat{G}}\|_{\mathrm{fro}} \lesssim \left(\sum_{\boldsymbol{\xi} \in \Lambda_1} r_{\mathrm{cut}}^{-3} (\log r_{\mathrm{cut}})^2 \right)^{1/2} \simeq r_{\mathrm{cut}}^{-3/2} \log r_{\mathrm{cut}}. \tag{A.96}$$

This procedure translates verbatim to $d = 3$. Instead of a square domain the surface of a *cubic* domain $\Gamma_{⧉}$ which encloses Γ is now chosen. Then

$$\int_{\Gamma \setminus B_{r_{\mathrm{cut}}}} r^{-6} \mathrm{d}\, A \le \int_{\Gamma_{⧉} \setminus B_{r_{\mathrm{cut}}}} r^{-6} \mathrm{d}\, A \;\propto\; r_{\mathrm{cut}}^{-4} \tag{A.97}$$

as $\operatorname{diam}(\Gamma_{⧉}) \to \infty$ since $\int_{\Gamma} \bullet \, \mathrm{d}A$ is now a double integral. Using the estimate (A.97) in (A.93) yields

$$\|\hat{G} - \hat{\hat{G}}\|_{\mathrm{fro}} \lesssim \left(\sum_{\boldsymbol{\xi} \in \Lambda_1} r_{\mathrm{cut}}^{-4} \right)^{1/2} \simeq r_{\mathrm{cut}}^{-2}. \tag{A.98}$$

The second estimate can be obtained using (A.85) and the fact the representation of $\hat{L}$ is exact. $\square$

Proof of Proposition 3

Using Proposition 5 the error induced by Sinclair's method can directly be estimated as

$$\begin{aligned} \|\hat{u}^{\mathrm{p}} - \hat{\hat{u}}^{\mathrm{p}}\| = \|(\hat{G}^{\mathrm{p/i+}} - \hat{\hat{G}}^{\mathrm{p/i+}}) \hat{f}^{\mathrm{i+}}_{\mathrm{inh}}\| &\le \|\hat{G}^{\mathrm{p/i+}} - \hat{\hat{G}}^{\mathrm{p/i+}}\|_{\mathrm{fro}} \|\hat{f}^{\mathrm{i+}}_{\mathrm{inh}}\| \\ &\lesssim r_{\mathrm{cut}}^{-(d+1)/2} (\log r_{\mathrm{cut}})^{3-d}. \end{aligned} \tag{A.99}$$

For the A/DBEM coupling it holds

$$\begin{aligned} \hat{u}^{\mathrm{p}} - \hat{\hat{u}}^{\mathrm{p}} &= (\hat{F}^{\mathrm{p/i}} - \hat{\hat{F}}^{\mathrm{p/i}}) \hat{u}^{\mathrm{i}} - \hat{G}^{\mathrm{p/i}} \hat{f}^{\mathrm{i}} + \hat{\hat{G}}^{\mathrm{p/i}} \hat{\hat{f}}^{\mathrm{i}}. \\ &= (\hat{F}^{\mathrm{p/i}} - \hat{\hat{F}}^{\mathrm{p/i}}) \hat{u}^{\mathrm{i}} - \hat{G}^{\mathrm{p/i}} (\hat{f}^{\mathrm{i}} - \hat{\hat{f}}^{\mathrm{i}}) - (\hat{G}^{\mathrm{p/i}} - \hat{\hat{G}}^{\mathrm{p/i}}) \hat{\hat{f}}^{\mathrm{i}}. \end{aligned} \tag{A.100}$$

Taking the norm on both sides and using the triangle and Cauchy-Schwarz inequalities leads to

$$\|\hat{u}^{\mathrm{p}} - \hat{\hat{u}}^{\mathrm{p}}\| \le \|\hat{F}^{\mathrm{p/i}} - \hat{\hat{F}}^{\mathrm{p/i}}\|_{\mathrm{fro}}\|\hat{u}^{\mathrm{i}}\| + \|\hat{G}^{\mathrm{p/i}}\|_{\mathrm{fro}}\|\hat{f}^{\mathrm{i}} - \hat{\hat{f}}^{\mathrm{i}}\| + \|\hat{G}^{\mathrm{p/i}} - \hat{\hat{G}}^{\mathrm{p/i}}\|_{\mathrm{fro}}\|\hat{\hat{f}}^{\mathrm{i}}\|. \tag{A.101}$$

The first and the third term can be directly estimated as

$$\|\hat{F}^{\mathrm{p/i}} - \hat{\hat{F}}^{\mathrm{p/i}}\|_{\mathrm{fro}} \lesssim r_{\mathrm{cut}}^{-(d+1)/2}(\log r_{\mathrm{cut}})^{3-d}, \tag{A.102}$$

$$\|\hat{G}^{\mathrm{p/i}} - \hat{\hat{G}}^{\mathrm{p/i}}\|_{\mathrm{fro}} \lesssim r_{\mathrm{cut}}^{-(d+1)/2}(\log r_{\mathrm{cut}})^{3-d}. \tag{A.103}$$

For the second term use is made of (2.96) to write

$$\begin{aligned} \hat{f}^{\mathrm{i}} - \hat{\hat{f}}^{\mathrm{i}} &= -(\hat{G}^{\mathrm{i/i}})^{-1}(\hat{I} - \hat{F}^{\mathrm{i/i}})\hat{u}^{\mathrm{i}} + (\hat{\hat{G}}^{\mathrm{i/i}})^{-1}(\hat{I} - \hat{\hat{F}}^{\mathrm{i/i}})\hat{u}^{\mathrm{i}} \\ &= -((\hat{G}^{\mathrm{i/i}})^{-1} - (\hat{\hat{G}}^{\mathrm{i/i}})^{-1} - \hat{F}^{\mathrm{i/i}} + \hat{\hat{F}}^{\mathrm{i/i}})\hat{u}^{\mathrm{i}}. \end{aligned} \tag{A.104}$$

Now define

$$(\hat{G}^{\mathrm{i/i}})^{-1} = \hat{E}_1 + (\hat{\hat{G}}^{\mathrm{i/i}})^{-1}, \qquad \hat{I} - \hat{F}^{\mathrm{i/i}} = \hat{E}_2 + \hat{I} - \hat{\hat{F}}^{\mathrm{i/i}}. \tag{A.105}$$

Plugging the latter into (A.104) and taking norms yields

$$\begin{aligned} \|\hat{f}^{\mathrm{i}} - \hat{\hat{f}}^{\mathrm{i}}\| &\le \|\hat{E}_1\hat{E}_2 + \hat{E}_1(\hat{I} - \hat{\hat{F}}^{\mathrm{i/i}}) + \hat{E}_2(\hat{\hat{G}}^{\mathrm{i/i}})^{-1}\|_{\mathrm{fro}}\|\hat{u}^{\mathrm{i}}\| \\ &\le \|\hat{E}_1\|_{\mathrm{fro}}\|\hat{E}_2\|_{\mathrm{fro}} + \|\hat{E}_1\|_{\mathrm{fro}}\|\hat{I} - \hat{\hat{F}}^{\mathrm{i/i}}\|_{\mathrm{fro}} + \|\hat{E}_2\|_{\mathrm{fro}}\|(\hat{\hat{G}}^{\mathrm{i/i}})^{-1}\|_{\mathrm{fro}}. \end{aligned} \tag{A.106}$$

To estimate $\|\hat{E}_1\|_{\mathrm{fro}}$ define $\hat{G}^{\mathrm{i/i}} = \hat{G}^{\mathrm{i/i}}(\hat{X}) = \hat{\hat{G}}^{\mathrm{i/i}} + \hat{X}$. Applying a Taylor expansion to $(\hat{G}^{\mathrm{i/i}}(\hat{X}))^{-1}$ around $\hat{X} = \hat{0}$ such that

$$\begin{aligned} (\hat{G}^{\mathrm{i/i}})^{-1} - (\hat{\hat{G}}^{\mathrm{i/i}})^{-1} &= \left.\frac{\partial(\hat{\hat{G}}^{\mathrm{i/i}} + \hat{X})^{-1}}{\partial\hat{X}}\right|_{\hat{X}=\hat{0}}\hat{X} + \text{h. o. t.} \\ &\approx -(\hat{G}^{\mathrm{i/i}})^{-1}\hat{X} \end{aligned} \tag{A.107}$$

from which it follows that

$$\|\hat{E}_1\|_{\mathrm{fro}} \approx \|(\hat{G}^{\mathrm{i/i}})^{-1}\hat{X}\|_{\mathrm{fro}} \le \|(\hat{G}^{\mathrm{i/i}})^{-1}\|_{\mathrm{fro}}\|\hat{X}\|_{\mathrm{fro}} \lesssim r_{\mathrm{cut}}^{-(d+1)/2}(\log r_{\mathrm{cut}})^{3-d}. \tag{A.108}$$

It is then easy to see that the A/DBEM coupling satisfies (2.101). □

Bibliography

Abeyaratne, R., Knowles, J. K., 1990. On the driving traction acting on a surface of strain discontinuity in a continuum. Journal of the Mechanics and Physics of Solids 38 (3), 345 – 360.

Acharya, A., Bassani, J., 2000. Lattice incompatibility and a gradient theory of crystal plasticity. Journal of the Mechanics and Physics of Solids 48 (8), 1565–1595.

Alder, B. J., Wainwright, T. E., 1959. Studies in molecular dynamics. i. general method. The Journal of Chemical Physics 31 (2), 459–466.

Amelang, J., Kochmann, D., 2015. Surface effects in nanoscale structures investigated by a fully-nonlocal energy-based quasicontinuum method. Mechanics of Materials 90, 166–184.

Amelang, J., Venturini, G., Kochmann, D., 2015. Summation rules for a fully nonlocal energy-based quasicontinuum method. Journal of the Mechanics and Physics of Solids 82, 378–413.

Amodeo, R. J., Ghoniem, N. M., Apr 1990. Dislocation dynamics. i. a proposed methodology for deformation micromechanics. Phys. Rev. B 41, 6958–6967.

Anciaux, G., 2018. Private communication.

Anciaux, G., Coulaud, O., Roman, J., 2006. High performance multiscale simulation for crack propagation. pp. 473–480.

Anciaux, G., Junge, T., Hodapp, M., Cho, J., Molinari, J.-F., Curtin, W., 2018. The coupled atomistic/discrete-dislocation method in 3d part i: Concept and algorithms. Journal of the Mechanics and Physics of Solids 118, 152 – 171.

Anciaux, G., Molinari, J.-F., 2009. Contact mechanics at the nanoscale, a 3d multiscale approach. International Journal for Numerical Methods in Engineering 79 (9), 1041–1067.

Ariza, M., Ortiz, M., 2005. Discrete crystal elasticity and discrete dislocations in crystals. Archive for Rational Mechanics and Analysis 178 (2), 149–226.

Arsenlis, A., Cai, W., Tang, M., Rhee, M., Oppelstrup, T., Hommes, G., Pierce, T. G., Bulatov, V. V., 2007. Enabling strain hardening simulations with dislocation dynamics. Modelling and Simulation in Materials Science and Engineering 15 (6), 553.

Bacon, D., Barnett, D., Scattergood, R., 1980. Anisotropic continuum theory of lattice defects. Progress in Materials Science 23, 51 – 262.

Bacon, D., Osetsky, Y., Rodney, D., 2009. Chapter 88 dislocation–obstacle interactions at the atomic level. Vol. 15 of Dislocations in Solids. Elsevier, pp. 1 – 90.

Balluffi, R., 2012. Introduction to Elasticity Theory for Crystal Defects. Cambridge University Press.

Barnett, D., 1985. The displacement field of a triangular dislocation loop. Philosophical Magazine A: Physics of Condensed Matter, Structure, Defects and Mechanical Properties 51 (3), 383–387.

Barnett, D., Balluffi, R., 2007. The displacement field of a triangular dislocation loop-a correction with commentary. Philosophical Magazine Letters 87 (12), 943–944.

Bathe, K., Zimmermann, P., 2002. Finite-Elemente-Methoden. Springer.

Bebendorf, M., 2009. Hierarchical Matrices: A Means to Efficiently Solve Elliptic Boundary Value Problems. Vol. 63. Springer.

Bebendorf, M., Kriemann, R., Dec 2005. Fast parallel solution of boundary integral equations and related problems. Computing and Visualization in Science 8 (3), 121–135.

Beex, L., Peerlings, R., Geers, M., 2014. A multiscale quasicontinuum method for lattice models with bond failure and fiber sliding. Computer Methods in Applied Mechanics and Engineering 269, 108 – 122.

Begau, C., Hartmaier, A., George, E., Pharr, G., 2011. Atomistic processes of dislocation generation and plastic deformation during nanoindentation. Acta Materialia 59 (3), 934–942.

Begau, C., Hua, J., Hartmaier, A., 2012. A novel approach to study dislocation density tensors and lattice rotation patterns in atomistic simulations. Journal of the Mechanics and Physics of Solids 60 (4), 711–722.

Bertram, A., 2012. Plasticity. In: Elasticity and Plasticity of Large Deformations. Springer, pp. 255–320.

Bilby, B., Bullough, R., Smith, E., 1955. Continuous distributions of dislocations: a new application of the methods of non-riemannian geometry. Proceedings of the Royal Society of London A: Mathematical, Physical and Engineering Sciences 231 (1185), 263–273.

Bitzek, E., Koskinen, P., Gähler, F., Moseler, M., Gumbsch, P., Oct 2006. Structural relaxation made simple. Phys. Rev. Lett. 97, 170201.

Bonnet, M., Maier, G., Polizzotto, C., Nov. 1998. Symmetric galerkin boundary element methods. Applied Mechanics Reviews 51 (11), 669–704.

Börm, S., Grasedyck, L., Hackbusch, W., 2003. Introduction to hierarchical matrices with applications. Engineering Analysis with Boundary Elements 27 (5), 405–422.

Born, M., Oppenheimer, R., 1927. Zur quantentheorie der molekeln. Annalen der Physik 389 (20), 457–484.

Braun, M., 1997. Configurational forces induced by finite-element discretization. Proceedings of the Estonian Academy of Sciences. Physics - Mathematics 46 (1/2), 24–31.

Brebbia, C., 1978. The boundary element method for engineers. John Wiley & Sons, Incorporated.

Brunner, D., Junge, M., Rapp, P., Bebendorf, M., Gaul, L., 2010. Comparison of the fast multipole method with hierarchical matrices for the helmholtz-bem. Computer Modeling in Engineering & Sciences 58 (2), 131–160.

Bulatov, V., Cai, W., 2006. Computer Simulations of Dislocations. Oxford Series on Materials Modelling. OUP Oxford.

Bulatov, V., Hsiung, L., Tang, M., Arsenlis, A., Bartelt, M., Cai, W., Florando, J., Hiratani, M., Rhee, M., Hommes, G., Pierce, T., De La Rubia, T., 2006. Dislocation multi-junctions and strain hardening. Nature 440 (7088), 1174–1178.

Cai, W., Arsenlis, A., Weinberger, C., Bulatov, V., 2006. A non-singular continuum theory of dislocations. Journal of the Mechanics and Physics of Solids 54 (3), 561–587.

Cho, J., 2017. Coupled 3d dislocation modeling at nano- and micro-scales. Ph.D. thesis, École polytechnique fédérale de Lausanne.

Cho, J., Junge, T., Molinari, J.-F., Anciaux, G., 2015. Toward a 3d coupled atomistic and discrete dislocation dynamics simulation: dislocation core structures and peierls stresses with several character angles in fcc aluminum. Advanced Modeling and Simulation in Engineering Sciences 2 (1), 1–17.

Cho, J., Molinari, J.-F., Curtin, W. A., Anciaux, G., 2018. The coupled atomistic/discrete-dislocation method in 3d. part iii: Dynamics of hybrid dislocations. Journal of the Mechanics and Physics of Solids 118, 1 – 14.

Coleman, B., Gurtin, M., 1967. Thermodynamics with internal state variables. The Journal of Chemical Physics 47 (2), 597–613.

Crone, J. C., Chung, P. W., Leiter, K. W., Knap, J., Aubry, S., Hommes, G., Arsenlis, A., 2014. A multiply parallel implementation of finite element-based discrete dislocation dynamics for arbitrary geometries. Modelling and Simulation in Materials Science and Engineering 22 (3), 035014.

Curtin, W., Deshpande, V., Needleman, A., Van Der Giessen, E., Wallin, M., 2010. Hybrid discrete dislocation models for fatigue crack growth. International Journal of Fatigue 32 (9), 1511–1520.

Curtin, W. A., Miller, R. E., 2017. A perspective on atomistic-continuum multiscale modeling. Modelling and Simulation in Materials Science and Engineering 25 (7), 071004.

Daw, M., Baskes, M., 1984. Embedded-atom method: Derivation and application to impurities, surfaces, and other defects in metals. Physical Review B 29 (12), 6443–6453.

Deshpande, V., Needleman, A., Van der Giessen, E., 2003. Finite strain discrete dislocation plasticity. Journal of the Mechanics and Physics of Solids 51 (11-12), 2057–2083.

Dewald, M., Curtin, W., 2006. Analysis and minimization of dislocation interactions with atomistic/continuum interfaces. Modelling and Simulation in Materials Science and Engineering 14 (3), 497–514.

Dobson, M., Luskin, M., Ortner, C., 2010. Sharp stability estimates for the force-based quasicontinuum approximation of homogeneous tensile deformation. Multiscale Modeling & Simulation 8 (3), 782–802.

Dobson, M., Luskin, M., Ortner, C., 2011. Iterative methods for the force-based quasicontinuum approximation: Analysis of a 1d model problem. Computer Methods in Applied Mechanics and Engineering 200 (37-40), 2697–2709.

Dupuy, L., Tadmor, E., Miller, R., Phillips, R., 2005. Finite-temperature quasicontinuum: Molecular dynamics without all the atoms. Physical Review Letters 95 (6).

Eckart, C., Young, G., Sep 1936. The approximation of one matrix by another of lower rank. Psychometrika 1 (3), 211–218.

Ehrlacher, V., Ortner, C., Shapeev, A. V., 2016. Analysis of boundary conditions for crystal defect atomistic simulations. Archive for Rational Mechanics and Analysis 222 (3), 1217–1268.

Epstein, M., Elzanowski, M., 2007. Material Inhomogeneities and their Evolution: A Geometric Approach. Interaction of Mechanics and Mathematics. Springer Berlin Heidelberg.

Ercolessi, F., Adams, J. B., 1994. Interatomic potentials from first-principles calculations: The force-matching method. EPL (Europhysics Letters) 26 (8), 583.

Eringen, A., 2002. Nonlocal Continuum Field Theories. Springer New York.

Escaig, B., 1968. Sur le glissement dévié des dislocations dans la structure cubique à faces centrées. Journal de Physique 29 (2-3), 225–239.

Eshelby, J., 1949. Edge dislocations in anisotropic materials. The London, Edinburgh, and Dublin Philosophical Magazine and Journal of Science 40 (308), 903–912.

Eshelby, J., Read, W., Shockley, W., 1953. Anisotropic elasticity with applications to dislocation theory. Acta Metallurgica 1 (3), 251 – 259.

Eshelby, J. D., 1951. The force on an elastic singularity. Philosophical Transactions of the Royal Society of London. Series A, Mathematical and Physical Sciences 244 (877), 87–112.

Fitzgerald, S., Aubry, S., 2010. Self-force on dislocation segments in anisotropic crystals. Journal of Physics Condensed Matter 22 (29).

Fleck, N., Hutchinson, J., 2001. A reformulation of strain gradient plasticity. Journal of the Mechanics and Physics of Solids 49 (10), 2245–2271.

Forest, S., 2009. Micromorphic approach for gradient elasticity, viscoplasticity, and damage. Journal of Engineering Mechanics 135 (3), 117–131.

Forest, S., Guéoninchault, N., 2013. Inspection of free energy functions in gradient crystal plasticity. Acta Mechanica Sinica/Lixue Xuebao 29 (6), 763–772.

Frank, F., 1951. Lxxxiii. crystal dislocations.—elementary concepts and definitions. Philosophical Magazine Series 7 42 (331), 809–819.

Frenkel, D., Smit, B., 01 1996. Understanding molecular simulation : from algorithms to applications. 2nd ed. Vol. 50.

Frenkel, J., Jul 1926. Zur theorie der elastizitätsgrenze und der festigkeit kristallinischer körper. Zeitschrift für Physik 37 (7), 572–609.

Fritzen, F., Hodapp, M., 2016. The finite element square reduced (fe^{2r}) method with gpu acceleration: towards three-dimensional two-scale simulations. International Journal for Numerical Methods in Engineering 107 (10), 853–881.

Gallego, R., Ortiz, M., 1993. A harmonic/anharmonic energy partition method for lattice statics computations. Modelling and Simulation in Materials Science and Engineering 1 (4), 417.

Girifalco, L. A., Weizer, V. G., May 1959. Application of the morse potential function to cubic metals. Phys. Rev. 114, 687–690.

Gracie, R., Oswald, J., Belytschko, T., 2008. On a new extended finite element method for dislocations: Core enrichment and nonlinear formulation. Journal of the Mechanics and Physics of Solids 56 (1), 200–214.

Gracie, R., Ventura, G., Belytschko, T., 2007. A new fast finite element method for dislocations based on interior discontinuities. International Journal for Numerical Methods in Engineering 69 (2), 423–441.

Greengard, L., Rokhlin, V., 1987. A fast algorithm for particle simulations. Journal of Computational Physics 73 (2), 325 – 348.

Gurtin, M., 1999. Configurational Forces as Basic Concepts of Continuum Physics. Applied Mathematical Sciences. Springer New York.

Gurtin, M., 2002. A gradient theory of single-crystal viscoplasticity that accounts for geometrically necessary dislocations. Journal of the Mechanics and Physics of Solids 50 (1), 5–32.

Hackbusch, W., Apr 1999. A sparse matrix arithmetic based on $\mathcal{H}$ -matrices. part i: Introduction to $\mathcal{H}$ -matrices. Computing 62 (2), 89–108.

Hackbusch, W., 12 2015. Hierarchical Matrices: Algorithms and Analysis. Vol. 49.

Hartley, C., Mishin, Y., 2005a. Characterization and visualization of the lattice misfit associated with dislocation cores. Acta Materialia 53 (5), 1313–1321.

Hartley, C., Mishin, Y., 2005b. Representation of dislocation cores using nye tensor distributions. Materials Science and Engineering A 400-401 (1-2 SUPPL.), 18–21.

Hirth, J., Lothe, J., 1982. Theory of Dislocations. Krieger Publishing Company.

Hochrainer, T., Sandfeld, S., Zaiser, M., Gumbsch, P., 2014. Continuum dislocation dynamics: Towards a physical theory of crystal plasticity. Journal of the Mechanics and Physics of Solids 63 (1), 167–178.

Hochrainer, T., Zaiser, M., Gumbsch, P., 2007. A three-dimensional continuum theory of dislocation systems: Kinematics and mean-field formulation. Philosophical Magazine 87 (8-9), 1261–1282.

Hodapp, M., 2017. Analysis of a lattice green function method for a/c coupling problems. Tech. rep., École polytechnique fédérale de Lausanne.

Hodapp, M., Anciaux, G., Molinari, J.-F., Curtin, W., 2018a. Coupled atomistic/discrete dislocation method in 3d part ii: Validation of the method. Journal of the Mechanics and Physics of Solids 119, 1 – 19.

Hodapp, M., Anciaux, G., Molinari, J.-F., Curtin, W., 2018b. Three-dimensional coupled atomistic/discrete dislocation method for effectively infinite problems. *In preparation*.

Hodapp, M., Curtin, W. A., Anciaux, G., 2018c. Lattice green function methods for atomistic/continuum coupling: Theory and data-sparse implementation. Computer Methods in Applied Mechanics and Engineering *(under review)*.

Hohenberg, P., Kohn, W., 1964. Inhomogeneous electron gas. Physical Review 136 (3B), B864–B871.

Honeycutt, J., Andersen, H., 1987. Molecular dynamics study of melting and freezing of small lennard-jones clusters. Journal of Physical Chemistry 91 (19), 4950–4963.

Hull, D., Bacon, D., 2001. Introduction to Dislocations. Elsevier Science.

Indenbom, V., Lothe, J., 1992. Elastic strain fields and dislocation mobility. Modern problems in condensed matter sciences. North-Holland.

Irani, N., Remmers, J., Deshpande, V., 2015. Finite strain discrete dislocation plasticity in a total lagrangian setting. Journal of the Mechanics and Physics of Solids 83, 160 – 178.

Jirasek, M., Bazant, Z., 2002. Inelastic Analysis of Structures. John Wiley & Sons.

Junge, T., 2014. Modelling plasticity in nanoscale contact. Ph.D. thesis, École polytechnique fédérale de Lausanne.

Junge, T., Anciaux, G., Molinari, J.-F., 2015. Dynamic stability of displacement-based atomistic/continuum coupling methods. Journal Of The Mechanics And Physics Of Solids 80, 18. 103–120.

Kelchner, C. L., Plimpton, S. J., Hamilton, J. C., Nov 1998. Dislocation nucleation and defect structure during surface indentation. Phys. Rev. B 58, 11085–11088.

Knap, J., Ortiz, M., 2001. An analysis of the quasicontinuum method. Journal of the Mechanics and Physics of Solids 49 (9), 1899–1923.

Knoll, D., Keyes, D., 2004. Jacobian-free newton–krylov methods: a survey of approaches and applications. Journal of Computational Physics 193 (2), 357 – 397.

Kochmann, D., Venturini, G., 2014. A meshless quasicontinuum method based on local maximum-entropy interpolation. Modelling and Simulation in Materials Science and Engineering 22 (3).

Kohlhoff, S., Gumbsch, P., Fischmeister, H., 1991. Crack propagation in b.c.c. crystals studied with a combined finite-element and atomistic model. Philosophical Magazine A: Physics of Condensed Matter, Structure, Defects and Mechanical Properties 64 (4), 851–878.

Kohlhoff, S., Schmauder, S., 1989. A New Method for Coupled Elastic-Atomistic Modelling. Springer US, Boston, MA, pp. 411–418.

Kriemann, R., 2017. Private communication.

Kriemann, R., Le Borne, S., Jun 2015. $\mathcal{H}$-fainv: hierarchically factored approximate inverse preconditioners. Computing and Visualization in Science 17 (3), 135–150.

Kröner, E., 1958. Kontinuumstheorie der Versetzungen und Eigenspannungen. Ergebnisse der Angewandten Mathematik. Springer.

Lazar, M., 2013. The fundamentals of non-singular dislocations in the theory of gradient elasticity: Dislocation loops and straight dislocations. International Journal of Solids and Structures 50 (2), 352–362.

Le, K., Stumpf, H., 1993. Constitutive equations for elastoplastic bodies at finite strain: thermodynamic implementation. Acta Mechanica 100 (3-4), 155–170.

Leibfried, G., Lücke, K., May 1949. Über das spannungsfeld einer versetzung. Zeitschrift für Physik 126 (5), 450–464.

LeSar, R., 2004. Ambiguities in the calculation of dislocation self energies. physica status solidi (b) 241 (13), 2875–2880.

Li, X., 2009. Efficient boundary conditions for molecular statics models of solids. Physical Review B - Condensed Matter and Materials Physics 80 (10).

Lifshits, I., Rozentsveig, L., 1947. On construction of green's tensor for the basic equation of elasticity in the case of unbounded elastoanisotropic medium. Zh. Vych. Mat. Mat. Fiz. 17 (9), 783–791.

Liu, X.-Y., Adams, J., Ercolessi, F., Moriarty, J., 1996. Eam potential for magnesium from quantum mechanical forces. Modelling and Simulation in Materials Science and Engineering 4 (3), 293–303.

Lubarda, V., Blume, J., Needleman, A., 1993. Analysis of equilibrium dislocation distributions. Acta metallurgica et materialia 41 (2), 625–642.

Luskin, M., Ortner, C., 2013. Atomistic-to-continuum coupling. Acta Numerica 22, 397–508.

Martin, J. W., 1975. Many-body forces in metals and the brugger elastic constants. Journal of Physics C: Solid State Physics 8 (18), 2837.

Martinsson, P.-G., 2002. Fast multiscale methods for lattice equations. Ph.D. thesis.

Martinsson, P.-G., 2011. A fast randomized algorithm for computing a hierarchically semiseparable representation of a matrix. SIAM Journal on Matrix Analysis and Applications 32 (4), 1251–1274.

Maugin, G., 1993. Material Inhomogeneities in Elasticity. Applied Mathematics. Taylor & Francis.

Maugin, G., 2016. Non-Classical Continuum Mechanics: A Dictionary. Advanced Structured Materials. Springer Singapore.

Maugin, G. A., 2010. Configurational Forces: Thermomechanics, Physics, Mathematics, and Numerics. Modern Mechanics and Mathematics. CRC Press, Hoboken, NJ.

Miller, R., Shilkrot, L., Curtin, W., 2004. A coupled atomistics and discrete dislocation plasticity simulation of nanoindentation into single crystal thin films. Acta Materialia 52 (2), 271–284.

Miller, R., Tadmor, E., 2009. A unified framework and performance benchmark of fourteen multiscale atomistic/continuum coupling methods. Modelling and Simulation in Materials Science and Engineering 17 (5).

Möller, J. J., Bitzek, E., 2015. On the influence of crack front curvature on the fracture behavior of nanoscale cracks. Engineering Fracture Mechanics 150, 197 – 208.

Monkhorst, H. J., Pack, J. D., Jun 1976. Special points for brillouin-zone integrations. Phys. Rev. B 13, 5188–5192.

Morse, P. M., Jul 1929. Diatomic molecules according to the wave mechanics. ii. vibrational levels. Phys. Rev. 34, 57–64.

Moës, N., Dolbow, J., Belytschko, T., 1999. A finite element method for crack growth without remeshing. International Journal for Numerical Methods in Engineering 46 (1), 131–150.

Mura, T., 1982. Micromechanics of Defects in Solids. Comparative Studies in Overseas History. Springer Netherlands.

Nabarro, F., 1967. Theory of crystal dislocations. International series of monographs on physics. Clarendon P.

Nemat-Nasser, S., 1979. Decomposition of strain measures and their rates in finite deformation elastoplasticity. International Journal of Solids and Structures 15 (2), 155 – 166.

Nocedal, J., Wright, S., 2006. Numerical Optimization. Springer Series in Operations Research and Financial Engineering. Springer New York.

Nye, J., 1953. Some geometrical relations in dislocated crystals. Acta Metallurgica 1 (2), 153–162.

Osetsky, Y. N., Bacon, D. J., 2003. An atomic-level model for studying the dynamics of edge dislocations in metals. Modelling and Simulation in Materials Science and Engineering 11 (4), 427.

Parks, M. L., Bochev, P. B., Lehoucq, R. B., 2008. Connecting atomistic-to-continuum coupling and domain decomposition. Multiscale Modeling & Simulation 7 (1), 362–380.

Pastewka, L., Sharp, T. A., Robbins, M. O., Aug 2012. Seamless elastic boundaries for atomistic calculations. Phys. Rev. B 86, 075459.

Pavia, F., Curtin, W., 2015. Parallel algorithm for multiscale atomistic/continuum simulations using lammps. Modelling and Simulation in Materials Science and Engineering 23 (5).

Peach, M., Koehler, J. S., Nov 1950. The forces exerted on dislocations and the stress fields produced by them. Phys. Rev. 80, 436–439.

Plimpton, S., 1995. Fast parallel algorithms for short-range molecular dynamics. Journal of Computational Physics 117 (1), 1–19.

Po, G., Lazar, M., Seif, D., Ghoniem, N., 2014. Singularity-free dislocation dynamics with strain gradient elasticity. Journal of the Mechanics and Physics of Solids 68 (1), 161–178.

Qu, S., Shastry, V., Curtin, W., Miller, R., 2005. A finite-temperature dynamic coupled atomistic/discrete dislocation method. Modelling and Simulation in Materials Science and Engineering 13 (7), 1101–1118.

Quarteroni, A., Valli, A., 1999. Domain Decomposition Methods for Partial Differential Equations. Numerical mathematics and scientific computation. Clarendon Press.

Rao, S., 2017. Private communication.

Rao, S., Hernandez, C., Simmons, J., Parthasarathy, T., Woodward, C., 1998. Green's function boundary conditions in two-dimensional and three-dimensional atomistic simulations of dislocations. Philosophical Magazine A: Physics of Condensed Matter, Structure, Defects and Mechanical Properties 77 (1), 231–256.

Regueiro, R., Bammann, D., Marin, E., Garikipati, K., 2002. A nonlocal phenomenological anisotropic finite deformation plasticity model accounting for dislocation defects. Journal of Engineering Materials and Technology, Transactions of the ASME 124 (3), 380–387.

Roters, F., Eisenlohr, P., Bieler, T. R., Raabe, D., 2011. Crystal Plasticity Finite Element Methods: In Materials Science and Engineering. John Wiley & Sons.

Saad, Y., 1980. Variations on arnoldi's method for computing eigenelements of large unsymmetric matrices. Linear Algebra and its Applications 34, 269 – 295.

Saad, Y., Schultz, M. H., 1986. Gmres: A generalized minimal residual algorithm for solving nonsymmetric linear systems. SIAM Journal on Scientific and Statistical Computing 7 (3), 856–869.

Shenoy, V., Miller, R., Tadmor, E., Rodney, D., Phillips, R., Ortiz, M., 1999. An adaptive finite element approach to atomic-scale mechanics - the quasicontinuum method. Journal of the Mechanics and Physics of Solids 47 (3), 611–642.

Shenoy, V. B., Kukta, R. V., Phillips, R., Feb 2000. Mesoscopic analysis of structure and strength of dislocation junctions in fcc metals. Phys. Rev. Lett. 84, 1491–1494.

Shenoy, V. B., Phillips, R., 1997. Finite-sized atomistic simulations of screw dislocations. Philosophical Magazine A 76 (2), 367–385.

Shiari, B., Miller, R., Curtin, W., 2005. Coupled atomistic/discrete dislocation simulations of nanoindentation at finite temperature. Journal of Engineering Materials and Technology, Transactions of the ASME 127 (4), 358–368.

Shilkrot, L., Curtin, W., Miller, R., 2002a. A coupled atomistic/continuum model of defects in solids. Journal of the Mechanics and Physics of Solids 50 (10), 2085–2106.

Shilkrot, L., Miller, R., Curtin, W., 2002b. Coupled atomistic and discrete dislocation plasticity. Physical Review Letters 89 (2), 255011–255014.

Shilkrot, L., Miller, R., Curtin, W., 2004. Multiscale plasticity modeling: Coupled atomistics and discrete dislocation mechanics. Journal of the Mechanics and Physics of Solids 52 (4), 755–787.

Shimokawa, T., Mortensen, J., Schiøtz, J., Jacobsen, K., 2004. Matching conditions in the quasicontinuum method: Removal of the error introduced at the interface between the coarse-grained and fully atomistic region. Physical Review B - Condensed Matter and Materials Physics 69 (21), 214104–1–214104–10.

Sinclair, J., Gehlen, P., Hoagland, R., Hirth, J., 1978. Flexible boundary conditions and nonlinear geometric effects in atomic dislocation modeling. Journal of Applied Physics 49 (7), 3890–3897.

Sinclair, J. E., 1971. Improved atomistic model of a bcc dislocation core. Journal of Applied Physics 42 (13), 5321–5329.

Sinclair, J. E., 1975. The influence of the interatomic force law and of kinks on the propagation of brittle cracks. The Philosophical Magazine: A Journal of Theoretical Experimental and Applied Physics 31 (3), 647–671.

Steinberger, D., Leimberger, M., Sandfeld, S., 2016. D2C — Converting and Compressing Discrete Dislocation Microstructure Data. Wiley-Blackwell, Ch. 64, pp. 531–538.

Steinmann, P., 1996. Views on multiplicative elastoplasticity and the continuum theory of dislocations. International Journal of Engineering Science 34 (15), 1717–1735.

Stukowski, A., 2010. Visualization and analysis of atomistic simulation data with ovito–the open visualization tool. Modelling and Simulation in Materials Science and Engineering 18 (1), 015012.

Stukowski, A., 2014. A triangulation-based method to identify dislocations in atomistic models. Journal of the Mechanics and Physics of Solids 70 (1), 314–319.

Stukowski, A., Albe, K., 2010a. Dislocation detection algorithm for atomistic simulations. Modelling and Simulation in Materials Science and Engineering 18 (2).

Stukowski, A., Albe, K., 2010b. Extracting dislocations and non-dislocation crystal defects from atomistic simulation data. Modelling and Simulation in Materials Science and Engineering 18 (8).

Stukowski, A., Arsenlis, A., 2012. On the elasticplastic decomposition of crystal deformation at the atomic scale. Modelling and Simulation in Materials Science and Engineering 20 (3).

Stukowski, A., Bulatov, V., Arsenlis, A., 2012. Automated identification and indexing of dislocations in crystal interfaces. Modelling and Simulation in Materials Science and Engineering 20 (8).

Sutradhar, A., Paulino, G., Gray, L., 2008. Symmetric Galerkin Boundary Element Method. Springer Berlin Heidelberg.

Szajewski, B., Curtin, W., 2015. Analysis of spurious image forces in atomistic simulations of dislocations. Modelling and Simulation in Materials Science and Engineering 23 (2).

Szajewski, B., Pavia, F., Curtin, W., 2015. Robust atomistic calculation of dislocation line tension. Modelling and Simulation in Materials Science and Engineering 23 (8).

Tadmor, E., Miller, R., 2011. Modeling Materials: Continuum, Atomistic and Multiscale Techniques. Cambridge University Press.

Tadmor, E., Ortiz, M., Phillips, R., 1996. Quasicontinuum analysis of defects in solids. Philosophical Magazine A: Physics of Condensed Matter, Structure, Defects and Mechanical Properties 73 (6), 1529–1563.

Taylor, G. I., 1934. The mechanism of plastic deformation of crystals. part i. theoretical. Proceedings of the Royal Society of London A: Mathematical, Physical and Engineering Sciences 145 (855), 362–387.

Tembhekar, I., Amelang, J. S., Munk, L., Kochmann, D. M., 2017. Automatic adaptivity in the fully nonlocal quasicontinuum method for coarse-grained atomistic simulations. International Journal for Numerical Methods in Engineering 110 (9), 878–900.

Teodosiu, C., Sidoroff, F., 1976. A theory of finite elastoviscoplasticity of single crystals. International Journal of Engineering Science 14 (2), 165–176.

Tewary, V., 1973. Green-function method for lattice statics. Advances in Physics 22 (6), 757–810.

The CGAL Project, 2017. CGAL User and Reference Manual, 4.9.1 Edition. CGAL Editorial Board.

Trefethen, L., 2000. Spectral Methods in MATLAB. Society for Industrial and Applied Mathematics.

Trinkle, D. R., Jul 2008. Lattice green function for extended defect calculations: Computation and error estimation with long-range forces. Phys. Rev. B 78, 014110.

Truesdell, C., Noll, W., 1965. The Non-Linear Field Theories of Mechanics. No. Bd. 3 in The non-linear field theories of mechanics. Springer.

Truesdell, C., Toupin, R., 1960. The classical field theories. Springer.

Van Der Giessen, E., Needleman, A., 1995. Discrete dislocation plasticity: A simple planar model. Modelling and Simulation in Materials Science and Engineering 3 (5), 689–735.

Van Koten, B., Li, X. H., Luskin, M., Ortner, C., 2012. A Computational and Theoretical Investigation of the Accuracy of Quasicontinuum Methods. Springer Berlin Heidelberg, Berlin, Heidelberg, pp. 67–96.

Varvenne, C., Luque, A., Nöhring, W., Curtin, W., 2016. Average-atom interatomic potential for random alloys. Physical Review B 93 (10).

Volterra, V., 1907. Sur l’équilibre des corps élastiques multiplement connexes. Annales scientifiques de l’École Normale Supérieure 24, 401–517.

Warner, D., Curtin, W., Qu, S., 2007. Rate dependence of crack-tip processes predicts twinning trends in f.c.c. metals. Nature Materials 6 (11), 876–881.

Weygand, D., Friedman, L., Van Der Giessen, E., Needleman, A., 2002. Aspects of boundary-value problem solutions with three-dimensional dislocation dynamics. Modelling and Simulation in Materials Science and Engineering 10 (4), 437–468.

Woodward, C., Rao, S. I., 2001. Ab-initio simulation of isolated screw dislocations in bcc mo and ta. Philosophical Magazine A 81 (5), 1305–1316.

Xiao, S., Belytschko, T., 2004. A bridging domain method for coupling continua with molecular dynamics. Computer Methods in Applied Mechanics and Engineering 193 (17-20), 1645–1669.

Yavari, A., Ortiz, M., Bhattacharya, K., Jan 2007. A theory of anharmonic lattice statics for analysis of defective crystals. Journal of Elasticity 86 (1), 41–83.

Glossary

Miscellaneous

$\mathbb{R}$	Set of real numbers
$\mathbb{N}$	Set of natural numbers
$\mathbb{Z}$	Set of integers
$\mathbb{C}$	Set of complex numbers
$\mathbb{R}^d$	d-dimensional Euclidean space
$\boldsymbol{n}$	Unit normal vector
$\boldsymbol{\epsilon}$	Third-order permutation tensor (Levi-Civita tensor)
δ	Dirac delta function (or: Kronecker delta with subindices i, j, i.e. δ_{ij})
$\boldsymbol{u}$	Displacement
$\mathit{\Pi}$	Total energy of a mechanical system
$\mathit{\Pi}^{\mathrm{int}}$, $\mathit{\Pi}^{\mathrm{ext}}$	Internal and external energy of a mechanical system ($\mathit{\Pi} = \mathit{\Pi}^{\mathrm{int}} + \mathit{\Pi}^{\mathrm{ext}}$)
$\boldsymbol{f}$	Force vector
r_{cut}	Cut-off radius

Continuum and discrete dislocation mechanics

$\mathit{\Omega}_0$, $\mathit{\Omega}$	Reference and current placement of a continuous body
$\mathit{\Omega}^{\mathrm{core}}$	Dislocation core region
$\boldsymbol{X}, \boldsymbol{Y}$	Material points in the reference configuration
$\boldsymbol{x}, \boldsymbol{y}$	Material points in the current configuration
χ	Motion of a material point $\boldsymbol{X}$
$\boldsymbol{v}$	Dislocation velocity vector
$\boldsymbol{F}$	Deformation gradient
$\boldsymbol{\varepsilon}$	Small strain tensor
$\boldsymbol{\varepsilon}^{\mathrm{e}}$, $\boldsymbol{\varepsilon}^{\mathrm{p}}$	Elastic and plastic part of $\boldsymbol{\varepsilon}$
$\boldsymbol{\varepsilon}^{\mathrm{ns,p}}$	Nonsingular plastic strain
$\boldsymbol{\beta}$	Distortion tensor

$\boldsymbol{\beta}^{\mathrm{e}}$, $\boldsymbol{\beta}^{\mathrm{p}}$	Elastic and plastic distortion tensors
$\boldsymbol{\beta}^{\mathrm{p,ns}}$	Nonsingular plastic distortion
ψ	Helmholtz free energy density
$\mathit{\Pi}^{\mathrm{e}}$, $\mathit{\Pi}^{\mathrm{core}}$	Elastic and core energy contribution of $\mathit{\Pi}$
W	Energy per unit length of the dislocation line
W^{e}, W^{core}	Elastic and core energy per unit length of γ ($W = W^{\mathrm{e}} + W^{\mathrm{core}}$)
$\boldsymbol{\sigma}$	Cauchy stress tensor
τ	Scalar shear stress
$\boldsymbol{P}$	First Piola-Kirchhoff stress tensor
$\boldsymbol{t}$	Traction vector
$\boldsymbol{B}$	Eshelby stress tensor
$\boldsymbol{f}^{\mathrm{body}}$	Body force
$\boldsymbol{f}^{\mathrm{pk}}$	Peach-Koehler force
$\boldsymbol{f}^{\mathrm{core}}$	Force on γ due to core energy contribution $\mathit{\Pi}^{\mathrm{core}}$
$\mathbb{C}$	Material stiffness tensor
μ, λ	Lamé constants
ν	Poisson ratio
$\mathscr{S}$	Slip plane
γ	Discrete dislocation line
$\boldsymbol{s}$	Material point on γ
$\boldsymbol{t}$, $\boldsymbol{m}$	Unit tangent and normal vector of the dislocation line
b	Magnitude of the Burgers vector
$\boldsymbol{b}$	Burgers vector
$\boldsymbol{\alpha}$	Dislocation density tensor
$r_{\mathrm{cut}}^{\mathrm{core}}$	Dislocation core cut-off radius
ϑ	Character angle of the dislocation line
w	Isotropic spreading function of the Burgers vector ($\boldsymbol{\beta}^{\mathrm{p,ns}} = \boldsymbol{\beta}^{\mathrm{p}} * w$)
a	Isotropic core spreading width
E^{core}	Scalar core energy parameter of the isotropic core energy model
$\boldsymbol{M}$, $\boldsymbol{D}$	Mobility and drag tensor of the dislocation line γ
$\tilde{\boldsymbol{u}}$, $\tilde{\boldsymbol{\sigma}}$	Displacement and stress field of an isolated dislocation in $\mathbb{R}^3$
$\hat{\boldsymbol{u}}$, $\hat{\boldsymbol{\sigma}}$	Corrective fields due to boundary conditions on $\partial\mathit{\Omega}$
$\mathcal{P}^{\mathrm{c/p}}$	Physical continuum problem (:= balance of linear momentum)
$\mathcal{P}^{\mathrm{c/dd}}$	DDD problem
$\mathcal{P}^{\mathrm{c}}$	Continuum problem (:= $\mathcal{P}^{\mathrm{c/p}} \wedge \mathcal{P}^{\mathrm{c/dd}}$)
$\boldsymbol{G}^{\mathrm{cgf}}$	Continuum Green tensor
$\mathcal{V}$	Space of square-integrable functions with weak derivative

Atomistic modeling and flexible boundary conditions

$\mathit{\Lambda}$	Bravais lattice
ξ, η, ζ	Atomic indices

$\boldsymbol{\xi}, \boldsymbol{\eta}, \boldsymbol{\zeta}$	Positions of atoms ξ, η, ζ
$\mathcal{E}_\xi$	Site energy of an atom ξ
$\boldsymbol{f}^{\text{ext}}$	External force vector (defined on a lattice)
$\mathcal{R}_\xi$	Interaction range of atom $\boldsymbol{\xi}$
a_0	Lattice constant
$\mathcal{P}^{\text{a}}$	Atomistic force balance
$\mathcal{L}$	Differential operator ($\mathcal{L}[\boldsymbol{u}](\boldsymbol{\xi}) = \delta_{\boldsymbol{\xi}}\mathit{\Pi}$)
$\mathcal{L}_{\text{h}}, \mathcal{L}_{\text{ah}}$	Harmonic and anharmonic operators ($\mathcal{L} = \mathcal{L}_{\text{h}} + \mathcal{L}_{\text{ah}}$)
$\mathcal{G}$	Green operator ($\mathcal{G}\mathcal{L}_{\text{h}} = \mathcal{I}$)
$\mathcal{F}$	Force operator for boundary forces (e.g. $\mathcal{G}^{\text{i+/i}}\mathcal{L}_{\text{h}}^{\text{i/i+}}$ etc.)
$\boldsymbol{K}$	Nodal stiffness tensor
$\boldsymbol{G}^{\text{lgf}}$	Lattice Green tensor
$\hat{L}, \hat{G}, \hat{F}$	Matrix representations of $\mathcal{L}$, $\mathcal{G}$ and $\mathcal{F}$
$\mathcal{U}$	Space of lattice functions
$\mathcal{U}^\star$	Space of square-summable lattice functions

Coupled atomistic/discrete dislocations

$\mathit{\Gamma}_{\text{i}}$	Artificial interface between the atomistic and the continuum domain
$\mathcal{P}^{\text{cadd}}$	CADD problem ($:= \mathcal{P}^{\text{a}} \wedge \mathcal{P}^{\text{c}}$)
$\mathcal{P}^{\text{p}}$	Physical subproblem of $\mathcal{P}^{\text{cadd}}$ ($:= \mathcal{P}^{\text{a}} \wedge \mathcal{P}^{\text{c/p}}$)
$\tilde{\mathcal{P}}^{\text{c/p}}$	Infinite part of $\mathcal{P}^{\text{c/p}}$
$\hat{\mathcal{P}}^{\text{c/p}}$	Finite part of $\mathcal{P}^{\text{c/p}}$
$\mathcal{P}^{\text{c}/\infty}$	Infinite continuum problem $\tilde{\mathcal{P}}^{\text{c/p}} \wedge \mathcal{P}^{\text{c/dd}}$
$\tilde{\mathcal{P}}^{\text{cadd}}$	Approximate CADD problem
γ^{hyb}	Hybrid discrete dislocation line ($:= \gamma^{\text{a}} \cup \gamma^{\text{c}}$)
$\mathit{\Delta}\tilde{\boldsymbol{u}}^{\text{corr}}$	Core template correction
$\boldsymbol{s}^{\text{trans}}$	Transmission node
$\mathit{\Omega}^{\text{detn}}$	Detection domain
γ^{detn}	Detected discrete dislocation line $\mathit{\Omega}^{\text{detn}}$
$\gamma^{\text{a}}_{\text{v}}$	Virtual subset of a discrete dislocation line in $\mathit{\Omega}^{\text{a}} \setminus \mathit{\Omega}^{\text{detn}}$ which is used to artificially close a loop in $\mathit{\Omega}^{\text{a}}$
$\tilde{\gamma}^{\text{a}}$	$:= \gamma^{\text{detn}} \cup \gamma^{\text{a}}_{\text{v}}$
$\tilde{\gamma}^{\text{hyb}}$	$:= \tilde{\gamma}^{\text{a}} \cup \gamma^{\text{c}}$

Acronyms

A/C coupling	atomistic/continuum coupling
bcc	body-centered cubic
BEM	boundary element method
BIE	boundary integral equation

Glossary

BSE	boundary summation equation
CB model	Cauchy-Born model
CADD	coupled atomistic/discrete dislocations
DBEM	discrete boundary element method
DDD	discrete dislocation dynamics
DXA	dislocation extraction algorithm
EAM	embedded atom method
fcc	face-centered cubic
FIRE	fast inertia relaxation engine
FEM	finite element method
GMRes method	generalized minimal residual method
CGF, LGF	continuum/lattice Green function
LM	libMultiscale
MD	molecular dynamics
PK force	Peach-Koehler force
PAD	periodic array of dislocations
QC	Quasicontinuum

Max Hodapp

Phone (work): +41 21 69 31965 E-Mail: max.hodapp@epfl.ch

Personal Details

Place of Birth: Freiburg i. Breisgau, Germany
Nationality: German
Martial Status: Single

Education

10/2006 – 05/2013 *Diplom-Ingenieur*[*] (*Dipl.-Ing.*)
Diploma Degree Program in Mechanical Engineering, average grade: “very good”
Karlsruhe Institute of Technology (**KIT**), Karlsruhe, Germany
Field of study: Theoretical Mechanics
Specialized subjects: 1) Computational Mechanics
2) Material Science and Molecular Dynamics

Experience

02/2014 – today *Research assistant / PhD student*
Ecole polytechnique fédérale de Lausanne (**EPFL**), Lausanne, Switzerland
School of Engineering, Institute of Mechanical Engineering
Laboratory for Multiscale Mechanics Modeling (LAMMM)
Scope of work: Numerical and algorithmic aspects of coupled multiscale problems

07/2013 – 12/2013 *Research assistant*
Karlsruhe Institute of Technology (**KIT**), Karlsruhe, Germany
Institute of Engineering Mechanics, **Chair for Continuum Mechanics**
Young Investigator Group Computer Aided Material Modeling (**YIG-CAMM**)
Scope of work: Scientific computing in the field of computer aided homogenization methods

11/2012 – 05/2013 *Graduation candidate* (diploma thesis)
Karlsruhe Institute of Technology (**KIT**), Karlsruhe, Germany
Institute of Engineering Mechanics, **Chair for Continuum Mechanics**
Thesis title: “Parallelization of order-reduction based homogenization methods on Nvidia GPUs”

07/2005 – 04/2006 *Armored infantryman*, final rank: *Obergefreiter,* equivalent to *Private First Class* (U.S. Army)
German Armed Forces, Stetten a. k. M./Immendingen, Germany
Mandatory military service

---

[*] The degree „Diplom-Ingenieur“ corresponds to a „Master of Science“ at universities or equivalent higher education institutions (see the report of the Kultusministerkonferenz from March 5, 1999)